



Université de Neuchâtel

Institut de Microtechnique

**Thin Film Microcrystalline
Silicon Layers and Solar Cells:
Microstructure and Electrical Performances**

Thèse

Présentée à la Faculté des Sciences
pour l'obtention du titre de Docteur ès Sciences

par

Corinne Droz

Novembre 2003

IMPRIMATUR POUR LA THESE

**Thin film microcrystalline silicon layers
and solar cells: microstructure and
electrical performances**

Mme Corinne DROZ

UNIVERSITE DE NEUCHATEL

FACULTE DES SCIENCES

La Faculté des sciences de l'Université de
Neuchâtel, sur le rapport des membres du jury

MM. A. Shah (directeur de thèse),
J. Faist, A. Perret (CSEM), B. Rech (Jülich D),
H. Schade (Putzbrunn D) et
M. Vanecek (Prague CZ)

autorise l'impression de la présente thèse.

Neuchâtel, le 22 décembre 2003

La doyenne:



Martine Rahier

Table of Contents

<i>Abstract</i>	1
<i>Résumé</i>	3
<u>Chapter 1: Introduction</u>	5
1.1. Motivation	5
1.1.1. The need for photovoltaics (PV).....	5
1.1.2. The role of silicon thin films in PV.....	6
1.2. Hydrogenated microcrystalline silicon ($\mu\text{c-Si:H}$)	8
1.2.1. Microstructure of $\mu\text{c-Si:H}$	8
1.2.1.1. Techniques for the characterisation of the microstructure	10
1.2.2. Deposition technique for thin film silicon layers and solar cells: VHF PE-CVD	10
1.2.3. Hydrogenated amorphous silicon (a-Si:H).....	12
1.2.4. Stability of $\mu\text{c-Si:H}$	13
1.3. Outline of this thesis	14
<u>Chapter 2: Micro-Raman spectroscopy</u>	17
2.1. Introduction	17
2.2. Theory of Raman spectroscopy	19
2.2.1. Raman scattering effect.....	19
2.2.2. Raman spectra	21
2.2.3. Application to silicon thin films.....	21
2.3. Experimental	23
2.3.1. Description of the experimental micro-Raman set-up	23
2.3.2. Acquiring Raman spectra.....	26
2.4. Basic experimental considerations and issues	27
2.4.1. Confocal spectroscopy	27

2.4.2. Effect of the excitation light intensity.....	29
2.4.3. Background noise and CCD hot pixels.....	30
2.5. Bifacial depth-dependent micro-Raman technique.....	32
2.5.1. Influence of the excitation light wavelength.....	32
2.5.2. Layer-side and glass-side measurements.....	34
2.6. Interpretation of the Raman spectra	36
2.6.1. Deconvolution.....	36
2.6.1.1. Relation between spectra and material.....	37
2.6.1.2. Gaussian or Lorentzian peaks?.....	39
2.6.1.3. Choice of the range, the baseline and the peak parameters.....	39
2.6.2. Evaluation of the Raman crystallinity volume fraction	41
2.7. Determination of the “real” crystalline volume fraction	42
2.7.1. Evaluation of the Raman cross-section ratio y	42
2.7.2. Discussion.....	47
2.7.2.1. Interpretation of the $C(z)$ curves.....	47
2.7.2.2. Dependence of y on the experimental data used for its evaluation....	49
2.7.2.3. Evaluation of the actual crystallinity of the \square c-Si:H phase (\square)	51
2.8. Conclusions.....	53
<i>Chapter 3: Coplanar electrical transport in intrinsic \squarec-Si:H layers and its relation with microstructure</i>	<i>55</i>
3.1. Introduction.....	55
3.2. Techniques for electrical characterisation of intrinsic thin film silicon layers	56
3.2.1. Dark conductivity.....	57
3.2.2. Measurement techniques of the electronic transport under illumination.....	58
3.2.2.1. Photoconductivity.....	59
3.2.2.2. Ambipolar diffusion length (SSPG technique).....	60
3.2.2.3. The parameter b (indicator of the Fermi level position).....	61
3.2.2.4. The $\square^p \square^q$ product (material transport "quality factor")	62
3.3. Electrical transport in \squarec-Si:H : comparison with a-Si:H.....	64

3.3.1. Introduction.....	64
3.3.2. Power law dependencies of L_{amb}^2 , η_{photo} and b	65
3.3.3. Anticorrelated behaviour of the $\eta^p \eta^R$ products.....	67
3.3.4. Conclusions.....	70
3.4. Electrical transport versus microstructure in a silane concentration (SC) series of silicon layers	71
3.4.1. Introduction.....	71
3.4.2. Electronic transport.....	72
3.4.2.1. Transport without illumination (dark conductivity)	72
3.4.2.2. Transport under illumination (SSPC and SSPG)	73
3.4.3. Evolution of the microstructure and optical properties with SC.....	76
3.4.3.1. Transmission Electron Microscopy (TEM).....	77
3.4.3.2. X-Ray Diffraction (XRD).....	78
3.4.3.3. Atomic Force Microscopy (AFM).....	81
3.4.3.4. Micro-Raman spectroscopy	83
3.4.3.5. Constant Photocurrent Method (CPM) and optical properties.....	85
3.4.3.6. Infra-Red (IR) spectroscopy (hydrogen content)	87
3.4.4. Relation between electronic transport and microstructure.....	88
3.5. Conclusions.....	91

Chapter 4: Microstructure and electrical properties of $\square c$ -Si:H solar cells...93

4.1. Introduction.....	93
4.2. Microcrystalline silicon ($\square c$-Si:H) solar cells.....	94
4.2.1. Structure and principle of operation of $\square c$ -Si:H solar cells.....	94
4.2.2. p-i-n and n-i-p solar cell technologies	96
4.2.3. Description of the solar cells analysed in this chapter.....	97
4.3. Electrical characterisation of solar cells.....	99
4.3.1. Current voltage (IV) characteristics.....	99
4.3.1.1. Theory	99
4.3.1.2. Values obtained for the SC series of n-i-p solar cells	100
4.3.2. Quantum efficiency (QE) measurements.....	101
4.3.2.1. Theory	101
4.3.2.2. Values obtained for the SC series of n-i-p solar cells	102

4.4. Micro-Raman spectroscopy as a probing tool for entire solar cells.....	103
4.4.1. Influence of the additional layers on Raman spectra	104
4.4.1.1. Transparent Conductive Oxide (TCO).....	104
4.4.1.2. <n> and <p> doped layers	105
4.4.2. Raman crystallinity of solar cells versus silane concentration	109
4.4.2.1. Series of n-i-p solar cells deposited on (flat) sputtered ZnO.....	109
4.4.2.2. Series of n-i-p solar cells deposited on (rough) LP-CVD ZnO	112
4.4.2.3. Comparison of both SC series.....	115
4.4.2.4. Average Raman crystallinity.....	118
4.4.3. Discussion	121
4.5. Raman crystallinity versus electrical performances	121
4.5.1. Dependence of the open-circuit voltage on the microstructure	122
4.5.2. Dependence of the short-circuit current on the microstructure	126
4.5.3. Discussion	127
4.5.3.1. Dependence of the open-circuit voltage.....	127
4.5.3.2. Dependence of the short-circuit current.....	131
4.6. Conclusions.....	132
<i>Chapter 5: Final conclusions.....</i>	<i>135</i>
<i>Appendix: Comparison of the $\square^p \square^q$ products for a-Si:H and \square^c-Si:H evaluated in intrinsic layers and in solar cells.....</i>	<i>139</i>
<i>References</i>	<i>143</i>
<i>Acknowledgements.....</i>	<i>149</i>
<i>Curriculum vitae.....</i>	<i>151</i>

Abstract

Hydrogenated microcrystalline silicon ($\mu\text{c-Si:H}$), as grown by the Very High Frequency Plasma Enhanced Chemical Vapour Deposition (VHF PE-CVD) technique, has now been successfully introduced as active layer in complete $\mu\text{c-Si:H}$ solar cells of p-i-n and n-i-p structure. A fundamental question yet to be answered regards the link between the material microstructure, on one hand, and the transport properties of the intrinsic photogenerator layers as well as solar cell electrical performances, on the other hand. This thesis attempts to clarify this link.

$\mu\text{c-Si:H}$ is a complex material that exhibits a wide range of microstructures, depending both on the deposition conditions and on the substrate material. At present, best conversion efficiencies are achieved for $\mu\text{c-Si:H}$ solar cells deposited near the transition between $\mu\text{c-Si:H}$ and a-Si:H (hydrogenated amorphous silicon). The microstructure of $\mu\text{c-Si:H}$ varies while growth of the film proceeds: a fully amorphous incubation layer is frequently observed as the initial grown region. Thereafter, the microcrystalline phase itself follows, consisting of pencil-like conglomerates (of roughly half a micrometer diameter) made of nanocrystals with a diameter of a few tens of nanometres.

Micro-Raman spectroscopy is a non-destructive technique used here for monitoring the crystallinity of $\mu\text{c-Si:H}$ layers and complete solar cells. By applying 514 nm and 633 nm laser excitation light on both top- and bottom-sides of the samples (single layers or complete solar cells), one obtains bifacial depth-dependent Raman spectra that reveal inhomogeneities in thickness, as observed also on Transmission Electron Microscopy (TEM) micrographs.

A Raman crystallinity factor (Γ_c) indicative of the crystalline volume fraction (i.e. crystallinity) is obtained from each Raman spectrum by evaluating the respective scattered intensities assigned to the amorphous and crystalline phases. In order to determine the actual crystalline volume fraction, the value of the Raman cross-section ratio (γ) of $\mu\text{c-Si:H}$ over a-Si:H is needed. By comparing the bifacial depth-dependent spectra of a sample with its TEM micrographs, we have found a value of $\gamma \approx 1.7$, larger than the values published so far ($\gamma \approx 0.1 - 0.9$). This value does not contest, however, the use of the factor Γ_c for the characterisation of $\mu\text{c-Si:H}$ layers and solar cells.

Coplanar electronic transport measured under illumination on various silicon thin-film layers reveals that transport properties in $\mu\text{c-Si:H}$ are similar to those in a-Si:H. Transport properties and microstructural features are compared for a series of layers deposited at various silane concentrations. The normalized mobility μ lifetime product $\mu\tau$ relates to the size of

the conglomerates, rather than to the average size of the individual nanocrystals. Moreover, the ambipolar diffusion length measured in these samples equals, in average, half of the diameter of the conglomerates. These experimental observations indicate that coplanar electronic transport in \square c-Si:H is limited by the defective material present at the conglomerate boundaries.

Bifacial micro-Raman spectroscopy has been carried out on entire single-junction \square c-Si:H solar cells, on which electrical performances were also measured. We have identified the algebraic average \square_c^A of the two Raman crystallinity factors measured with 514 nm excitation light beam (that probes the regions close to the n-i and p-i interfaces), i.e. $\square_c^A = [\square_c^{ni} + \square_c^{pi}]/2$, as constituting a fundamental microstructural parameter for solar cell characterisation. Indeed, **the open-circuit voltage (V_{oc}) linearly decreases when \square_c^A increases**. This has been observed for a large set of n-i-p and p-i-n type solar cells deposited at various deposition conditions.

Résumé

"Couches minces et cellules solaires en silicium microcristallin: microstructure et performances électriques"

Le **silicium microcristallin hydrogéné ($\mu\text{c-Si:H}$)**, tel que fabriqué par la technique de dépôt chimique en phase vapeur assisté par plasma à très haute fréquence (VHF PE-CVD), est maintenant utilisé avec succès en tant que couche active dans des cellules solaires. Cependant, une question fondamentale concerne le lien entre la microstructure du matériau, d'une part, et les propriétés de transport électronique des couches intrinsèques ainsi que les performances électriques des cellules solaires, d'autre part. Cette thèse tente de clarifier cette question.

Le $\mu\text{c-Si:H}$ est un matériau complexe qui présente une grande variété de microstructures, qui dépendent autant des conditions de dépôt que de la nature du substrat. Actuellement, les meilleurs rendements de conversion sont obtenus pour les cellules solaires en $\mu\text{c-Si:H}$ déposé près de la transition entre le $\mu\text{c-Si:H}$ et le silicium amorphe hydrogéné (a-Si:H). La microstructure du $\mu\text{c-Si:H}$ telle qu'observée sur des micrographies prises dans un microscope électronique à transmission (TEM) varie également au cours de la croissance de la couche: on observe souvent une couche complètement amorphe dans la région initiale de croissance. La phase microcristalline proprement dite apparaît ensuite; elle se compose de conglomerats, en forme de crayons (d'environ un demi-micromètre de diamètre), composés de nanocristaux ayant un diamètre de quelques dizaines de nanomètres.

La **micro-spectroscopie Raman** est une technique non-destructive utilisée ici pour mesurer la cristallinité de couches et cellules solaires complètes en $\mu\text{c-Si:H}$. En utilisant des longueurs d'onde d'excitation de 514 nm et 633 nm, et en focalisant le faisceau d'excitation sur le dessus et le dessous des échantillons, on obtient des spectres Raman différents. Ils révèlent les inhomogénéités en épaisseur telles qu'évoquées ci-dessus.

En évaluant, pour chaque spectre Raman, les intensités des pics Raman diffusées respectivement par les phases amorphe et cristalline, on obtient un facteur de cristallinité Raman (\overline{f}_c) indicatif de la fraction cristalline volumique. De manière à déterminer la fraction cristalline volumique réelle, il est nécessaire de connaître la valeur du rapport (γ) des sections efficaces Raman du silicium microcristallin par rapport à l' a-Si:H . En comparant les spectres bifaces obtenus pour les deux longueurs d'onde d'excitation sur un échantillon avec les micrographies TEM correspondantes, nous avons obtenu une valeur de $\gamma \approx 1.7$. Cette valeur est plus grande que les valeurs publiées jusqu'ici ($\gamma \approx 0.1 - 0.9$); cependant, elle ne remet pas

en cause l'utilisation du facteur $\bar{\mu}_c$ pour la caractérisation des couches et des cellules solaires.

Des mesures de **transport électronique coplanaire** sous illumination réalisées sur diverses couches minces de silicium montrent que les propriétés de transport du \square c-Si:H sont similaires à celles de l'a-Si:H. Pour une série de couches déposées à diverses concentrations de silane, correspondant à du matériau de structure variant de très microcristalline à amorphe, nous avons comparé les propriétés de transport avec les caractéristiques microstructurales. Le produit "mobilité \times temps de vie" normalisé $\bar{\mu}_c^p \bar{\tau}_c^p$ est lié à la taille des conglomerats plutôt qu'à la taille moyenne des nanocristaux individuels. De plus, la longueur de diffusion ambipolaire de ces échantillons est égale, en moyenne, à la moitié du diamètre des conglomerats. Ces observations expérimentales indiquent que le transport électronique coplanaire dans le \square c-Si:H est limité par le matériau défectueux présent aux joints des conglomerats.

Nous avons réalisé des mesures de micro-spectroscopie Raman bifaces sur des cellules solaires en \square c-Si:H, sur lesquelles les performances électriques ont aussi été mesurées. Nous avons identifié la moyenne algébrique $\bar{\mu}_c^A$ des deux facteurs de cristallinité Raman mesuré avec une longueur d'onde d'excitation de 514 nm et qui sont sensibles aux régions près des interfaces n-i et p-i, i.e. $\bar{\mu}_c^A = [\bar{\mu}_c^{mi} + \bar{\mu}_c^{pi}]/2$, comme étant un paramètre microstructural fondamental pour la caractérisation des cellules solaires. En effet, la **tension en circuit ouvert (V_{oc}) diminue linéairement quand $\bar{\mu}_c^A$ augmente**. Ceci a été observé pour diverses cellules solaires de type p-i-n et n-i-p déposées avec différentes condition de dépôt. Cette relation est une des premières observations du lien direct entre la microstructure du matériau aux jonctions (interfaces n-i et p-i) et le fonctionnement du dispositif.

Chapter 1: Introduction

1.1. Motivation

1.1.1. The need for photovoltaics (PV)

During the last decades, the energy requirements of our technical civilisation have drastically increased. In Switzerland, for example, the energy consumption has increased fivefold from 1950 to 1990. If this growth rate is maintained, the reserves of oil, uranium and gas will soon run out. Moreover, the consumption of non-renewable resources results obviously in serious problems that affect both the environment (climate changes, pollution) and the society (conflicts between States to control the remaining fossil fuel reserves). In the history of humanity, it is the first time that human activity threatens the ecological balance of the whole planet. It is, thus, imperative to find solutions without too much delay. In the medium to long term, only renewable energies, i.e. energies whose consumption does not lead to the reduction of natural resources, can ensure the supply of energy to future generations. The energy one receives on Earth from the Sun has a very large potential, in the direct form (solar energy) as well as in the indirect form (wind, biomass and hydraulic energy). In parallel with the exploitation of such "clean" energies, it is, however, essential to encourage energy efficiency, in order to decrease or, at least, to stabilize our present consumption. Indeed, it would be absurd to develop new energy sources and, at the same time, to keep on wasting such a precious resource. Provided that sufficient efforts are undertaken, an energy policy based exclusively on the exploitation of renewable resources is actually compatible with our technical civilization [ADER 1997].

Amongst the different renewable energies that have to be developed, solar energy is a candidate with high potential. Indeed, the energy supply from the sun is quite enormous: on an average, the solar power received on the Earth's surface during one hour is equivalent to the energy demand of the human population during a whole year [Markvart 2000]. Solar energy can be divided into two categories: thermal solar energy, that converts solar energy into thermal energy, and photovoltaics (PV), that is the direct conversion of light into electricity. The history of photovoltaics started in 1839, when A.-E. Becquerel discovered the

photogalvanic effect. In 1954, Chapin et al. announced the first "usable" silicon solar cell, exhibiting 6% efficiency [Chapin 1954]. Only four years later, one employed solar cells on a satellite. In the last decade, PV has become increasingly significant: the global total production volume of PV modules has been increasing at over 20% annually. PV has actually many advantages: the power generation is reliable and involves no moving parts, resulting in very low operation and maintenance costs (the lifetime of PV modules is over 20 years). The operation of PV is silent and creates no atmospheric pollution. Moreover, PV shows the clear advantage of being geographically independent. Electricity can be generated wherever required, without the need for transmission lines. Such electricity generation systems can be installed directly next to the final users and can be easily integrated on roofs (see Fig. 1.1) or even in facades. Indeed, there are a lot of available surfaces on buildings. In Japan, PV tiles have even demonstrated better performances as roofing material compared with conventional Japanese roofing tile [Takenaka 2003]. One can, thus, propose that in the (near) future most of conventional roofing should be replaced with PV roofing systems. For more information about the different aspects linked to solar electricity, see for example [Markvart 2000], that gives a good overview of this subject.



Fig. 1.1: Solar roof made of amorphous silicon PV modules, sailing club, Auvernier (CH).

1.1.2. The role of silicon thin films in PV

At present, the PV market is still largely dominated by the crystalline silicon (c-Si) and poly- (or "multi-") crystalline silicon (poly-Si) technologies. However, thin films, and more particularly amorphous silicon (a-Si:H) thin films are more and more attractive. Since many years, one has indeed introduced a-Si:H solar cells for small-size applications like solar calculators. Large a-Si:H solar modules have, however, also numerous attractive attributes compared to "traditional" wafer-based silicon modules. The main one is probably their substantial potential of cost reduction in the medium term. In silicon thin-film technology, only a very thin layer of silicon is used (i.e. a layer that is about 1 micrometer thick). The substrate on which the active layers are deposited is usually glass, although other substrates

like stainless steel or even plastics can be used. Compared to this, wafer-based technology (c-Si and poly-Si) has silicon thicknesses of hundreds of micrometers. In addition, silicon thin-film technology requires far less fabrication energy than wafer-based technology. Thus, the energy payback time of thin film silicon modules is consequently reduced. Another substantial advantage of thin-film technology is the possibility to use the laser-scribing technique, that enables monolithic series connection [Meier 1998b]. Besides simplifying the fabrication of modules, this also definitely improves the esthetical aspect of such PV modules. Moreover, compared to other thin-film technologies currently under development and industrialisation (CIGS, CdTe), silicon thin films have the key advantage of using silicon as raw material, a raw material that is non-toxic and widely available.

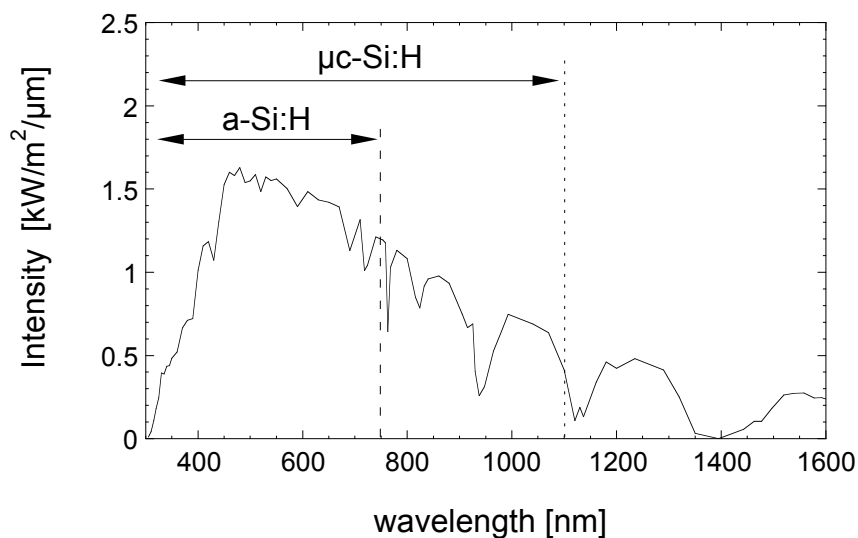


Fig. 1.2: Spectral distribution of the AM1.5 solar spectrum incident on the Earth's surface. The spectral ranges which are absorbed by a-Si:H and μ c-Si:H, respectively, are indicated.

The only weakness of a-Si:H thin film PV modules is their present relatively lower conversion efficiency as compared to c-Si or poly-Si, which in practice reach 10 to 15% efficiency. However, a-Si:H can be advantageously combined with microcrystalline silicon (μ c-Si:H) to form so-called "micromorph" (**microcrystalline/amorphous**) tandem solar cells. This technology has been pioneered by our group at IMT Neuchâtel [Meier 1994a, Meier 2003], but is now developed on a world-wide level for large-scale PV modules [Noda 2003, Repmann 2003, Yamamoto 2002]. A micromorph solar cell consists of the "stack" of a "top" (where light enters first) a-Si:H cell and of a "bottom" μ c-Si:H cell. Compared to a-Si:H, μ c-Si:H absorbs light coming from a wider spectral range (see Fig. 1.2). On the other hand, within its range of absorption, the absorption of a-Si:H is higher than that of μ c-Si:H (this is so because the latter has an indirect gap). Therefore, such a combination of materials takes advantage of a larger part of the solar spectrum (compared to a single-junction cell) and the conversion efficiency of the incoming light into electricity is consequently

increased. Some research groups are now even developing triple-junction solar cells made up of bottom and middle $\mu\text{c-Si:H}$ cells with a top a-Si:H cell [Saito 2003, Schropp 2003].

1.2. Hydrogenated microcrystalline silicon ($\mu\text{c-Si:H}$)

Although hydrogenated microcrystalline silicon ($\mu\text{c-Si:H}$) was first deposited in 1968 [Veprek 1968], it took several years before it could be successfully used for solar cell applications [Meier 1994b]. Intrinsic $\mu\text{c-Si:H}$ layers are now successfully introduced as photogeneration layers into complete $\mu\text{c-Si:H}$ thin films solar cells, that have a p-i-n (or n-i-p) structure (see § 4.2.2). Conversion efficiencies of around 9% have been reported by several research groups [Meier 2001, Nasuno 2001a, Repmann 2001]. Comprehensive reviews about $\mu\text{c-Si:H}$ as used for solar cell applications are given in [Shah 2002, Shah 2003].

Despite this successful application, there have so far been few precise indications on the relationship between material microstructure and electrical characteristics, although such a relationship can certainly be suspected. **The subject of this thesis is the characterisation of intrinsic layers and of solar cells made of $\mu\text{c-Si:H}$. More particularly, we will analyse the link between the microstructure and the electrical performances in single layers as well as in complete solar cells.**

1.2.1. Microstructure of $\mu\text{c-Si:H}$

Hydrogenated microcrystalline silicon ($\mu\text{c-Si:H}$) is known to be a complex material consisting of crystalline and amorphous silicon phases plus grain boundaries. In this work, we study exclusively $\mu\text{c-Si:H}$ deposited by the Very High Frequency Plasma Enhanced Chemical Vapour Deposition (VHF PE-CVD) technique (see § 1.2.2). $\mu\text{c-Si:H}$ is not a single material, but exhibits a wide range of microstructures that depend both on the deposition conditions [Luysberg 1997, Vallat-Sauvain 2000] and on the substrate material [Bailat 2002]. At present, the best electrical conversion efficiencies are achieved for $\mu\text{c-Si:H}$ solar cells incorporating an intrinsic (i-) layer deposited near the $\mu\text{c-Si:H/a-Si:H}$ transition [Klein 2003, Roschek 2002, Shah 2002]. For such $\mu\text{c-Si:H}$ material, the microstructure varies whilst the growth of the film proceeds: a fully amorphous incubation layer has frequently been observed at the bottom (i.e. in the initial growth stage) of layers grown with deposition conditions close to the $\mu\text{c-Si:H/a-Si:H}$ transition. Thereafter, the microcrystalline phase follows, consisting of pencil-like conglomerates made of nanocrystals of a size of a few tens of nanometres (see Fig. 1.3) [Bailat 2003, Houben 2002, Kocka 2002].

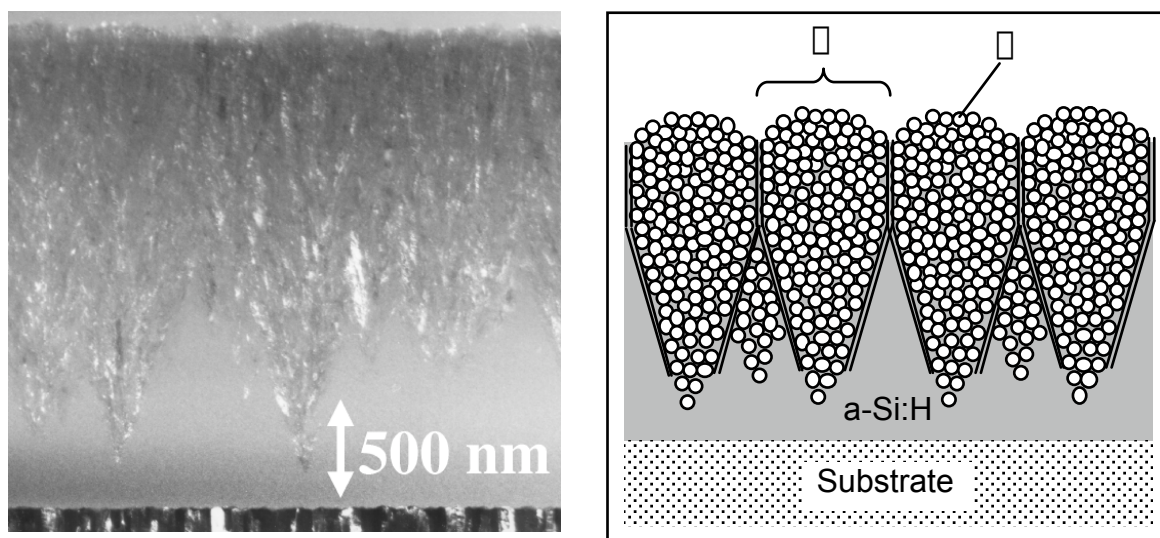


Fig. 1.3: Hydrogenated microcrystalline silicon ($\mu\text{c-Si:H}$). *Left*: TEM dark field micrograph of the cross-section of a $\mu\text{c-Si:H}$ layer deposited near the $\mu\text{c-Si:H}$ / a-Si:H transition on sputtered ZnO. At the bottom of the layer, amorphous silicon appears uniformly grey, between pencil-like conglomerates of nanocrystals that constitute the microcrystalline silicon phase. *Right*: schematic representation of a $\mu\text{c-Si:H}$ layer: pencil-like conglomerates (\square) formed by a multitude of nanocrystals (\square), plus their corresponding boundaries.

The microstructure of $\mu\text{c-Si:H}$ is actually a "mix" between that of amorphous silicon (i.e. no periodicity and no long-range order) and that of crystalline silicon (i.e. fully regular network of atoms). In fact, three main length scales for disorder can be identified in microcrystalline silicon:

1. Local disorder: $\mu\text{c-Si:H}$ contains a more or less large part of **amorphous material**, i.e. of material that consists of an arrangement of atoms without any long-distance order and that also contains a substantial density of defects (dangling bonds) (see § 1.2.3).
2. Nanometrical disorder: **nanocrystals** consist of small crystalline (c-Si) grains of random orientation and a few tens of nanometres size. They can be observed on Transmission Electron Microscopy (TEM) micrographs (see Fig. 1.3, white domains); their average size (\square) can be evaluated from X-Ray Diffraction (XRD) spectra (see § 3.4.3.2). Between the nanocrystals, there are the grain boundaries of the nanocrystals, consisting of a certain form of amorphous tissue.
3. Micrometrical disorder: **conglomerates** are formed by a multitude of nanocrystals and generally have a pencil-like shape (see Fig. 1.3). The size of the conglomerates (\square) emerging at the free surface of the layers can be evaluated from Atomic Force Microscopy (AFM) scans (see § 3.4.3.3) and is roughly half a micrometer. Between the

conglomerates one finds also a kind of amorphous tissue that forms the conglomerate boundaries.

As the constituents of \square c-Si:H, i.e. a-Si:H and c-Si, possess quite different transport properties, one of the main issues concerning \square c-Si:H is to **identify which part of its complex microstructure governs electrical transport**, in single intrinsic layers as well as in complete solar cells.

1.2.1.1. Techniques for the characterisation of the microstructure

In this work, we will mainly focus on the use of **Raman spectroscopy** for monitoring the microstructure of \square c-Si:H layers and solar cells. As will be discussed in Chapter 2, this is a fast and non-destructive characterisation technique that is applicable to entire (functioning) solar cells. Moreover, it allows a depth profiling of the crystallinity of the top and bottom regions of the samples.

An illustrative way to study the microstructure of \square c-Si:H samples is **Transmission Electron Microscopy (TEM)** micrograph, as shown in Fig. 1.3 (left). This technique enables a direct imaging of the microstructure and, thus, reveals its complexity and the inhomogeneities in thickness (although the resolution for detecting amorphous material is limited here). However, the preparation of TEM samples is time consuming and, above all, it is destructive, because the samples must be prepared as cross-sections. In this work, we used the "tripod method" [Benedict 1992, Dubail 2000]: Two pieces of the sample are glued head to head to obtain a "sandwich" (with the layers in the centre and the glass substrate on each side). Then, with the help of a small instrument with three micrometrical feet called a "tripod", the sandwich is mechanically polished to obtain a corner with an angle of about 0.6 to 0.8°. At that edge, the sample becomes thin enough (less than 100 nm thick) to allow transmission of the electrons. Finally, a short ion-milling procedure is used for sample cleaning. The samples are observed on a Philips CM200 microscope operated at 200 kV.

Other microstructure characterisation techniques include **X-Ray Diffraction (XRD)**, that gives information about the average crystallinity and from which one can evaluate the average size of the smallest coherent domains, and **Atomic Force Microscopy (AFM)**, that probes the surface topography (see § 3.4.3).

1.2.2. Deposition technique for thin film silicon layers and solar cells: VHF PE-CVD

All the samples studied in this work paper were produced by the Very High Frequency Plasma Enhanced Chemical Vapour Deposition (VHF PE-CVD) technique. The PE-CVD

technique consists in the decomposition of gases by a plasma. The gases used for the deposition of intrinsic silicon thin films are silane (SiH_4) and hydrogen (H_2). The amorphous or microcrystalline nature of the deposited material depends on the value of the different deposition parameters that have to be adjusted.

The use of plasma excitation frequencies in the Very High Frequencies (VHF) range (70 to 130 MHz) was pioneered by our group [Curtins 1987]. Compared to standard RF frequency (13.56 MHz), it leads to a remarkable increase of the deposition rate (of both a-Si:H and \square c-Si:H samples) while achieving good material quality. In the VHF range, the sheath potential is reduced, leading to a reduced peak ion energy and thus to less ion bombardment [Howling 1992].

The main deposition parameters are the following:

- The **plasma excitation frequency**: The VHF-range used for the samples studied here was from 70 to 130 MHz. In the case of \square c-Si:H, the deposition rate is definitely an issue regarding industrialisation as, at present, the thickness of \square c-Si:H solar cells is about 5 to 10 times higher than that of a-Si:H solar cells. Moreover the VHF-range can be considered generally to be very favourable for the growth of \square c-Si:H material.
- The **temperature**: An advantage of PE-CVD is that it enables one to use relatively low deposition temperatures. All the \square c-Si:H samples analysed in this work (layers and solar cells) were deposited at an effective deposition temperature around 220°C.
- The **pressure** within the chamber during the deposition depends on the pumping rate and the gas feeding. The deposition pressure used here was in the range 0.1 - 0.9 mbar.
- The **Silane Concentration** in the plasma gas phase: $\text{SC} = \text{SiH}_4 / (\text{SiH}_4 + \text{H}_2)$. This parameter is the parameter that is most effective in changing the structure of the deposited layer from amorphous material (at high SC-values) to microcrystalline material (at low SC-values). In order to study \square c-Si:H material deposited near the \square c-Si:H / a-Si:H transition, we will, therefore, in particular study silane concentration series ("SC series") of single intrinsic layers (SC = 5 - 8%, see § 3.4) and of n-i-p solar cells (SC = 5 - 7%, see § 4.4.2).
- The applied **VHF plasma excitation power**: by increasing the power one can also increase the deposition rate as well as control the morphological transition from a-Si:H to \square c-Si:H [Torres 1997]. However, use of higher plasma excitation power generally results in stronger ion bombardment and in defectorial material, i.e. in a drop in solar cell efficiency. The power used for the deposition of the samples studied in this work was about 5 - 30 W.

All the samples characterised in this work were deposited on AF45 (Schott) glass substrate. To obtain nearly intrinsic \square c-Si:H material, a gas purifier was used [Torres 1996]. For more details about the deposition technique of \square c-Si:H layers and solar cells by VHF PE-CVD, see [Flückiger 1995], [Torres 1998] and [Feitknecht 2003].

1.2.3. Hydrogenated amorphous silicon (a-Si:H)

\square c-Si:H is closely related to hydrogenated amorphous silicon (a-Si:H). The deposition technique for both materials is the same. Only the deposition parameters (such as temperature, silane concentration, power, frequency, pressure...) must be adjusted in order to obtain a-Si:H or \square c-Si:H material. On the other hand, \square c-Si:H can be considered as nothing else but a (complex) mixture between crystalline silicon (c-Si) and a-Si:H. Therefore, it is of high interest to present the basic characteristics of a-Si:H before studying \square c-Si:H.

a-Si:H is a solid-state material made of silicon atoms which are arranged on a lattice that has a certain short range order, but no long range order. Compared to crystalline silicon (c-Si), the average bond angles between neighbouring atoms are distorted. Some bonds are even broken and result in so-called "dangling bonds". The presence of hydrogen during the fabrication of amorphous silicon material enables one to passivate a large part of these dangling bonds. These two main "defects" of the lattice of a-Si:H – bond distortion and dangling bonds – give rise to an electronic band structure containing localised states within the so-called "mobility" bandgap (see Fig. 1.4). Note that the value of the "optical" bandgap, that is extrapolated from optical measurements, can be slightly different from that of the mobility gap.

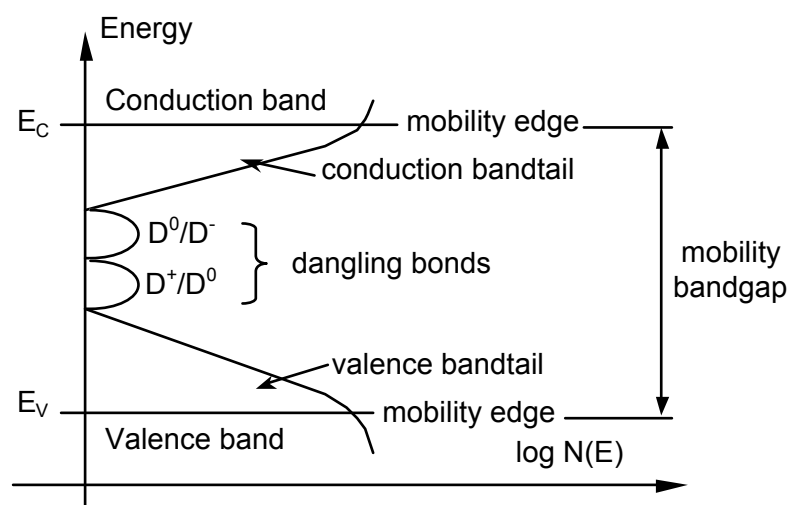


Fig. 1.4: Density of states $N(E)$ for intrinsic a-Si:H. Within the mobility bandgap (delimited by E_C and E_V), the states are localised (dangling bonds and bandtails).

The bond distortion results in **bandtails** near the valence and conduction bands. In these bandtails, the electrons (or holes) are localised in space and do not participate (directly) in the electronic transport. The (non-passivated) **dangling bonds** create deep states near the middle of the bandgap. They can either be positively charged (i.e. absence of electron, D^+), neutral (i.e. one electron, D^0) or negatively charged (i.e. two electrons, D^-). The dangling bonds act as recombination centres for the free electron and holes, and lead to two recombination paths: one over D^0/D^- and one over D^+/D^0 (see Fig. 1.4). They can also affect the electronic transport by influencing the total electric charge. In a-Si:H as well as in \square c-Si:H, hydrogen has the important role to reduce the number of dangling bonds, or "defects", and, thus, to make the material "device-grade", i.e. suitable for use in optoelectronic devices like solar cells and detectors.

The difference in the range of absorption of a-Si:H and \square c-Si:H, as shown in Fig. 1.2, is due to different bandgap energy values (E_g). For a-Si:H material, $E_g \approx 1.75$ eV, whereas for highly microcrystalline silicon $E_g \approx 1.1$ eV, similarly to c-Si. Due to its indirect gap, the absorption of \square c-Si:H is lower than that of a-Si:H (that has a so-called non-direct gap [Shah 1995a]).

1.2.4. Stability of \square c-Si:H

It is well known that the electrical properties of a-Si:H change when this material is exposed to light. This light-induced degradation effect is known as the "Staebler-Wronski" effect [Staebler 1977]. On the other hand, it has been stated for a long time that one of the main advantages of \square c-Si:H was its stability under light exposure. Indeed, up to recently, no light-induced degradation had been observed in the transport properties of our \square c-Si:H layers [Goerlitzer 1997] as well as in the efficiency of \square c-Si:H solar cells [Meier 1994a]. In the past, mainly "highly microcrystalline" material, i.e. material deposited far from the \square c-Si:H/a-Si:H transition, had been studied.

At present, the solar cells exhibiting the highest efficiencies are, however, fabricated near the \square c-Si:H/a-Si:H transition. For such material, the question of light-induced degradation is of topical interest. A light induced degradation effect has already been reported in 1986 for \square c-Si:H films containing grain size smaller than 120 Å [Liu 1986]. More recently, Fonrodona et al. [Fonrodona 2003] have reported, for nanocrystalline solar cells deposited by HW (hot wire)-CVD, a reversible change in the dangling bond density (N_{DB}), for a solar cell deposited at a SC-value of 6.2%. On the other hand, at SC-values of 5 and 5.6%, they report on having deposited fully stable solar cells. Klein et al. [Klein 2003] have reported up to 10% degradation in the efficiency of \square c-Si:H HW-CVD solar cells containing a high amorphous volume fraction, after 1000 hours exposure to light at an intensity of 100 mW/cm² and at a

temperature of 50°C.

In this thesis, we have not studied the stability of \square c-Si:H solar cells against light-soaking. A preliminary study by Kuendig [Kuendig 2003] on cells similar to those used in this work has, however, not revealed a significant degradation effect. In the future, systematic analysis regarding light-induced degradation should be done for all \square c-Si:H solar cells deposited near the transition.

On the other hand, unlike a-Si:H, \square c-Si:H is very sensitive to the incorporation of oxygen, both during deposition and after deposition (post-oxidation). This is why a gas purifier must be used during deposition in order to get "device-grade" microcrystalline silicon material [Torres 1996]. Fortunately, once incorporated into complete solar cells, \square c-Si:H is usually not prone to post-oxidation. On the other hand, the electrical properties of single intrinsic layers can be dramatically affected by post-oxidation [Goerlitzer 1998b], the latter depending on the deposition conditions (especially on the power applied to the plasma). Therefore, the interpretation of transport measurements performed on layers can be problematical.

1.3. Outline of this thesis

Besides this introduction and the final chapter containing the conclusions, this thesis is divided into three main parts:

- The **first part** (Chapter 2) deals with **micro-Raman spectroscopy**. This characterisation technique is used to monitor the crystallinity of \square c-Si:H layers and solar cells. We will discuss the application of "bifacial depth-dependent" micro-Raman spectroscopy to our samples, and define a "Raman crystallinity factor" calculated by evaluating the scattered intensities assigned to the amorphous and to the crystalline phases. We will finally evaluate the ratio of the Raman cross-sections for \square c-Si:H over that of a-Si:H by comparing our measured Raman crystallinity factors with the TEM micrograph of the same \square c-Si:H layer.
- The **second part** (Chapter 3) is focused on the analysis of **\square c-Si:H intrinsic layers**. After introducing the characterisation techniques for coplanar transport in intrinsic thin-film silicon layers, we will compare the electronic transport measured in \square c-Si:H layers with that of a-Si:H samples. Then, for a silane concentration series of layers comprising the \square c-Si:H/a-Si:H transition, we will study, on one hand, the electronic transport and, on the other hand, the microstructure. Both aspects will finally be compared, in order to identify which part of the microstructure governs coplanar electrical transport.

- The **third part** (Chapter 4) is devoted to the study of **nc-Si:H solar cells**. First, we will briefly explain the structure and the principle of operation of such solar cells, as well as the basic electrical characterisation techniques used for them. Afterwards, we will discuss the particularities of the application of Raman spectroscopy to entire solar cells and present the results obtained on two silane concentration series of n-i-p cells. Then, for various p-i-n and n-i-p solar cells, we will compare the electrical performances with the Raman crystallinity evaluated on the very same cells. In particular, we will demonstrate a link between the open-circuit voltage and the crystallinity of the interface regions.

Chapter 2: Micro-Raman spectroscopy

2.1. Introduction

In this chapter, we will present the characterisation method that has been used throughout this work: **Raman spectroscopy**. It is a powerful analytical technique based on the analysis of the inelastic scattering of light interacting with the material under test. This method can be applied either to gas, liquid or solid state materials. Raman spectroscopy provides spectra characteristic of molecular vibrations (or of phonons in solids) that can be used for sample identification and/or phase quantification. A Raman spectrum represents the intensity of the scattered light as a function of the shift in frequency (i.e. energy) from the excitation light frequency. This “Raman shift” is directly linked to the vibrational energy of the bonds between the atoms within the probed material. More specifically, in the case of silicon thin films, Raman spectroscopy is particularly well suited to discriminate between the amorphous phase and the crystalline phase. Therefore, **this analysis technique allows one to quantify the degree of crystallinity of microcrystalline silicon (μ c-Si:H) samples.**

Micro-Raman spectroscopy (or Raman microscopy) refers to the kind of apparatus used. The excitation light is guided and focused on the sample via a microscope, and the backscattered Raman signal is also collected via the microscope.

The main advantage of Raman spectroscopy is to be a **fast and non-destructive tool**. Indeed, no sample preparation is required and this non-contact experimental technique enables characterization of samples while avoiding sample contamination or deterioration. The deconvolution of Raman spectra that yield quantitative information regarding crystallinity can, thus, be correlated to the electronic transport properties measured on the same μ c-Si:H layers. Moreover, Raman spectroscopy is not only applicable to simple layers, but **can also be performed on entire silicon thin film solar cells** [Droz 2001, Droz 2003, Droz 2004, Vetterl 2001a]. Thus, this tool will give us the interesting possibility to characterise the volume fractions of amorphous and crystalline phases within actual (functioning) μ c-Si:H solar cells. As the electrical performances of the very same solar cells will be measured, the relationship between crystallinity and electrical properties will be

established (see Chapter 4).

Our intention here is not to study the physics of Raman scattering in \square c-Si:H material. Our goal in this chapter is to discuss and establish the experimental conditions and limits under which Raman spectroscopy can furnish reliable and useful information about crystallinity of \square c-Si:H layers and especially of \square c-Si:H solar cells.

In § 2.2, the Raman scattering effect, on which Raman spectroscopy is based, will be introduced. Then, we will explain what is a Raman spectrum, and present the main features of the Raman spectra of a-Si:H, \square c-Si:H and c-Si materials. Based on that, we will show the interest of its application to silicon thin films for the monitoring of the crystallinity.

The characteristics of the experimental micro-Raman set-up used throughout this work will be presented in § 2.3, as well as the main parameters that need to be adjusted when acquiring a spectrum. Then, some remarks concerning the practical operation of the Raman system will be discussed, in § 2.4. In particular, the effect of the excitation light intensity and problems related to background noise will be addressed.

It will be shown, in § 2.5, that micro-Raman spectroscopy can yield information about the microstructure of a \square c-Si:H sample over a more or less deep volume of the sample, providing different excitation wavelengths are used. Moreover, measurements from the top surface of the sample as well as measurements from the bottom surface of the sample are discussed. In that last case, the sample is probed through the glass substrate and, thus, the beginning of growth of the sample can be studied as well.

The task of obtaining Raman spectra and deducing rough qualitative information regarding film quality is relatively simple. However, the subject of interpreting Raman spectra with the aim to obtain quantitative information regarding crystallinity is more complex and requires some care. This issue will be discussed in § 2.6, where different aspects linked with the deconvolution of Raman spectra and with the evaluation of the Raman crystallinity volume fraction will be addressed.

Finally, in § 2.7, we will discuss the difference between our measured Raman crystallinity volume fraction and the real crystallinity. This involves the value of ratio (γ) of the Raman cross-section for \square c-Si:H over that of a-Si:H. Therefore, we will attempt to determine γ by comparing our Raman measurements with the TEM micrograph of a sample.

2.2. Theory of Raman spectroscopy

Raman spectroscopy is nowadays used in very different fields such as chemistry, materials science, semiconductors, biological and medical applications, forensic science, mineralogy, art and archaeology. Raman spectroscopy is based on the phenomenon of inelastic scattering of light, or Raman scattering effect, discovered in 1928 by C. V. Raman (see Fig. 2.1) [Raman 1928] who was awarded the Nobel Prize in Physics for this discovery in 1930.



Fig. 2.1: Sir Chandrasekhra Venkata RAMAN (1888-1970), Indian physicist, who discovered the scattering effect called after his name.

2.2.1. Raman scattering effect

The scattering of light results from the interaction of light and matter. This phenomenon can be of two types:

1. Elastic scattering, or **Rayleigh scattering**, where the scattered light has the same wavelength (λ) or frequency as that of the incident light: $\lambda_1 = \lambda_2$. This scattering mode is largely predominant.
2. Inelastic scattering, or **Raman scattering**, where the scattered light has a different wavelength or frequency than that of the incident light: $\lambda_1 \neq \lambda_2$. This scattering mode is only experienced by a very tiny fraction ($\sim 10^{-5}$ - 10^{-7}) of the total scattered light.

The Raman effect results from the interaction of vibrational and/or rotational motions of molecules or atoms in a crystal with the electromagnetic radiation (i.e. photons). The incident photons interact with the matter in such a way that energy is either gained or lost, so that the scattered photons are shifted in frequency. Thus, it results in Stokes and anti-Stokes peaks

around the Rayleigh scattering peak at the incident frequency (see Fig. 2.2). Note that the anti-Stokes peaks are generally weaker. The Raman spectra given later in this work will only display the Stokes peaks (on the positive Raman shift axis). The difference in energy between the incoming and the outgoing photons corresponds to the energy of vibrations (phonons for a crystal) of the studied material (i.e. to a very small change of the excitation energy (≈ 2 eV), as phonons in semiconductors have typical energy of around 0.01 eV). The frequency shift observed in Raman scattering is, thus, characteristic of the chemical bonds present in the material. The analysis of the scattered frequencies, or **Raman spectroscopy**, thus, reveals information about the structure of the scattering medium. It can also give information about other factors like stress or temperature.

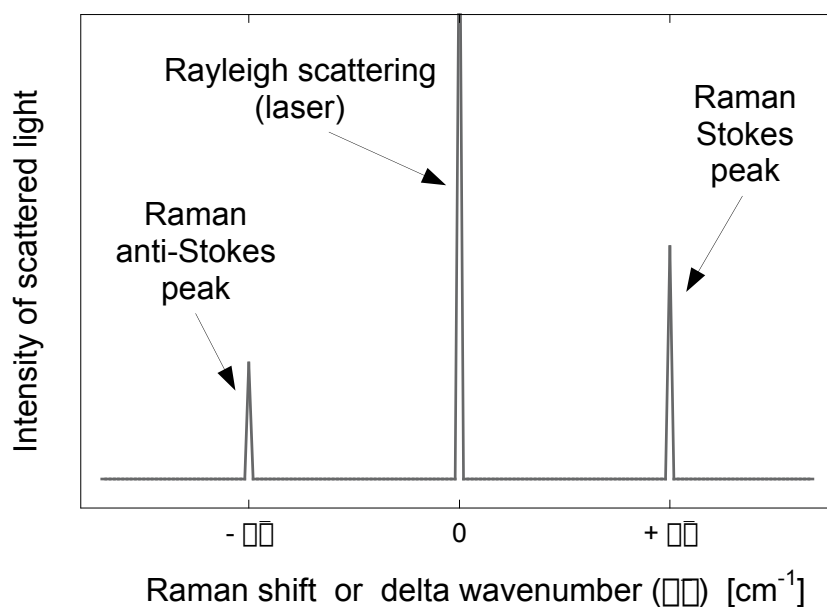


Fig. 2.2: Schematic Raman spectra representing the anti-Stokes (absorption of phonons) and Stokes (emission of phonons) Raman (inelastic) scattering peaks around the Rayleigh (elastic) scattering line. The scale is inverted in order that the more intense Stokes scattering peak corresponds to a positive energy.

From an experimental point of view, the laser is an excitation light source that is ideally suited to Raman spectroscopy. Indeed, it provides a powerful beam of monochromatic radiation at a known and stable frequency that is needed to get enough inelastic scattered light to be detected. As the Raman peak position is independent of the wavelength used (except for resonant Raman scattering), any type of continuous wave laser with emission around 400 - 800 nm can be used.

For more details about Raman scattering in materials, see for example [Weber 2000].

2.2.2. Raman spectra

A Raman spectrum is the representation of the intensity of the “shifted” or Raman scattered light as a function of the Raman shift expressed in absolute wavenumber shift (cm^{-1}) (see Fig. 2.2). The wavenumber, that is inversely proportional to the wavelength (λ), is a suitable unit for Raman spectra, because it is directly proportional to the vibration frequency. A phonon in c-Si at room temperature has a typical value of about of $\omega \approx 1.5 \cdot 10^{13} \text{ s}^{-1}$ [Sze 1981]. Usually, the values of the frequencies are divided by the velocity of light (c) expressed in $\text{cm} \cdot \text{s}^{-1}$. The resulting quantity is then an "absolute" wavenumber (in units of cm^{-1}), which is defined by:

$$\bar{\omega} = \omega / c = 1 / \lambda . \quad (\text{equ. 2.1})$$

The Raman shift ($\Delta\bar{\omega}$) (= delta wavenumber) corresponding to the x-axis of a Raman spectrum is, thus, calculated as follows:

$$\Delta\bar{\omega}(\text{cm}^{-1}) = \bar{\omega}_{\text{laser}} - \bar{\omega}_{\text{Raman}} = \frac{10^7}{\lambda_{\text{laser}}(\text{nm})} - \frac{10^7}{\lambda_{\text{Raman}}(\text{nm})} , \quad (\text{equ. 2.2})$$

where $\bar{\omega}_{\text{Raman}}$, that corresponds to the scattered light, is determined by the spectrometer and $\bar{\omega}_{\text{laser}}$ is a known and fixed constant ($\bar{\omega}_{\text{laser}} \approx 19450 \text{ cm}^{-1}$ for the 514 nm line of a Ar laser and $\bar{\omega}_{\text{laser}} \approx 15800 \text{ cm}^{-1}$ for the 633 nm line of a HeNe laser). The position of a peak in a Raman spectrum (that displays $\Delta\bar{\omega}$ and not $\bar{\omega}_{\text{Raman}}$) is therefore independent of the excitation wavelength used. For example, $\Delta\bar{\omega} = 520 \text{ cm}^{-1}$ for the peak of crystalline silicon. The value “0” on the x-axis corresponds to the position of the excitation wavelength (Rayleigh scattering, see Fig. 2.2).

2.2.3. Application to silicon thin films

In the case of silicon thin films, Raman spectroscopy can be utilised for the monitoring of the crystallinity. Indeed, the different phases (amorphous or crystalline material) present in a $\square\text{c-Si:H}$ sample result in different peaks on a Raman spectrum.

Fig. 2.3 shows typical Raman spectra (i.e. Stokes peaks) measured on a crystalline silicon (c-Si) wafer and on various silicon thin films. The Raman spectrum of c-Si (Fig. 2.3 (a)) exhibits a narrow peak centred at 520 cm^{-1} . This peak corresponds to the position of the Transverse Optic (TO) mode in crystalline silicon. The Raman spectrum of a highly $\square\text{c-Si:H}$ layer (Fig. 2.3 (b)) is closely related to that of c-Si. However, the main peak is centred at a frequency slightly lower than 520 cm^{-1} , usually around 518 cm^{-1} . The width of this peak is slightly larger than that of the c-Si peak. Moreover, the peak, characteristic of

μ c-Si:H, is not symmetric (as it is the case for c-Si), but always exhibits a tail towards smaller wavenumbers. This tail can be attributed to the defective part of the crystalline phase (see § 2.6.1.1). The Raman spectrum of an a-Si:H layer (Fig. 2.3 (d)) exhibits a broad peak centred at 480 cm^{-1} . This is characteristic of the TO mode of the amorphous silicon phase. Finally, the Raman spectrum of a μ c-Si:H layer deposited near the μ c-Si:H / a-Si:H transition (Fig. 2.3 (c)) consists of a mixture between the Raman spectrum of a highly μ c-Si:H sample and that of a fully a-Si:H sample.

The Raman signal collected in the micro-Raman experiment is dependent on the depth distribution of each phase. The relative proportion of each peak attributed to the amorphous and (micro-)crystalline phases on the Raman spectra of a silicon thin-film sample can, thus, be considered as being an indication of the crystallinity of the volume probed within the sample (see § 2.6).

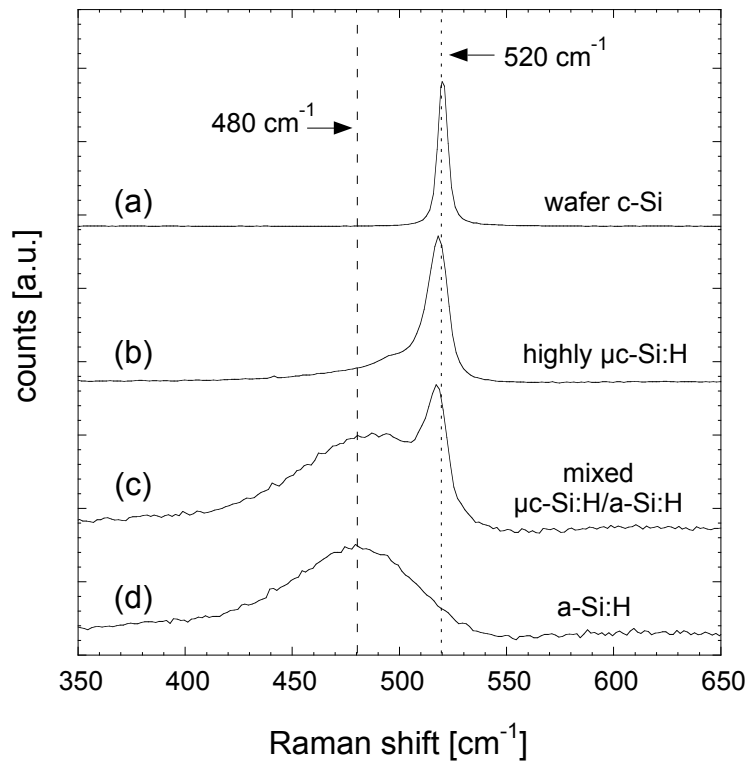


Fig. 2.3: Examples of Raman spectra taken on our set-up for (a) a c-Si wafer, (b) a highly μ c-Si:H sample, (c) a sample deposited near the μ c-Si:H / a-Si:H transition, and (d) an a-Si:H sample. Note that only the relative intensities of the different peaks within a same spectrum are meaningful (and not the absolute intensity (counts) of an individual peak).

2.3. Experimental

2.3.1. Description of the experimental micro-Raman set-up

Micro-Raman spectroscopy, or Raman microscopy, is a very specialized optical microscopy. As in any optical microscopy its lateral spatial resolution is close to the micron. Raman spectroscopy became a useful technique with the introduction of lasers as a convenient, powerful monochromatic light source. It has become widely available only after the introduction of holographic filters (or “notch” filter) to reject the light scattered without frequency change. In Raman microscopy the sample is illuminated with a laser beam focused through a conventional optical microscope, and the light scattered (or more precisely backscattered) by the material is analyzed by the Raman spectrometer coupled to the microscope. More details about the specificities of micro-Raman spectroscopy, or Raman microscopy, can be found in [Turrell 1996].

The experimental set-up used throughout this work for collecting Raman spectra is the compact *Renishaw Raman Imaging Microscope, system 2000* (see Fig. 2.4). The complete Raman system consists of four main elements (see Fig. 2.5):

1. **The laser source.** The light for illuminating the sample and exciting Raman scattering is provided by a laser. The system is equipped with an **Argon (Ar) laser** (Melles Griot 532R-Gs-A03) **emitting at a wavelength of 514 nm** (green light) and a **Helium-Neon (HeNe) laser** (Melles Griot 31-2108-000) **emitting at a wavelength of 633 nm** (red light). In order to adapt the laser intensity that enters the spectrometer, the laser beam goes through a laser attenuation filter wheel containing four Neutral Density (ND) filters plus an empty hole letting either 1%, 10%, 25%, 50% or 100% of the light pass through. Then, the beam goes through a band-pass filter that prevents spurious light from entering the spectrometer.
2. **The Raman spectrometer itself.** Its lower part expands and directs the excitation laser beam to the microscope (see Fig. 2.5 elements C and D: beam expander; elements B, E and F: mirrors). Subsequently, the upper part processes the signal collected from the sample. A set of holographic notch filters (element G) gets rid of Rayleigh scattered light (as a notch filter suppresses one precise wavelength, it must be changed if the excitation wavelength is changed). After passing through a slit preceded by a lens (element I), the Raman scattered light enters the spectrograph constituted of a single grating plus a triangle mirror (elements K and J, respectively). The grating spreads out spatially the different wavelengths constituting the Raman signal. Finally, signal

detection is achieved through the use of a sensitive charge coupled device (CCD) array detector (element N) that is thermoelectrically cooled. (Note that the elements H, O, P, Q, R and L are intended to make "global imaging" via a filter light path, a technique that has not been used in this work.)

3. **The microscope.** By moving a mirror and a beam-splitter, the microscope can be used either as a common instrument for observing samples or as the interface between the spectrometer and the sample during Raman measurements. It focuses the excitation beam onto the sample through an objective and then collects the backscattered light by the same way. In addition to an objective with a magnification of 20 \times , that is mainly used for sample observation, four other objectives used for Raman measurements are mounted on the microscope. Their characteristics are listed in Table 2.1. For both 50 \times and 100 \times magnifications, there are a standard objective and an objective with a Long Working Distance (LWD), that enable Raman measurements on the bottom side of thin films deposited on glass (see § 2.5). The focused laser beam diameter is about 1 μm with a 100 \times objective.
4. **A personal computer.** Data acquired from the CCD are read, stored and processed by the computer, which also controls all spectrometer functions. The software package consists of two softwares working together: the instrument control software "Renishaw WIRETM version 1.3" and the data analysis software "Galactic GRAMS/32C[®]".

Magnification	Type	NA	Relative output power	Focused beam diameter [μm]
50 \times	std	0.80	1	2
50 \times	LWD	0.50	0.80-0.85	2
100 \times	std	0.95	0.32	1
100 \times	LWD	0.80	0.37	1

Table 2.1: Microscope objectives available on the micro-Raman system. The "type" discriminates between standard (std) or long working distance (LWD) objectives, NA gives the numerical aperture and the "relative output power" corresponds to the power measured at the exit of the objective normalized to that out of the 50 \times standard objective.



Fig. 2.4: Picture of the Renishaw Raman imaging microscope

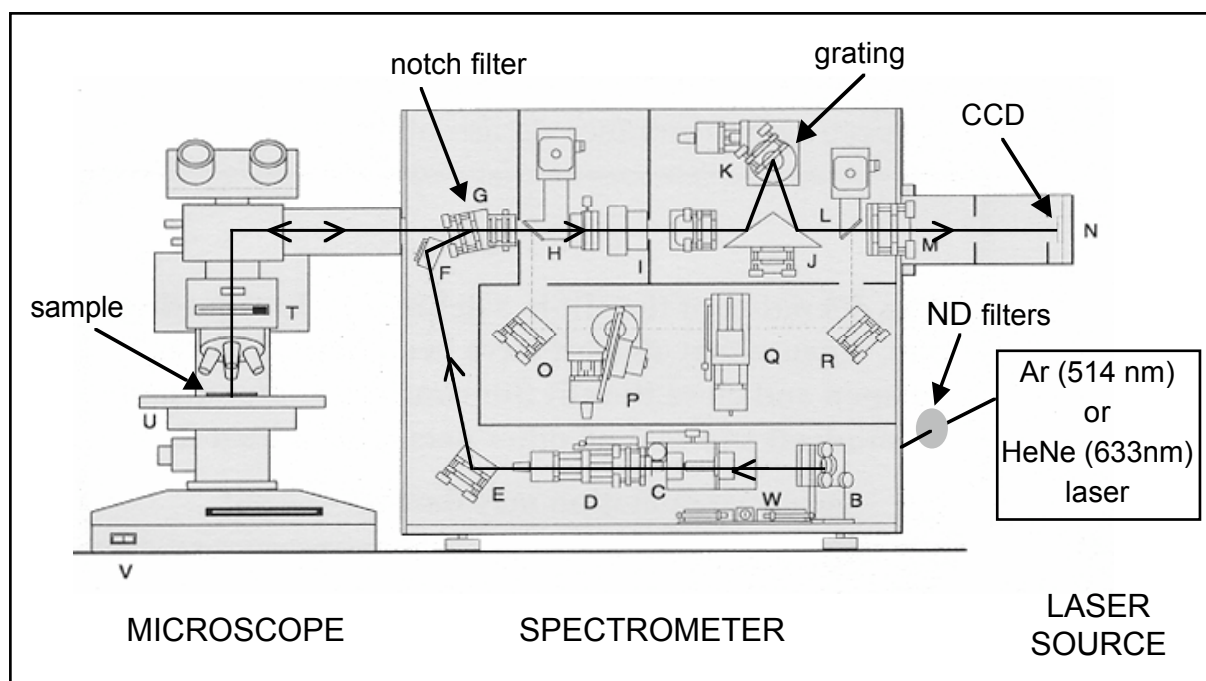


Fig. 2.5: Illustration (taken from [Renishaw]) of the Renishaw Raman imaging microscope, with the spectrometer door removed (to show the main assemblies inside). The complete system includes also a personal computer for data acquisition and analysis.

2.3.2. Acquiring Raman spectra

For acquiring a Raman spectrum, the sample is placed on the microscope platform and the laser beam is focused on the sample surface. During operation of the Raman system, the room is blacked-out and the white light of the microscope is switched off, in order to limit the background noise in the Raman spectrum. No laser polarisation-related studies have been performed in this work, as the polarisation of light mainly affect Raman spectra of crystalline material, what is not the subject of our study. The main parameters that must be adapted or chosen when acquiring a Raman spectrum are the following:

- The laser **excitation light wavelength** (i.e. 514 nm or 633 nm). This choice depends on the probing depth wanted (see § 2.5.1 for more details).
- The **microscope objective** (i.e. the numerical aperture and the magnification, the latest defining the diameter of the focused beam). For most of our measurements, the 50 \times objectives have been used.
- The **excitation light intensity** (see § 2.4.2 for details about its effect on Raman measurements).
- The **central position of the Raman spectra**, that also defines the spectrum range, depending on the wavelength used and on the grating. For characterisation of silicon-based material, the usual central position is 520 cm⁻¹ (and the calibration must be done at this position), although slightly different positions may be used (see § 2.4.3). (Note that most of the Raman characteristic peaks occur from around 100 to 3600 cm⁻¹. In order to analyse an unknown sample, another method of data capture (“extended spectra”) allows one to choose the lower and upper wavenumber limits of the spectrum.)
- The **exposure time**. It allows the CCD array to be exposed to more or less Raman scattered light. Increasing the exposure time can improve the quality of the data if the Raman signal is weak and if the signal to noise ratio is poor.
- The **number of accumulations**. Accumulating the spectral data involves capturing identical spectra and co-adding them together. This is also used to increase the signal to noise ratio, as signal is systematic and noise is random.

By using micro-Raman system, Raman spectra are obtained from a microscopically small volume of the sample; typically this volume depends on the sample response (absorption and refractive index), wavelength, the objective used and whether the system is set up confocally or not (see § 2.4.1). The intensity of a Raman peak (as measured either by the amplitude of the peak, or by the integrated area under the peak) will be dependent upon the volume probed, the nature of the material, the possible texture of the sample, the laser light power, the

objective, the slit width setting, and the method of capture of the spectral data (exposure time, number of accumulations,...). This will determine the number of photons generated, captured and converted to signal. Therefore, the intensity (or area) of a peak cannot be used as an absolute measurement of any microstructural feature. **Only the relative intensity (or area) of different peaks present on a same Raman spectrum can be compared and used as qualitative or quantitative information.** The resolution limit of the Raman spectra obtained with our micro-Raman system is about 1 cm^{-1} (as determined by the grating).

2.4. Basic experimental considerations and issues

2.4.1. Confocal spectroscopy

A micro-Raman spectrometer can either work in the standard (non-confocal) mode or in the “confocal mode”. The term “confocal” describes optical systems that limit the collection of light from a very small volume. Therefore, confocal micro-Raman spectroscopy is a method that enables one to collect spectra from well-defined regions of a sample (i.e. light which is in best optical conjugation with the Raman system) with minimised spectral contamination from the surrounding regions, as compared to standard operation. The main effect of setting the system in confocal mode is to improve the spatial resolution in the lateral plane (perpendicular to the optical axis) as well as regarding the depth of field (or depth of focus). Typically, lateral spatial resolution is $\sim 2\text{ }\mu\text{m}$ with the 50 \times objective and $\sim 1\text{ }\mu\text{m}$ with the 100 \times objective, providing optical set-up alignment is perfect. The depth of field gives a measure of the depth from which the collected light is emitted within the sample. The more confocal the system is, the thinner the volume above and below the plane of focus will be. For us, the interest of the confocal mode would be depth-profiling experiments (as the lateral resolution is not an issue in the case of our samples).

To set the Renishaw system in confocal mode, some simple manual reconfigurations affecting mainly the analysis (collection) path are required:

- The slit at the spectrograph entrance (see element I in Fig. 2.5) must be closed to $\sim 15\text{ }\mu\text{m}$ width (whereas it is $\sim 50\text{ }\mu\text{m}$ width for standard operation).
- The height of the image area used for capturing the spectra must be reduced to ~ 3 pixels (compared to 20 pixels for standard mode).
- A high-magnification objective (i.e. 100 \times objective) with high NA must be used.

Experimentally, the depth of field (for either standard or confocal mode) can be determined as follow: a silicon wafer (i.e. a sample homogeneous over a large thickness) is moved along the optical axis (z), and the intensity of the detected Raman peak is recorded.

Typical measurement values are given in Fig. 2.6. The Full Width at Half Maximum (FWHM) of the (Lorentzian) curve fitting the data set gives the depth of field (see Fig. 2.6). The FWHM (or depth of field) obtained for the standard configuration is $9.9\ \mu\text{m}$ with a $50\times$ standard objective and $5.9\ \mu\text{m}$ with a $100\times$ LWD (long working distance) objective, whereas it goes down to $2.7\ \mu\text{m}$ for the confocal configuration with the same $100\times$ LWD objective. The depth of field (in confocal mode) given by the micro-Raman spectrometer specifications is $\sim 5\ \mu\text{m}$ for a $50\times$ objective and $\sim 2\ \mu\text{m}$ for a $100\times$ objective [Renishaw]. The slightly higher experimental value we got ($2.7\ \mu\text{m}$ compared to $2\ \mu\text{m}$) is probably due to the fact that the $100\times$ LWD objective has a NA of only 0.80 as compared to 0.95 for a standard $100\times$ objective.

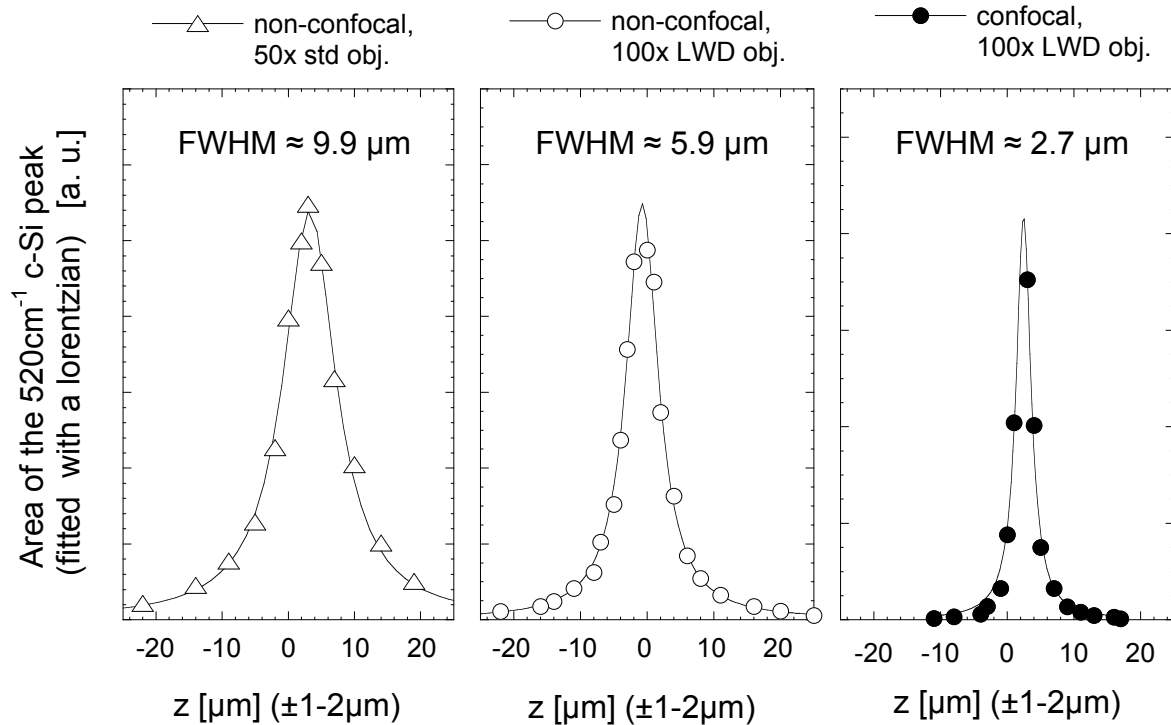


Fig. 2.6: Depth of field measurements for standard non-confocal (open symbols) and confocal (filled symbols) modes. Experiments were performed on a c-Si wafer with $633\ \text{nm}$ excitation light and two different objectives. The depth of field is given by the FWHM of the Lorentzian curve fitted on the data obtained by moving the c-Si wafer vertically along the optical axis (z) and recording the Raman signal intensity at each position.

The thickness of our c-Si:H samples to study is around $2\ \mu\text{m}$, a value that is similar to the depth resolution obtained in confocal mode. Therefore, this configuration does not allow depth-profiling experiments in our samples and is, thus, not useful for the present work. For that reason, confocal micro-Raman spectrometry has not been used further in this thesis.

Note that the depth of field, as defined above, and the Raman collection depth (RCD), that will be described in § 2.5.1, are two different things and must not be mixed up. The first one relates to the position of the plane of focus relative to the surface of the sample, whereas

the second is linked to the penetration depth of the excitation light into the sample (RCD \approx 500 nm for an excitation wavelength of 633 nm).

2.4.2. Effect of the excitation light intensity

The power of the laser light arriving on the sample must be carefully adapted in order to get meaningful Raman spectra. The power at the laser output (P_{laser}) can be considered as being fixed. Then, the power measured at the microscope objective output (P_{obj}) is reduced compared to P_{laser} . If a 50 \times standard objective and no attenuation filter is placed on the light path, P_{obj}/P_{laser} is about 7 - 8%. However, depending on the value of P_{laser} , this can be too high, and a neutral density (ND) filter (see Fig. 2.5) must be used in order to adapt the power of the light used for probing the sample.

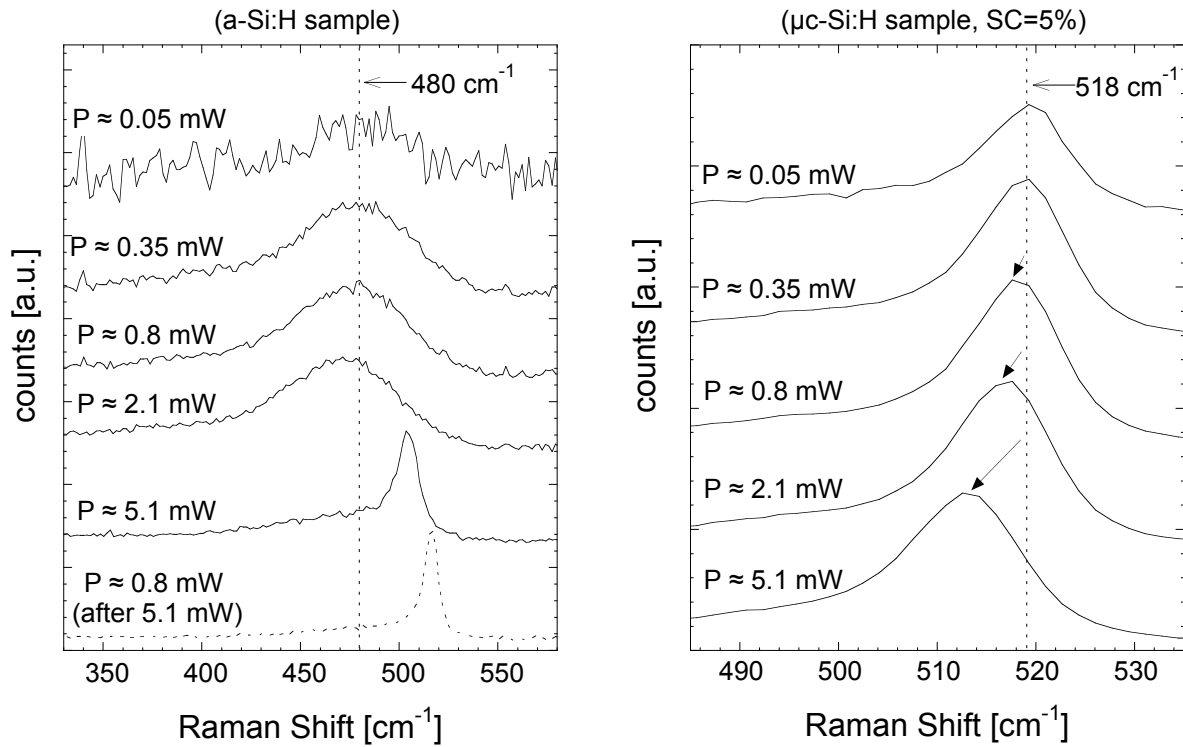


Fig. 2.7: Effect of the 514 nm excitation light power (P) on the Raman spectrum of an a-Si:H sample (left) and of a μ c-Si:H sample (right). P is measured at the objective output. Note that the focused beam diameter is about 2 μm (with the 50 \times standard objective used here).

In Fig. 2.7, the power of the light arriving on the sample has been varied by changing the transmission of the ND filter (see Fig. 2.5) from 1% (ND = 2) to 100% (no filter). For an amorphous sample (Fig. 2.7, left), recrystallisation of the probed volume is observed for an incident power of about 5 mW. Considering that the focused beam has a diameter of about 2 μm , the recrystallisation of this a-Si:H sample occurs at an incident intensity of about 100 kW/cm^2 , in accordance to what is found in the literature [Viera 2001]. This material

phase change is irreversible as the (micro-)crystalline peak is still observed, although shifted, if the measurement power is subsequently reduced to less than 1 mW (Fig. 2.7, left). This shift of the crystalline peak of a μ c-Si:H sample is shown in Fig. 2.7 (right): the peak position is shifted to lower wavenumber values as the excitation light power is increased over about 0.5 mW. This is due to sample heating by the probing light [Cerqueira 1999]. Note that this shift is reversible and that, for similar powers, the peak of a reference c-Si wafer sample is not affected (i.e. not shifted). Indeed, our thin film samples are deposited on a glass substrate, which is not a good heat conductor and does not allow to evacuate efficiently the exceeding heat of the sample.

Therefore, the power of the laser light used for acquiring Raman spectra must be adapted. As the aim of Raman measurements is to evaluate the crystallinity, the excitation light power must in all cases be lower than the threshold value over which recrystallisation occurs. Moreover, a compromise must be found between a sufficient signal and any temperature effect. In practice, for the measurements presented in his work, the neutral density filter was chosen in order to get the highest intensity for which no shift is observed. This corresponds for example to 0.35 mW with the standard 50 \times objective (see Fig. 2.7, right). In some cases where the signal was really poor, a filter with higher transmission has been used (leading, thus, probably to a slight shift of the peaks due to higher intensity). Note that if another objective is used, the filter giving the limits over which either a temperature effect appears or where recrystallisation occurs, will be different, as both the output power of the objective as well as the focused beam diameter are different (see Table 2.1). Moreover, when performing measurements through the glass substrate with a long working distance objective (glass-side measurements, see § 2.5), the power reaching the film to test is lower than the power measured at the objective output, due to losses in the glass.

Similar tests as those presented in Fig. 2.7 have been carried out for each of the objectives and each of the available wavelengths. Thus, the ideal measurement conditions for each particular case have been established and used throughout this work.

2.4.3. Background noise and CCD hot pixels

In order to get meaningful Raman spectra, the silicon-related peaks must be clearly distinct from the background noise. However, as seen before, a low illumination power is necessary for a correct interpretation of the measurements. This decreases the signal to noise ratio. Therefore the other experimental parameters must be well adapted. A CCD camera is basically subject to two types of noise:

1. The “dark noise”: charges are created even without light. This noise can be decreased by cooling down the CCD and it increases with the total time of exposition of the CCD.

2. The “reading noise”: it occurs each time the CCD signal is read. This noise depends on the number of readings (that can either increase the reading noise or averaging it).

With our Raman set-up, increasing the number of accumulations is very efficient in increasing the signal to noise ratio. On the other hand, it has been experimentally observed that increasing the exposure time is ineffective to improve the signal, and actually even makes the signal worse in some cases (see Fig. 2.8). Therefore, the acquisition of the Raman spectra in this work has been done with a large value of accumulations (100-500), each of short exposure time (1-2 seconds).

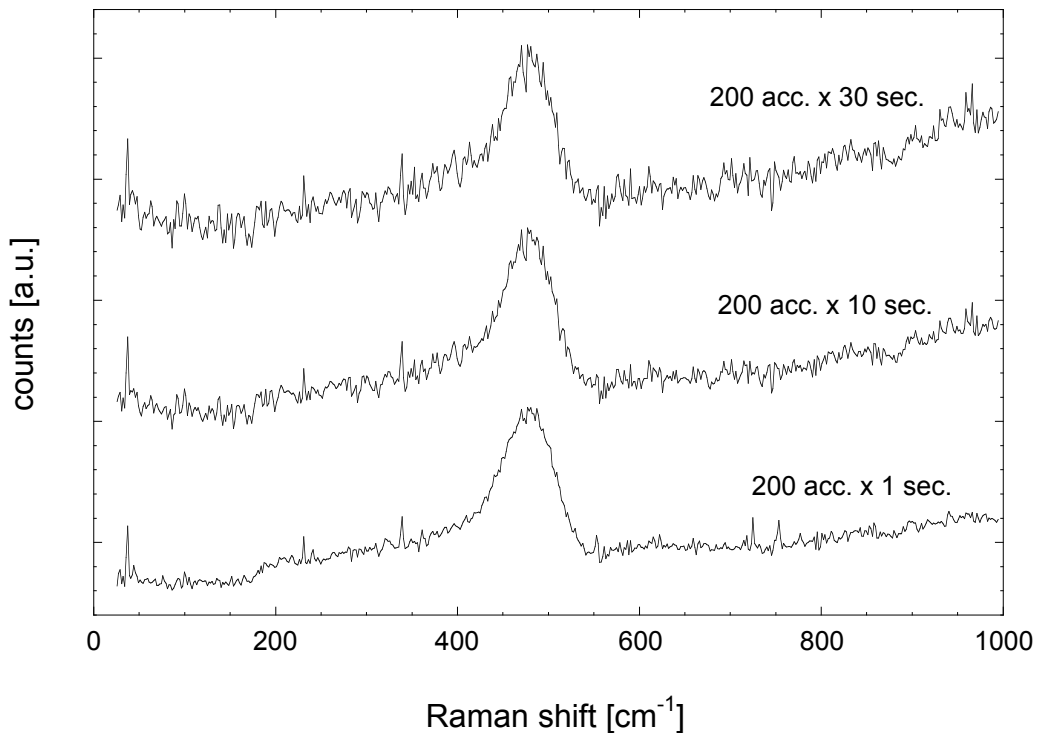


Fig. 2.8: Raman spectra of an *a*-Si:H sample acquired with 200 accumulations and different exposure times. The shortest exposure time leads here to the best signal to noise ratio.

As can be seen from Fig. 2.8, noise is not that much reduced at some x-positions, even for an exposure time of 1 second. Fig. 2.9 shows that these positions are not related to the Raman shift value, but rather to the pixel position. The Raman spectra represented in Fig. 2.9 has been acquired with the same number of accumulations and with the same exposure time, but with different central position of the spectrum. This reveals the presence of “hot pixels”, that correspond to some pixels having a very high intrinsic noise. Hot pixels can be detected by acquiring a spectrum without any light arriving on the CCD (i.e. dark room and laser switched off; see “dark” curve in Fig. 2.9). It can be important to know where the hot pixels are situated, in order to correctly interpret Raman spectra. If needed, the central position of the Raman spectrum can be changed so that a hot pixel does not merge with a Raman peak.

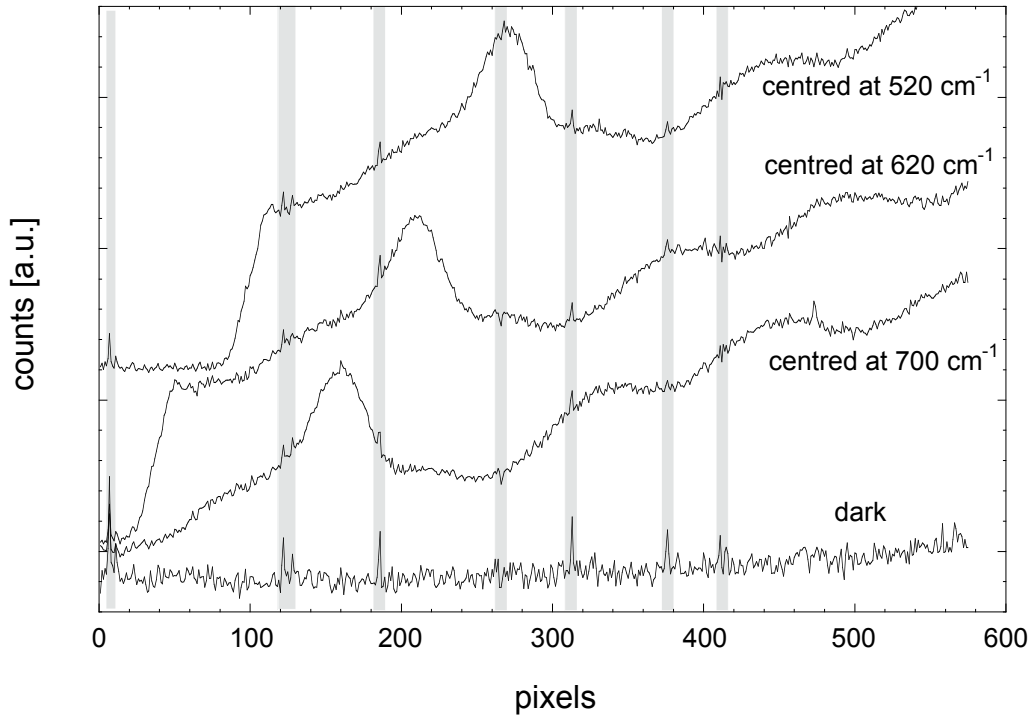


Fig. 2.9: “Raman spectra” of an *a*-Si:H sample taken with three different central positions, as a function of the CCD pixel position. The lower spectrum is acquired without any light arriving on the CCD, in order to highlight the hot pixel positions (grey vertical lines).

2.5. Bifacial depth-dependent micro-Raman technique

Micro-Raman spectroscopy can give information about the microstructure (or crystallinity) over a more or less deep volume of a \square c-Si:H sample, providing excitation wavelengths with different penetration depths are used (see § 2.5.1). Moreover, measurements from the top surface of the sample as well as measurements from the bottom surface of the sample are possible (provided that the substrate is transparent and has no Raman peak in the region of interest) (see § 2.5.2). In the last case, the sample is probed through the glass substrate and, thus, the beginning of growth of the sample can be studied. “Bifacial depth-dependent micro-Raman technique” is here defined as the micro-Raman spectroscopy technique combining these two aspects.

2.5.1. Influence of the excitation light wavelength

As previously stated, the position of a peak on a Raman spectrum is in principle independent of the wavelength of the excitation light, see (equ. 2.2). This is true for samples that are homogeneous in thickness. Indeed, the volume probed in Raman experiments depends on the absorption coefficient of the sample at the excitation wavelength used for the measurement. Therefore, for samples like \square c-Si:H layers, where the microstructure evolves

while growth proceeds, Raman spectra measured with different wavelengths may exhibit different features. By using different excitation wavelengths, we can thus obtain depth-dependent information. Indeed, with the strongly absorbed 514 nm line of an Ar laser, we will probe the first tens or hundreds of nanometres of our samples. In the case of solar cells, this comprises the doped layer plus a small part of the intrinsic layer. On the other hand, with the weakly absorbed 633 nm line of a HeNe laser, a deeper volume is probed. This results in an average crystallinity information that is less sensitive to the thickness inhomogeneities of the samples. In the case of solar cells, the 633 nm excitation light still probes the doped layer, but also a quite important part of the intrinsic layer. The absorption coefficients (α) given in Table 2.2 are typical values for a-Si:H, α c-Si:H and c-Si materials [Beck 1996a] at these two wavelengths. Similar values were obtained for a series of α c-Si:H/a-Si:H samples (see § 3.4.3.5).

514 nm (2.41 eV)	α [cm^{-1}]	RCD = $1/(2\alpha)$	633 nm (1.96 eV)	α [cm^{-1}]	RCD = $1/(2\alpha)$
a-Si:H	$\sim 10^5$	50 nm	a-Si:H	$\sim 10^4$	500 nm
α c-Si:H	$\sim 3\text{-}4 \cdot 10^4$	120-170 nm	α c-Si:H	$\sim 10^4$	500 nm
c-Si	$\sim 10^4$	500 nm	c-Si	$\sim 3\text{-}4 \cdot 10^3$	1.2-1.7 μm

Table 2.2: Typical absorption coefficients (α) and Raman collection depths (RCD) for a-Si:H, α c-Si:H and c-Si materials at the wavelengths of 514 nm (left) and 633 nm (right).

The Raman signal collected in the micro-Raman experiment is equal to the integral, taken over the excited volume, of the depth distribution of each phase [Hang 1988]. The excited volume depends on the penetration depth ($= 1/\alpha$) of the laser light used. The penetration depth at 514 nm is of the order of 100 nm for a-Si:H and of 300 nm for α c-Si:H, whereas at 633 nm it reaches about 1 μm for both materials. However, in our experimental backscattering set-up, the collected Raman light is scattered from half of these depths [Hang 1988, Paillard 2002]. Indeed, we must consider the optical attenuation of the excitation light and the optical attenuation of the Raman scattered light (i.e. two optical paths in the material). Fig. 2.10 shows this double optical attenuation as a function of the depth in the sample (z) for the different absorption coefficients of Table 2.2. Therefore, the **Raman Collection Depth (RCD)** for our experimental set-up working in backscattering configuration is here defined as:

$$\text{RCD} = 1/(2\alpha), \quad (\text{equ. 2.3})$$

where α is the absorption coefficient of the probed material at the considered wavelength. The typical values of RCD for a-Si:H, α c-Si:H and c-Si materials and for both 514 nm and 633 nm

excitation lights are given in Table 2.2. Whereas RCD is similar for a-Si:H and \square c-Si:H at 633 nm, the value of RCD at 514 nm for a-Si:H is about one third of the corresponding value for \square c-Si:H. One should keep in mind that the volume probed with the HeNe laser ($\lambda = 633$ nm) contains the volume probed with the Ar laser ($\lambda = 514$ nm) *plus* an additional deeper volume. By using different excitation wavelengths, we therefore probe volumes contained between the sample surface and the depth $z = \text{RCD}$.

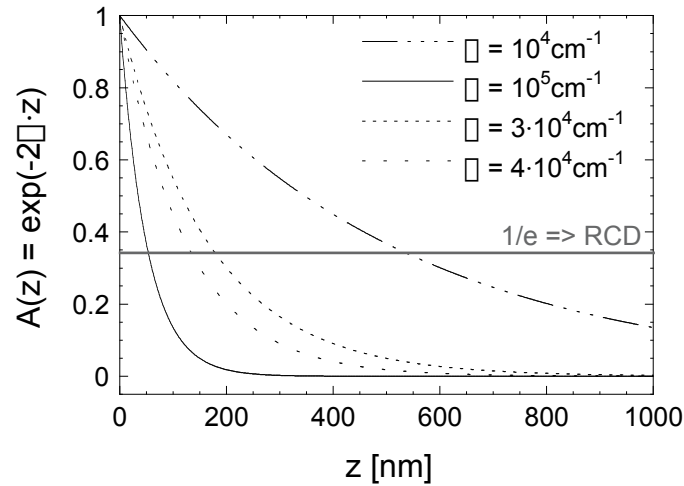


Fig. 2.10: Double optical attenuation ($A(z) = e^{-2\alpha z}$) as a function of the depth in the sample (z), for different absorption coefficients corresponding to a-Si:H and \square c-Si:H materials for 514 nm and 633 nm excitation lights (see Table 2.2). $z = 0$ corresponds to the silicon sample surface.

2.5.2. Layer-side and glass-side measurements

Provided that the sample to be analysed is deposited on a transparent substrate (i.e. for example glass, which is the case for all the samples studied in this work), bifacial Raman measurements can be carried out. A specificity of this work is indeed to use Raman spectroscopy applied on the glass substrate side of \square c-Si:H samples. This is achievable for simple silicon thin films deposited on glass substrate as well as for complete thin film silicon solar cells including the different silicon layers plus the TCO (Transparent Conductive Oxide) layers. The latter case will be discussed in details in Chapter 4. Bifacial Raman measurements (Fig. 2.11) consist in exciting the sample successively from the top side (or layer/cell side) and from the bottom side (or glass-side). Thereby we can evaluate selectively the last part of growth or the beginning of growth of the sample, respectively.

For glass-side measurements, the Raman system must be equipped with a long working-distance (LWD) objective. This enables the probing beam to go through the glass substrate and to be focused on the surface of the silicon layer, i.e. at the interface between the glass and the layer deposited on it (see Fig. 2.11). Fig. 2.12 shows bifacial Raman spectra measured on

a \square c-Si:H intrinsic layer deposited near the \square c-Si:H / a-Si:H transition. Whereas the beginning of growth of the layer consists of amorphous material (as seen in the glass-side spectrum), the top of the sample exhibits a good crystallinity. **This illustrates well the thickness inhomogeneity of our \square c-Si:H samples, and the usefulness of a characterisation tool that enables one to reveal such inhomogeneities.**

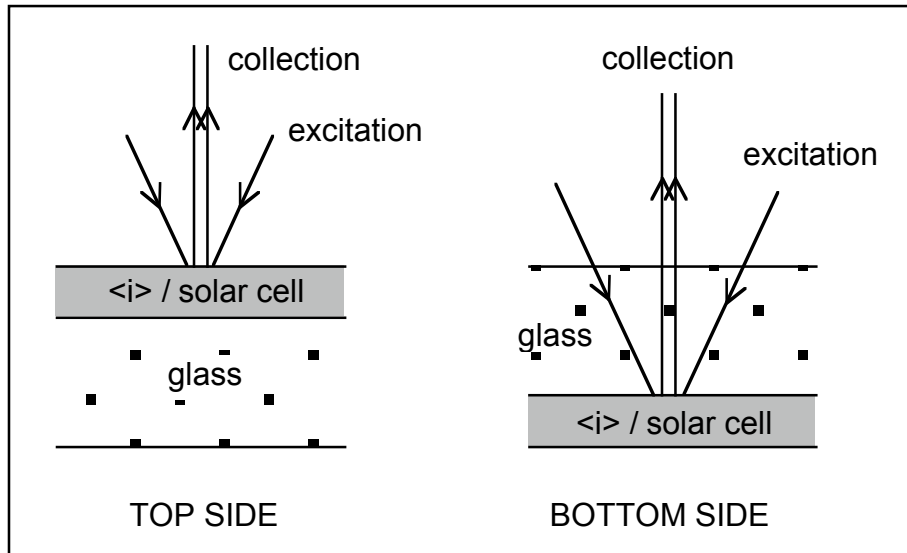


Fig. 2.11: Bifacial Raman measurements: the excitation light is focused either on the top of the layer (or on the last-deposited silicon layer in the case of solar cells) (left), or through the glass substrate on the bottom of the layer (or on the first-deposited silicon layer of the solar cell) (right).

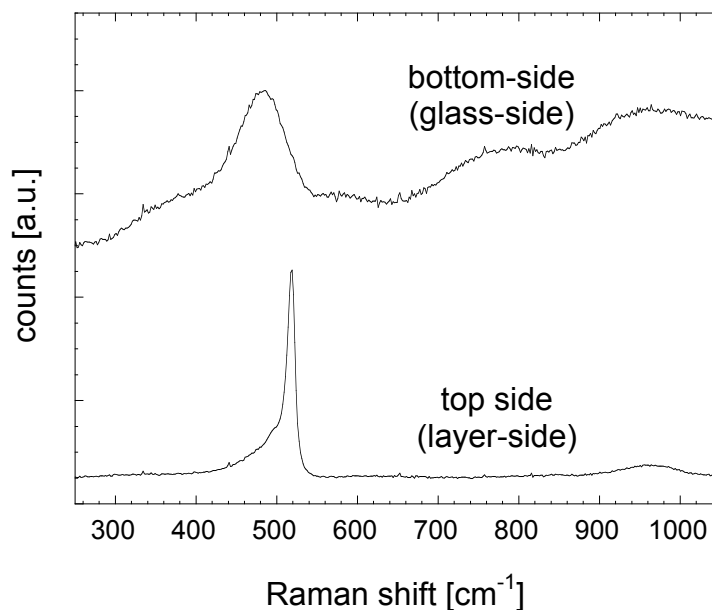


Fig. 2.12: Bifacial Raman measurements of an intrinsic \square c-Si:H layer (thickness $\approx 2 \mu\text{m}$) deposited near the \square c-Si:H / a-Si:H transition. The measurement was performed at 514 nm.

The bottom-side Raman spectrum of Fig. 2.12 exhibits an important background signal. This is due to the luminescence of the glass. However, the silicon-related peak is still well distinct and measurement as well as interpretation of the spectrum is not hindered by the presence of the glass.

2.6. Interpretation of the Raman spectra

For each sample (intrinsic layer or complete solar cell), both wavelengths (514 nm and 633 nm) were applied in each excitation configuration (top-side and bottom-side), as described above. This results in four "bifacial, depth-dependent" Raman spectra for each sample. The Raman spectra give us a qualitative information. Indeed, the relative heights of the amorphous and crystalline peaks enable us to compare the degree of crystallinity corresponding to different spectra. For example, from the four bifacial depth-dependent Raman spectra of a sample, one can have an idea about the evolution of the respective amorphous and crystalline phases along the growth axis. On the other hand, one can compare the spectra of different samples measured in the same way.

Although this qualitative information is relevant, our aim is to extract a quantitative value of the crystallinity from a Raman spectrum. As peak areas are proportional to the corresponding phase concentration, Raman spectroscopy is thus amenable to quantitative analysis. To obtain that, "deconvolution", or "curve fitting", of Raman spectra is necessary and will be addressed in § 2.6.1. Then, the Raman crystallinity volume fraction can be calculated by evaluating the scattered intensities assigned to the amorphous and crystalline silicon phases, respectively (see § 2.6.2).

2.6.1. Deconvolution

The purpose of deconvolution is to fit to a measured Raman spectrum well-defined peaks to which a physical meaning can be attributed, plus a continuous background. Then, the different phases present in the material under test can be quantified by comparing the area of each peak fitted to the spectrum. To deconvolute a Raman spectrum with the commercial software available on our computer, several parameters have to be chosen:

1. The **range** (i.e. the lower and upper wavenumber limit values) of the spectrum over which the fit will be performed.
2. The **kind of baseline** to be used in order to isolate the Raman-related peaks.
3. The **number of peaks** to fit to the Raman spectra.
4. The **shape of peaks**, i.e. if they have a Gaussian or Lorentzian shape (or a mixture of both).

5. The **centre position** (i.e. frequency), the **width** and the **height** of each peak.

In practice, deconvolution is performed by the GRAMS software with an algorithm based on the Levenberg-Marquardt method [Marquardt 1963], which adjusts the parameters of a set of peaks to fit to a measured spectrum. The parameters adjusted for each input peak are frequency, height, width at half height, and possibly the ratio of Lorentzian/Gaussian lineshape. The user defines the range of the spectrum to fit, chooses the kind of baseline, and enters a set of initial values that will be varied in order to find the best fit.

2.6.1.1. Relation between spectra and material

As discussed in § 1.2, microcrystalline silicon is a material with a complex microstructure. As shown in Fig. 2.13, the Raman spectra obtained for our \square c-Si:H samples cannot be correctly fitted with only two peaks corresponding to the amorphous and crystalline phases (at 480 cm^{-1} and 520 cm^{-1} , respectively, see § 2.2.3). This holds for Raman spectra of highly microcrystalline samples (Fig. 2.13, top) as well as for those of samples near the transition (Fig. 2.13, bottom). Therefore, the Raman spectra of our \square c-Si:H layers and solar cells have to be deconvoluted with three peaks, as illustrated in Fig. 2.14.

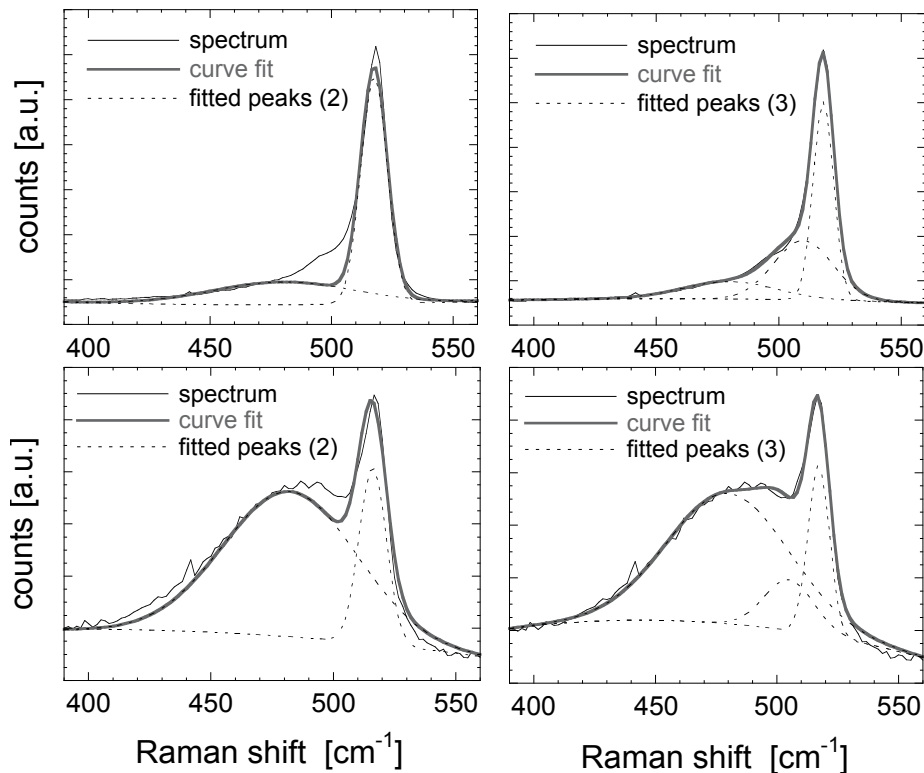


Fig. 2.13: Raman spectra of a highly microcrystalline sample (top) and a sample near the \square c-Si:H / a-Si:H transition (bottom) fitted with two (left) or three (right) contributions.

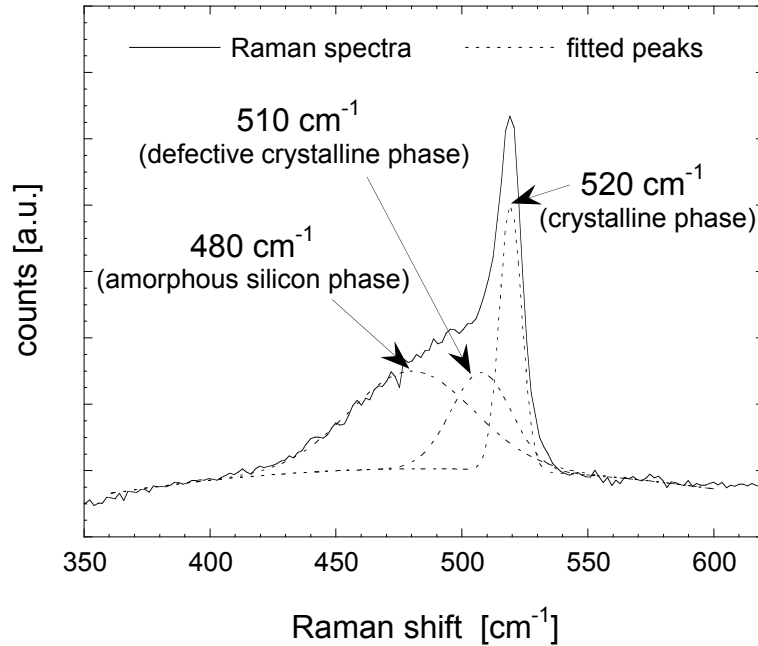


Fig. 2.14: Deconvolution of the Raman spectrum of a [c-Si:H] sample into three contributions: The peak centred around 520 cm^{-1} corresponds to the crystalline phase, the peak centred around 510 cm^{-1} corresponds to the defective crystalline phase and the peak centred at 480 cm^{-1} corresponds to the amorphous phase. The three contributions are Gaussian peaks.

The three peaks used for the deconvolution are attributed to different phases present in the sample:

1. The narrow peak centred at about 520 cm^{-1} , which is the position of the TO (transverse optical) mode in **crystalline silicon** (c-Si), is attributed to silicon crystallites. In our samples, it exhibits a maximum centred at a mean value of $518\pm 1\text{ cm}^{-1}$, and has a mean Full Width at Half Maximum (FWHM) value of $10\pm 1\text{ cm}^{-1}$.
2. The preceding peak exhibits a tail towards smaller wavenumbers (around 510 cm^{-1}). This tail has, in the literature, been attributed either to crystallites of diameters lower than 10 nm [Islam 2001, Xia 1995], or to a silicon Wurzite phase [Kobliska 1973], that could result from twins [Luysberg 1997]. In our deconvolution procedure, this tail is fitted with a peak at about 510 cm^{-1} , and has a mean FWHM value of $26\pm 2\text{ cm}^{-1}$. In the following part of this work, the 510 cm^{-1} peak will be attributed to the **defective part of the crystalline phase** and will be included in the crystalline fraction.
3. The broad peak at 480 cm^{-1} is characteristic of the TO mode in a-Si:H, and is thus attributed to the **amorphous silicon phase**. Its mean FWHM value is $53\pm 7\text{ cm}^{-1}$.

The position and shape of the peaks can be affected by different parameters such as sample temperature (see § 2.4.2) [Cerqueira 1999, Viera 2001], stress in the sample [Anastassakis 1999, Paillard 2002], and size of the crystallites [Viera 2001, Zi 1996].

2.6.1.2. Gaussian or Lorentzian peaks?

In Spectroscopy, instrument and Doppler broadening effects create a Gaussian line shape, while the natural form and collision broadening cause a Lorentzian line shape. Experimental tests have shown that the Gaussian line shape is better adapted than the Lorentzian line shape for fitting the three contributions present in our Raman spectra. On the other hand, a mixed Gaussian-Lorentzian shape could be chosen. However, this would add an extra parameter to fit. Therefore, in this work a Gaussian profile has been chosen to fit the three contributions (amorphous phase, defective crystalline phase and crystalline phase) present in the Raman spectrum of a \square c-Si:H sample.

2.6.1.3. Choice of the range, the baseline and the peak parameters

When applying the bifacial depth-dependent micro-Raman technique on our samples (intrinsic layers or complete solar cells), a wide variety of spectra were obtained (see Fig. 2.15).

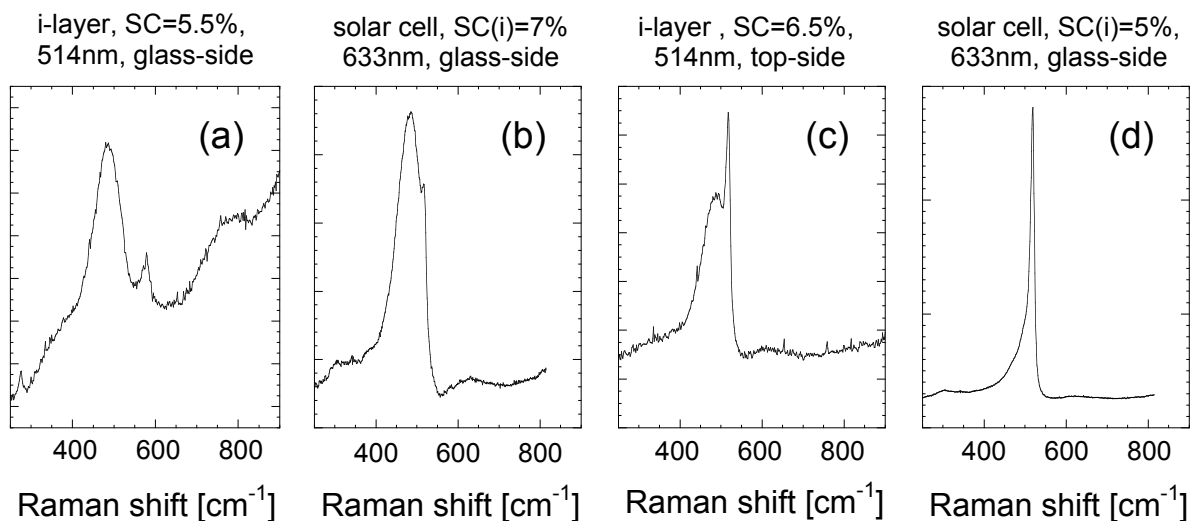


Fig. 2.15: Examples of Raman spectra to be fitted for the quantitative evaluation of the crystallinity. These spectra were measured on various \square c-Si:H intrinsic (i)-layers or entire solar cells, by the bifacial depth-dependent micro-Raman spectroscopy.

In order to deconvolute these spectra in a systematic way that can be applied to any kind of spectrum, the questions that arise at that point are therefore:

- How to choose the spectrum range and the baseline...

- Do we have to give lower and upper limit-values or to fix at a given value the parameters used for fitting the peaks (position, width, height)...

...in order to get **quantitative results that can be compared** ?

The baseline can be either an offset, or a linear, quadratic or cubic function. However, in the Renishaw system used by us, the user can only choose the nature of baseline, but not its equation. According to our tests, the best solution is a **quadratic baseline**. It can actually become a flat line to fit spectra like (d) in Fig. 2.15, or it can represent the large background "signal" due to glass luminescence as observed in spectrum (a) in the same figure. However, the range in which the spectrum will be fitted is very important. If the range within which the fit is performed is too wide, the baseline will not be able to fit the background of spectrum (a) (Fig. 2.15). On the other hand, if the range is too narrow, there is a risk to cut off a part of the silicon-related peaks of the spectrum. Therefore, the optimum range found experimentally, that is applicable to any kind of spectrum measured on our \square c-Si:H samples, is **from 360-380 cm^{-1} to 580-600 cm^{-1}** .

If no lower and upper limit-values or no fixed value are chosen for some of the parameters (position, width, height) of the **three Gaussian peaks**, the deconvolution can lead in certain cases to some absurd results. The position and width of the 520 cm^{-1} peak is not critical, as they are clearly defined on the spectrum of a \square c-Si:H sample. On the other hand, a "competition" between the 480 cm^{-1} and the 510 cm^{-1} peaks can occur, leading to a mathematically good fit that has however no physical meaning [Droz 2001]. Therefore, in the deconvolution procedure, the **position or the 480 cm^{-1} peak has been fixed to this value, and the width of this peak has been limited to the maximal value of 70 cm^{-1}** . The **position of the 510 cm^{-1} peak**, that naturally takes this position for the deconvolution of highly microcrystalline samples, **has been bounded between 505 cm^{-1} and 515 cm^{-1}** . Its **width has been limited to the maximal value of 35 cm^{-1}** . **No limit has been applied to the 520 cm^{-1} peak.**

In the case of glass-side measurements, a more or less important background signal due to the luminescence of the glass is present, principally on the spectra measured with the 514 nm excitation light. For samples deposited on thick glass (some millimetres), the Raman signal can be blurred in the background. In this case, one can subtract from such spectrum a spectrum acquired on raw glass, in order to isolate the silicon-related peaks. Then, the standard deconvolution procedure can be applied to the resultant spectrum. However, in the case of our samples deposited on glass substrates of 0.7 mm thickness, this subtraction is not needed. Indeed, results obtained with and without subtraction are similar.

Note that the different choices and values given above have been based on quite a large quantity of experimental tests, and not on theoretical considerations.

2.6.2. Evaluation of the Raman crystallinity volume fraction

In Raman spectroscopy, the crystalline volume fraction (X_c) of a sample is defined as:

$$X_c = V_c / V_{exp} , \quad (\text{equ. 2.4})$$

where V_c is the crystalline volume and V_{exp} is the total scattering volume in the Raman experiment. For a mixed phase material (i.e. $V_{exp} = V_a + V_c$, with V_a the amorphous volume), the respective integrated Raman scattered intensities of the amorphous and crystalline phase can be expressed as [Bustarret 1988]:

$$I_a = \square_a \cdot V_a = \square_a \cdot (1 - X_c) \cdot V_{exp} , \quad (\text{equ. 2.5})$$

$$I_c = \square_c \cdot V_c = \square_c \cdot X_c \cdot V_{exp} , \quad (\text{equ. 2.6})$$

where $\square_{a,c}$ is the integrated Raman cross-section of the TO mode of the amorphous and crystalline phases, respectively. From (equ. 2.5) and (equ. 2.6), one can express the crystalline volume fraction as:

$$X_c = I_c / (I_c + y \cdot I_a) , \quad (\text{equ. 2.7})$$

where y is defined as the ratio of the integrated Raman cross-sections [Tsu 1982]:

$$y = \square_c / \square_a . \quad (\text{equ. 2.8})$$

Whereas I_c and I_a can be directly measured from the Raman spectra, the value of y is quite a matter of debate. Values of y from 0.88 [Tsu 1982] down to 0.1 [Brodsky 1977] have been published. Furthermore, y depends on the size of the crystallites (\square) and on the excitation wavelength [Bustarret 1988]. For a grain size of 20 nm, the relation given by Bustarret et al. ($y(\square) = 0.1 + \exp[-(\square/250)]$, with \square in Å) results in $y \approx 0.55$ for an excitation wavelength of 514 nm and $y \approx 0.23$ for an excitation wavelength of 633 nm. This is the reason why we will define here the parameter \square_c as a “**Raman crystallinity factor**”, for which we arbitrarily set $y = 1$. This factor does not reflect the actual crystalline volume fraction, but is simply a ratio of Raman intensities that is expressed as:

$$\square_c = I_c / (I_c + I_a) . \quad (\text{equ. 2.9})$$

In practice, \square_c is evaluated from the deconvoluted Raman spectra as the ratio of the area of the peak(s) related to the crystalline parts over the total area of the silicon-related peaks. The Raman spectra of our \square_c -Si:H layers or solar cells is fitted with three contributions (see § 2.6.1.1). As discussed before, the 510 cm^{-1} peak, attributed to the defective part of the

crystalline phase, has to be included in the crystalline part. Therefore the Raman crystallinity factor will be calculated as follow:

$$\square_c = I_{(\square)c} / (I_{(\square)c} + I_a) = (I_{520} + I_{510}) / (I_{520} + I_{510} + I_{480}) , \quad (\text{equ. 2.10})$$

where I_i is the **area** under the Gaussian centred at i and $I_{520} + I_{510} + I_{480}$ is the total integrated intensity (see Fig. 2.14). **Note that the crystalline silicon material present in our \square c-Si:H samples cannot be considered to be identical to large scale mono-crystalline silicon, as it includes the defective crystalline part.** By analogy, the Raman cross-section ratio considered here (see § 2.7) is:

$$y = \square_{(\mu)c} / \square_a , \quad (\text{equ. 2.11})$$

where $\square_{(\mu)c}$ is the Raman cross-section of the (micro-)crystalline phase present in our samples (i.e. the material giving rise to the 520 cm^{-1} and 510 cm^{-1} peaks in the Raman spectra).

2.7. Determination of the “real” crystalline volume fraction

The Raman crystallinity factor \square_c gives a ratio of the integrated intensities of the corresponding Raman peaks. It does not give the "real" ratio of the crystalline to total volume fraction, as the Raman cross-section ratio has arbitrarily been set to $y = 1$ for its evaluation. However, we would like to know how \square_c relates to the "actual crystallinity" of the sample. In order to overcome this limitation, we would now like to determine the value of y corresponding to our samples and to our deconvolution procedure.

2.7.1. Evaluation of the Raman cross-section ratio y

In order to evaluate the Raman cross-section ratio y , we will compare, for one \square c-Si:H sample, the bifacial depth-dependent values obtained for \square_c with the microstructure observed on TEM micrographs. The sample used for this evaluation is a \square c-Si:H layer deposited near the \square c-Si:H / a-Si:H transition, with a silane concentration of SC = 6% (see Fig. 2.16, Fig. 2.22, and § 3.4).

In Raman measurement, the collected signal is dependent upon the double optical attenuation function A [Hang 1988] (see Fig. 2.10):

$$A(z) = e^{\square z} , \quad (\text{equ. 2.12})$$

where z is the depth in the silicon sample ($z = 0$ corresponds to the silicon layer surface). The total scattering volume in the Raman experiment (V_{exp}) is proportional to the integral of $A(z)$

over the total sample thickness (d):

$$V_{\text{exp}} = \int_0^d e^{-2\Gamma z} dz. \quad (\text{equ. 2.13})$$

As the integrated intensity of the Raman peak is proportional to the scattering volume, it is therefore also proportional to the integral given in (equ. 2.13). The proportion of the Raman signal coming from a slice of thickness Δz at the depth z in the material can, thus, be expressed as:

$$p(z, \Delta z) = \frac{\int_z^{z+\Delta z} e^{-2\Gamma z} dz}{\int_0^d e^{-2\Gamma z} dz} = \frac{e^{-2\Gamma z} \cdot (e^{2\Gamma \Delta z} - 1)}{(e^{-2\Gamma d} - 1)}. \quad (\text{equ. 2.14})$$

From (equ. 2.14), one can for example calculate the proportion p_{RCD} of the Raman signal coming from the volume included between the sample surface ($z = 0$) and the depth $\Delta z = \text{RCD}$, as defined in § 2.5.1. This proportion depends on the sample thickness, as shown in Table 2.3. If the sample thickness is large enough compared to RCD, still one third of the collected Raman signal arises from the part of the sample that is deeper than RCD.

$d =$	1.1·RCD	2·RCD	3·RCD	4·RCD	5·RCD	10·RCD
p_{RCD}	0.94	0.73	0.66	0.64	0.63	0.63

Table 2.3: Proportion of the collected Raman signal (p_{RCD}) coming from the volume comprised between the silicon layer surface and the depth $z = \text{RCD}$ (see § 2.5.1), for different total sample thicknesses (d).

From one TEM micrograph of a sample cross-section, we have drawn and digitalized a two grey levels (white and black) micrograph of the amorphous and microcrystalline phases (see Fig. 2.16, white and black parts, respectively). Although a TEM micrograph is a projected view of a thin sample, it is indeed still representative of the volume of the structure [Underwood 1970]. We have measured at various depths (z), on a line of one single pixel thick, the proportion of black pixels compared to the total number of pixels. This has been done here with a commercial image processing software (analySIS, version 3.2). One can, thus, obtain a “linear microcrystalline fraction” $C(z)$, represented in Fig. 2.17.

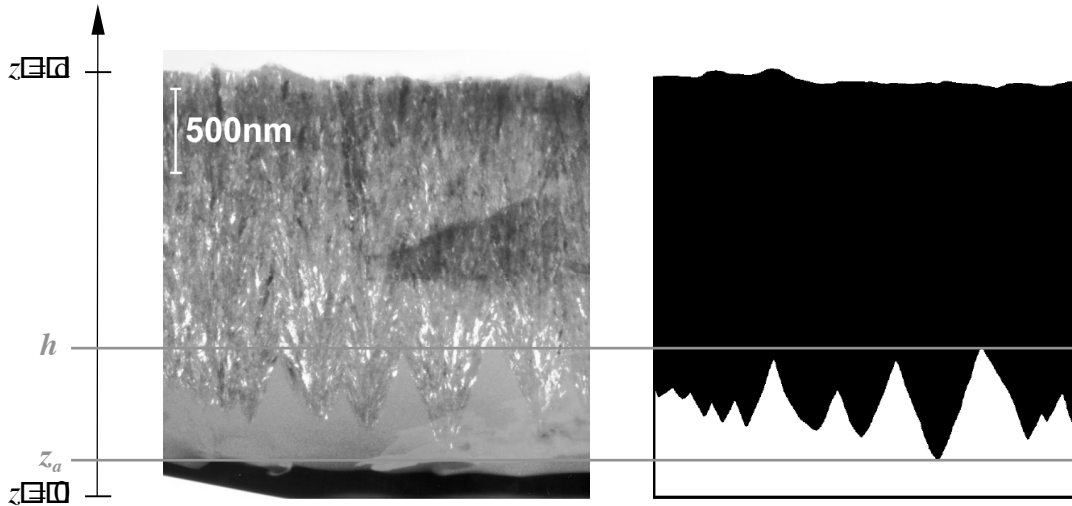


Fig. 2.16: Left: TEM dark field micrograph of the cross-section of an intrinsic \square c-Si:H layer deposited at $SC = 6\%$ on glass (thickness $\approx 2.4 \mu\text{m}$). At the bottom of the i-layer, amorphous silicon appears uniformly grey, between conical conglomerates of nanocrystals. The latter is the microcrystalline silicon phase. After coalescence of the microcrystalline cones, the amorphous material is no longer observable in this medium-resolution micrograph. Right: digitalized micrograph with the amorphous (white) and microcrystalline (dark) phases.

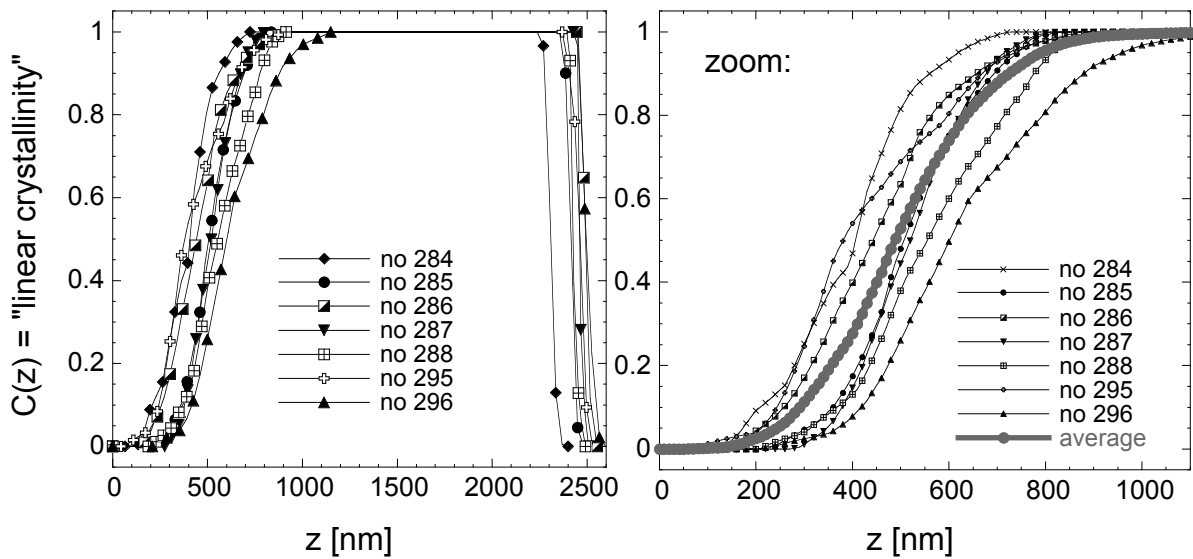


Fig. 2.17: Evolution of the “linear” microcrystallinity $C(z)$ with the sample depth (z), evaluated as the percent of black pixels on an horizontal line (i.e. for a given z value) on seven digitalized TEM micrographs (indicated by a code number) taken in different positions in the 6% \square c-Si:H layer (see Fig. 2.16). Left: curves over the whole z range. Right: zoom for the first (bottom) micrometer, plus the average curve.

From the experimental “linear” microcrystallinity curves $C(z)$ (see Fig. 2.17) and the double optical attenuation function $A(z)$ (see Fig. 2.10 and (equ. 2.12)), one can calculate the volume fraction of the \square c-Si:H phase of the probed volume in Raman experiments:

$$X_{\square c} = \frac{V_{\square c}}{V_{tot}} = \frac{\int_0^d A(z) \cdot C(z) dz}{\int_0^d A(z) dz}. \quad (\text{equ. 2.15})$$

This expression gives the microcrystalline fraction relative to the amorphous part. We are, however, interested in determining the crystalline fraction. Indeed, the $\square c$ -Si:H phase (black part of Fig. 2.16, right) contains grain boundaries more or less filled with amorphous material, as clearly seen in the TEM micrograph of the sample (Fig. 2.16, left). Let us define \square as the fraction of crystallinity of the $\square c$ -Si:H phase, and suppose that \square is a constant within the sample (i.e. not a function of z). The real crystalline volume fraction of the probed volume becomes:

$$X_c = \square X_{\mu c}. \quad (\text{equ. 2.16})$$

By putting the expressions for I_a (equ. 2.5) and I_c (equ. 2.6) into the equation defining $\square c$ (equ. 2.9), one can relate X_c , $\square c$ and y . The Raman cross-section ratio can thus be expressed as:

$$y = \frac{\square c (1 - \square X_c)}{X_c (1 - \square c)} = \frac{\square c (1 - \square \square X_{\square c})}{\square X_{\square c} (1 - \square c)}. \quad (\text{equ. 2.17})$$

For our $\square c$ -Si:H layer deposited at SC = 6%, the experimental values of $\square c$ obtained from deconvoluted bifacial depth-dependent Raman measurements as well as the calculated values for $X_{\mu c}$ (for the average curve, see Fig. 2.17) are given in Table 2.4. Note that the small variation in the $X_{\mu c}$ -value (514 nm, glass-side) is due to the difference of the absorption coefficients for a-Si:H and for $\square c$ -Si:H at 514 nm (see in Table 2.2).

	633 nm, layer-side	633 nm, glass-side	514 nm, layer-side	514 nm, glass-side
$\square c$	0.70	0.33	0.72	0.00
$X_{\mu c}$ (average)	0.984	0.38	1	0.00-0.08

Table 2.4: Experimental values of $\square c$ obtained from deconvoluted bifacial depth-dependent Raman measurements, as well as calculated values for $X_{\mu c}$ (according to (equ. 2.15), with absorption coefficients for a-Si:H and $\square c$ -Si:H given in Table 2.2, and $C(z)$ for the average curve, see Fig. 2.17), for the $\square c$ -Si:H layer deposited at SC = 6%.

The value of y can now be calculated with (equ. 2.17). However, we have to find the value for \square . We assert that the correct value for \square is that for which $y_{\text{glass-side}} = y_{\text{layer-side}}$, at a given wavelength. As can be seen from Table 2.4, the strongly absorbed light (514 nm) is not

useful for the determination of y , as the “extreme” value $\square_c = 0$ for glass-side is present. Fig. 2.18 shows y as a function of \square according to (equ. 2.17) for the values of \square_c and $X_{\mu c}$ given in Table 2.4. For the average $C(z)$ curve (see Fig. 2.17), $y(\square)_{\text{glass-side}} = y(\square)_{\text{layer-side}}$ when $\square \approx 0.59$ and $y_{633} \approx 1.68$. As the crystallinity of the microcrystalline phase \square is obviously independent of the wavelength, the values for y at 514 nm (y_{514}) can be obtained on the layer-side curve at 514 nm (see Fig. 2.18) for the values of \square obtained for 633 nm: one obtain $y_{514} \approx 1.78$.

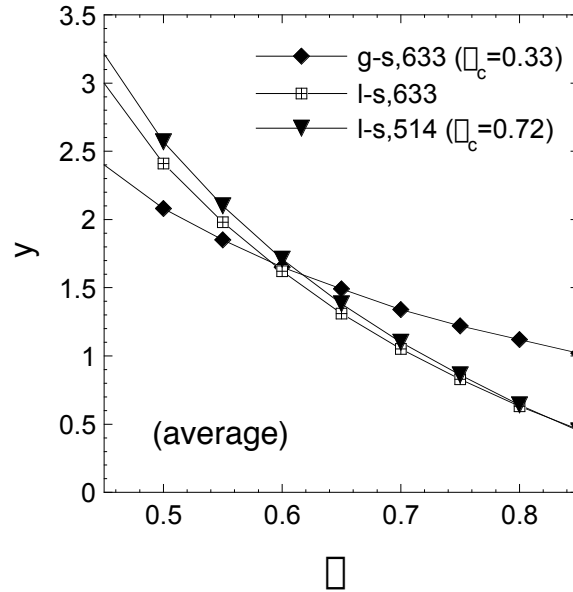


Fig. 2.18: Relation between the Raman cross-section ratio y and the crystallinity of the microcrystalline phase \square calculated with (equ. 2.17) from the Raman crystallinity factors \square_c and the $X_{\mu c}$ -values given in Table 2.4. The correct values for y and \square are those obtained where the curves for the glass-side (g-s) measurement cross that for the layer-side (l-s) measurement, at a given wavelength. Therefore, $y_{633} = 1.68$ and $y_{514} = 1.78$ for $\square = 0.59$.

On the basis of the \square -Si:H sample deposited at SC = 6%, we have, thus, determined the **Raman cross section ratio for μ c-Si over a-Si:H** $y = \square_{(\mu)c} / \square_a$ (equ. 2.11) as being $y \approx 1.7$ at **633 nm** and $y \approx 1.8$ at **514 nm**. This evaluation is based on the hypothesis that the crystallinity \square within the \square -Si:H phase is not dependent on the thickness z . These values for y are surprisingly quite different than those ranging from 0.1 to 0.88 obtained by [Brodsky 1977], [Bustarret 1988] and [Tsu 1982] (see 2.6.2).

As a countercheck, one can compare the Raman intensities obtained for a fully amorphous sample and for a fully microcrystalline or crystalline sample. The integrated Raman intensities obtained on such samples must be corrected with the respective absorption coefficients according to:

$$y = \frac{\mu_{(D)c}}{\mu_a} \frac{I_{(D)c}}{I_a} \cdot \frac{\mu_{(D)c}}{\mu_a} \quad (\text{equ. 2.18})$$

This expression is obtained from (equ. 2.5), (equ. 2.6) and (equ. 2.13) and is valid when thick enough samples are considered (for which $\mu d > 1$). Note that most of the values for y found in the literature are obtained by this way. We have measured under the same experimental conditions (at 514 nm) the Raman spectra on an entire a-Si:H sample, an entire \square c-Si:H sample (deposited at SC = 2%) and a c-Si reference wafer. By taking into account the absorption coefficients μ given in Table 2.2 for the respective materials, one obtains $y_{514}^{\mu c/a} \approx 2.1 - 2.8$ and $y_{514}^{c/a} \approx 0.4 - 1.1$. The difference between $y_{514}^{\mu c/a}$ and $y_{514}^{c/a}$ as obtained here could explain (at least partly) the difference between the value of y evaluated above ($y \approx 1.7 - 1.8$) and the values found in the literature ($y \approx 0.1 - 0.9$).

2.7.2. Discussion

2.7.2.1. Interpretation of the $C(z)$ curves

The most interesting part of the $C(z)$ curves lies in the first micrometer over which $C(z)$ varies from 0 to 1 (see Fig. 2.17, right). This evolution depends on four main parameters (see Fig. 2.16 and Fig. 2.19): the height of the amorphous incubation layer z_a , the opening angle \square of the \square c-Si:H cones, the mean distance between the cones $1/n_d$ (n_d being the nuclei density), and the height h at which the cones coalesce. z_a corresponds to the beginning of the rise of the $C(z)$ curve, while h corresponds to the point of saturation at 1. The slope of $C(z)$ depends on \square and n_d .

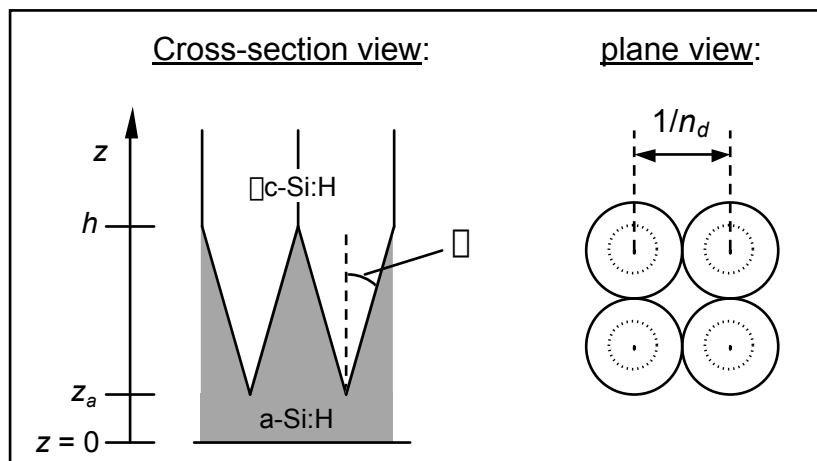


Fig. 2.19: Simple model from which one can calculate the theoretical evolution $C_{th}^{3D}(z)$ of the microcrystallinity (equ. 2.19). z_a is the height of the amorphous incubation layer, h is the height at which the \square c-Si:H cones coalesce, \square is the opening angle of the \square c-Si:H cones, and $1/n_d$ is the distance between the cones.

On the basis of a simple 3-dimensional model (see Fig. 2.19), one can calculate the theoretical evolution of the \square c-Si:H phase $C_{th}^{3D}(z)$ (equ. 2.19). This model considers identical \square c-Si:H cones placed periodically at $1/n_d$ and which start at the same height z_a . The simple expression (equ. 2.19) is only valid from $z = z_a$ (i.e. height of the amorphous incubation layer); it does only fit the increasing part of $C(z)$ and not its saturation (that is due to the coalescence of the cones).

$$C_{th}^{3D}(z) = \frac{\square \cdot \text{tg}^2(\square)}{(1/n_d)^2} \cdot (z - z_a)^2. \quad (\text{equ. 2.19})$$

The height h at which the cones have completely coalesced (i.e. when the radius of the cones equal $1/(\sqrt{2} \cdot n_d)$) can be calculated on the basis of simple geometrical consideration:

$$h = \frac{1}{\sqrt{2} \cdot n_d \cdot \text{tg}(\square)} + z_a. \quad (\text{equ. 2.20})$$

The expression (equ. 2.19) has been fitted from $z \approx z_a$ until $C(z) \approx 0.5$ on the experimental curves of Fig. 2.17. The resulting parameters z_a , \square and n_d are given in Table 2.5. h has been subsequently calculated from (equ. 2.20), whereas h^* has been "manually" evaluated from Fig. 2.17 at $C(z) \approx 0.99$.

TEM micro-graph n°	z_a [nm]	\square [°]	n_d [μm^{-1}]	h [nm]	h^* [nm]
284	60	14.0	4.6	677	700
285	232	15.5	5.2	722	790
286	105	14.3	4.7	695	840
287	261	16.2	5.4	712	780
288	219	14.3	4.7	809	880
295	126	16.3	5.5	566	860
296	259	14.1	4.7	858	1110
average	127	13.7	4.5	772	920
mean	180	15.0	5.0	720	851
median	219	14.3	4.7	712	840
std deviation	82	1.0	0.4	94	129

Table 2.5: Height of the amorphous incubation layer (z_a), opening angle (\square) of the \square c-Si:H cones, and mean distance ($1/n_d$) between the cones (n_d being the nuclei density) fitted with a simple 3-dimensional model (equ. 2.19) (see Fig. 2.19) on the experimental $C(z)$ curves of Fig. 2.17. The height h at which the cones coalesce has been calculated with (equ. 2.20), whereas h^* has been "manually" evaluated from Fig. 2.17 at $C(z) \approx 0.99$.

From Table 2.5, one sees that, for this intrinsic \square c-Si:H layer deposited at SC = 6%, the mean value of the opening angle of the cones is $\square = 15 \pm 1^\circ$ whereas the mean value of the nuclei density is $n_d = 5 \pm 0.4 \mu\text{m}^{-1}$. These values are quite in accordance with the values given by Bailat et al. [Bailat 2003] for the case of solar cells incorporating i-layers deposited in similar conditions as the intrinsic layer studied here. As stated above, \square and n_d are responsible for the slope of the $C(z)$ curves. The small standard deviation values observed for \square and n_d in the seven micrographs evaluated here (see Table 2.5) corresponds well with the similar slopes observed on the $C(z)$ curves in Fig. 2.17. On the other hand, one observes in Table 2.5 a large standard deviation for the value of the height of the amorphous incubation layer ($z_a \approx 180 \pm 80$ nm). This corresponds well to the significant lateral shift of the various $C(z)$ curves of Fig. 2.17; it can be intuitively related to the critical process of nucleation of the microcrystalline phase in the amorphous phase.

2.7.2.2. Dependence of y on the experimental data used for its evaluation

The value of z_a has obviously an incidence on the value of y . In order to evaluate the influence of the large standard deviation of the z_a -values on the value of y , we have followed the same reasoning as in § 2.7.1 for the two extreme $C(z)$ curves of Fig. 2.17 (n° 284 and n° 296). Moreover, we will also discuss the influence of a variation in the experimental \square_c -value (due to sample lateral inhomogeneity). Results are given in Table 2.6, Fig. 2.20 and Table 2.7

	633 nm, layer-side	633 nm, glass-side	514 nm, layer-side	514 nm, glass-side
\square_c	0.70	0.33-(0.38)	(0.70)-0.72	0.00
$X_{\mu\text{c}}$ (n° 284)	0.985	0.47	1	0.05-0.13
$X_{\mu\text{c}}$ (average)	0.984	0.38	1	0.00-0.08
$X_{\mu\text{c}}$ (n° 296)	0.978	0.30	1	0.00-0.04

Table 2.6: Experimental values of \square_c obtained from deconvoluted bifacial depth-dependent Raman measurements, as well as calculated values for $X_{\mu\text{c}}$ (according to (equ. 2.15), with absorption coefficients for a-Si:H and \square c-Si:H given in Table 2.2, and $C(z)$ for the curve n° 284, n° 296 and for the average curve, see Fig. 2.17), for the \square c-Si:H layer deposited at SC = 6%. The variation in the \square_c -values is due to lateral inhomogeneity of the sample (the \square_c -values in brackets were measured in a place different from that used for the TEM sample fabrication). The small variation in the $X_{\mu\text{c}}$ -value (514 nm, glass-side) is due to the difference of the absorption coefficients for a-Si:H and for \square c-Si:H at 514 nm.

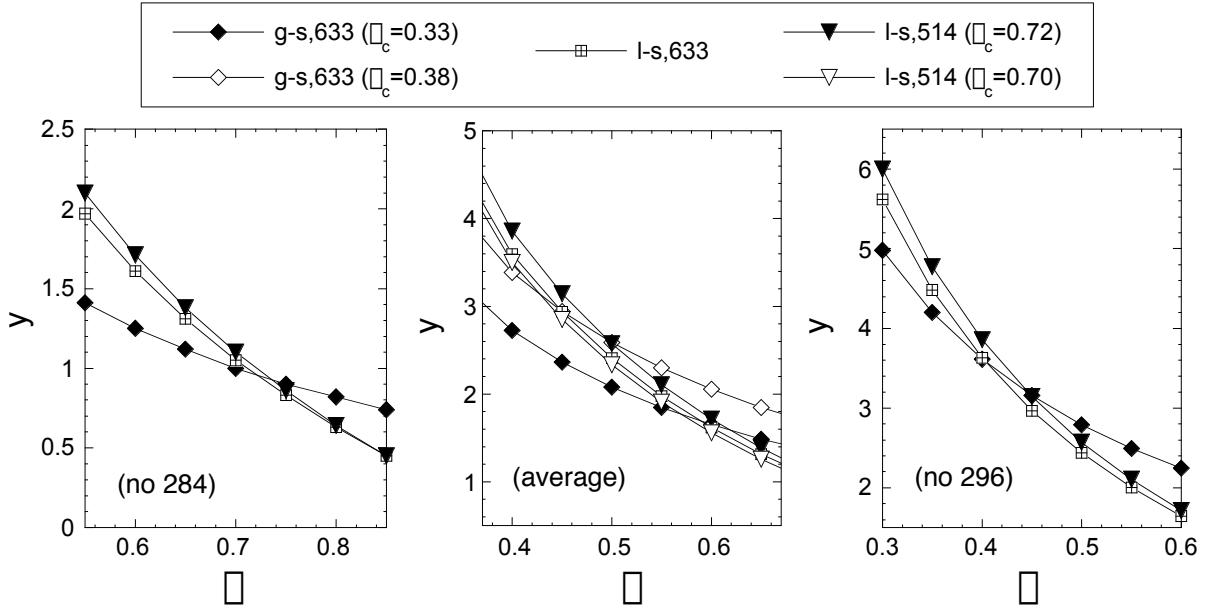


Fig. 2.20: Relation between the Raman cross-section ratio y and the crystallinity of the microcrystalline phase \square calculated with (equ. 2.17) from the Raman crystallinity factors \square_c and the $X_{\mu c}$ -values given in Table 2.6. The "correct" values for y and \square are those obtained where the curves for the glass-side (g-s) measurement cross that for the layer-side (l-s) measurement, at a given wavelength. These values are given in Table 2.7.

	\square	y_{633}	y_{514}
C(z) curve n° 284	0.72	0.96	0.90-1.00
average C(z) curve	0.59	1.68	1.78
average C(z) curve ($\square_c^{gs, 633} = 0.38$)	0.45	2.94	2.84-3.14
C(z) curve n° 296	0.41	3.53	3.75

Table 2.7: Raman cross-section ratio y obtained from Fig. 2.20 for the wavelengths of 633 and 514 nm and for the different cases listed in Table 2.6. If not indicated the value $\square_c^{gs, 633} = 0.33$ has been used.

Table 2.7 shows that the value of y varies quite a lot depending on which C(z) curve of Fig. 2.17 is used for its evaluation. Indeed, one obtains y -value varying from 1 to more than 3. However, the C(z) curves n° 284 and n° 296 are both quite extreme as compared to the others (see Fig. 2.17) Therefore, they should not be taken as representative of the sample. Thus, one should be careful when analysing only one TEM micrograph of a sample. Although it includes 10 to 20 cones, it is far from being representative of a layer. On the other hand, a Raman crystallinity value not measured on the very same place where the TEM sample is then fabricated (leading in our case to $\square_c^{gs, 633} = 0.38$ instead of 0.33, due to the lateral inhomogeneity of the sample) also results in quite different y -value (see Table 2.7). According

to our values obtained for y (and in particular to those corresponding to the average $C(z)$ curve, see Table 2.7) one can say that **our Raman crystallinity factor \square_c slightly overestimates the real crystalline volume fraction X_c** . The relation between X_c and \square_c is given in Fig. 2.21 for different values of y .

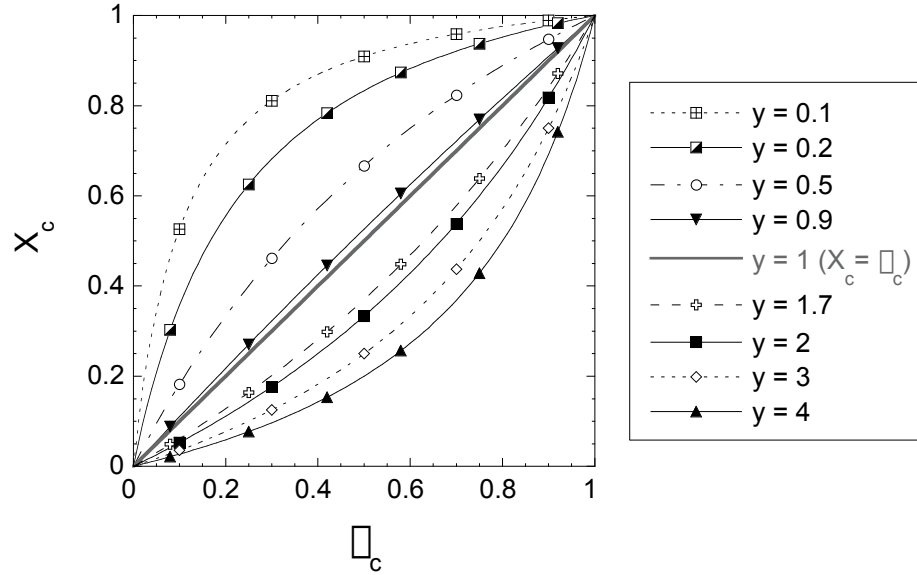


Fig. 2.21: Evolution of the crystalline fraction X_c as a function of the Raman crystallinity factor \square_c (equ. 2.17) for various value of the Raman cross-section ratio y . For $y < 1$, \square_c underestimate the real crystallinity, whereas for $y > 1$, \square_c overestimate the real crystallinity.

2.7.2.3. Evaluation of the actual crystallinity of the \square c-Si:H phase (\square)

The values of y obtained for the average $C(z)$ curve correspond to a crystallinity of the \square c-Si:H phase of $\square \approx 0.6$ (see Table 2.7). Thus, the top (layer-side) crystallinity of our sample deposited at SC = 6% is about 60%. In order to verify this statement, we shall estimate the crystallinity of the \square c-Si:H phase (i.e. \square). If we consider that the \square c-Si:H phase is formed of cubic nanocrystals of edge \square separated by grain boundaries of thickness k , the crystalline fraction can be calculated as:

$$F_c = \frac{\square^3}{(\square + k)^3} . \quad (\text{equ. 2.21})$$

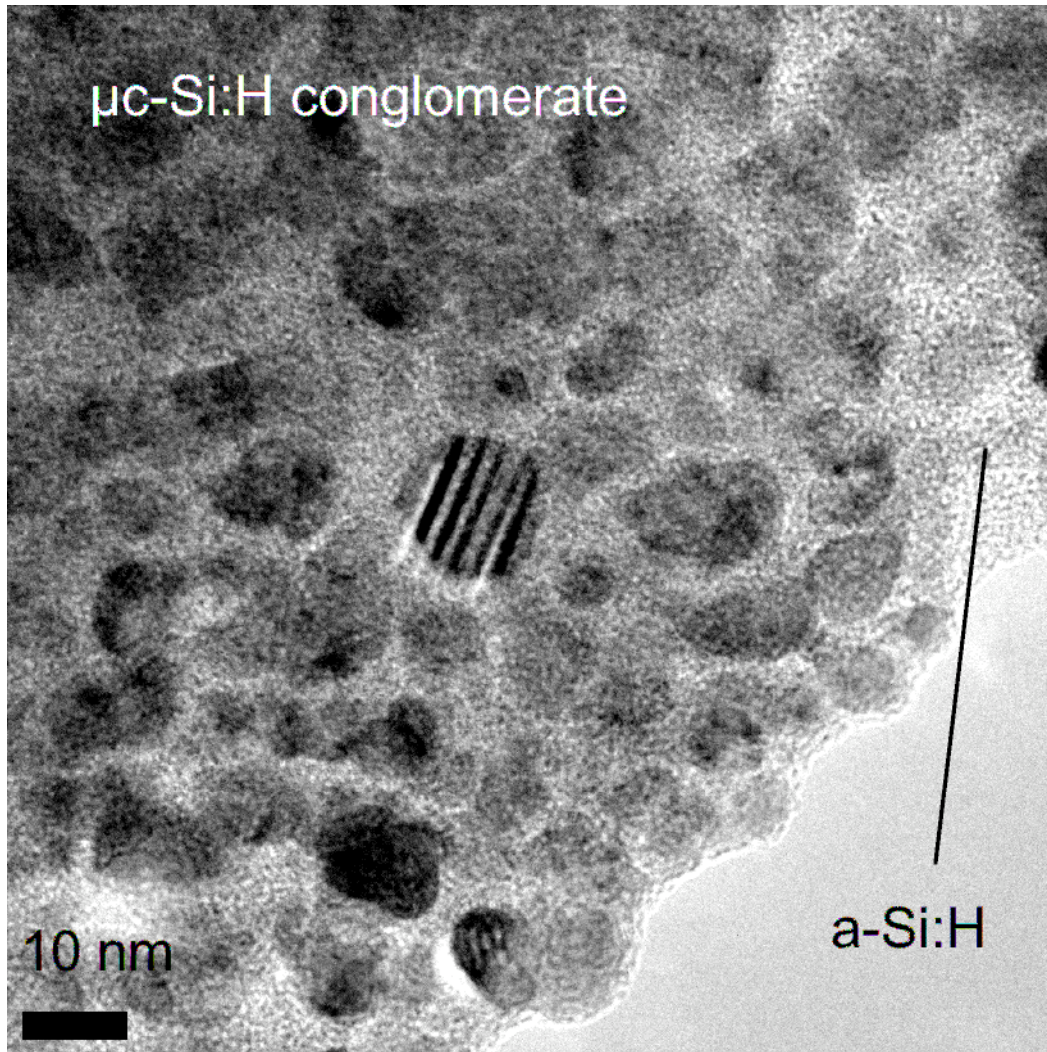


Fig. 2.22: High resolution (HR) TEM micrograph of the top surface (plane view) of the $\mu\text{c-Si:H}$ layer deposited at $SC = 6\%$ (the TEM micrograph of the cross-section of this same sample is given in Fig. 2.16).

In the sample used for this evaluation of γ , X-ray diffraction data analysis yields a value of $\bar{\lambda} \approx 20$ nm (see Chapter 3). According to (equ. 2.20), a value of $\bar{\lambda}$ ($= F_c$) of 60% thus corresponds to **grain boundaries having a thickness of about 3.7 nm between the crystallites**. Fig. 2.22 show a High Resolution (HR) TEM micrograph of the top surface of the layer studied here (whose cross-section TEM micrograph is given in Fig. 2.16). We can distinguish the nanocrystals (dark round shape) embedded in a significant amorphous matrix (light grey). The amorphous thickness between two nanocrystals can be estimated to be around 2 to 4 nm. On the TEM micrograph of Fig. 2.22, the nanocrystals have a diameter of about 10 nm. Fig. 2.23 shows the relation between $\bar{\lambda}$ and k for $F_c = 0.6 \pm 0.1$. One sees that for a nanocrystal size between 10 nm and 20 nm, a grain boundary thickness from about 2 to 4 nm yields $F_c = 0.6$. The qualitative observations of the HR plane view micrograph of Fig. 2.22 are, therefore, consistent with a value of $\bar{\lambda} = 0.6$.

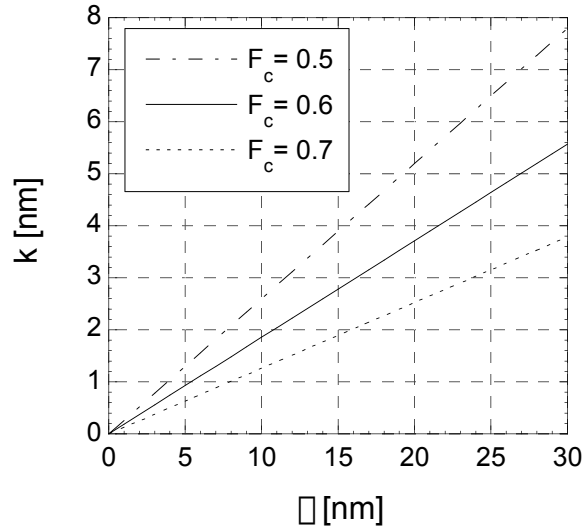


Fig. 2.23: Relation between the grain boundary thickness k and the nanocrystal size l for different crystalline fraction F_c , evaluated from (equ. 2.21).

2.8. Conclusions

In this chapter, we have discussed the application of micro-Raman spectroscopy for the evaluation of the crystallinity in \square c-Si:H samples. Providing some care is taken regarding the experimental parameters (in particular the excitation power used, in order to avoid recrystallisation of the sample), micro-Raman spectroscopy is a powerful and non-destructive technique, that can be applied either to single intrinsic \square c-Si:H layers of the complete \square c-Si:H solar cells. The interest of this tool is, thus, that it gives us the possibility to characterise the volume fractions of amorphous and crystalline phases within devices, on which electrical performances can be measured.

In this work we are conducting bifacial depth-dependent Raman measurements, i.e. we are probing the sample either from the top or from the bottom side, with two different excitation wavelengths (514 nm and 633 nm). Thus, we can evaluate selectively the crystallinity of the last part of the sample or the beginning of growth of the sample, while having depth-dependent information. This enables to measure the inhomogeneity in thickness of our samples and, in the case of solar cells, to probe either the n-i or the p-i interface region.

The Raman spectrum of our \square c-Si:H samples can be deconvoluted into three contributions corresponding to the crystalline phase, the defective crystalline phase and amorphous phase. With a systematic deconvolution procedure, a "Raman crystallinity factor" \square_c can be calculated from each Raman spectra by dividing the integrated intensity assigned to the crystalline phase by the total integrated intensity of the silicon-related peak.

However, such crystallinity factor does not take into account the Raman cross-section

ratio y of $\mu\text{-Si}$ over a-Si:H . In order to evaluate y corresponding to our measurement and deconvolution technique, we have compared the Raman crystallinity factors measured on one $\mu\text{-Si:H}$ layer with its microstructure as observed on TEM micrographs. By taking into account the penetration depth of the excitation light and the evolution of the microcrystalline phase (compared to the amorphous phase) as a function of the depth into the sample, we have found that $y \approx 1.7$ at 633 nm and $y \approx 1.8$ at 514 nm, assuming that the crystallinity of the microcrystalline phase remains constant with the thickness. These values for y contain, however, a large uncertainty related to the critical nucleation of the microcrystalline phase within the amorphous material. In order to get statistically valuable values of y , a large number of TEM micrographs of the same sample have to be analysed. Indeed, a variation in the value of y of up to ± 1 can be obtained from the analysis of one single TEM micrograph exhibiting 10 to 20 microcrystalline conglomerates. Furthermore, a variation of ± 0.05 on the \int_c -value utilised for the evaluation of y results in a variation of 0.5 for y . Such variations could be observed due to lateral inhomogeneities of the microcrystalline fraction on our layers. In order to confirm the values obtained for the Raman cross-section ratio y , our evaluation procedure as described here should be done on a larger set of samples. Such layers, deposited on a flat substrate, should ideally be thinner than the 2 μm thick layer used here while still exhibiting a high structure inhomogeneity in thickness. Thus, \int_c measured at 514 nm on the bottom side would be different from zero and a cross check for the values obtained would be possible.

In the following of this work, due to the quite large uncertainty related to the value of y , we have used the Raman crystallinity factor \int_c . However, if y equals actually 1.7 - 1.8, \int_c is not that much different from the real crystallinity ($\pm 30\%$). The results presented in the following of this work for the characterisation of $\mu\text{-Si:H}$ layers and solar cells can, thus, not be contested regarding the use of the factor \int_c instead of X_c . Note that most research groups use the simplified Raman crystallinity factor as monitoring for the crystallinity of $\mu\text{-Si:H}$ devices. However, one should be careful when comparing such values given in the literature. Indeed, the value of \int_c is dependent on how it is measured (i.e. excitation wavelength, top- or bottom-side, thickness of the sample,...) and how it is deconvoluted (two or three contributions, baseline, integrated intensities of amplitude of the peaks,...).

Chapter 3: Coplanar electrical transport in intrinsic \square c-Si:H layers and its relation with microstructure

3.1. Introduction

The intrinsic layer of a p-i-n (or n-i-p) silicon thin film solar cell plays two important roles in the functioning of the device. On one hand, it must have good light absorption properties, in order to generate as many electron-hole pairs as possible for a given incident light intensity. On the other hand, it must have good electrical transport properties, in order to enable the free electron and holes to exit the device before recombining. This section deals with the second topic.

\square c-Si:H is a photoconductive material successfully incorporated as intrinsic layer in p-i-n ($\square = 8.5\%$, [Meier 1998b] or n-i-p ($\square = 9.2\%$, [Terrazzoni-Daudrix 2003]) solar cells. In order to achieve an efficient collection of the photogenerated carriers in the cell, high mobility (μ) and recombination time (τ) (i.e. high $\mu\tau$ products) are required. We are therefore interested in studying the electronic transport properties of intrinsic \square c-Si:H layers, in view of their incorporation into solar cells. One of the main issues concerning \square c-Si:H is to identify which part of its complex microstructure (as described in Chapter 1) governs electrical transport. Indeed, the constituents of \square c-Si:H, i.e. hydrogenated amorphous silicon (a-Si:H) and crystalline silicon, possess quite different transport properties. To this end, electrical transport properties have been studied in intrinsic \square c-Si:H layers and compared, first, with those of a-Si:H samples and, second, with the microstructure of the \square c-Si:H samples.

Note that we have exclusively studied *coplanar* transport in intrinsic layers, i.e. electronic transport with current flowing parallel to the substrate, and therefore perpendicular to the conglomerate boundaries (see Fig. 1.3). On the other hand, the functioning of \square c-Si:H solar cells is based on carrier transport perpendicular to the substrate, i.e. in "transverse" or "sandwich" configuration. However, from the complexity of the microstructure of \square c-Si:H

material (see § 1.2.1), we can suspect that the coplanar electrical transport properties may be different from the transverse electrical transport properties. Indeed, Kocka et al. [Kocka 2003] as well as Wyrsh et al. [Wyrsh 2000] have shown that some \square c-Si:H samples are anisotropic regarding electrical properties.

Our approach of studying coplanar transport properties has been motivated by the following reasons: First, well-established characterisation methods are indeed available for coplanar transport measurements both with and without illumination, but such methods are not applicable to "transverse" or "sandwich" configuration. Second, the technical difficulty of obtaining Ohmic contacts in transverse configuration has prevented the use of the same simple characterisation tools as usable for the coplanar configuration. Finally, the understanding of the mechanisms governing the transport in \square c-Si:H material from a microscopic point of view, even if studied only for the coplanar configuration, will certainly still be helpful for the understanding of carrier transport and collection in solar cells.

The experimental techniques used in this work for the electrical characterisation of the thin film silicon layers will be presented in § 3.2. These are techniques for measurement both in the dark (dark conductivity) and under illumination. The latter consisting of photoconductivity and ambipolar diffusion length measurements; from these last two measurements methods, a parameter b , indicative of the Fermi level position, as well as the material transport "quality factor" $\mu^0 \mu^{\text{eff}}$ are evaluated [Beck 1996b].

In § 3.3, the general electronic transport properties of \square c-Si:H will be discussed in comparison with those of a-Si:H, for which a transport model is well established. To that aim, numerous a-Si:H and \square c-Si:H samples will be analysed by the same characterisation techniques under steady-state illumination condition. Results have been published in [Droz 2000].

Thereafter, in § 3.4, a series of samples, deposited with a varying silane concentration (SC) in the plasma gas phase, and resulting in samples ranging from microcrystalline material to amorphous material (crossing over the \square c-Si:H / a-Si:H transition), will be analysed more deeply. In this case, the electrical transport properties (with and without illumination) will be studied, as well as the microstructure of the samples. The link between both aspects (electrical transport and sample microstructure) will be discussed. The main results regarding this series have been published in [Droz 2003].

3.2. Techniques for electrical characterisation of intrinsic thin film silicon layers

In order to study the transport properties of intrinsic thin film silicon layers, three

techniques were used: dark conductivity measurement (as a function of the temperature T), steady state photoconductivity (SSPC) measurement and steady-state photocarrier grating (SSPG) measurement. These three characterisation techniques were initially developed for a-Si:H, and are here applied to \square c-Si:H as well [Goerlitzer 1998a]. All three of them allow to assess transport properties in coplanar configuration. To this end, two aluminium electrodes of 8 mm \square 3 mm size separated by a gap of 0.5 mm and with a thickness of about 100 nm were thermally evaporated on the intrinsic \square c-Si:H layers deposited on glass substrates. Thereafter, each layer with the electrodes was annealed at 180°C during 90 minutes. In fact, this was done while actually carrying out the dark conductivity measurement. The Ohmic nature of the contacts was tested by checking the linearity of the current vs. voltage curve obtained by applying a voltage varying between 0 and 100 V (at room temperature and after annealing). For the a-Si:H samples, the same procedure was applied, except that the typical electrode size were 2 mm \square 3 mm, in order to allow a fast and homogeneous degradation procedure [Hof 1998] on the whole a-Si:H surface between the electrodes.

As the \square c-Si:H layers are prone to post-oxidation once in the ambient air [Goerlitzer 1998b], the following steps were in most cases done as fast as possible (i.e. within 2-3 days after the deposition): electrode evaporation – annealing / dark conductivity measurement – SSPC and SSPG measurements.

3.2.1. Dark conductivity

The dark conductivity (\square_{dark}) is the conductivity measured without illumination. It is defined as the constant of proportionality between the current density (J) and the electrical field (E), and is expressed as:

$$J = \square_{dark} \cdot E . \quad (\text{equ. 3.1})$$

Microscopically, in the framework of the classical transport model [Overhof 1989], it can be expressed as:

$$\square_{dark} = q (\square_n^0 n_f + \square_p^0 p_f) , \quad (\text{equ. 3.2})$$

where q is the elementary charge, \square_n^0 and \square_p^0 are the band mobilities of the electron and holes, respectively, n_f is the free electron density and p_f is the free hole density.

The measurement of \square_{dark} as a function of the temperature (T) gives us access to the activation energy (E_{act}), as they are linked by the relation:

$$\square_{dark}(T) = \square_0 \cdot \exp(-E_{act} / kT) , \quad (\text{equ. 3.3})$$

where k is the Boltzmann constant and \square_0 the dark conductivity prefactor, expressed for

a-Si:H as [Overhof 1989]:

$$\square_0 = 2q\square_n^0 N(E_C)kT, \quad (\text{equ. 3.4})$$

with $N(E_C)$ the density of states at the mobility edge energy in the conduction band (E_C). \square_0 reflects thus the mobility \square_n^0 .

Experimentally, the sample covered with electrical contacts is placed on a heating plate in a dark vacuum chamber under a nitrogen atmosphere of 10 mbar, in order to allow an homogeneous heating of the sample while limiting the post-oxidation. The computer-controlled measurement of $\square_{dark}(T)$ consists in three steps: first, the sample is rapidly heated up to 180°C (i.e. 10-20°C less than the deposition temperature of the sample); then the temperature is kept constant for 90 minutes ("annealing" step); and finally a controlled decreasing temperature ramp is applied to the sample. During this last step, one measures the current (I) while applying a voltage (U) between the two metallic electrodes. \square_{dark} is then calculated as follows by taking into account the geometry:

$$\square_{dark} = \frac{g}{l \cdot d} \cdot \frac{I}{U}, \quad (\text{equ. 3.5})$$

where g is the gap between the electrodes, l is their length, and d is the sample thickness that was typically 2 \square m for the \square c-Si:H samples and 1 \square m for the a-Si:H samples. Note that the values for \square_{dark} given thereafter are those measured at room temperature ($T = 300\text{K}$).

3.2.2. Measurement techniques of the electronic transport under illumination

The steady-state photoconductivity (SSPC) and the steady-state photocarrier grating (SSPG) techniques are the two methods used to analyse coplanar electronic transport of silicon thin films under illumination. In this case, a steady-state situation is achieved between the generation (G) of free carriers resulting from the light absorption and their recombination (R) in the material:

$$G = R. \quad (\text{equ. 3.6})$$

The general recombination times for the electron and for the holes are, respectively, **defined** as:

$$\square_n^R = n_f / G, \quad (\text{equ. 3.7})$$

$$\tau_p^R = p_f / G, \quad (\text{equ. 3.8})$$

where n_f is the free electron density and p_f is the free hole density. These recombination times take into account all recombination processes via all available recombination centres (i.e. they are the average recombination times).

The SSPC and SSPG techniques were applied concurrently on each layer at room temperature and under the same variable generation rate, calculated as follows:

$$G = \square \frac{I_0(1 - R)}{h\nu} \frac{(1 - e^{-\square d})}{d}, \quad (\text{equ. 3.9})$$

where \square is the quantum efficiency, I_0 is the incident light intensity, R is the reflection coefficient, \square is the absorption coefficient and $h\nu$ is the energy of the incident photons. In our evaluations, we used $\square = 1$ for all the samples. For the a-Si:H samples, R and \square were measured for each layer, whereas fixed values were used for the \square c-Si:H samples ($R = 0.33$ and $\square = 1 \cdot 10^4 \text{ cm}^{-1}$). A krypton laser emitting at a wavelength of $\lambda = 647 \text{ nm}$ was used as illumination source. At this wavelength, the light is weakly absorbed within the sample and we can therefore assume a homogeneous generation of free carriers throughout the whole thickness of the layer. The values for the generation rate used for measuring \square c-Si:H samples was $G \square 2 \cdot 10^{20} \text{ cm}^{-3} \text{ s}^{-1}$, whereas for a-Si:H it was $G \square 2 \cdot 10^{19} \text{ cm}^{-3} \text{ s}^{-1}$ for the samples in the annealed state (in order to reduce the light-induced degradation of a-Si:H during the measurement) and $G \square 1 \cdot 10^{20} \text{ cm}^{-3} \text{ s}^{-1}$ for the samples in the degraded state. For the measurements of the non-linear dependencies of the transport parameters on the generation rate (see § 3.3.2), higher and lower values of G were also applied.

3.2.2.1. Photoconductivity

The steady-state photoconductivity (SSPC) method is the measurement of the conductivity of a sample under constant illumination, and consists in measuring the current while illuminating uniformly the area between the two metallic electrodes on which a voltage is applied. Introducing the relations for the recombination times under steady-state illumination (equ. 3.7) and (equ. 3.8) into the general equation for the conductivity (equ. 3.2) gives us the photoconductivity:

$$\square_{photo} = qG \left(\square_n^0 \square_n^R + \square_p^0 \square_p^R \right). \quad (\text{equ. 3.10})$$

This relation is independent of any recombination model. Thus, we can use \square_{photo} to describe layer transport properties both for \square c-Si:H and for a-Si:H.

We see from (equ. 3.10) and that the photoconductivity gives us a direct access to the mobility-lifetime ($\mu^0 \tau^R$) product of the majority carriers ($\mu^0 \tau^R_{Maj}$). Even in the case of non-intentionally doped a-Si:H or \square c-Si:H layers, the material is slightly n-type. Therefore, in this case, σ_{photo} is linked to the mobility-lifetime product of the electron.

We will see in § 3.3.2 that a power law dependency of the photoconductivity with the generation rate is observed for \square c-Si:H, as for a-Si:H [Rose 1963]:

$$\sigma_{photo} \propto G^\alpha, \quad (\text{equ. 3.11})$$

where α is the power law exponent of the photoconductivity.

3.2.2.2. Ambipolar diffusion length (SSPG technique)

The steady-state photocarrier grating (SSPG) technique is a method used for measuring the ambipolar diffusion length (L_{amb}) in intrinsic semiconductors [Ritter 1987, Ritter 1986, Smith 1978], and its application to amorphous silicon has been extensively studied [Balberg 1992, Sauvain 1992]. Contrarily to σ_{photo} , the ambipolar diffusion length is linked to the mobility-lifetime product of the minority carriers ($\mu^0 \tau^R_{min}$):

$$L_{amb}^2 = \frac{kT}{q} \frac{\mu_n^0 \tau_n^R \cdot \mu_p^0 \tau_p^R}{\mu_n^0 \tau_n^R + \mu_p^0 \tau_p^R} C, \quad (\text{equ. 3.12})$$

where C is a correction factor between 1 and 2 [Sauvain 1992]. Here again, no specific recombination model has been introduced, so that we can use these quantities to describe layer transport properties both for \square c-Si:H and for a-Si:H. Note that C can be expressed as $C = 1 + \alpha + \beta$ if power laws are observed for L_{amb}^2 ($L_{amb}^2 \propto G^\alpha$) and σ_{photo} ($\sigma_{photo} \propto G^\beta$) as a function of the generation rate (see §3.3.2).

The application of the SSPG technique to \square c-Si:H has been intensively studied by Goerlitzer et al. [Goerlitzer 1998a, Goerlitzer 1996]. Therefore we will here only recall the main points. The SSPG technique consists in measuring the small-signal photocurrent in a sample exposed to optical fringes, and to compare this photocurrent to that obtained under uniform illumination (without fringes). The optical fringes or "grating", created by the interference of two laser beams, generate a spatially non-uniform carrier density in the sample. The conductivity of the sample perpendicular to this optical grating depends on the ratio between the grating spacing λ and the ambipolar diffusion length L_{amb} . More precisely, providing that some conditions are fulfilled, and that a power law is observed for $\sigma_{photo}(G)$, the ratio λ of the currents measured with and without grating is directly related to λ and L_{amb} .

Whereas the application of the SSPC method to μ c-Si:H layers does not cause any specific problems, the validity of the SSPG method is more critical. First, the relatively low $\sigma_{photo} / \sigma_{dark}$ ratio obtained for μ c-Si:H as compared to a-Si:H implies the use of higher generation rates and renders the evaluation of SSPG more difficult in the case of μ c-Si:H. Moreover, in the SSPG technique, the so-called ‘‘Balberg plot’’ ($1/\mu^2$ as a function of $\sqrt{2/(1-\mu)}$) [Balberg 1992] must be a linear function to evaluate L_{amb} from the intersection of this line with the y -axis. However, the Balberg plot of μ c-Si:H samples is usually not linear, but curved. This non-linearity is probably due to the fact that in μ c-Si:H the ambipolar condition is not assured for all considered values of the grating period. However, it has been demonstrated in [Goerlitzer 1998a, Goerlitzer 1996] that L_{amb} can still be correctly determined from that region of the data which can be fitted with a linear function (i.e. for large μ -values, see Fig. 3.1).

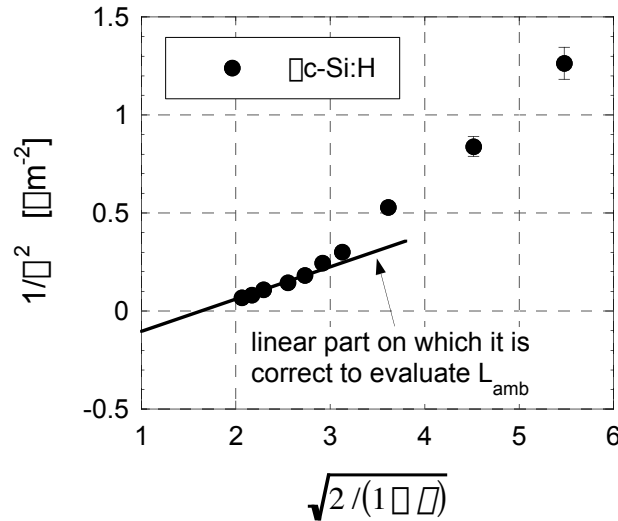


Fig. 3.1: Typical ‘‘Balberg plot’’ obtained when measuring μ c-Si:H samples (here a sample deposited with $SC = 6\%$) by the SSPG method. Note the deviation from a linear function. The ambipolar diffusion length L_{amb} can nevertheless be evaluated by fitting the linear part observed at large μ -values.

For more details about the application of the SSPG method to μ c-Si:H please refer to [Goerlitzer 1998a, Goerlitzer 1996], where the conditions for the validity of the procedure for determining L_{amb} from SSPG measurements in μ c-Si:H layers are extensively discussed. The result found there is that these conditions hold in μ c-Si:H layers, providing that certain additional precautions are taken.

3.2.2.3. The parameter b (indicator of the Fermi level position)

As described above, the photoconductivity measurement leads to the $\sigma^p \mu^R$ product of the

majority carriers (generally the electrons, for as-grown material), i.e. to $\square_n^0 \square_n^R$, whereas the SSPG technique leads to the $\square^0 \square^R$ product of the minority carriers (generally the holes for as-grown material), i.e. to $\square_p^0 \square_p^R$. However, because of the unintentional incorporation of oxygen in \square c-Si:H layers (both during and after deposition (post-oxidation)), which depends on the deposition conditions, the position of the Fermi level is consequently changed and the interpretation of the transport properties can become a problem [Goerlitzer 1998b], because the values of $\square_n^0 \square_n^R$ and $\square_p^0 \square_p^R$ are directly affected by the position of the Fermi level. To overcome this problem, we will introduce the parameter b which is defined here as it was originally done for a-Si:H [Sauvain 1992, Shah 1997], in the following manner:

$$b = \square_n^0 n_f / \square_p^0 p_f . \quad (\text{equ. 3.13})$$

The parameter b is experimentally deduced from \square_{photo} (equ. 3.10) and L_{amb} (equ. 3.12) by setting:

$$\frac{b}{(b+1)^2} = \frac{L_{amb}^2 q^2 G}{kT \square_{photo} C} \quad (\text{equ. 3.14})$$

Even if it is determined under non-equilibrium conditions, the parameter b reflects the position of the Fermi level E_f [Shah 1997], because the n- or p-type character of the material is not changed by illumination. For a-Si:H, a value of b of the order of one ($b \approx 1$) corresponds to the position of E_f at midgap (i.e. to "truly" intrinsic material). It is then possible to compare electronic transport in a-Si:H and in \square c-Si:H, at a chosen value of b , or to compare \square c-Si:H layers between them, since b takes into account the shift in E_f due to the post-oxidation. A same value of b corresponds to a same free carrier ratio ($b \propto n_f / p_f$), if one assumes thereby that the band mobility ratio for both types of carriers ($\square_n^0 / \square_p^0$) in \square c-Si:H is similar to that observed in a-Si:H. A comparison of the $\square^0 \square^R$ products for the majority and for the minority carriers as a function of b allows one, thus, to compare \square c-Si:H and a-Si:H samples even though the bandgap values are certainly different and the recombination processes may be also. Note that \square_{photo} (equ. 3.10), L_{amb} (equ. 3.12) and b (equ. 3.14) are evaluated without supposing a priori any specific recombination model and can thus be applied to \square c-Si:H without any restrictions.

3.2.2.4. The $\square^0 \square^R$ product (material transport "quality factor")

Assuming that the recombination mechanism is similar in \square c-Si:H and in a-Si:H, we can go one step further and apply to \square c-Si:H the quality parameter $\square^0 \square^R$ [Beck 1996b], introduced from the recombination model of a-Si:H, and used there to link the material quality with solar cell performance. The quality parameter $\square^0 \square^R$, which is experimentally deduced from both

$\square^0 \square^R_{Maj}$ and $\square^0 \square^R_{min}$ products, corresponds to the value which the measured $\square^0 \square^R$ product would take if all dangling bonds in the material were neutral; $\square^0 \square^0$ is independent of the Fermi level of the considered sample.

The $\square^0 \square^R$ products of the majority and minority carriers (as deduced from SSPC and SSPG) cannot be directly considered as a measure of the material quality, since they depend on the dangling bond occupation, and, thus, on the experimental conditions. Furthermore, they specifically depend on the position of the Fermi level within the individual layer that is being measured. On the other hand, the $\square^0 \square^0$ product [Beck 1994, Beck 1996b] is a parameter which combines both $\square^0 \square^R_{Maj}$ and $\square^0 \square^R_{min}$ and is in fact basically independent of dangling bond occupation. Therefore, it can be used as a material quality parameter and it has been shown to correlate with solar cell behaviour [Beck 1994, Beck 1996b, Hof 1995]. $\square^0 \square^0$, where \square^0 is the band mobility and \square^0 is the capture time, corresponds to the “nominal” value that the measured $\square \square$ -product (i.e. $\square^0 \square^R$) would take if all defects in the material were neutral. However, $\square^0 \square^0$ cannot be directly measured as both neutral and charged defects always co-exist in actual a-Si:H layers; however, $\square^0 \square^R$ can be deduced by combining SSPC and SSPG from the simultaneous measurement of \square_{photo} and L_{amb} on the same layer with the same contacts, and with the same value of bias light.

Undoped (or, rather, not intentionally doped) a-Si:H or \square c-Si:H is, in general (mainly because of the incorporation of a certain quantity of oxygen), slightly n-type, so that usually the majority carriers are the electrons and the minority carriers are the holes. The recombination traffics of electrons and holes are related via the density and charge state of their common recombination centres (i.e. of the dangling bonds). This can be expressed analytically and the $\square^0 \square^0$ product is then deduced [Beck 1996b] and given by

$$\square^0 \square^0 = \frac{\square_{photo}}{qG} \frac{1}{z}, \quad (\text{equ. 3.15})$$

where

$$z = \frac{\square_n^0}{\square_n^+} \frac{1}{b} + 1 + \frac{\square_p^0}{\square_p^+} b \frac{\square_n^+}{\square_p^+}. \quad (\text{equ. 3.16})$$

In (equ. 3.15), the $\square^0 \square^0$ product is adjusted via the parameter b (equ. 3.14), which is implicitly contained in the term $1/z$. The ratio of charged to neutral capture cross sections \square^\pm/\square^0 that appears in (equ. 3.16) is thereby estimated to be about 50 [Beck 1996b].

3.3. Electrical transport in \square c-Si:H : comparison with a-Si:H

3.3.1. Introduction

The goal of this section is to compare the electronic transport properties of intrinsic \square c-Si:H layers with those of intrinsic a-Si:H layers. To this end, coplanar electronic transport under illumination is analysed in \square c-Si:H layers with the same characterisation tools as those used for a-Si:H: the SSPC and SSPG techniques, as described above, from which the $\square^0 \square^R$ products of the majority and minority carriers, respectively, are deduced. In this approach, we do not purposely specify any recombination model. Thus, we can use the photoconductivity (\square_{photo}), the ambipolar diffusion length (L_{amb}), and the parameter b to describe layer transport properties for both \square c-Si:H and a-Si:H. Indeed, unlike a-Si:H, where transport models have been successfully developed (see e.g. [Hubin 1995]), no simple generally accepted transport model is so far available for \square c-Si:H. Here, instead of using the \square_{photo} and L_{amb} , we will preferably use $\square^0 \square^R_{Maj}$ and $\square^0 \square^R_{min}$ (which are directly linked to the previous values, cf. (equ. 3.10) and (equ. 3.12)), in order to compare a-Si:H and \square c-Si:H samples. Our approach here is first to study the dependence of \square_{photo} , L_{amb} , and b on the generation rate for as-grown slightly n-type \square c-Si:H as well as for slightly p-type doped \square c-Si:H samples. Then, we will compare the $\square^0 \square^R$ -products measured on a large variety of \square c-Si:H samples with those measured on many a-Si:H samples. These studies have been published in [Droz 2000].

All the samples studied in this section were deposited on AF45 (Schott) glass by the VHF PE-CVD technique [Curtins 1987] at frequencies between 70 and 130 MHz. Various concentrations of silane in hydrogen as well as various values of VHF-power were used. The \square c-Si:H samples, whose typical thickness is $2 \pm 0.5 \mu\text{m}$, were produced at an effective deposition temperature of 220°C and a gas purifier was used [Torres 1996] to obtain nearly intrinsic \square c-Si:H layers. The a-Si:H samples used for the comparison were deposited at moderately high temperatures and at various other deposition conditions (including the hydrogen dilution technique) [Ziegler 2001]. They all have a typical thickness of $1 \pm 0.3 \mu\text{m}$. Their degraded state was obtained after applying the fast degradation technique using pulsed laser light [Hof 1998]. While as-grown undoped \square c-Si:H, similarly to a-Si:H, is a slightly n-type material, some samples were deposited with about 10 ppm of diborane to obtain slightly p-type \square c-Si:H layers. Note that transport properties do vary with the thickness of the layer (i.e. measured values of $\square \square$ -products are lower in thinner layers). This is observed for both a-Si:H [Hof 1999] and \square c-Si:H [Kuendig 2002] samples (see also Appendix).

3.3.2. Power law dependencies of L_{amb}^2 , σ_{photo} and b

The first similarity in transport between α -Si:H and a-Si:H is observed in the power law dependencies of the photoconductivity ($\sigma_{photo} \propto G^\beta$), the ambipolar diffusion length ($L_{amb}^2 \propto G^\beta$), and the parameter b ($b \propto G^\beta$) as a function of the generation rate G [Goerlitzer 1996].

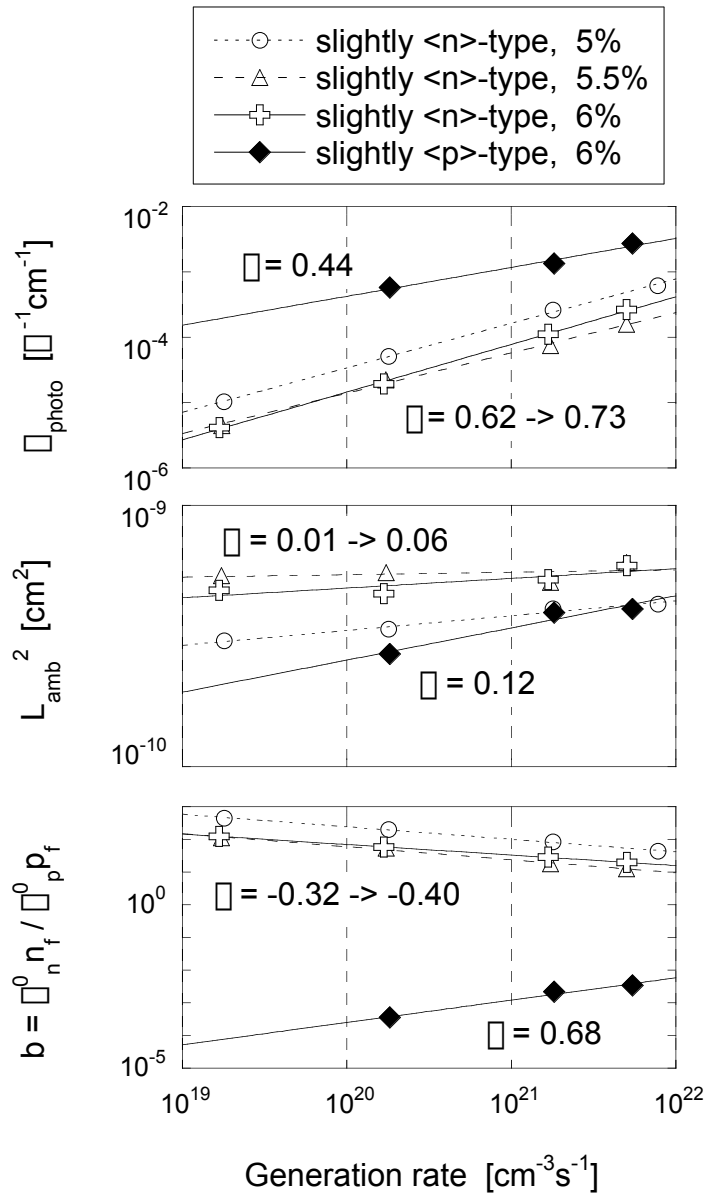


Fig. 3.2: Power law dependencies, and their fits, with the generation rate G of the photoconductivity ($\sigma_{photo} \propto G^\beta$), the ambipolar diffusion length ($L_{amb}^2 \propto G^\beta$), and the parameter b ($b \propto G^\beta$), for typical as-grown slightly n -type α -Si:H layers (open symbol) and a typical slightly p -type α -Si:H layer (filled symbols). The silane concentration used for the deposition of each layer is indicated; the p -type layer was obtained by adding 10 ppm of diborane.

An illustration of these power laws is shown in Fig. 3.2 for as-grown slightly n-type \square c-Si:H as well as for slightly p-type doped \square c-Si:H, for values of G between 10^{19} and 10^{22} $\text{cm}^{-3}\text{s}^{-1}$. These non-linearities (i.e. power laws) can be attributed to variation of the occupation of charged defects, and are therefore a mark of the prevailing type of recombination process. Here, similarly to a-Si:H, a recombination mechanism via recombination centres having three possible states of charge can explain these power-laws as seen for the dependencies of \square_{photo} , L_{amb}^2 and b on the generation rate [Hubin 1992, Hubin 1995].

The power law exponents \square and \square measured on \square c-Si:H layers are in the same range as those measured on a-Si:H [Goerlitzer 1996]. On the other hand, the exponent of b (\square) is usually negative for \square c-Si:H, whereas it is in most cases positive for a-Si:H. Note that the variation in the power exponent values as shown in Fig. 3.2 for the three slightly n-type samples may be attributed to (post-)oxidation of the material. The power law exponents are characteristic of the charge state of the defects intervening in the recombination process (in the case of c-Si, these exponents are generally equal to one). In the recombination model used for the interpretation of transport measurement in a-Si:H, similar power law exponent in \square c-Si:H would indicate that the recombination in \square c-Si:H is dominated by the same kind of defects as those in a-Si:H. Therefore, a-Si:H and \square c-Si:H may have the same type of recombination centres (localised amphoteric recombination centres). The question arising then for \square c-Si:H is where to locate these recombination centres. For that purpose, we have studied the microstructure of \square c-Si:H, and tried to understand the effect of the microstructure on the electronic transport. This point is discussed in section 3.4.

Another representation of these power law dependencies on G is given in Fig. 3.3, where $\square^0 \square^R_{Maj}$ and $\square^0 \square^R_{min}$, deduced from \square_{photo} and L_{amb} of Fig. 3.2, are plotted as a function of b . Here, the change in b is due to a change in G . Fig. 3.3, based on the same data as that of Fig. 3.2, reveals the strong dependency of \square_{photo} with G , and the typical weak dependency of L_{amb}^2 with G . Fig. 3.3 also demonstrates the symmetry of the power law dependencies for the majority and minority free carriers in slightly p- and n-type \square c-Si:H samples (such a symmetry is not directly visible from Fig. 3.2). Therefore, for variation of b representing both slightly n-type and slightly p-type \square c-Si:H samples, the transport properties of \square c-Si:H behave similarly to those of a-Si:H. This observation strengthens the validity of the transport model developed for a-Si:H for \square c-Si:H.

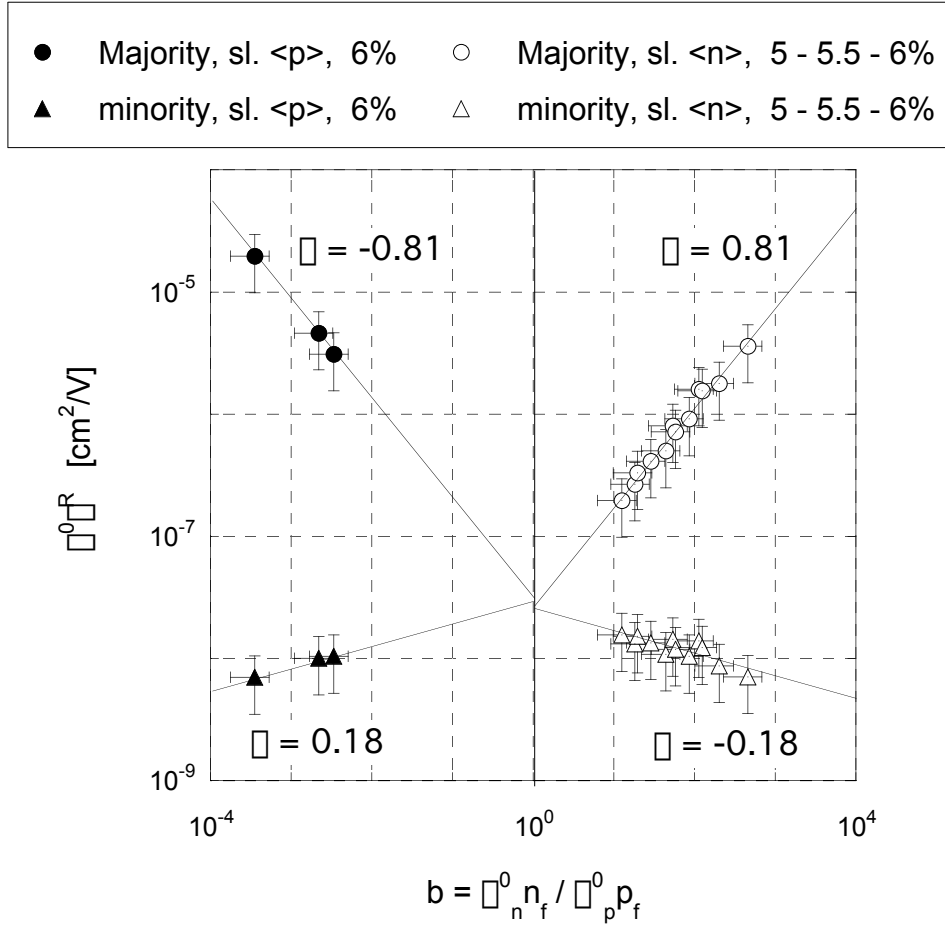


Fig. 3.3: $\sigma^0 \sigma^R$ products of the majority carriers (as deduced from \square_{photo}) (circles) and of the minority carriers (as deduced from L_{amb}) (triangle) as a function of the parameter b , representing the Fermi level position. Data points (obtained by changing the generation rate) were taken from Fig. 3.2, and correspond to non-intentionally n -doped \square c-Si:H samples deposited under various SC and one slightly p -doped \square c-Si:H sample deposited at SC = 6%. The lines are power law fits: $\sigma^0 \sigma^R \propto (n_f / p_f)^{\square}$. This representation is symmetric for slightly n -type ($b > 1$) (open symbols) and slightly p -type ($b < 1$) (filled symbols) \square c-Si:H layers, i.e. $\square^{n\text{-type}} = -\square^{p\text{-type}}$, for both majority and minority carriers.

3.3.3. Anticorrelated behaviour of the $\sigma^0 \sigma^R$ products

It has been observed [Beck 1994, Sauvain 1992] that, in the case of a series of slightly doped a-Si:H layers, the $\sigma^0 \sigma^R$ products of the majority and minority carriers, when plotted as a function of b , display an anticorrelated behaviour (i.e. for a variation of the Fermi level (monitored by the parameter b) $\sigma^0 \sigma^R_{\text{Maj}} \square \sigma^0 \sigma^R_{\text{min}}$ is almost constant) for both slightly n -type ($b > 1$) and slightly p -type ($b < 1$) a-Si:H materials. To compare \square c-Si:H with a-Si:H, we have represented in Fig. 3.4 the $\sigma^0 \sigma^R_{\text{Maj}}$ and $\sigma^0 \sigma^R_{\text{min}}$ products, as a function of b , for \square c-Si:H samples measured with a constant G (filled symbols). In other words, Fig. 3.4 is the plot of $\sigma^0 n_f$ and $\sigma^0 p_f$ vs. b . The change in b is here mainly due to unintentional incorporation of

oxygen (during deposition or by postoxidation), which acts as a n-type dopant in μ c-Si:H.

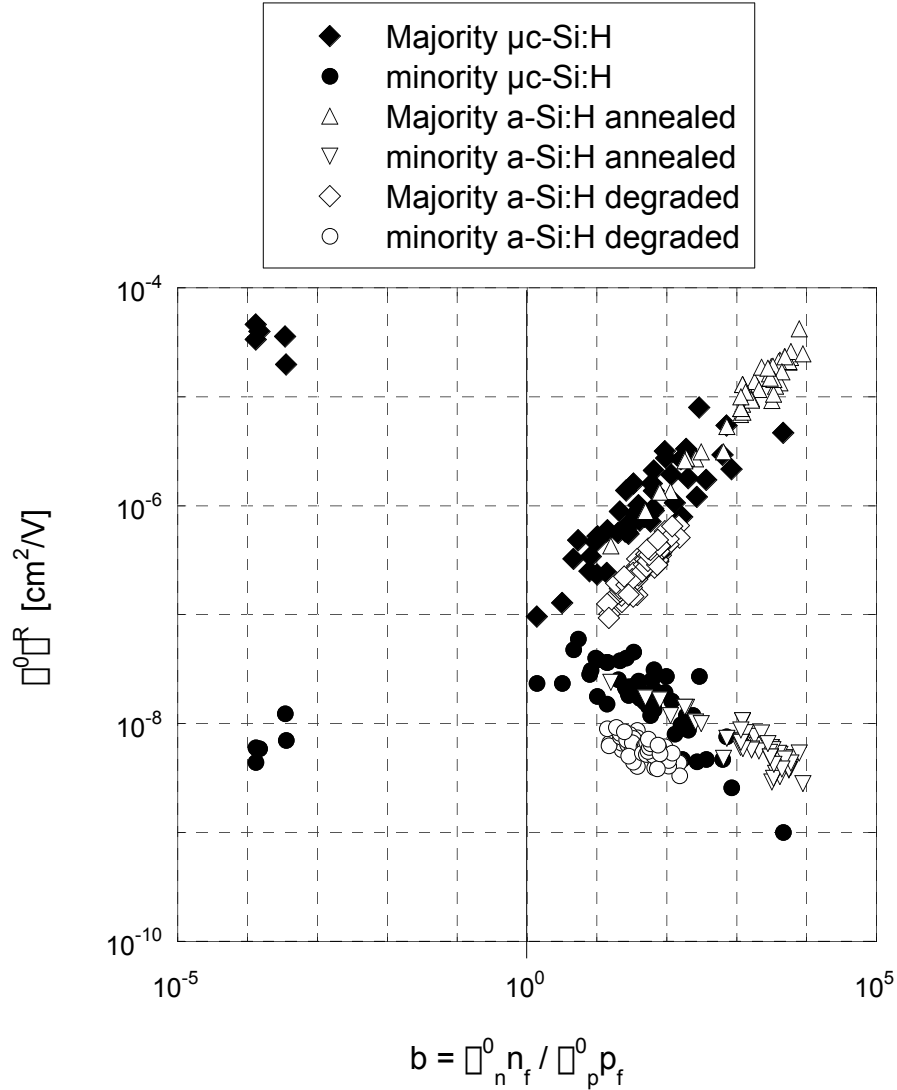


Fig. 3.4: Majority and minority $n_f^0 p_f^0$ products measured on various μ c-Si:H layers with a constant generation rate ($G \approx 2 \cdot 10^{20} \text{ cm}^{-3} \text{ s}^{-1}$), as a function of the parameter b . In order to compare quantitatively electronic transport in μ c-Si:H and in a-Si:H, majority and minority $n_f^0 p_f^0$ products measured on annealed (at $G \approx 3 \cdot 10^{19} \text{ cm}^{-3} \text{ s}^{-1}$) and degraded (at $G \approx 2 \cdot 10^{20} \text{ cm}^{-3} \text{ s}^{-1}$) a-Si:H samples [Ziegler 2001] are also represented.

Note that Fig. 3.4 only shows data for μ c-Si:H samples for which the variation in the defect densities is less than a factor 10 (as deduced from sub-bandgap absorption measurements by the constant photocurrent method, see § 3.4.3.5). In the case of μ c-Si:H, as shown in Fig. 3.4, the behaviour of majority and minority carriers $n_f^0 p_f^0$ products is surprisingly, as in a-Si:H, anticorrelated (i.e. $n_f^0 p_f^0 \approx \text{constant}$). In Fig. 3.4 are also represented the $n_f^0 p_f^0_{Maj}$ and $n_f^0 p_f^0_{min}$ products measured on various a-Si:H layers [Ziegler 2001] in the annealed (open triangles) and degraded states (open diamonds and circles). We remark

that the $\mu^0 \tau^0$ products of \square c-Si:H samples are slightly higher than those of degraded a-Si:H samples, and are approximately equal to those of annealed a-Si:H layers.

As shown in Fig. 3.4, the values of $\mu^0 \tau^0$ products of the majority and minority carriers vary substantially with the Fermi level, represented here through the parameter b . When comparing electronic transport of various samples (\square c-Si:H between them or \square c-Si:H with a-Si:H), it is then crucial to know the position of the Fermi level. In this context, the use of the parameter b is therefore essential for a correct interpretation of transport measurements.

The $\mu^0 \tau^0$ products of majority and minority carriers measured on \square c-Si:H samples show the same behaviours - power laws (Fig. 3.2 and Fig. 3.3) and anticorrelation (Fig. 3.4) - as those observed on a-Si:H samples, and their values are within the same order of magnitude. (One has yet to keep in mind that, within an order of magnitude, the relationship $\mu \tau^{\text{a-Si}}_{\text{annealed}} \approx \mu \tau^{\text{c-Si}} > \mu \tau^{\text{a-Si}}_{\text{degraded}}$ may not strictly hold if the thickness of the samples under comparison is different). **We can thus conclude that the coplanar electronic transport under illumination in \square c-Si:H material is similar to that in a-Si:H material.** The similitude in the values of the mobility μ lifetime products for \square c-Si:H and a-Si:H ($\mu \tau^{\text{a-Si}} \approx \mu \tau^{\text{c-Si}}$) is quite surprising, as transport properties in crystalline silicon are much better than in a-Si:H (i.e. $\mu \tau^{\text{c-Si}} > \mu \tau^{\text{a-Si}}$). **These observations suggest that the electronic transport in \square c-Si:H layers is governed by the amorphous (or defective) phase present at the grain boundaries (nanocrystal boundaries or conglomerate boundaries) of \square c-Si:H.** This hypothesis will be confirmed in section 3.4. Furthermore, this hypothesis motivated us to apply the transport model developed for a-Si:H [Hubin 1995] to \square c-Si:H. In this model, the dangling bonds with their amphoteric character (i.e. three charge states) act as recombination centers, whereas the band tails act as traps. The recombination traffics of electrons and holes are related via their common recombination centers (i.e. the dangling bonds). As a consequence, the free carrier densities cannot vary independently. Indeed, basic conservation laws (generation equals recombination rate, charge neutrality) imply a relationship between the free carriers densities. Experimentally, this relationship translates into the anticorrelation of $\mu^0 \tau^0$ products of the majority and minority carriers ($\mu_n^0 n_f \mu_p^0 p_f \approx \text{constant}$), exactly as observed here for \square c-Si:H layers (see Fig. 3.4).

Assuming that the recombination mechanism is similar in \square c-Si:H and in a-Si:H, we can go one step further and apply to \square c-Si:H the quality parameter $\mu^0 \tau^0$ (see § 3.2.2.4), introduced from the recombination model of a-Si:H [Beck 1996b], and used there to link the material quality with solar cell performance (see Fig. 3.5, open symbols). In a-Si:H, such a correlation between $\mu^0 \tau^0$ and cell efficiency can be observed provided that the latter is limited by the intrinsic layer. The $\mu^0 \tau^0$ products have been evaluated on \square c-Si:H intrinsic layers pertaining to a silane concentration series and to a series obtained by changing the VHF-power. Fig. 3.5

(filled symbols) shows that, even in the case of $\mu\text{c-Si:H}$, the efficiency of n-i-p solar cells incorporating the aforementioned layers as i-layers relates roughly to the $\mu\tau$ -values of corresponding individual intrinsic layers. This successful attempt to correlate the quality of $\mu\text{c-Si:H}$ layers with solar cell efficiencies is a further indication that it is indeed legitimate to apply the transport model developed for a-Si:H to $\mu\text{c-Si:H}$.

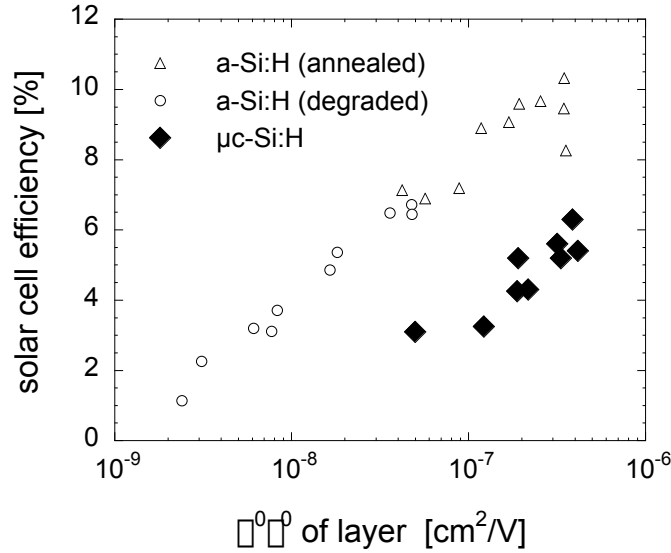


Fig. 3.5: Layer quality parameter $\mu\tau$ compared to the efficiencies of solar cells incorporating such layers as intrinsic layers. The a-Si:H data, taken from [Beck 1996b], correspond to two temperature series of i-layers (thickness: $d \approx 2.5 \mu\text{m}$) and corresponding p-i-n cells ($d^{\text{i-layer}} \approx 0.6 \mu\text{m}$). The $\mu\text{c-Si:H}$ data correspond to one silane concentration series and one VHF-power series of i-layers ($d \approx 2.0 \pm 0.5$) and corresponding n-i-p solar cells ($d^{\text{i-layer}} \approx 2.2 \pm 0.2 \mu\text{m}$ and $3.5 \pm 0.4 \mu\text{m}$, respectively). Note that the vertical shift (in efficiency) between the a-Si:H data and the $\mu\text{c-Si:H}$ data could be explained by a more efficient light-trapping in our present a-Si:H solar cells.

3.3.4. Conclusions

In the present section, we have studied the electronic transport properties in coplanar configuration and under illumination on $\mu\text{c-Si:H}$ layers grown by the VHF PE-CVD technique under various deposition conditions. Steady-state photoconductivity (SSPC) and steady-state photocarrier grating (SSPG) techniques have been used to evaluate the variations of the mobility and recombination time ($\mu\tau$) products of the majority and minority carriers as a function of b (representing the Fermi level) for different generation rates and doping levels. Similarly to a-Si:H, power law dependencies as a function of the generation rate are observed for the photoconductivity, for the ambipolar diffusion length and for the parameter b . For $\mu\text{c-Si:H}$, similarly to what is observed for a-Si:H, a nearly constant product of (mobility \times recombination time) of majority and minority carriers (i.e. $\mu_n n_f \times \mu_p p_f \approx \text{constant}$) is observed as a function of the parameter b . Based on these similarities, one can presume that

the electronic transport model developed for a-Si:H remains valid for \square c-Si:H. Moreover, the quality parameter $\frac{\rho}{\mu}$ (based on the recombination model for a-Si:H) seems to correlate roughly, also in \square c-Si:H, with the solar cell performances. Although a possible anisotropy of the transport properties in \square c-Si:H could prevent a relation between the transport properties (based on coplanar measurements) and solar cell performance, a rough estimation for the latter from layer quality remains possible [Wyrsh 2000] as long as one mainly wants to distinguish "good" (i.e. device-grade quality) intrinsic material from "bad" intrinsic material.

The use of the parameter b allows one to directly compare transport properties in \square c-Si:H and in a-Si:H. In this way, we can conclude that electronic transport in \square c-Si:H is slightly better (i.e. $\frac{\rho}{\mu}$ products are slightly higher) than in degraded a-Si:H, and quite similar to that in annealed a-Si:H.

However, despite the remarkable similarities in the transport properties between \square c-Si:H and a-Si:H in layers, some significant differences still remain between these two materials. Microcrystalline silicon (at least material deposited under conditions leading to highly microcrystalline material) is stable against light-soaking [Goerlitzer 1998a], whereas transport properties of amorphous silicon strongly degrade during exposition to light. As far as devices are concerned, in p-i-n solar cells, the collection is exclusively controlled by drift in the case of a-Si:H cells (in short-circuit conditions), whereas a collection by drift *and* diffusion has been claimed to have been observed for \square c-Si:H cells [Wyrsh 1998].

In this section, we have seen that, on the whole, transport in \square c-Si:H layers is similar to that in a-Si:H. However, \square c-Si:H is still different from a-Si:H, at least from a microstructural point of view. Therefore, in the next section, the transport in \square c-Si:H will be studied and compared to the microstructure, in order to understand which microstructural features limit electrical transport in \square c-Si:H.

3.4. Electrical transport versus microstructure in a silane concentration (SC) series of silicon layers

3.4.1. Introduction

In this section, the electronic transport properties as well as the microstructure of one series of intrinsic (undoped) silicon layers will be extensively studied. Some optical properties will be also addressed. Each sample of this series was deposited on a glass substrate, with identical deposition parameters, except for the silane concentration $SC = \text{SiH}_4/(\text{SiH}_4+\text{H}_2)$ in the plasma gas phase that was varied from 5% to 8%, by steps of 0.5%. The thickness and the deposition rate of these samples are given in Table 3.1. We will show that a SC of 5% results

in typical microcrystalline material, whereas a SC of 8% results in completely amorphous material. Thus, this SC series goes through the \square c-Si:H / a-Si:H transition and is therefore well adapted to study electrical transport properties vs. (varying) microstructure.

First, the coplanar electronic transport properties will be analysed by dark conductivity measurement as well as by SSPC and SSPG techniques (measurements under illumination). Then, the microstructure and the optical properties will be analysed by means of Transmission Electron Microscopy (TEM) observations of layer cross-sections, X-Ray Diffraction (XRD), Atomic Force Microscopy (AFM) scans of the surface topography, bifacial depth-dependent micro-Raman spectroscopy, Infra-Red (IR) spectroscopy (to evaluate the hydrogen content), and Constant Photocurrent Method (CPM). Finally, the transport properties will be discussed with respect to the microstructural features. The main results of this study have been published in [Droz 2003].

SC [%]	5	5.5	6	6.5	7	7.5	8
Thickness (± 0.2) [μm]	2.2	2.4	2.4	2.3	2.3	2.0	2.0
Deposition rate [$\text{\AA}/\text{s}$]	6.3	6.4	7.8	8.5	9.6	10.1	11.1

Table 3.1: Thickness and deposition rate of the silane concentration (SC) series of silicon thin films deposited on glass substrate studied throughout section 3.4 [Feitknecht 2003].

3.4.2. Electronic transport

3.4.2.1. Transport without illumination (dark conductivity)

Dark conductivity is the simplest way to characterise the transport properties of a-Si:H and \square c-Si:H layers (see § 3.2.1). Fig. 3.6 shows the evolution of the dark conductivity (\square_{dark}), the prefactor (\square_0) of conductivity and the activation energy (E_{act}) for the SC series of layers.

\square_{dark} slowly decreases with increasing SC from 10^{-5} (SC = 5%) to $10^{-8} \square^{-1}\text{cm}^{-1}$ (SC = 7.5%) and then drops to $8 \cdot 10^{-12} \square^{-1}\text{cm}^{-1}$ at SC = 8%. This last value is typical for a-Si:H layer conductivity. The prefactor \square_0 , that is linked to the mobility (equ. 3.4), is constant for SC-values between 5% and 7%, and then increases. E_{act} increases more and more as SC increases. A variation in the value of \square_{dark} (and E_{act}) can be due to several causes. The band gap (E_g) of the material has of course a direct influence. Indeed, a higher value of E_g , as in the case of a-Si:H ($E_g^{a-Si} \approx 1.75$ eV) compared to \square c-Si:H ($E_g^{\square c} \approx 1.1$ eV), will lead to a lower value of \square_{dark} and a higher value of E_{act} (in the case of intrinsic material with Fermi level (E_f) at midgap). For samples having a same E_g , the "more intrinsic" the material is, the lower \square_{dark} will be, whereas E_{act} should be maximised at the half value of E_g . Thus, the involuntary incorporation of oxygen, that is a n-type dopant in \square c-Si:H and therefore pushes E_f towards

the conduction band, will increase \square_{dark} while decreasing E_{act} . However, such an effect can be hidden by the presence of a lot of defects at midgap that will pin E_f at midgap. Note that the incorporation of oxygen in \square c-Si:H occurs both during deposition (although a gas purificator is used) and after deposition (post-oxidation). The strongly columnar microstructure of highly \square c-Si:H material can be supposed to enhance both types of oxygen incorporation.

This first analysis of the SC series (see Fig. 3.6) reveals that the samples deposited at SC between 5% and 7% are probably microcrystalline, while the one at SC = 7.5% already shows some amorphous features (see E_{act} and \square_0) and the one at SC = 8% is certainly amorphous (see \square_{dark}).

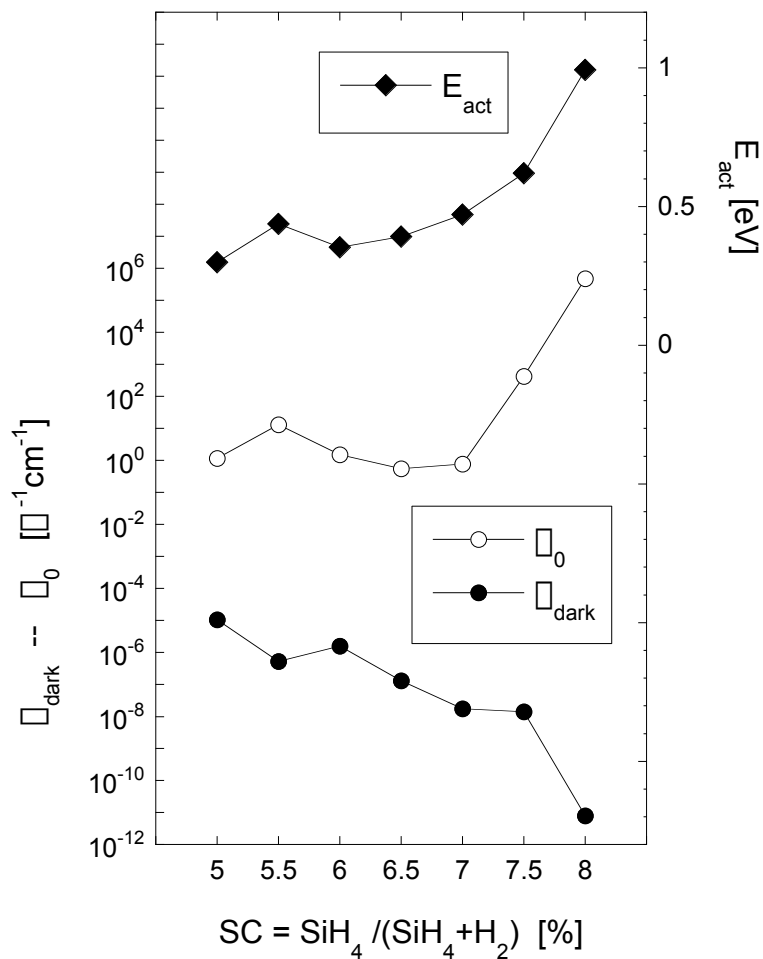


Fig. 3.6: Transport measurements without illumination: dark conductivity (\square_{dark}), conductivity prefactor (\square_0) and activation energy (E_{act}) of the silane concentration series of layers deposited on glass. The measurements were performed directly after deposition, in order to minimise post-oxidation.

3.4.2.2. Transport under illumination (SSPC and SSPG)

Transport measurements under illumination have been studied by steady-state

photoconductivity (SSPC) and steady-state photocarrier grating (SSSPG) methods (see § 3.2.2). They give access to the photoconductivity (\square_{photo}) and to the ambipolar diffusion length (L_{amb}), respectively. Then, the parameter b (indicative of the Fermi level position) and the normalised mobility-lifetime product $\square^0 \square^0$ (indicative of the material quality regarding electrical transport) are deduced from \square_{photo} and L_{amb} (see § 3.2.2). The measurements were performed under various generation rates (G). For the most microcrystalline samples (SC = 5-6%), G up to $10^{22} \text{ cm}^{-3} \text{ s}^{-1}$ has been used for studying the power law dependencies of \square_{photo} , L_{amb} and b (see §3.3.2). The standard illumination used to characterise \square c-Si:H samples is 20 mW/cm^2 (that corresponds to $G \approx 2 \cdot 10^{20} \text{ cm}^{-3} \text{ s}^{-1}$). However, some samples of this series were presumed to be (at least partially) amorphous. In order to minimise the light-induced degradation (Staebler-Wronski effect) of these samples, a reduced illumination of only 2 mW/cm^2 (corresponding to $G \approx 2 \cdot 10^{19} \text{ cm}^{-3} \text{ s}^{-1}$) was used for the samples deposited at SC = 7 - 8%. This reduced intensity was also applied to the more microcrystalline samples, in order to be able to compare all the samples while measured at a same intensity.

Fig. 3.7 shows the evolution of \square_{photo} , L_{amb} , b and $\square^0 \square^0$ with SC for the series of layers. \square_{photo} (Fig. 3.7 (a)) slightly decreases with SC for the layers deposited at lowest SC, then, it increases again (at SC = 7.5%) to get back for SC = 8% to the same value as that obtained for SC = 5%. However, these variations are small compared to those of \square_{dark} (see Fig. 3.6). As a result, the photo-gain, that is the gain in conductivity due to the illumination (i.e. the $\square_{photo} / \square_{dark}$ ratio) increases with SC (see Fig. 3.8), first slowly, and then more rapidly from SC = 7%. The photo-gain is about unity for the layer deposited at SC = 5%, and ends up at a value of 10^6 for the layer deposited at SC = 8%. Note that the evolution of the photo-gain with SC is very similar to that of E_{act} with SC (see Fig. 3.6).

Fig. 3.7 (b) shows that L_{amb} increases with SC. Three regions are observed: $L_{amb} = 175 \text{ nm}$ for SC = 5%, $L_{amb} = 215 - 240 \text{ nm}$ for SC = 5.5 - 7%, and $L_{amb} \approx 310 \text{ nm}$ for SC = 7.5 and 8%. The diffusion length is therefore the smallest for the sample deposited under conditions leading to the most microcrystalline material, whereas it is about double for the amorphous samples, where the highest value is obtained.

The parameter b (Fig. 3.7 (c)) evolves with SC in a similar way as \square_{photo} . b reflects the position of the Fermi level, i.e. low values of b obtained for a specific sample mean that this material has its Fermi level near mid-gap ("true" intrinsic material), whereas high values of b correspond to a quite extrinsic material. Oxidation will of course affect the value of b .

As seen in Fig. 3.7 (d), the value for $\square^0 \square^0$ is almost constant at $4 - 5 \cdot 10^{-7} \text{ cm}^2/\text{V}$ for the microcrystalline samples deposited with SC between 5 and 7%, whereas the most amorphous samples (SC = 7.5 - 8%) have a $\square^0 \square^0$ value two times higher and thus reach $10^{-6} \text{ cm}^2/\text{V}$.

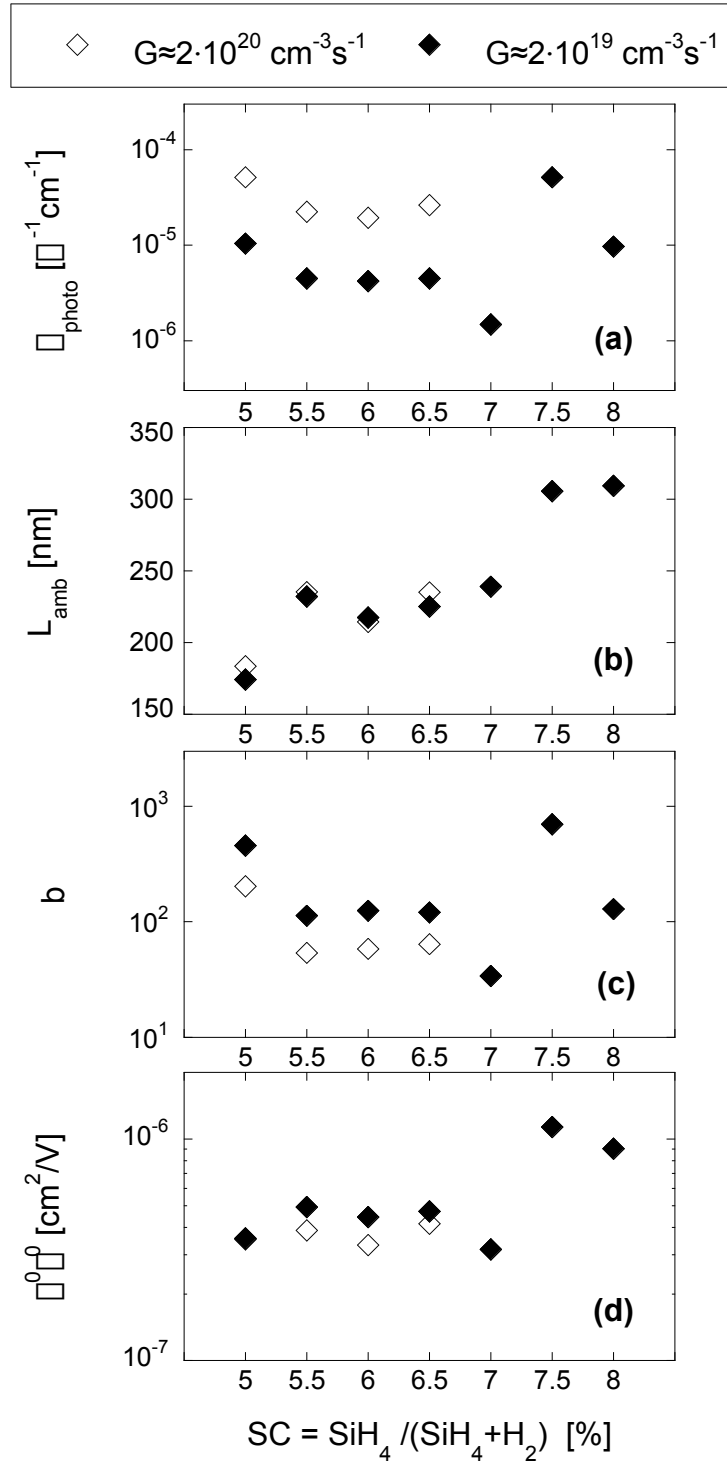


Fig. 3.7: Transport measurements under illumination: (a) photoconductivity (σ_{photo}), (b) ambipolar diffusion length (L_{amb}), (c) parameter b , and (d) normalised mobility-lifetime product ($\mu^0 \tau^0$) evaluated on the SC series of layers. The generation rates used were $G \approx 2 \cdot 10^{20} \text{ cm}^{-3} \text{ s}^{-1}$ for the samples deposited at SC = 5 - 6.5% (“strongly” α -Si:H material) and $G \approx 2 \cdot 10^{19} \text{ cm}^{-3} \text{ s}^{-1}$ for all the samples (to limit light-induced degradation in the α -Si:H samples). The measurements were performed a few days after deposition, in order to minimise post-oxidation.

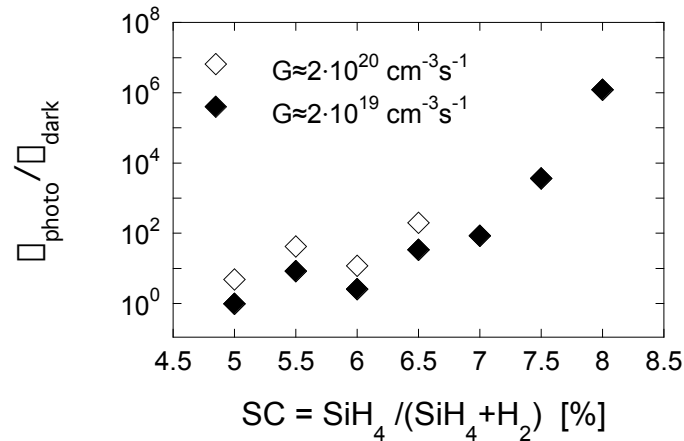


Fig. 3.8: Photo-gain ($\square_{\text{photo}} / \square_{\text{dark}}$ ratio) as a function of the SC for the series of layers.

On the whole, the behaviour with SC of the four parameters obtained from transport measurement under illumination is separated into two regions: one region for the samples deposited at SC between 5 and 7%, and the other for those deposited at SC = 7.5 and 8%. We can thus assume that the first region corresponds to transport characteristics typical of \square c-Si:H samples, whereas the second one is representative of transport of a-Si:H samples. Note that the parameters obtained from transport measurements without illumination (see Fig. 3.6) follow these trends as well, except that in some case (\square_{dark} and possibly E_{act}) the 7.5% sample behaves similarly to the \square c-Si:H samples. Thus, from the point of view of electrical transport (as determined by coplanar measurements on the top surface of the samples), the transition between microcrystalline and amorphous material is, in this series, between the sample deposited at SC = 7% and the one deposited at 7.5%.

(Note that during the deposition of the SC = 5.5% layer, contrary to the other layers, the cooling of the chamber has not been used. Consequently, outgasing of the chamber walls during deposition was probably enhanced, resulting possibly in more impurity incorporation. This fact could explain the slight deviation of the 5.5% sample from the general trends observed in Fig. 3.6, Fig. 3.7 and Fig. 3.8, and that will still be observed thereafter. Moreover, this particular sample had a marked tendency to peel off, a fact that prevented us from applying some measurement techniques in the following part of the work.)

3.4.3. Evolution of the microstructure and optical properties with SC

In the preceding section, we have studied the variation of the electrical properties of silicon films with a change in the ratio between hydrogen and silane present in the plasma gas phase during deposition, whilst the other deposition parameters remained fixed. Now, if the electrical properties evolve with a change in SC, it is certainly because the microstructure of

the material changes with SC. Indeed, the SC used for deposition will affect the growth of the material and the final microstructure. Then, a given microstructure will induce certain specific electrical properties. Therefore the effect of SC on electrical properties is indirect (via the microstructure), and we have to study the microstructural features of our samples in order to have a direct link between microstructure and electrical properties.

Several tools are available for the characterisation of the microstructure of Si films. In this work, we have used Transmission Electron Microscopy (TEM), X-Rays Diffraction (XRD), Atomic Force Microscopy (AFM), and Raman spectroscopy. Each of these methods has its own particularities, advantages or disadvantages regarding its application and regarding the information and results it gives. TEM observations, carried out on samples prepared as cross-sections, have the main advantage to give a direct imaging of the microstructure, so that amorphous or (micro-) crystalline materials can be spatially distinguished. On the other hand, the preparation of the sample is destructive and time consuming. XRD, in the way we used it in this work (i.e. \square - $2\square$ scans), gives information about the average crystallinity (over the whole thickness) of the sample. The preferential orientation as well as the average size of the smallest coherent domains, or nanocrystals (\square), can be evaluated from XRD spectra. AFM is used to analyse the surface topography of samples. The surface roughness as well as the conglomerate size (\square) can be deduced from AFM images. AFM can also be applied to entire solar cells. Raman spectroscopy has been already discussed in depth in Chapter 2. It gives information about the crystallinity of a more or less deep volume (from the top or bottom surface) of the sample, depending on the wavelength used. Its main advantage is to be a fast and non-destructive tool, which is not only applicable on simple layers, but also to entire (functioning) solar cells.

Note that the XRD, AFM and Raman measurements have been performed exactly on the same part of the sample where the electrical measurements were carried out, i.e. on the silicon part between the aluminium electrodes. Thus, problems related to possible lateral inhomogeneities are avoided.

3.4.3.1. Transmission Electron Microscopy (TEM)

Fig. 3.9 shows the TEM dark field micrograph of the \square c-Si:H intrinsic layer deposited with SC = 6% on glass substrate. At the bottom of the layer, amorphous silicon appears uniformly grey. As growth proceeds, the nucleation of the \square c-Si:H phase then occurs in the a-Si:H matrix. After the coalescence of the cones, the growth results in a columnar structure. The pencil-like conglomerates made out of nanocrystals constitute the microcrystalline silicon phase.

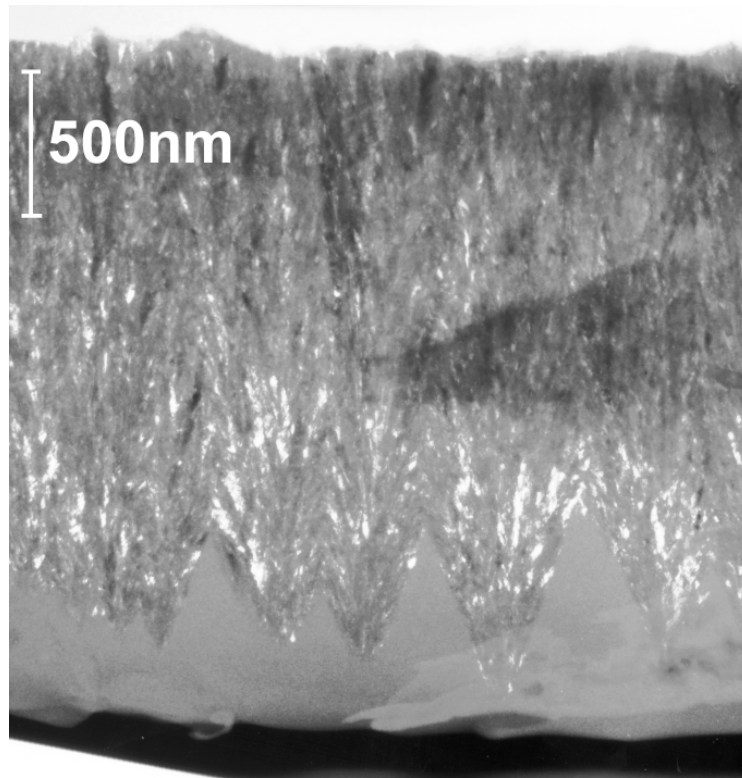


Fig. 3.9: TEM dark field micrograph of a \square c-Si:H layer deposited with SC = 6% on glass.

The TEM imaging has a limited resolution for distinguishing amorphous material inside the \square c-Si:H phase, so that it is not possible to evaluate the amorphous volume fraction inside the \square c-Si:H phase from TEM observations.

3.4.3.2. X-Ray Diffraction (XRD)

X-Rays Diffraction (XRD) is a measurement technique that gives information about the crystallinity of samples. The XRD measurements were performed on a Philips PW3020 diffractometer using the Bragg-Brentano geometry (\square -2 \square scans). In this measurement configuration, the penetration depth of the radiation source is much higher than the thickness of our samples of a few nanometre thick. As a result, the whole volume of the sample is probed, and the crystallinity information is thus averaged over the thickness. The CuK \square radiation source having a wavelength of 1.5418 Å was produced with an accelerating voltage of 30 kV and a current of 40 mA. XRD was performed on the SC series of layers. The spectra obtained are represented in Fig. 3.10 (as the SC = 5.5% sample peeled off, it could not be measured by XRD).

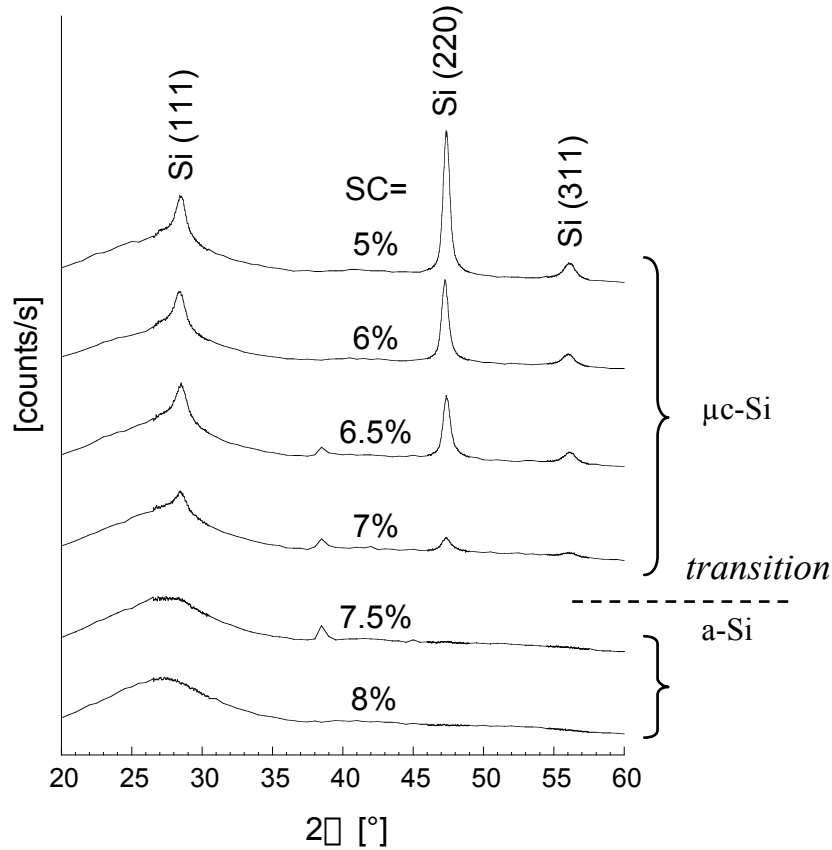


Fig. 3.10: X-ray diffraction spectra of the SC series of intrinsic silicon layers deposited on glass. The spectra are shifted for clarity. The three main diffraction peaks corresponding to the (111), (220) and (311) silicon planes are indicated. Note that the small peak centred around 38.5° present in the spectra of the 6.5%, 7% and 7.5% samples is due to the presence of aluminium contacts in a part of the area exposed to the X-ray beam.

With the $\text{CuK}\alpha$ radiation at the wavelength of 1.5418 \AA used here, the three main diffraction peaks corresponding to the (111), (220) and (311) silicon planes appear at 2θ positions of 28.47° , 47.34° and 56.17° , respectively. As shown in Fig. 3.10, the samples deposited at $\text{SC} = 7.5\%$ and 8% do not exhibit any crystalline silicon related peak (the large bump around 27° is due to the amorphous phase of the glass substrate). Then, as SC decreases, the intensity of the three peaks increases, indicating an increase in the crystallinity. Therefore, from the point of view of XRD, the transition between microcrystalline and amorphous material is observed between the sample deposited at $\text{SC} = 7\%$ and the one deposited at 7.5% , similarly to what was observed for electrical transport (see § 3.4.2.2).

A material has a preferential orientation if the ratio of the area of two given peaks is bigger than the area ratio of these same peaks measured for a reference c-Si powder. The ratio of the (220) peak area over the (111) peak area as well as that of the (311) peak area over the (111) peak area are represented as a function of SC in Fig. 3.11. For a c-Si powder, the

(220)/(111) area ratio is 0.55, whereas the (311)/(111) area ratio is 0.3 (indicated in Fig. 3.11 by dotted lines). All the \square c-Si:H samples of the SC series (except perhaps the SC = 7% sample) have a (220) preferential orientation.

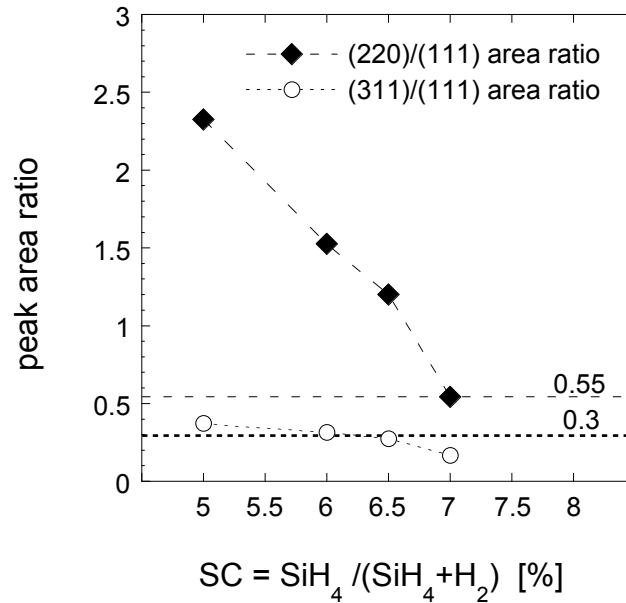


Fig. 3.11: XRD preferential orientation (see text) of the SC series of layers

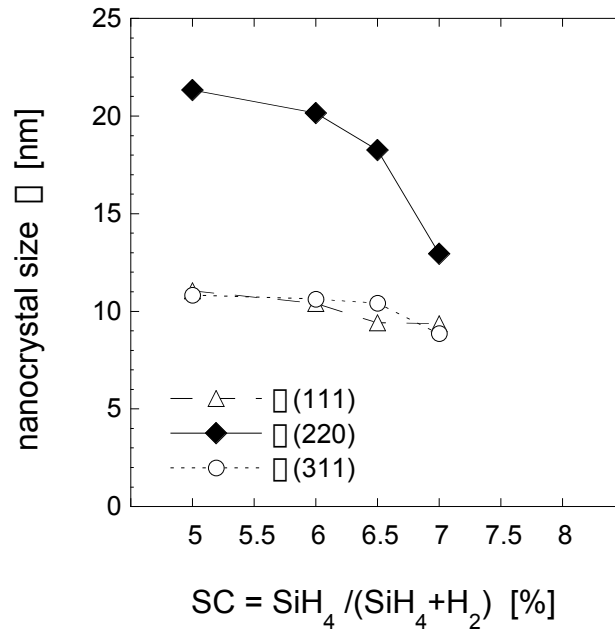


Fig. 3.12: Average nanocrystal size \square evaluated from the different peaks observed in the XRD spectra of the SC series of layers (see Fig. 3.10).

From the Full Width at Half Maximum (FWHM) of the peaks of a XRD spectrum, one can calculate the average size of the smallest coherent domains (or nanocrystals) of a sample with the Scherrer formula [Cullity 1978]. The average nanocrystal size \square evaluated from the (111), (220) and (311) peaks is plotted as a function of SC in Fig. 3.12. As our samples have a (220) preferential orientation, we will consider, as representative average nanocrystal size, the one evaluated from the (220) peaks (that is in fact larger than the sizes evaluated from the two other peaks). Fig. 3.12 shows that \square varies from 13 nm (at SC = 7%) to 20 ± 2 nm (at SC = 5 – 6.5%), and increases with decreasing values of SC: the more microcrystalline the deposition conditions are, the larger the nanocrystal size is.

3.4.3.3. Atomic Force Microscopy (AFM)

The surface topography was analysed by Atomic Force Microscopy (AFM), that was performed in the non-contact (tapping) mode on a Vista Burleigh Instruments scanning probe microscope. The surface topography of each layer of the SC series is shown in Fig. 3.13. The samples deposited with SC = 5% to 7.5% have a quite rough surface, whereas the 8% sample surface is quite different. A cauliflower-like structure of the surface is particularly well visible for the 7% and 7.5% samples. The Root Mean Square (RMS) surface roughness corresponding to the AFM scan of Fig. 3.13 is given in Fig. 3.14: it is approximately constant around 25 nm for the samples deposited at SC between 5% and 6.5%, then increases for the 7% and 7.5% samples to reach more than 40 nm, and finally drops to almost zero for the 8% sample. In Fig. 3.14 is also represented the size of the conglomerates (\square) emerging at the surface, evaluated from the Fourier transform power spectrum of the AFM scans: \square is approximately constant around 500 - 600 nm for the samples 5% to 6.5%, then reaches a maximum at ~ 800 nm for the 7% sample, and finally rapidly decreases for the 7.5% and 8% samples, down to 150 nm.

Unlike what was observed previously in the case of XRD, L_{amb} or $\square^0 \square^0$, the 7.5% sample is very different from the 8% sample from the point of view of the surface nature. It should therefore still be considered as a sample in the \square c-Si:H / a-Si:H transition region and not as a completely amorphous sample.

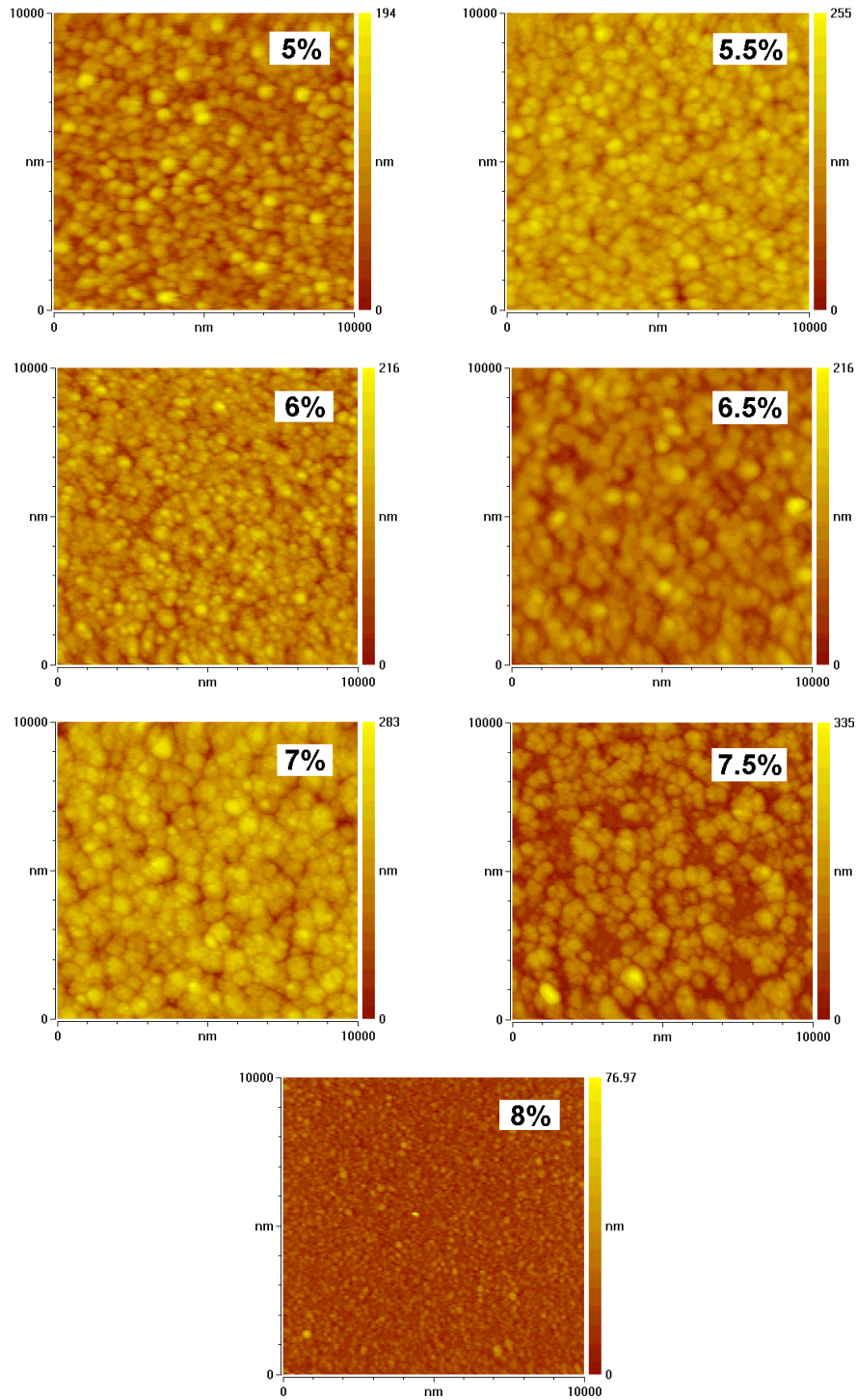


Fig. 3.13: AFM scan of the top of the layers of the SC series. The lateral size of the surface feature, or “conglomerate” lateral size, measured from the Fourier transform power spectrum of these AFM scans, is represented in Fig. 3.14.

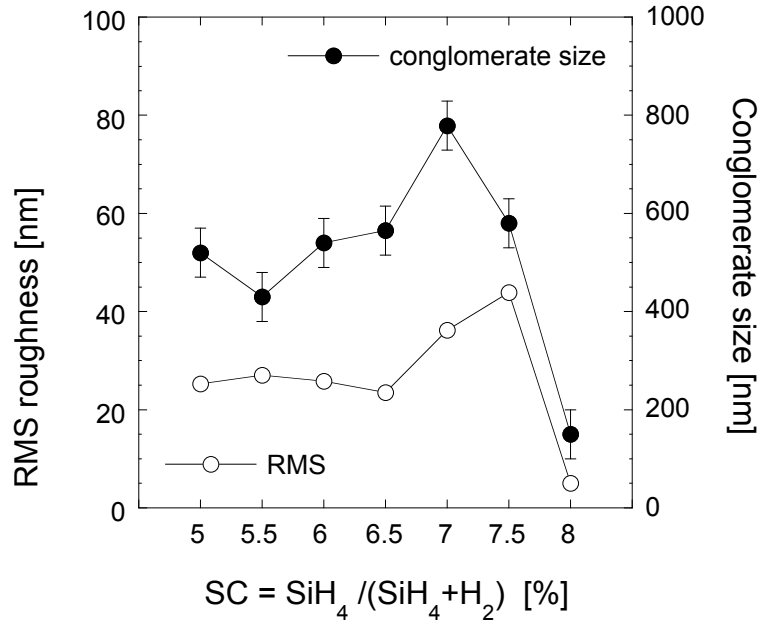


Fig. 3.14: RMS surface roughness measured by AFM and conglomerate lateral size measured from the Fourier transform power spectrum of the AFM scan (see Fig. 3.13) of the SC series of layers.

3.4.3.4. Micro-Raman spectroscopy

Bifacial depth-dependent micro-Raman technique (see § 2.5), i.e. measurements performed with $\lambda = 514$ nm and $\lambda = 633$ nm excitation light from the top side and from the bottom side (through the glass), has been applied to the SC series of layers deposited on glass. Then, the Raman crystallinity factor (\square_c) has been evaluated according to § 2.6.2 from each of the four Raman spectra obtained for each layer (i.e. for each value of SC).

Fig. 3.15 shows that the different \square_c -values vary smoothly with SC. The value $\square_c \approx 0$ obtained for bottom illumination at 514 nm indicates that the beginning of growth is, for all values of SC of this series of layers, amorphous over a thickness which is at least equal to the corresponding Raman Collection Depth (RCD, see § 2.5.1), value (≈ 50 nm). The three other curves show a continuous decrease of \square_c with increasing value of SC. The two values of \square_c measured at 633 nm are representative of the bottom (less crystalline) and top (more crystalline) parts of the layer; thereby, **the crystallinity within the layers increases as growth proceeds**, in agreement with TEM observations (see Fig. 3.9). The \square_c -value for top illumination at 514 nm is very close to that at 633 nm, indicating that the crystallinity does not change very much in the last hundreds of nanometres of growth of these 2 μ m thick layers. **We can therefore say that there is a saturation of the crystallinity with the sample thickness, and that the saturated value depends on the deposition conditions (i.e. SC here).**

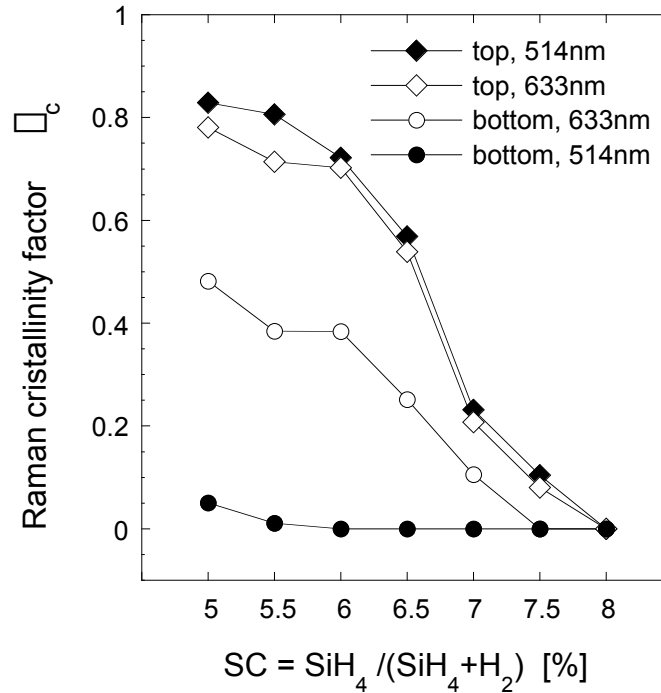


Fig. 3.15: Raman crystallinity factor (\bar{c}) (see § 2.6.2) for the SC series of *i*-layer (thickness $\approx 2.2 \pm 0.2 \mu\text{m}$) deposited on glass. \bar{c} is evaluated from the spectra measured by the bifacial depth-dependant micro-Raman technique (see § 2.5), i.e. measurements were performed with $\lambda=514 \text{ nm}$ (filled symbols) and $\lambda=633 \text{ nm}$ (open symbols) excitation light, from the top side (diamonds) and from the bottom side through the glass (circles).

In the section 3.4 hereafter, we will use the Raman crystallinity factor \bar{c} for top illumination at 514 nm ($\bar{c}^{\text{top}, 514}$) as the monitoring parameter instead of the SC value used for *i*-layer deposition. $\bar{c}^{\text{top}, 514}$ is quite high for the samples deposited at SC between 5% and 6%, and then decreases rapidly with increasing SC. Note that, from a point of view of the Raman crystallinity factor, only the 8% sample is completely amorphous, as already observed from the AFM measurements.

Similar Raman crystallinity factor evaluation has been performed with 514 nm excitation light on some other intrinsic silicon layers deposited at silane concentration value of 2%, 4%, 6% and 8%. Note that the thicknesses of these samples range from 1 to 1.5 μm and are therefore thinner than those of the SC series samples of Fig. 3.15 (ranging from 2 to 2.4 μm). Fig. 3.16 shows that the sample deposited at SC = 2% is as crystalline in the first tens (or hundreds) of nanometres of growth as in the last upper part. On the other hand, the 8% sample is completely amorphous. In between, the 4% and 6% samples make the transition. Note that the $\bar{c}^{\text{top}, 514}$ for the 6% sample of Fig. 3.16 is lower than $\bar{c}^{\text{top}, 514}$ for the 6% sample of the SC series (Fig. 3.15). This variation can be explained by the difference in thickness of the samples. Indeed the thicker sample of the SC series (Fig. 3.15) will reach higher crystallinity values in its upper part, as the crystallinity increases as growth proceeds.

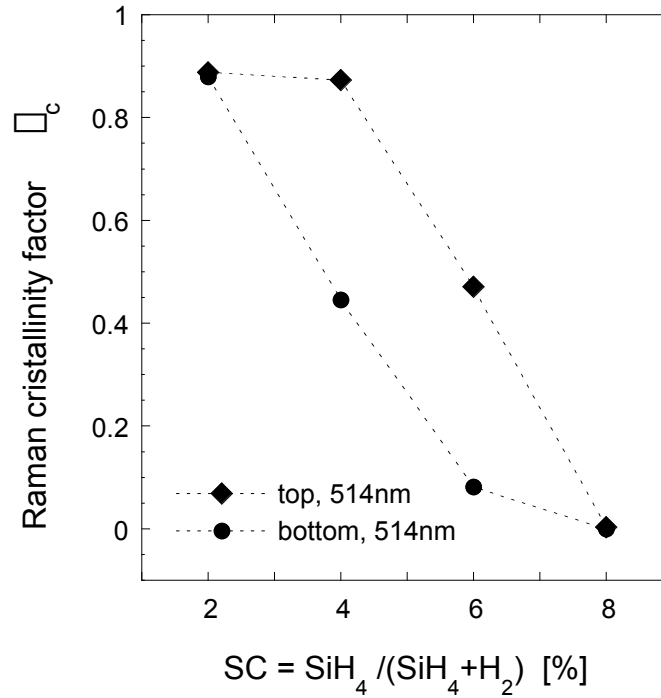


Fig. 3.16: Raman crystallinity factor (\bar{c}) for i -layers deposited at SC = 2%, 4%, 6% and 8% on glass (thickness $\approx 1.2 \pm 0.3 \mu\text{m}$).

3.4.3.5. Constant Photocurrent Method (CPM) and optical properties

A main advantage of \square c-Si:H over a-Si:H for solar cell application is its enhanced optical absorption in the range of near-infrared light ($\sim 700 - 1100 \text{ nm}$, i.e. $\sim 1.1 - 1.8 \text{ eV}$), due to its optical bandgap that is similar to that of crystalline silicon (c-Si) ($\sim 1.1 \text{ eV}$, compared to 1.75 eV for a-Si:H). This feature makes \square c-Si:H a well suited low-gap material for tandem solar cell application in association with a-Si:H (“micromorph” Si tandem solar cells, see [Meier 1998a]). Moreover, the optical absorption of \square c-Si:H is enhanced, compared to that of c-Si, on the whole spectral range, due to the light scattering effect inside the \square c-Si:H material.

In Fig. 3.17 we have represented the optical absorption coefficient (α) obtained by Absolute Constant Photocurrent Method (A-CPM) measurements [Vanecek 1995] for the samples 5% to 7% of the SC series. The CPM method [Vanecek 1981] allows the determination of very small values of the absorption coefficient down to the sub-bandgap range. On Fig. 3.17, the 5%, 5.5% and 6% samples show typical CPM curves as regularly obtained for “fully” microcrystalline material [Beck 1996a]. On the other hand, the curves obtained for the 6.5% and 7% samples are representative of \square c-Si:H material containing a more or less large amorphous fraction (roughly $< 50\%$ for the 6.5% sample and $> 50\%$ for the 7% sample).

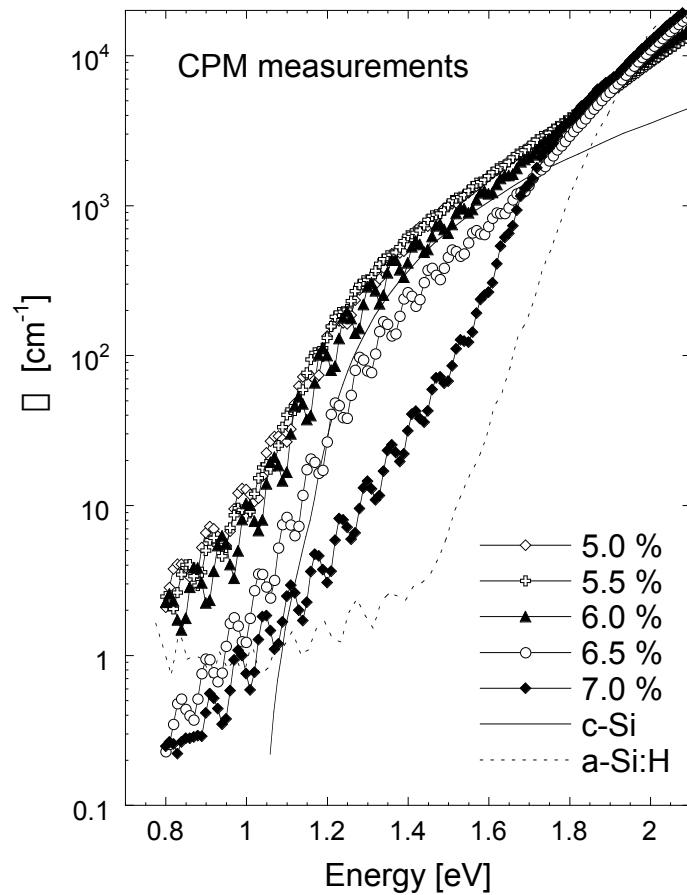


Fig. 3.17: Apparent optical absorption coefficient (α) measured by CPM [Vanecek 1995] on the SC series of silicon layers (except the SC = 7.5 and 8% samples). Measurements have been performed by the Institute of Physics in Prague.

Fig. 3.17 shows the “apparent” absorption, which is the absorption as obtained experimentally from the CPM measurement. However, the light scattering due to the textured surface of \square c-Si:H increase the “true” intrinsic absorption of the material by a factor of 10 [Poruba 2000b]. This fact explains the enhanced absorption of \square c-Si:H compared to c-Si (see Fig. 3.17). The true absorption curve can be calculated [Poruba 2000a] by taking into account the surface roughness (see Fig. 3.14) of the samples. The true defect absorption at 0.8 eV, connected to the defect density, is nearly the same for all the samples (except for the very rough and inhomogeneous 7% sample for which the true absorption could not be determined): 0.3 cm^{-1} for the 5% and 5.5% samples, 0.2 cm^{-1} for the 6% sample and 0.4 cm^{-1} for the 6.5 sample.

Fig. 3.18 shows, for the SC series of layers, the absorption coefficients (β) at 514 nm and at 633 nm (i.e. the wavelengths used as excitation light for Raman measurements, see § 2.5) taken from the CPM data (Fig. 3.17) and determined from transmission and reflection spectra measured with a commercial spectrometer (Perkin-Elmer type Lambda 900). Whereas β at

633 nm is about constant around 10^4 cm^{-1} for the whole SC series, \square at 514 nm increases from about $3\text{-}4 \cdot 10^4 \text{ cm}^{-1}$ for the "fully" microcrystalline samples (SC = 5 - 6%) to about 10^5 cm^{-1} for the completely amorphous sample (SC = 8%).

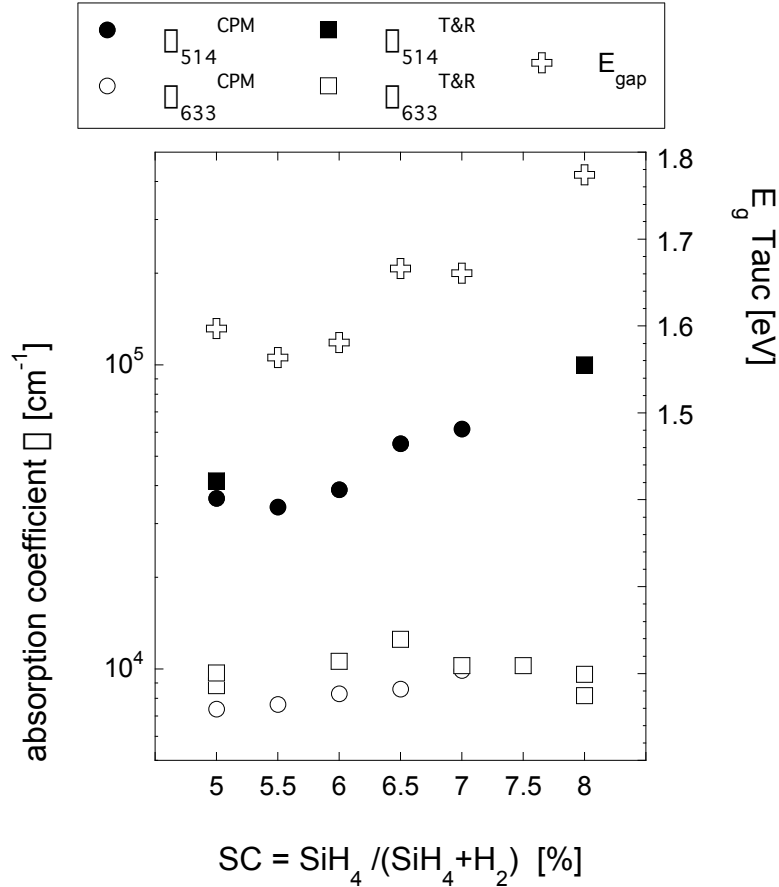


Fig. 3.18: Absorption coefficient at 514 nm (\square_{514} , filled symbols) and at 633 nm (\square_{633} , open circles and squares) evaluated by CPM measurements (circles) and from transmission and reflection (T&R) measurements (squares), as well as optical bandgap E_g evaluated by the Tauc method [Tauc 1966] (crosses) from the CPM data for the SC series of layers.

Fig. 3.18 also gives the values of the optical bandgap E_g evaluated from the CPM data by the Tauc method [Tauc 1966] as a function of SC used for the deposition of the layers. The Tauc method assumes a parabolic density of states as a function of the energy E , leading to a linear relation between $\sqrt{\square(E) \cdot E}$ and $(E - E_g)$. One has to note that quite high values of E_g are obtained for this series of layers deposited around the amorphous / microcrystalline transition.

3.4.3.6. Infra-Red (IR) spectroscopy (hydrogen content)

Each layers of the SC series was simultaneously deposited on Si wafer in order to measure transmission spectra in the infra-red (IR) region. Measurements were performed with a commercial Fourier transform IR (FTIR) Perkin-Elmer (1720-X) spectrometer. The

hydrogen content, determined from the peak around 650 cm^{-1} [Feitknecht 2003], is represented in Fig. 3.19 as a function of SC. Note that, as the films are here deposited on c-Si, the resulting growth may be different from that of the layers deposited on glass substrate. Fig. 3.19 shows that the hydrogen content is low for highly \square c-Si:H samples (SC = 5-5.5%), then increases as one approaches the transition region (from SC = 5.5 to 7%), and finally decreases for a-Si:H samples. Such enhanced hydrogen incorporation in samples deposited in or near the transition zone is quite frequently observed [Kroll 1996, Mates 2003].

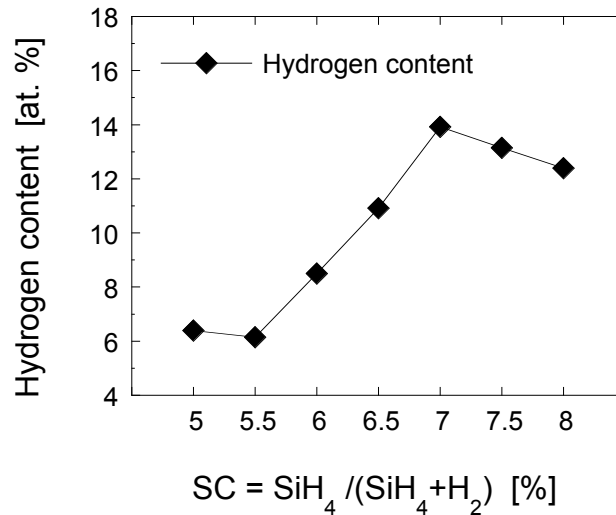


Fig. 3.19: Hydrogen content determined from IR spectra measured on layers deposited on Si wafer; data are taken from [Feitknecht 2003].

3.4.4. Relation between electronic transport and microstructure

In the preceding sections (§ 3.4.2 and § 3.4.3), we have studied, in one series of layers deposited on glass at various silane concentrations, the coplanar electronic transport and the evolution of the microstructure, respectively. We will now compare these two aspects. With this goal in mind, we have plotted in Fig. 3.20 electrical and microstructural features as a function of the Raman crystallinity factor measured with 514 nm excitation light on the top of the samples (instead of SC as used in the preceding sections).

From Fig. 3.20 (bottom), one can see that \square' is lower in the \square c-Si:H samples than in the a-Si:H ones, while remaining constant as long as \square c-Si:H material is detected in XRD spectra (i.e. for \square_c between 0.2 and 0.8). On the other hand, the average nanocrystal size increases roughly linearly with \square_c . This demonstrates, that at least for this particular series of samples, **coplanar transport is not affected by the average nanocrystal size.**

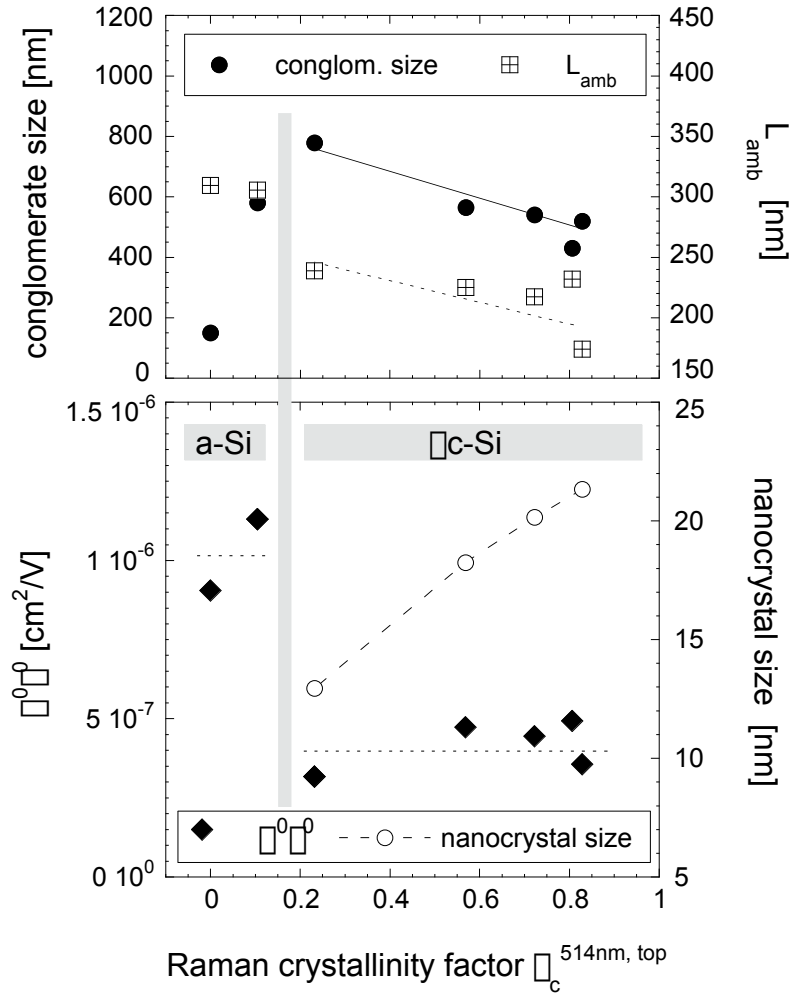


Fig. 3.20: Top: Conglomerate size (\square) evaluated from AFM surface topography (see Fig. 3.21 for comparison) and ambipolar diffusion length (L_{amb}), with corresponding linear fits (for the \square c-Si:H samples); Bottom: mobility \square lifetime product ($\square^0 \square$) and nanocrystal size (\square) evaluated from the (220) XRD peaks, with guides to the eye, as a function of the Raman crystallinity for the SC series of silicon layers deposited on glass.

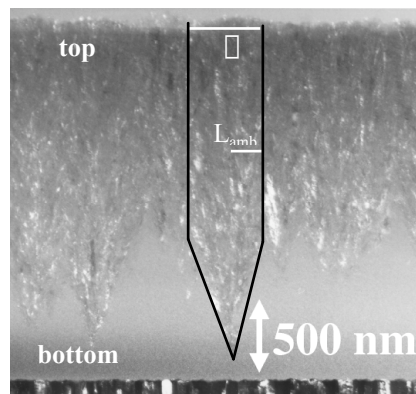


Fig. 3.21: TEM dark field micrograph of a \square c-Si:H layer deposited with $SC = 7\%$. The ambipolar diffusion length (L_{amb}) measured in coplanar geometry and the conglomerate size (\square) as measured from AFM are also indicated.

Fig. 3.20 (top) shows that both conglomerate size (\square) and L_{amb} slightly decreases with \square_c for the \square c-Si:H samples. Moreover, one sees that **the ambipolar diffusion length is equal to about half of the conglomerate size** ($L_{amb} \approx 0.5 \cdot \square$) in this series (see also Fig. 3.21). This relation can be expected if the diffusion length within the conglomerate is very large, but the carriers recombine at the boundaries.

The decrease of the conglomerate size with increasing crystallinity can be explained on the basis of the nuclei density. A nucleus is the starting point of a conglomerate, i.e. the tip of the inverted \square c-Si:H cone (see Fig. 3.21). One can assume that, as it was observed for the case of entire solar cells [Bailat 2003], the nuclei density decreases as SC increases and the opening angle of the \square c-Si:H cones is independent of SC. As a result, for a low nuclei density (i.e. high SC-value, leading also to a low crystallinity), the (few) microcrystalline cones will become quite large before coalescing. On the other hand, if the nuclei density is high (i.e. low SC-value, leading to high crystallinity), the (numerous) cones will coalesce rapidly and the resulting conglomerate size emerging at the surface will be smaller in this case.

From these observations, we can deduce that transport is not affected by the average nanocrystal size, but that it rather behaves in accordance with the conglomerate size, as already suggested by Kocka et al. [Kocka 2002]. Moreover, Fig. 3.22 shows that the activation energy (E_{act}), the dark conductivity prefactor (\square_0) and the dark conductivity (\square_{dark}) rapidly change for low values of \square_c (a-Si:H \rightarrow \square c-Si:H transition) and then smoothly evolve for the \square c-Si:H samples. The values measured for \square_0 and for E_{act} on our \square c-Si:H samples ($\square_c > 0.2$) are actually lower than the threshold values given by Kocka et al. [Kocka 2002, Mates 2003] under which transport is limited by the boundaries of the conglomerates (see Fig. 3.22). Indeed, for $\square_0 \geq 100 \square^{-1} \text{cm}^{-1}$ and $E_{act} \geq 0.5 \text{ eV}$, Kocka et al. showed that material is only made out of nanocrystals, and transport properties are therefore not deteriorated by the formation of conglomerate boundaries.

These observations are in accordance with what has been seen in the section 3.3, where similar $\square^0 \square^{\frac{1}{2}}$ products have been observed in \square c-Si:H as in a-Si:H. **We can therefore conclude that the conglomerate boundaries are made of amorphous material and that they limit the electronic transport in \square c-Si:H.**

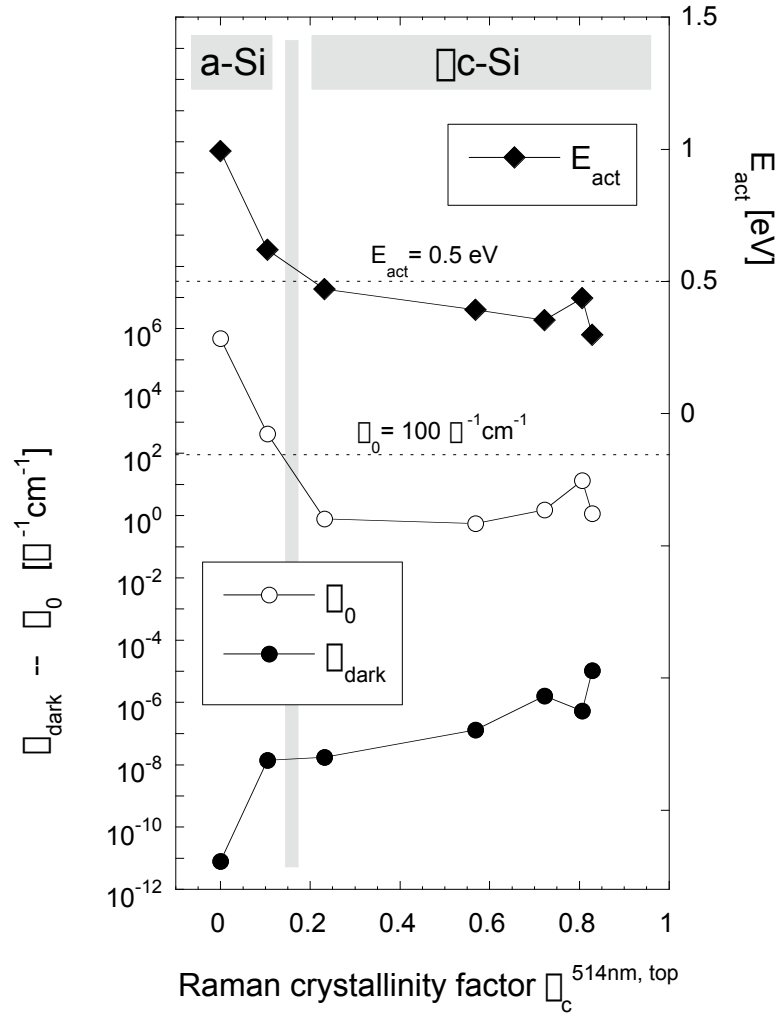


Fig. 3.22: Dark conductivity, conductivity prefactor and activation energy as a function of the Raman crystallinity factor measured at 514nm from the layer-side of the silane concentration series of layers deposited on glass. The dotted lines give the limit values ($\rho_0 \geq 100 \square^{-1}cm^{-1}$ and $E_{act} \geq 0.5 eV$) found by Kocka [Kocka 2002] over which the transport is not affected by the aggregates (or conglomerates), as they are not present.

3.5. Conclusions

In this chapter, we have first seen that the coplanar electronic transport under illumination in \square c-Si:H material is similar to that in a-Si:H material, as observed here for a large variety of a-Si:H and \square c-Si:H samples. The similitude in the values of the mobility \square lifetime products for \square c-Si:H and a-Si:H ($\mu\tau^{a-Si} \approx \mu\tau^{\square c-Si}$) is quite surprising, as transport properties are much better (i.e. the $\mu\tau$ products are higher) in crystalline silicon than in a-Si:H. These observations suggest that electronic transport in \square c-Si:H layers is governed by the amorphous (or defective) phase present at the grain boundaries (nanocrystal boundaries or conglomerate boundaries) of \square c-Si:H. Then, for one series of layers deposited on glass at various silane concentrations, we have pointed out that the coplanar electronic transport is not

affected by the average nanocrystal size. Moreover, the ambipolar diffusion length measured in these samples was found to be about half of the size of the conglomerates. It seems thus that it is the conglomerates (or more precisely the conglomerates boundaries) that are limiting the transport in \square c-Si:H layers. We can therefore conclude that the conglomerate boundaries are made of amorphous material and that they limit the electronic transport in \square c-Si:H layers.

Chapter 4: Microstructure and electrical properties of \square c-Si:H solar cells

4.1. Introduction

In the previous chapter, we have analysed both electrical and microstructural aspects of intrinsic \square c-Si:H layers, deposited with experimental conditions similar to those used for the deposition of the intrinsic active layer incorporated into n-i-p or p-i-n \square c-Si:H solar cells. The analysis of single i-layers is important for the fundamental understanding of the roles of the different microstructural components on the transport properties of \square c-Si:H material. However, a complete solar cell consists of a stack of several layers, the interfaces of which are very critical. Even if quite essential, the i-layer represents only one element of the entire device. Thus, the properties of the i-layer are only partly responsible for the properties of the whole solar cell. To gain understanding on the role of the microstructure on the functioning of such complete devices, it is therefore crucial to characterise entire solar cells rather than only the material used as active layer. From this perspective, micro-Raman spectroscopy is an ideal candidate as characterisation tool for the monitoring of the crystallinity of entire solar cells. Indeed, as already mentioned in previous chapters, Raman spectroscopy is a fast and non-destructive tool. Its main interest is that it gives us the basic possibility to characterise the volume fractions of amorphous and crystalline phases within actual (functioning) solar cells, and that electrical performances can be measured on the very same solar cells. The bifacial depth-dependent technique enables us to evaluate selectively the n-i or the p-i interface at different depths.

One of the key deposition parameters for obtaining \square c-Si:H material is the silane (SiH_4) and the hydrogen (H_2) content in the plasma gas phase. By decreasing the Silane Concentration $\text{SC} = \text{SiH}_4/(\text{SiH}_4+\text{H}_2)$ from 100% down to a few percent, the material undergoes an a-Si:H/ \square c-Si:H transition (roughly around 6%, this value depending also on the other deposition conditions). The value of SC used for the deposition of the intrinsic (i-) layer has been shown to play a significant role in determining the highest sofar attainable values for

the open-circuit voltage (V_{oc}) of a p-i-n cell [Meier 2001]. On the other hand, the material microstructure depends as well on SC [Houben 1998, Vallat-Sauvain 2000], as already shown in the previous chapter. At present, the best electrical performances are achieved for \square c-Si:H solar cells with their i-layer deposited near the transition [Roschek 2002, Shah 2002].

In § 4.2 we will briefly describe the structure and the principle of operation of \square c-Si:H solar cells. The main differences between n-i-p and p-i-n solar cell configurations will be pointed out and the solar cells analysed in this chapter will be presented. In particular, we have (mainly) analysed two series of n-i-p cells where the silane concentration (SC) used for the deposition of the intrinsic (i-) layer has been varied.

The main characterisation techniques generally used for the electrical characterisation of solar cells will be explained in § 4.3, and typical parameter values thereby obtained for the two SC series of n-i-p cells will be given.

§ 4.4 is devoted to the application of micro-Raman spectroscopy to entire \square c-Si:H solar cells. In a first part, we will address the effect of the additional layers present in a solar cell (i.e. the layers that are present in addition to the i-layer) on Raman measurements. Then, results obtained from the application of the bifacial depth-dependent Raman technique to complete \square c-Si:H solar cells will be discussed. In particular, the evolution of the four Raman crystallinity factors will be observed for the two SC series of n-i-p type solar cells and compared to the TEM micrographs of a few solar cell from these very same series.

In § 4.5, the electrical properties of both n-i-p and p-i-n type solar cells will be compared with their microstructural characteristics, as evaluated by the Raman crystallinity factors. A link between the value of the open-circuit voltage and the Raman crystallinity factor will be demonstrated for both n-i-p and p-i-n configurations.

The application of Raman spectroscopy for the analysis of entire solar cells as well as the main results presented § 4.4 and 4.5 have been published in [Droz 2001, Droz 2003, Droz to be published].

4.2. Microcrystalline silicon (\square c-Si:H) solar cells

4.2.1. Structure and principle of operation of \square c-Si:H solar cells

Similarly to a-Si:H solar cells, \square c-Si:H solar cells have a p-i-n (or n-i-p) structure (see Fig. 4.1). The addition of the i- (intrinsic) layer, compared to the "classical" p-n structure of the crystalline silicon (c-Si) solar cell, enables one to enlarge the depletion zone and to collect photogenerated carriers through drift in this region, rather than by diffusion as in the undepleted region in the p-n junction.

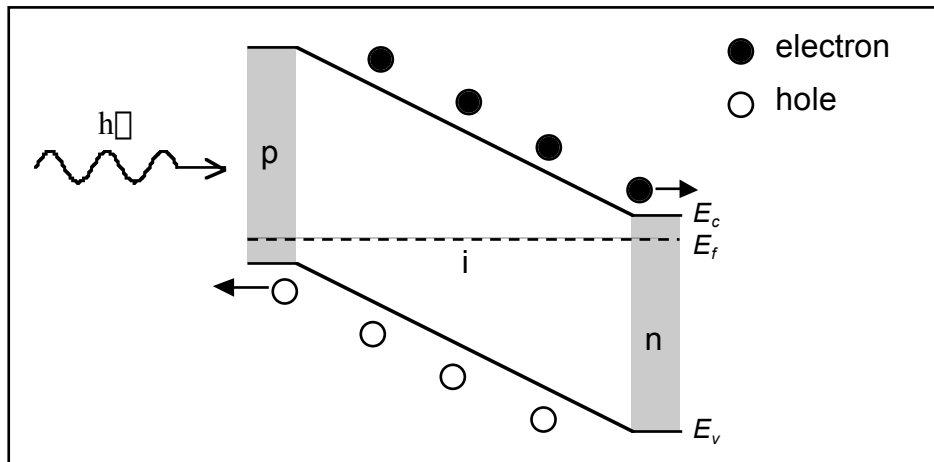


Fig. 4.1: Schematic band diagram of a *p-i-n* (or *n-i-p*) thin film silicon solar cell. The electrons photogenerated in the *i*-layer are collected by the *n*-layer whereas the holes are collected by the *p*-layer.

The **i-layer** has actually two main roles to play in the cell:

- It is the photoactive layer, i.e. it absorbs the incident photons and generates electron / hole pairs. Typical thickness of the *i*-layer is about 1 - 2 μm for \square c-Si:H solar cells, compared to 0.3 - 0.5 μm for a-Si:H cells. This difference is mainly due to the reduced absorption coefficient of \square c-Si:H in the short wavelength range as compared to a-Si:H. On the other hand, \square c-Si:H solar cells can actually be made thicker than a-Si:H solar cells. The properties of an a-Si:H solar cell with a thick *i*-layer are indeed more susceptible to light-induced degradation than those of corresponding \square c-Si:H solar cells.
- Once the electron and holes have been generated, they must be separated and then "travel" inside the *i*-layer to reach the electrical contacts. This is called "collection" of the free carriers. The potential difference, that creates the internal field E and assists this collection process, is indeed caused by the *p*- and *n*-type doped layers (see later). The quality of the *i*-layer must be sufficiently high so that the free carriers can travel inside the layer without recombining. This means that the drift length $L_d = \mu E$ (and, thus, the mobility and the recombination time of the carriers, see Chapter 3) must be as high as possible, but at least larger than the *i*-layer thickness.

The **p- and n- doped layers** are responsible for creating an internal field inside the *i*-layer that will allow the free electrons and holes to reach their respective contact by drift (see Fig. 4.1). For the deposition of the *n*-layer, phosphine gas (PH_3) is added to hydrogen (H_2) and silane (SiH_4) gases, in order to dope the \square c-Si:H layer with phosphorus (P). For the deposition of the *p*-layer, diborane gas (B_2H_6) is added to H_2 and SiH_4 gases, in order to dope the \square c-Si:H layer with boron (B). In the device, when the *p*-layer that contains an excess of

free holes (as compared to an i-layer) is put into contact with the i-layer, the free holes diffuse into the neighbouring part of the i-layer and therefore this leads to a fixed negative charge in the p-layer. On the other hand, when the n-layer, that contains an excess of free electrons, is put into contact with the i-layer, the free electrons diffuse into the i-layer and "leave behind" a fixed positive charge in the n-layer. The electrons that are photo-generated inside the i-layer will be collected by the n-layer, whereas the photogenerated holes will be collected by the p-layer. As the carriers photogenerated within the doped-layers do generally not contribute to the collected current (because of their high recombination centre density), they are required to be as thin as possible. Their thickness is usually about 10 - 30 nm, i.e. they are much thinner than the i-layer. As the mobility of the electrons is larger than that of the holes, better device efficiencies are attained when light enters the cell from the p-side, so that the holes generated by strongly absorbed light (i.e. by light with short wavelengths) near this layer have to cover a shorter distance before being collected.

In addition to the silicon-based layers that ensure the basic functioning of the solar cells, the complete device also includes Transparent Conductive Oxide (TCO) layers, on both sides. These have a double role as electrical contact and as layer with specific optical properties. The **front TCO layer** (on the p-side), through which the light enters the solar cell, must be as transparent as possible in order that all the light that can be absorbed enters into the photoactive layer. It is generally wanted that the front TCO is textured, in order to scatter the light inside the cell, and, thus, to increase its probability of being absorbed. The front TCO must have a sufficient conductivity ($\sim 10^3 \text{ } \Omega^{-1} \text{ cm}^{-1}$) that enables it to collect current into the external load with minimal resistive loss, if possible without the additional help of a metallic contact (only a grid can be allowed here, because metals are opaque and would not let the light through). The requirements for the back TCO layer (on the n-side) are similar to that for the front TCO, although often less strict. Indeed, a metallic back reflector is frequently used, especially if one wants to maximise the current generated in the solar cell.

4.2.2. p-i-n and n-i-p solar cell technologies

One talks about solar cells having a p-i-n or n-i-p configuration depending on the deposition sequence of the various layers. In a p-i-n solar cell, the deposition sequence of the layers is the following (see Fig. 4.2, left):

- **p-i-n solar cell:** substrate / front TCO / p-layer / i-layer / n-layer / back TCO / (reflector).

As the light enters the cell from the p-side, the substrate used with the p-i-n configuration must be transparent and is generally glass. In this configuration, the p-doped layer is the first silicon layer deposited.

On the other hand, in a n-i-p solar cell, the sequence of deposition of the layers is

inverted (see Fig. 4.2, right):

- **n-i-p solar cell:** substrate / (reflector) / back TCO / n-layer / i-layer / p-layer / front TCO.

In the n-i-p configuration the substrate is not necessarily transparent. Therefore, besides glass, materials such as stainless steel or plastic can be used as substrate. In this configuration, it is the n-doped layer that is deposited first (amongst the silicon layers).

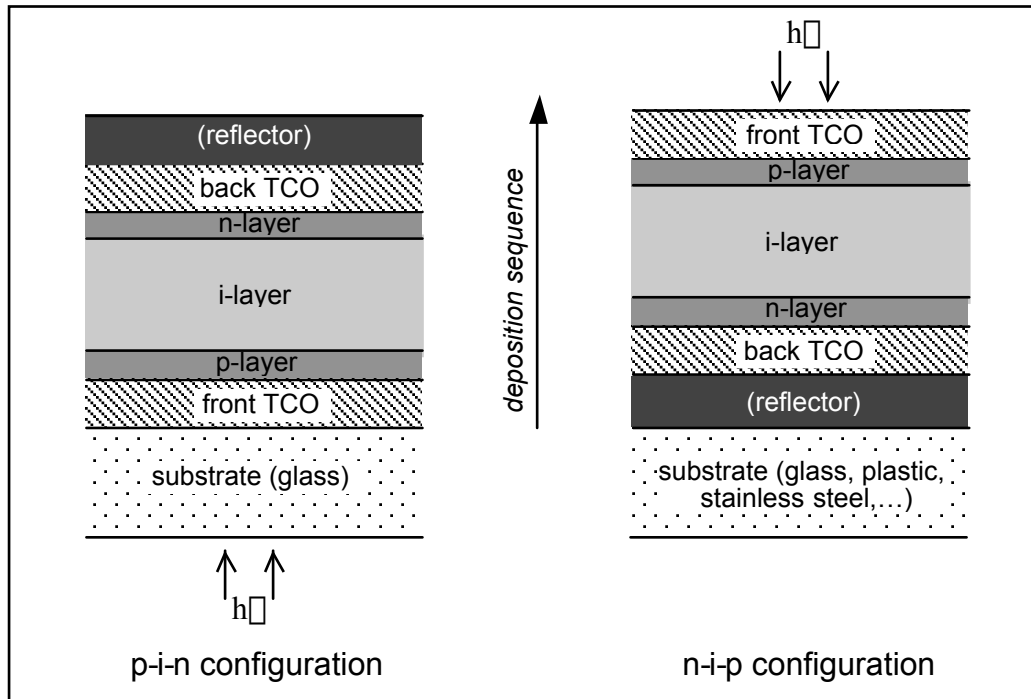


Fig. 4.2: Schematic representation of solar cells with p-i-n (left) and n-i-p (right) configurations. Note that the layers (especially the TCO's) can be rough, even if represented flat here.

In the following of this work, the word "substrate" will often refer to the substrate as defined above plus the TCO layer, or, simply, the substrate plus all the layers of any kind deposited before the silicon-based layers under consideration.

4.2.3. Description of the solar cells analysed in this chapter

The samples studied in this chapter are microcrystalline silicon ($\mu\text{c-Si:H}$) solar cells in the n-i-p and p-i-n configurations deposited by the Very High Frequency Glow Discharge (VHF-GD) technique, at plasma excitation frequencies between 70 and 130 MHz. Both n- and p-doped layers are deposited with $\mu\text{c-Si:H}$ conditions. The cells were deposited on glass substrates (AF45 Schott) coated with various types of Transparent Conducting Oxides (TCO), namely in-house Low-Pressure Chemical Vapour Deposited (LP-CVD) Zinc Oxide (ZnO) [Fay 2003, Meier 2002] and in-house sputtered ZnO, as well as commercial tin oxide (SnO_2).

LP-CVD ZnO and SnO₂ are textured TCO (rms \approx 40-60 nm) while sputtered ZnO is flat.

In particular, two series of n-i-p cells [Bailat 2003, Feitknecht 2003, Feitknecht 2001] were deposited simultaneously on sputtered ZnO and LP-CVD ZnO, respectively, with the same "highly microcrystalline" deposition conditions (low value of silane concentration (SC)) for the n- and p- layers. The SC used for deposition of the i-layers was varied from 5% (highly microcrystalline material) to 7% (mixed phase (\square c-Si:H/a-Si:H) material), by steps of 0.5%. During the growth of the i-layer, the deposition parameters were kept constant. The i-layer thicknesses all ranged between 2.0 and 2.5 μ m (see Table 4.1). The main difference between these two ZnO is that sputtered ZnO is flat and CVD ZnO is rough. Also, sputtered ZnO is doped with aluminium, whereas CVD ZnO is doped with boron. The solar cells of these two series do not contain any back reflector. Note that the i-layer of these cells were deposited with exactly the same deposition conditions as those used for the fabrication of the SC series of single layer studied in Chapter 3. Note that in the following of this text, the designation of "a cell deposited at SC = X%" will refer to "a cell incorporating an i-layer deposited at X%".

i-layer SC [%]	5	5.5	6	6.5	7
i-layer thickness [μ m]	2.1	2.0	2.4	2.4	2.3

Table 4.1: Thickness of the i-layers incorporated into the silane concentration (SC) series of n-i-p solar cells deposited on sputtered ZnO and CVD ZnO studied throughout this chapter. The thickness is calculated by multiplying the deposition time of the i-layer incorporated into the cells by the deposition rate measured on the single i-layers deposited on glass substrate (see Table 4.1).

In addition to these two series of n-i-p cells, some other n-i-p solar cells not pertaining to these series, as well as a large set of p-i-n solar cells (that can be considered to be typical products of the solar cell technology laboratory at IMT Neuchâtel) which cover a wide range of V_{oc} values (see ref. [Meier 2001]) were also analysed. For these p-i-n solar cells, various deposition parameters were used for the p-, i- and n-layers. Most of the p-i-n solar cells had a back reflector. However, it does not cover completely the cell, permitting to perform bifacial Raman measurements.

Each solar cell analysed in this work actually consists of a plate divided in about ten to twenty individual laboratory test solar cells having a surface of less than 1 cm². The values given in this work for the different electrical and microstructural parameters were evaluated on the test cell having the best and/or representative electrical values as compared to the other test cells of the plate.

4.3. Electrical characterisation of solar cells

4.3.1. Current voltage (IV) characteristics

4.3.1.1. Theory

The basic characterisation tool for a solar cell is the current-voltage (IV) measurement. It is performed under a solar simulator (double light source Wacom WXS-140S) that produced a light with an intensity of 100 mW/cm^2 and a spectrum close to the AM1.5 solar spectrum. Fig. 4.3 shows a typical IV curve measured on a good \square c-Si:H solar cell ($V_{oc} = 520 \text{ mV}$, $I_{sc} = 24.2 \text{ mA/cm}^2$, $FF = 73\%$, [Terrazzoni-Daudrix 2003]).

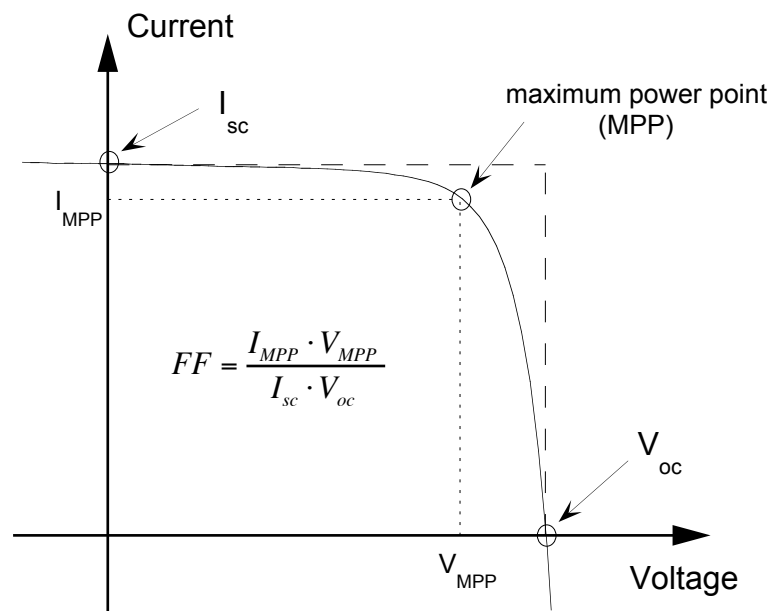


Fig. 4.3: Typical current-voltage (IV) curve of a \square c-Si:H solar cell under illumination. The open-circuit voltage (V_{oc}) and the short-circuit current (I_{sc}) are indicated. The fill factor (FF) is defined as the ratio of the area of the rectangle formed by the current and voltage obtained when the power is maximum over the area of the rectangle formed by I_{sc} and V_{oc} .

The **open-circuit voltage** V_{oc} is the voltage measured on the solar cell when no current flows through the device ($I = 0$). Similarly, the **short-circuit current** I_{sc} is the current flowing through the cell when the voltage is zero ($V = 0$). The **Fill Factor** FF is defined as:

$$FF = \frac{I_{MPP} \cdot V_{MPP}}{I_{sc} \cdot V_{oc}} \quad (\text{equ. 4.1})$$

where I_{MPP} and V_{MPP} are respectively the current and the voltage obtained when the output power is maximum (maximum power point, MPP).

Whereas the values for V_{oc} and FF are evaluated from IV measurement, I_{sc} is usually

preferably obtained from quantum efficiency (QE) measurement (see § 4.3.2). Indeed, one actually wants to know the current density of a solar cell, that can be obtained by measuring the current and knowing the active area. However, the surface of laboratory test cells is often not well defined and the estimation of the current density consequently difficult. On the other hand, the spectrum provided by a solar simulator is not exactly AM1.5. A difference in the spectrum will affect I_{sc} more noticeably than V_{oc} .

The **efficiency** η of a solar cell is the ratio of the maximal electrical output power over the incident light power (P_{light}):

$$\eta = \frac{I_{MPP} \cdot V_{MPP}}{P_{light}} = \frac{I_{sc} \cdot V_{oc} \cdot FF}{P_{light}} \quad (\text{equ. 4.2})$$

If the measurement of I_{sc} , V_{oc} and FF is performed under standard AM1.5 conditions, then $P_{light} = 100 \text{ mW/cm}^2 (= 1000 \text{ W/m}^2)$.

4.3.1.2. Values obtained for the SC series of n-i-p solar cells

Fig. 4.4 shows the evolution of V_{oc} with the silane concentration (SC) at which the i-layer has been deposited for the two series of n-i-p solar cells deposited on sputtered ZnO and on CVD ZnO, respectively.

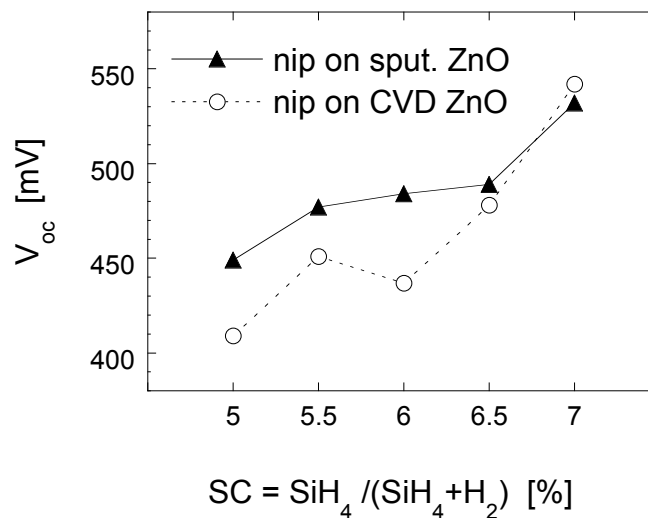


Fig. 4.4: Open-circuit voltage (V_{oc}) as a function of the silane concentration (SC) at which the i-layer has been deposited for two series of n-i-p solar cells deposited on sputtered ZnO (filled triangles) and on CVD ZnO (open circles).

On the whole, V_{oc} **increases as SC increases**. At SC = 5%, V_{oc} is about 450 mV for the cell on sputtered ZnO and about 400 mV for that on CVD ZnO. At SC = 7%, both cells have a V_{oc} -value of about 550 mV. Thus, by simply varying the silane concentration of the i-layer, an

increase of up to 150 mV in the V_{oc} -value can be achieved. Note that this tendency for the V_{oc} of \square c-Si:H solar cells to increase with the SC used for the deposition of the i-layer is generally observed [Klein 2002, Meier 2001, Stiebig 2000].

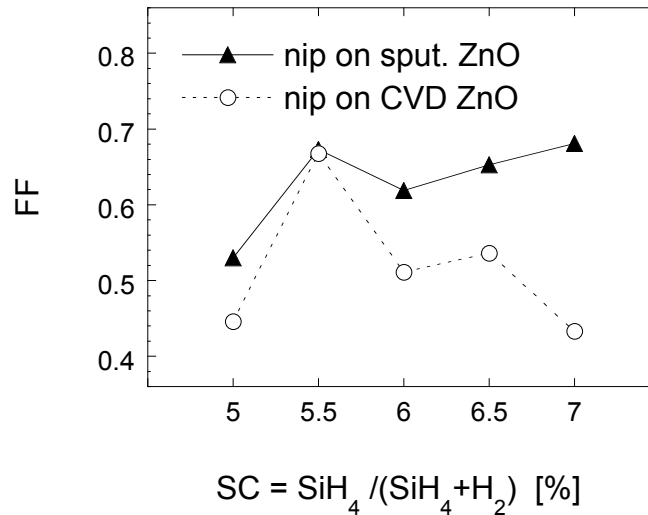


Fig. 4.5: Fill factor (FF) as a function of the silane concentration (SC) at which the i-layer has been deposited for two series of n-i-p solar cells deposited on sputtered ZnO (filled triangles) and on CVD ZnO (open circles).

Fig. 4.5 shows the evolution of FF as a function of SC for the two SC series of n-i-p cells. For the series deposited on sputtered ZnO, FF has a tendency to increase with SC . On the other hand, the FF -values obtained for the series deposited on CVD ZnO are quite low (except for $SC = 5.5\%$). The value of the fill factor depends on various different parameters (such as i-layer collection, shunt problems, series resistance due to a bad adequacy between two layers or to a bad conductivity of a TCO layer, etc...) and is therefore difficult to interpret.

4.3.2. Quantum efficiency (QE) measurements

4.3.2.1. Theory

The Quantum Efficiency (QE) measures the probability for an incident photon at a given wavelength to create an electron / hole pair that will contribute to the current extracted from the solar cell. It therefore includes the probability for the photon to be absorbed in the device and the probability for the photogenerated carriers to reach the external contacts without recombining. The measurement can be performed at different bias voltage, in order either to enhance or to decrease the existing internal field. The different curves obtained at positive, negative or without bias voltage can be compared in order to evaluate qualitatively the collection efficiency of the solar cells. On the other hand, the curves obtained at large

negative bias voltage can be considered to be exempt of any collection problem, and thus exhibiting only the effect related to carrier generation. Fig. 4.6 shows quantum efficiency curves measured at three bias voltage values on a good $\mu\text{c-Si:H}$ solar cell deposited on an optimized textured back reflector [Terrazzoni-Daudrix 2003].

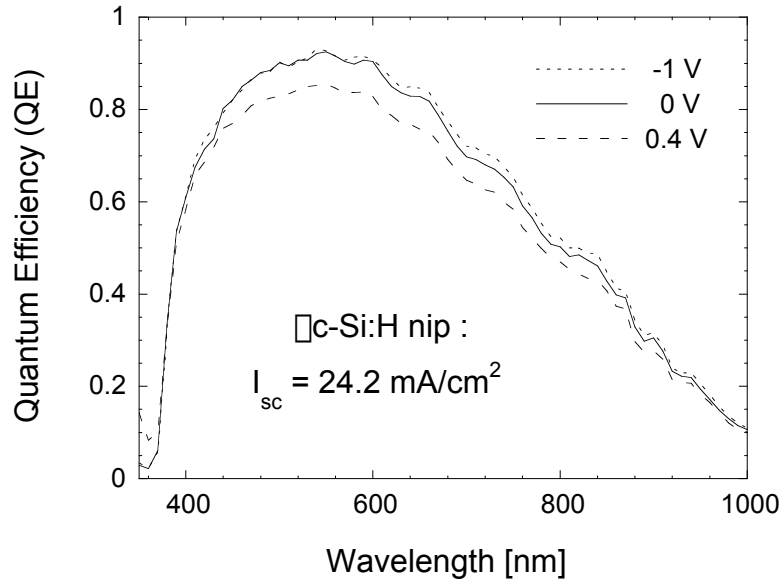


Fig. 4.6: Quantum efficiency measured at different bias voltages of a good $n-i-p$ $\mu\text{c-Si:H}$ solar cell deposited on a textured back reflector. Both collection and light trapping are excellent.

The QE curve of a $\mu\text{c-Si:H}$ solar cell still has positive value until wavelengths (λ) of about 1000 nm. On the other hand, the QE curve of an $a\text{-Si:H}$ cell is already low at $\lambda = 700$ nm and is equal to zero at $\lambda = 800$ nm. This reflects the difference of absorption for these two materials.

The short-circuit current I_{sc} is obtained by multiplying the QE curve at 0 V by the AM1.5 solar spectrum, and then integrating the resulting curve over the wavelengths. The values of I_{sc} given in this work have been obtained with this method.

4.3.2.2. Values obtained for the SC series of $n-i-p$ solar cells

Fig. 4.7 shows the evolution of I_{sc} as a function of SC for the two SC series of $n-i-p$ solar cells. On the whole, the I_{sc} -values obtained for the series deposited on sputtered ZnO are higher than those obtained for the series deposited on ZnO CVD. Except for SC = 7%, the variation of I_{sc} with SC is very small (for both series). Note that these series of solar cells do not contain any back reflector and the light-trapping has not been optimized.

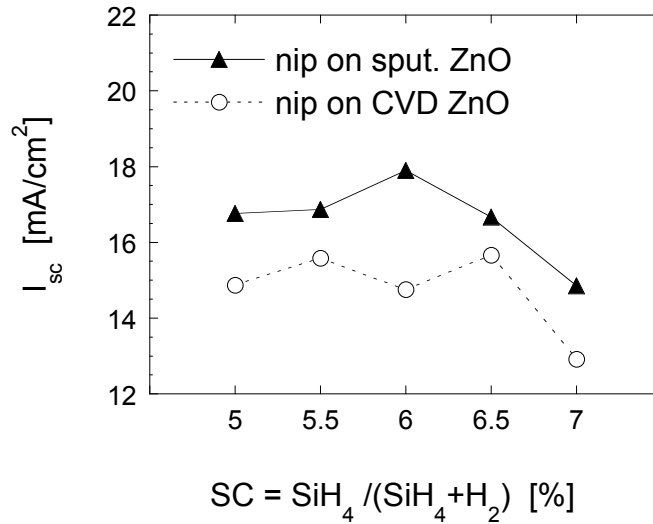


Fig. 4.7: Short-circuit current (I_{sc}) as a function of the silane concentration (SC) at which the *i*-layer has been deposited for two series of *n-i-p* solar cells deposited on sputtered ZnO (filled triangles) and on CVD ZnO (open circles).

4.4. Micro-Raman spectroscopy as a probing tool for entire solar cells

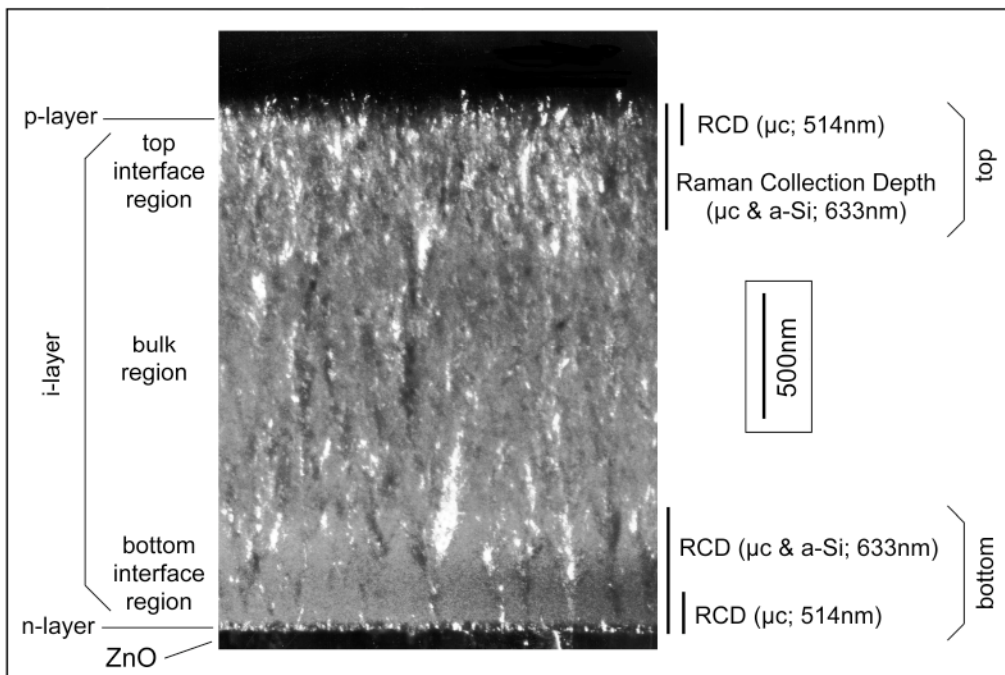


Fig. 4.8: TEM dark-field micrograph of a *nip* solar cell deposited with SC = 7% on sputtered ZnO (black layer at the bottom of the micrograph). The Raman Collection Depths (RCD, see § 2.5.1) probed with our bifacial depth-dependent micro-Raman technique in *a-Si:H* and \square c-Si:H, at 514 nm and 633 nm, respectively, are indicated. Note that the value of RCD at 514 nm for *a-Si:H* (not shown) is about a third of the corresponding value for \square c-Si:H.

The technique of micro-Raman spectroscopy has been extensively discussed in Chapter 2. In this work we are performing bifacial depth-dependent micro-Raman measurements (see § 2.5), i.e. we are illuminating the sample first from the top and then from the bottom side, in each case with two different source-light wavelengths (514 nm and 633 nm). In the case of solar cells, bifacial measurements make it possible to evaluate selectively the n-i or the p-i interface region (see Fig. 4.8), in both n-i-p and p-i-n configurations.

The collected Raman signal in the micro-Raman experiment is scattered from the Raman Collection Depth (RCD, see § 2.5.1), ranging from about 50 nm (within a-Si:H) to about 150 nm (within \square c-Si:H), for the 514 nm excitation light. For the 633 nm excitation light, RCD equals about 500 nm within all the silicon-based layers. These depths are schematically illustrated on Fig. 4.8. For the strongly-absorbed excitation light (514 nm), the collected Raman contribution arises from the doped layer (\square 20-30 nm) and from the first tens of nanometres of the i-layer. On the other hand, for the weakly-absorbed excitation light (633 nm), the collected Raman contribution arises from up to 500 nm below the illuminated surface and, thus, contains an important contribution from the i-layer, much larger than the contribution from the doped layer.

4.4.1. Influence of the additional layers on Raman spectra

Compared to single intrinsic \square c-Si:H layers deposited, for example, on glass substrate (as studied in the previous chapter), a complete \square c-Si:H solar cell includes additional layers (see § 4.2.1): the TCO (Transparent Conductive Oxide) layers and the doped layers.

4.4.1.1. Transparent Conductive Oxide (TCO)

The TCO layers are necessary as front and back contacts, in order to collect the carriers generated inside the solar cells. As a TCO layer is by definition transparent, it will not hinder, in Raman measurements, the excitation beam to reach the sample and the Raman signal to be collected. Fig. 4.9 shows the Raman spectra measured at 514 nm from the glass-side of two intrinsic layers deposited in the same run (i.e. with the same deposition conditions): one is directly deposited on glass and the second is deposited on glass coated with sputtered ZnO. Thus, in the second case, the path of the light in Raman experiment goes through the glass and the sputtered ZnO.

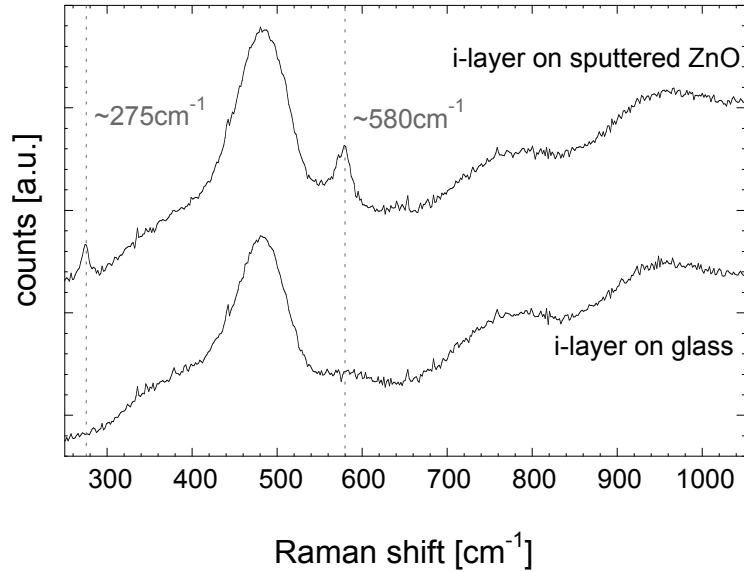


Fig. 4.9: Glass-side Raman spectra of a \square c-Si:H layer deposited at $SC = 6.5\%$ on "raw" glass (lower spectrum) and on glass coated with about $2 \mu\text{m}$ of sputtered ZnO (upper spectrum). The spectra are shifted for clarity.

Fig. 4.9 shows that the presence of sputtered ZnO gives rise to two Raman contributions at about 275 cm^{-1} and 580 cm^{-1} . However, these contributions are quite weak and even quasi nonexistent on spectra measured with 633 nm excitation light. Moreover, their positions are sufficiently distant from those of contributions due to silicon, so that they do not hinder or distort the deconvolution and interpretation of the spectra. On the other hand, no Raman contribution (other than the silicon-related peaks) was observed when measuring samples containing a CVD ZnO layer or a SnO_2 layer. **Consequently, for Raman measurements, the presence of a TCO layer in the light path is not a problem for measuring and for interpreting Raman spectra.**

Series of intrinsic layers have been deposited simultaneously on glass and on glass coated with sputtered ZnO. Bifacial Raman measurement performed on both series showed that the crystallinity is similar for the layers deposited on glass and for those deposited on sputtered ZnO. The flat sputtered ZnO, thus, does not appear to influence the \square c-Si:H growth differently than bare glass.

4.4.1.2. $\langle n \rangle$ and $\langle p \rangle$ doped layers

In a thin film silicon solar cell, the role of the doped layers (p-doped layer and n-doped layer) is mainly to create an internal field throughout the intrinsic (i-) layer. This electrical field enables to separate the free electrons and holes generated within the i-layer. Including this essential role, the doped layers must fulfil three conditions:

- They must have good **optical** properties, i.e. they must be as transparent as possible.
- They must have good **electrical** properties, i.e. they must be as conductive as possible (or, in others words, have a low value of the activation energy). A poor conduction of the doped layers would mainly results in a low value of the FF.
- The first deposited doped layer (i.e. the p-layer for p-i-n configuration and the n-layer for n-i-p configuration) must help the **nucleation** of the subsequent intrinsic layer in the case of μ c-Si:H solar cells.

Highly microcrystalline doped layers are ideally suited for the three requirements listed above. Indeed, compared to a-Si:H doped layers, μ c-Si:H doped layers have a lower absorption coefficient for wavelengths shorter than ~ 600 nm and a higher conductivity [Flückiger 1995]. Moreover, a highly microcrystalline doped layer will obviously be beneficial for the microcrystalline growth of the following intrinsic layer. Actually, highly crystalline p-doped layers have been shown to be beneficial for the electrical performance of μ c-Si:H p-i-n-type solar cells [Vallat-Sauvain 2001]. Indeed, such highly microcrystalline layers act as seeding layers for the microcrystalline growth of the i-layer; in fact these p-layers can also, in general, be very effectively doped, and their Fermi level pushed down to near the valence bandedge, this being a necessary condition for obtaining high values of the built-in voltage and, thus, also a pre-condition for obtaining a high value of the open-circuit voltage (V_{oc}).

The consequence on Raman spectra of the presence of such highly microcrystalline doped layers in μ c-Si:H solar cells is twofold:

- The first, direct effect is due to the presence itself of the highly microcrystalline layer in the volume probed by the Raman experiment. Indeed, especially in the case of the strongly-absorbed excitation light (514 nm), where RCD = 50 - 150 nm, a large part of the collected Raman contribution arises from the doped layer (~ 20 -30 nm). On the other hand, for the weakly-absorbed excitation light (633 nm), RCD = 500 nm and the collected Raman signal contains an important contribution from the i-layer, that is in this case much larger than the contribution from the doped layer.
- The second, indirect effect is due to the effect of the first-deposited highly microcrystalline doped layer on the growth of the subsequent intrinsic layer. Indeed, an intrinsic layer grown on a highly microcrystalline doped layer will have a higher crystallinity as compared to an intrinsic layer deposited (with the same deposition conditions) directly on the ZnO substrate (see Fig. 4.10). Indeed, Fig. 4.10 (right) shows that, in the case of a complete solar cell, the nucleation of the μ c-Si:H phase of the i-layer occurs directly on top of the highly microcrystalline n-doped layer. On the other hand, in the case of a single μ c-Si:H layer deposited with the same experimental

conditions (see Fig. 4.10, left), the nucleation of the \square c-Si:H occurs only within an amorphous incubation layer.

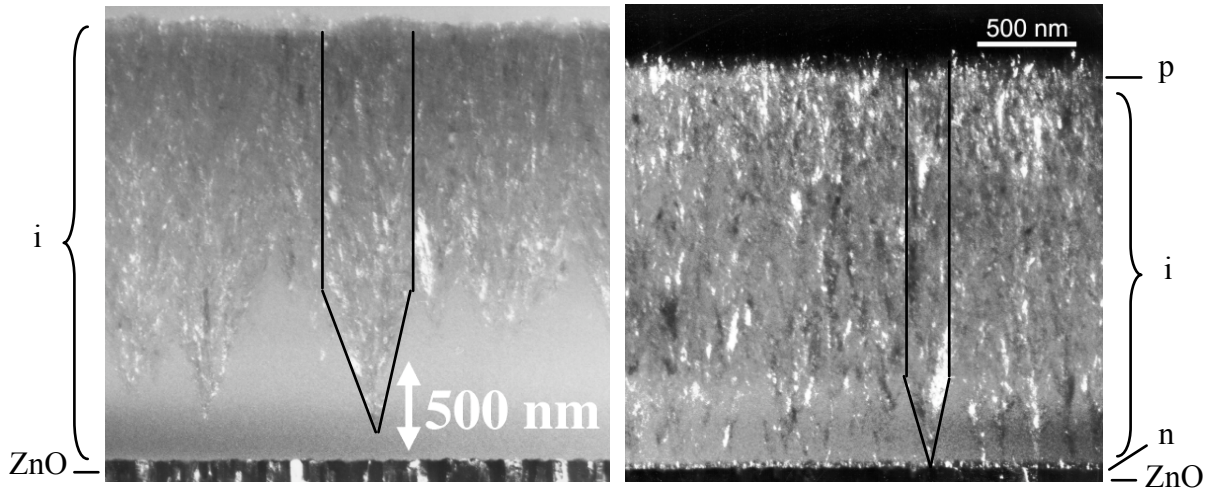


Fig. 4.10: TEM dark-field micrographs of a \square c-Si:H layer (left) and of a \square c-Si:H nip solar cell (right). In both cases, the intrinsic layer has been deposited with $SC = 7\%$, and the substrate is sputtered ZnO (black layer at the bottom of the micrographs). In the right micrograph, the n-doped highly microcrystalline layer appears as a thin dotted layer (≈ 30 nm thick) at the top of the ZnO. In both micrographs, at the bottom of the i-layer, amorphous silicon appears uniformly grey, between conical/pencil-like conglomerates of nanocrystals. The latter is the microcrystalline silicon phase. After the coalescence of the microcrystalline cones, the amorphous material is no longer observable in these medium-resolution micrographs. In the right micrograph, the p-layer (at the top of the picture) is not distinguishable from the i-layer due to local epitaxial growth.

The two aforementioned effects of the presence of highly microcrystalline doped layers in \square c-Si:H solar cells will result in an increase of the Raman measured crystallinity (compared to that of a single \square c-Si:H intrinsic layer deposited with the same experimental conditions). This is especially visible on the glass-side Raman measurements (see Fig. 4.11), as the presence of the first-deposited highly microcrystalline doped layer influences the nucleation of the i-layer. Moreover, the bottom of a \square c-Si:H i-layer grown with constant deposition parameters is always less crystalline than the top. Thus, the difference between the crystallinity of the doped layer and that of the intrinsic layer is more pronounced on the bottom side (i.e. the beginning of growth) than on the top (end of growth) of the cell (see Fig. 4.10).

The difference between the top crystallinity of a complete solar cell and that of a single intrinsic layer is mainly due to the influence of the first-deposited doped layer on the i-layer growth (as explained above) rather than to the presence of the last-deposited doped layer. Indeed, as can be seen in Fig. 4.12 for the case of a n-i-p solar cell, no interface can be observed between the i-layer and the p-layer. We can thus conclude that the p-layer has grown

epitaxially on the underlying i-layer. This is at least valid for relatively thick cells where the crystallinity of the top of the i-layer has reach a reasonably high value.

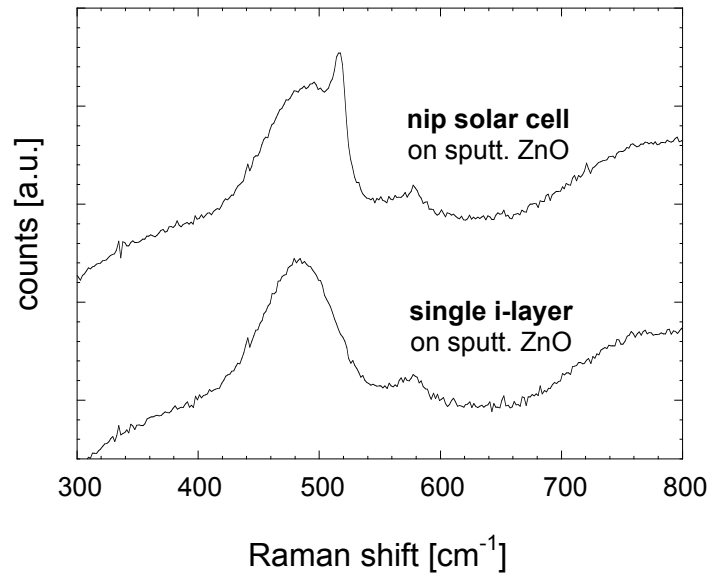


Fig. 4.11: Glass-side Raman spectra measured with an excitation light of 514 nm of a \square c-Si:H single layer (bottom) and of a \square c-Si:H n-i-p solar cell (top). In both cases, the intrinsic layer has been deposited with SC = 7%, and the substrate is sputtered ZnO (see Fig. 4.10).

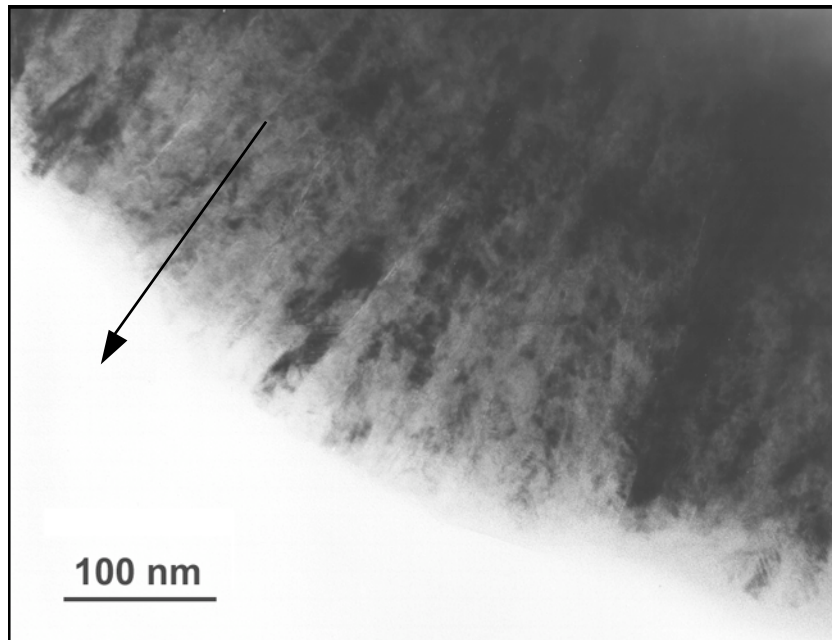


Fig. 4.12: TEM bright-field micrograph of the upper part of a \square c-Si:H n-i-p solar cell, including the last-deposited part of the i-layer and the p-doped layer (the arrow shows the growth direction). The long microcrystalline columns are well distinguishable; **no interface is visible between the i-layer and the p-doped layer**. The solar cell was deposited with SC = 5% on sputtered ZnO.

4.4.2. Raman crystallinity of solar cells versus silane concentration

The two series of n-i-p type solar cells, where the silane concentration (SC) used for the deposition of the intrinsic layer has been varied (see § 4.2.3), have been analysed by the bifacial depth-dependent micro-Raman technique (see Chapter 2). The results obtained for the SC series of cells deposited on sputtered ZnO are presented in § 4.4.2.1, whereas the results obtained for the series deposited on LP-CVD ZnO will be discussed in § 4.4.2.2. Then, in § 4.4.2.3, we will compare the crystallinities of both series and discussed the cause of the differences. In § 4.4.2.4, we will introduce the notion of "average crystallinity" and compare it with Raman crystallinity measured on cross-section samples. A comparison with such values obtained for single i-layers will also be made.

Note that the average nanocrystal sizes (evaluated from XRD spectra) of these series of solar cells (comprised within the range 20 ± 4 nm [Bailat 2003]) are similar to those obtained for the SC series of single layers (for SC between 5% and 6.5%).

4.4.2.1. Series of n-i-p solar cells deposited on (flat) sputtered ZnO

Fig. 4.13 shows for each cell of the SC series of n-i-p cells deposited on flat sputtered ZnO the four Raman spectra obtained with the bifacial depth-dependent technique.

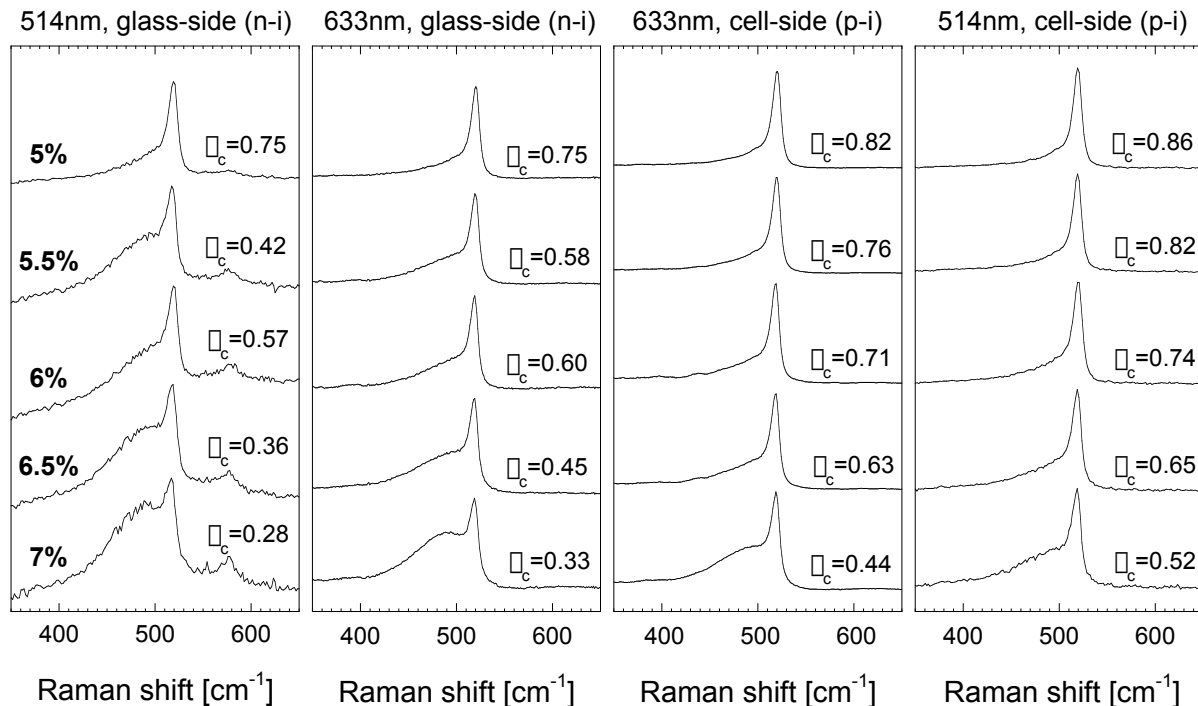


Fig. 4.13: Bifacial depth-dependent Raman spectra of the SC series of n-i-p cells deposited on (flat) **sputtered ZnO**. The spectra are normalized to similar height and shifted for clarity. The corresponding Raman crystallinity factors (\bar{c}) are indicated (see also Fig. 4.15).

As can be qualitatively seen from Fig. 4.13, the ratio of crystalline peak intensity to amorphous peak intensity continuously decreases from the top (cell-side) to the bottom (glass-side) of the device. Moreover, for each of the four kinds of spectra, this crystalline to amorphous peak ratio decreases as SC increases. These behaviours correspond well to device microstructure, as seen in the TEM micrographs of the cells deposited at SC = 5% and SC = 7% (see Fig. 4.14), where the top of the cell is microcrystalline, whilst a more or less important amorphous fraction is observed at the bottom of the device, depending on the high or low value of SC, respectively.

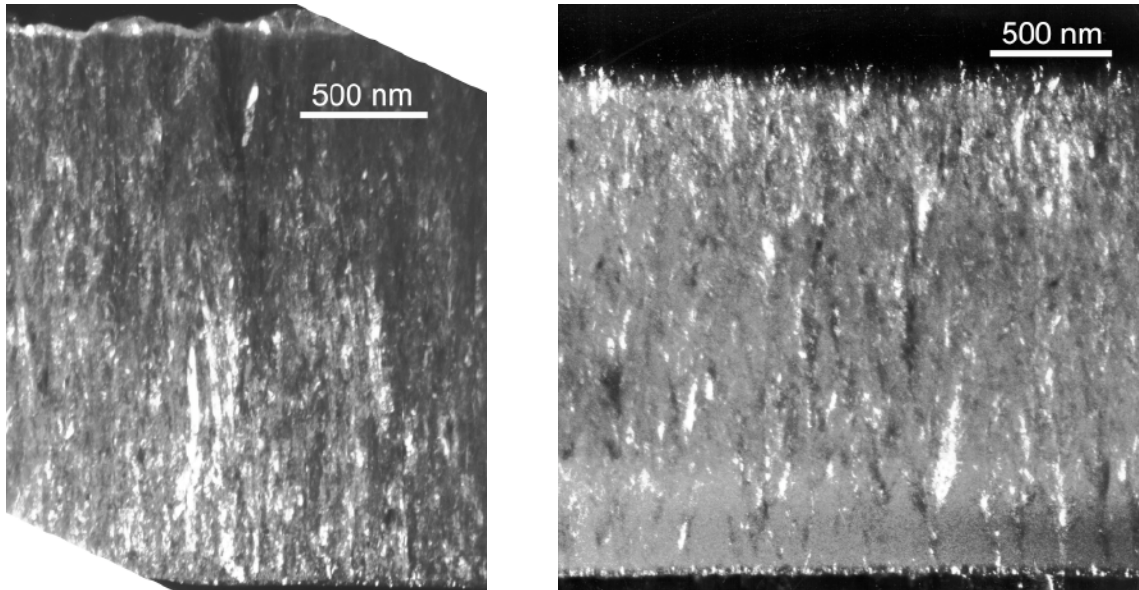


Fig. 4.14: TEM dark-field micrographs of the n - i - p cells deposited at SC = 5% (left) and SC = 7% (right) on flat sputtered ZnO, taken from [Bailat 2003].

From each of these Raman spectra, the Raman crystallinity factor χ_c has been calculated by evaluating the scattered intensities assigned to amorphous and crystalline silicon (see § 2.6). The values of χ_c corresponding to each spectrum are also given in Fig. 4.13. Whereas some Raman spectra could appear, at first sight, to be rather similar (see e.g. the top-side (p - i) spectra measured with 514 nm of all cells), the χ_c -values reveal however some significant differences. Fig. 4.15 shows the evolution of the four different values of χ_c evaluated from the deconvoluted bifacial depth-dependent Raman spectra measured on the SC series of cells deposited on sputtered ZnO, as a function of the silane concentration used for the deposition of the i -layer. The comparison of Fig. 4.13 and Fig. 4.15 shows the advantage of the deconvolution of the Raman spectra to extract quantitative information. Indeed, Fig. 4.15 exhibiting the quantitative value χ_c is much more effective to analyse a series of solar cells or to compare individual samples than the raw Raman spectra of Fig. 4.13.

We observe in Fig. 4.15 that the different χ_c -values vary smoothly with the silane concentration of the i -layer. The slight discontinuity at 5.5%, especially visible in the n - i

514nm curve, is due to a problem in the deposition sequence. Involuntarily, a reduction of power was applied to the plasma at the beginning of the i-layer growth (10 W instead of 30 W during the first time 10 minutes over a total of 52 minutes). As known for VHF PE-CVD deposition of silicon thin films, a lower applied power leads to a more amorphous material [Torres 1997]. This is exactly what happens here: the bottom (n-i) $\bar{\mu}_c$ -values at SC = 5.5% are lower as compared to the general tendency observed over the whole SC range. This results from a beginning of growth of the i-layer more amorphous (as the highly microcrystalline n-layer is not concerned). However, this discontinuity (i.e. lower crystallinity value compared to the general trend) disappears as growth proceeds. Indeed, the top (p-i) $\bar{\mu}_c$ -value at SC = 5.5% fits in the general trend and is no longer lower than the general trend. This example illustrates the usefulness of bifacial Raman measurements to detect technological defect or error within a series of samples.

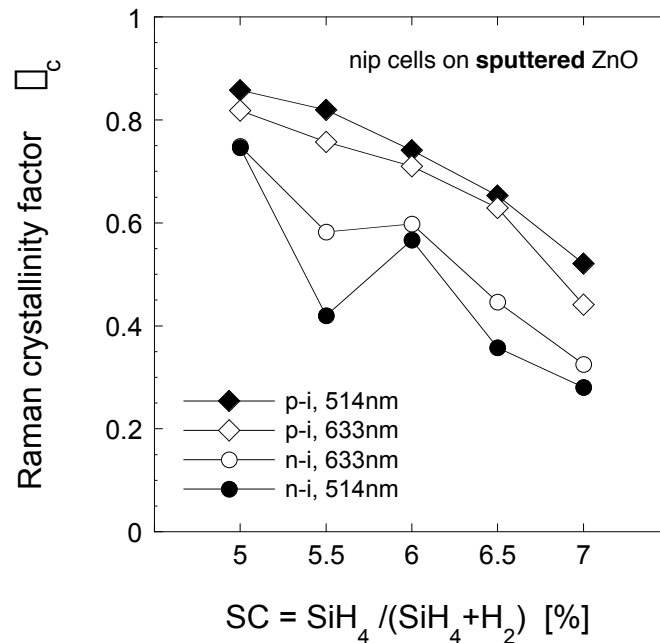


Fig. 4.15: Raman crystallinity factors ($\bar{\mu}_c$) for the SC series of n-i-p solar cells (thickness $\approx 2 \mu\text{m}$) deposited on **sputtered ZnO**. $\bar{\mu}_c$ is evaluated from the bifacial depth-dependant Raman spectra of Fig. 4.13.

In Fig. 4.15, the four curves are almost parallel: they show a continuous decrease of $\bar{\mu}_c$ with increasing SC as used for i-layer deposition. The values of $\bar{\mu}_c$ shown here are representative of the bottom n-i (less crystalline) and top p-i (more crystalline) parts of the cells; thereby, the crystallinity within the cell appears to increase as growth proceeds. This is confirmed by the TEM cross-section micrographs (Fig. 4.14) of the n-i-p cells where the i-layer was deposited at SC = 5% and SC = 7%. On these micrographs, conical conglomerates of nanocrystals start to grow from the n-layer onwards. Before the cones coalesce, they are embedded in amorphous silicon (especially visible on the TEM micrograph of the SC = 7%

cell). The top of the devices seems to exhibit, in these low-resolution micrographs, a good crystallinity, with little (or no) amorphous phase. However, the Raman measurements reveal that the top crystallinity of the cell deposited at SC = 7% is about 50% whereas that of the cell deposited at SC = 5% exceeds 80%. In such case, the quantitative information brought by Raman measurements is therefore more significant than the qualitative information supplied by TEM micrographs

In Fig. 4.15, the four values of χ_c are ordered in the same sequence for each SC: the χ_c -value for bottom illumination at 514 nm, which probes the beginning of growth (n-i part) of the solar cells, exhibits the lowest measured value as compared to the three other χ_c -values; after that follows the χ_c -value for bottom illumination at 633 nm, where we probe the same volume as in the preceding case plus a substantial (lower) part of the bulk of the i-layer, whose crystallinity increases with growth; afterwards, the χ_c -value for top illumination at 633 nm probes about the same volume as in the previous case but this time from the top, giving thus rise to superior values; finally, the χ_c -value for top illumination at 514 nm is the highest, although it is still very close to the preceding χ_c -value; indeed we are now probing the "last" part of the i-layer plus the p-layer that has grown epitaxially on the underlying i-layer.

4.4.2.2. Series of n-i-p solar cells deposited on (rough) LP-CVD ZnO

The n-i-p solar cells analysed in the preceding section have been "co-deposited" on rough CVD ZnO (i.e. the silicon layers have been deposited simultaneously on both sputtered ZnO and CVD ZnO substrates). Fig. 4.16 shows for each cell of the SC series deposited on rough CVD ZnO the four Raman spectra obtained with the bifacial depth-dependent technique. Similarly to what has been observed in Fig. 4.13 for the series deposited on sputtered ZnO, the qualitative analyse of Fig. 4.16 shows that the ratio of crystalline peak intensity to amorphous peak intensity continuously decreases from the top to the bottom of the device, as well as with increasing SC. However, compared to Fig. 4.13, the Raman spectra of Fig. 4.16 are on the whole more amorphous.

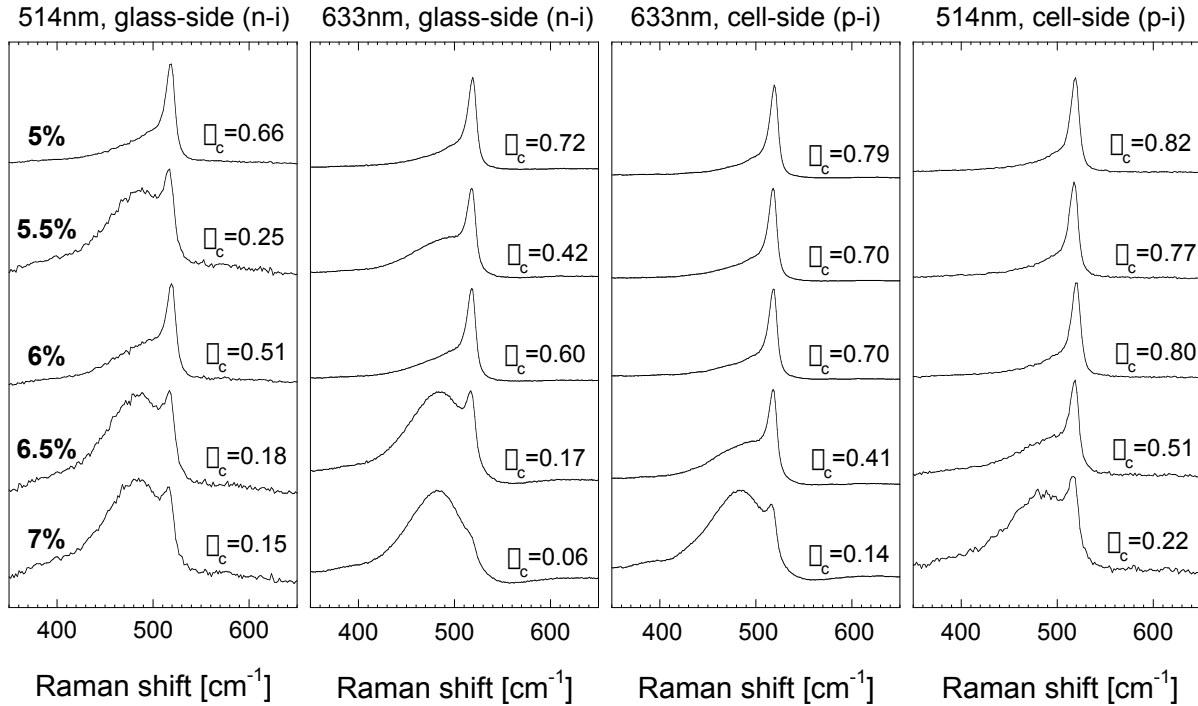


Fig. 4.16: Bifacial depth-dependent Raman spectra of the SC series of *n-i-p* cells deposited on (rough) **CVD ZnO**. The spectra are normalized to similar height and shifted for clarity. The corresponding Raman crystallinity factors (\square_c) are indicated (see also Fig. 4.16).

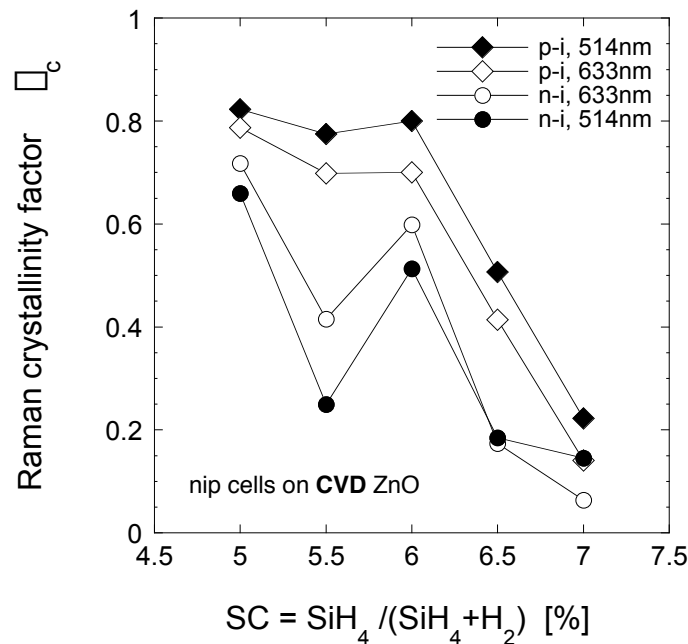


Fig. 4.17: Raman crystallinity factors (\square_c) for the SC series of *n-i-p* solar cells (thickness $\approx 2 \mu\text{m}$) deposited on **CVD ZnO**. \square_c is evaluated from the bifacial depth-dependant Raman spectra of Fig. 4.16.

Fig. 4.17 shows the more explicit representation of the four different values of \square_c evaluated from the Raman spectra of Fig. 4.16, as a function of the silane concentration used

for the deposition of the i-layer. Compared to the evolution of χ_c for the series deposited on sputtered ZnO (Fig. 4.15), a similar trend is observed for the series deposited on LP-CVD ZnO (Fig. 4.17), but with lower χ_c -values at SC = 6.5% and 7%. Moreover, the discontinuity at SC = 5.5% is more apparent and also visible in the top-side (p-i) curves. This conveys the bigger difficulty to obtain microcrystalline material in these conditions (CVD ZnO substrate, lower applied power).

The microstructure of solar cells deposited on CVD ZnO is presented in Fig. 4.18, that displays the TEM micrographs of the cells deposited at SC = 5% and SC = 6.5%.

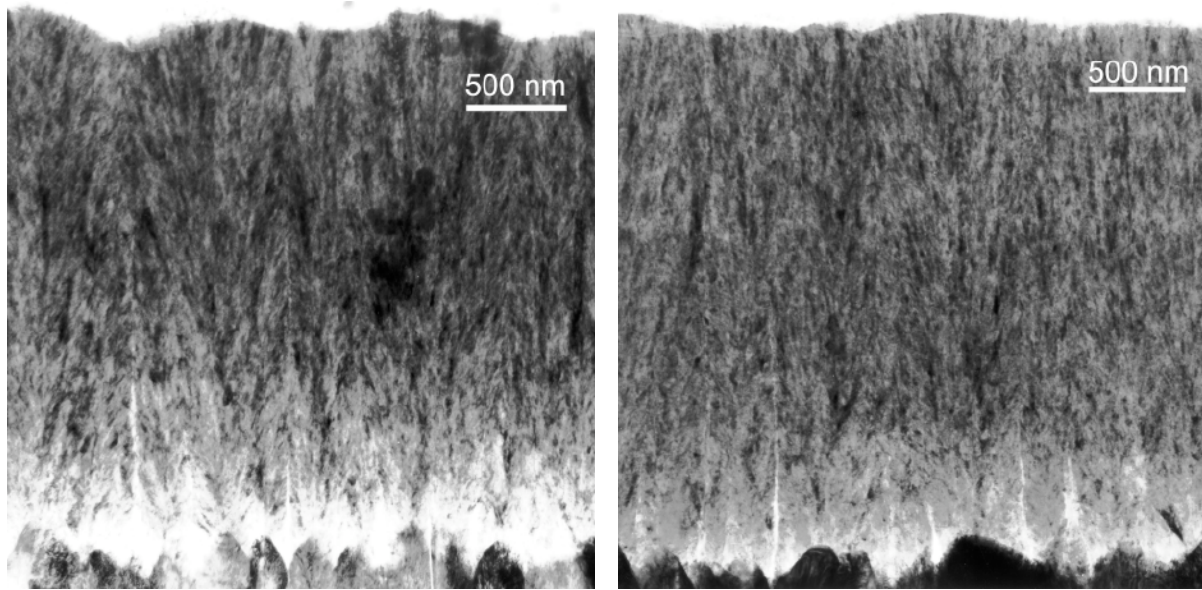


Fig. 4.18: TEM bright-field micrographs of the n-i-p cells deposited at SC = 5% (left) and SC = 6.5% (right) on rough CVD ZnO, taken from [Bailat 2003].

In Fig. 4.17, the four curves are generally more spread than in Fig. 4.15: this is representative of a rather strong gradient of crystallinity along the growth axis. In particular, the two top-side (p-i) curves are more spread in Fig. 4.17 than in Fig. 4.15. This means that, in the case of cells deposited on sputtered ZnO, the top crystallinity has already reached a roughly "saturated" value of the crystallinity after about 1.5 μ m of growth, whereas for the cells deposited on CVD ZnO, the evolution of the top crystallinity within the last 500 nm of growth is more significant.

In Fig. 4.17, similarly to Fig. 4.15, the four values of χ_c are ordered in the same sequence for each SC, except for SC = 7% (and maybe also SC = 6.5%). This crossing of the two curves of the glass-side (n-i) χ_c -values for high values of SC is also well illustrated in Fig. 4.16: at SC = 7%, the glass-side Raman spectrum measured at 514 nm contains a more important crystalline contribution than the glass-side spectrum measured at 633 nm. Then, the crystalline contribution increases again in the top-side spectra. One can conclude that the growth of the i-layer within $RCD^{633\text{ nm}}$ (Raman collection depth, see § 2.5.1), i.e. about

500 nm, results in amorphous material. The crystalline contribution observed in the glass-side spectra is only due to the microcrystalline n-doped layer. Indeed, the contribution of the doped layer to the total Raman signal is more important in the spectrum measured at 514 nm than in the one measured at 633 nm (as in this last case, a bigger part of the i-layer is probed). On the other hand, for each wavelength, the top-side spectrum measured at a given wavelength present a more important crystalline contribution than the glass-side spectrum measured with the same wavelength. Assuming that the crystallinity of the p-layer is the same as that of the n-layer, this would mean that, after the first 500 nm of growth, the i-layer become slightly microcrystalline.

4.4.2.3. Comparison of both SC series

In the two previous sections, we have seen that the evolution of the Raman crystallinity factor \square_c with SC for the two series of n-i-p cells co-deposited on sputtered ZnO and on CVD ZnO shows the same general trends. However, some differences remain. Fig. 4.19 enables to compare on a same plot the \square_c -values obtained for both series at a given wavelength.

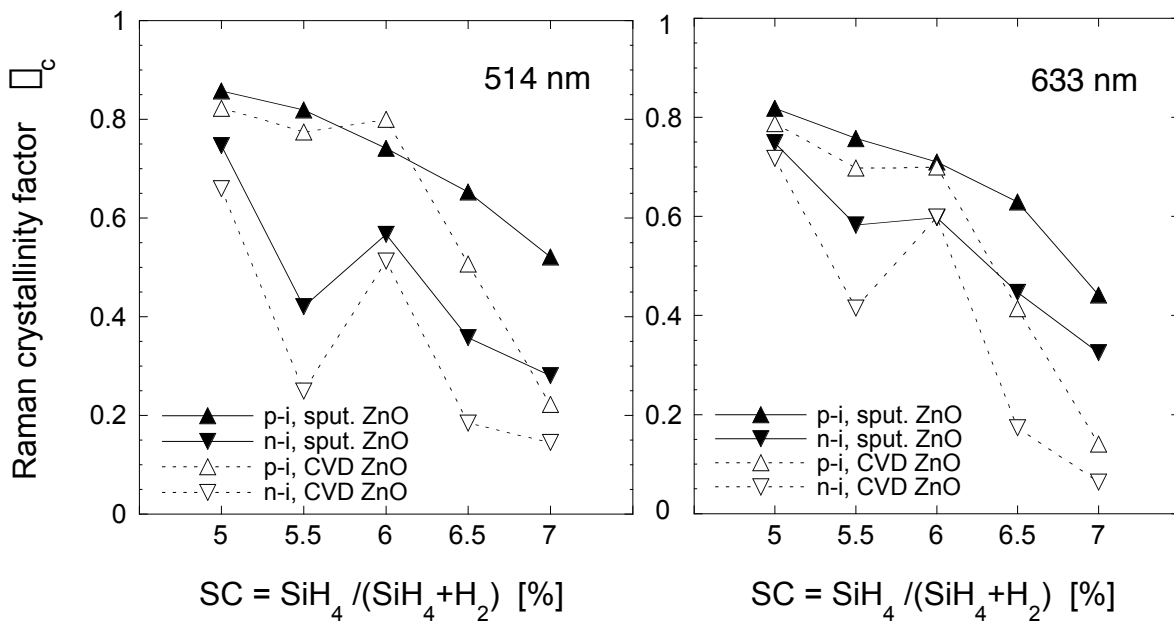


Fig. 4.19: Comparison of the effect of the substrate type on the Raman crystallinity factor \square_c measured on SC series of n-i-p solar cells. The cells have been deposited on sputtered ZnO (full symbols) and on CVD ZnO (open symbols). \square_c has been measured from the top- and bottom-side with 514 nm (left) and 633 nm (right) excitation lights. Data are the same as those represented in Fig. 4.15 and Fig. 4.17.

On the whole, one can say that \square_c is higher for the cells deposited on sputtered ZnO than for those deposited on CVD ZnO. This difference is enhanced for the SC values of 5.5, 6.5 and 7%, where the beginning of growth of the cell has a low crystallinity (i.e. \square_c^{n-i} at 514 nm

is lower than 0.4). One should note here that layers deposited at $\text{SC} = 6.5$ and 7% present lateral inhomogeneities. Consequently, although deposited simultaneously for a given value of SC , the i-layer of the cell on sputtered ZnO and that of the cell on CVD ZnO may have grown slightly differently.

The lower crystallinities observed for solar cells deposited on CVD ZnO can be explained by the difference of growth of the n-doped layer on both substrates. Indeed, Bailat et al. [Bailat 2002] have demonstrated that the role of the substrate on which a $\mu\text{c-Si:H}$ layer is grown is very critical. On sputtered ZnO, the $\mu\text{c-Si:H}$ n-layer is homogeneously constituted of closely-packed crystallites of diameter similar to the layer thickness (see Fig. 4.14). On the other hand, the quality of the n-layer deposited on CVD ZnO is not as good (see Fig. 4.20): the n-layer appears quite disordered, its thickness is not homogeneous and the n-i interface is not clearly defined. Moreover, cracks or voids occur at the bottom of the valley formed between the ZnO pyramids. One can thus easily understand that the i-layer growth will be more microcrystalline on sputtered ZnO covered with highly microcrystalline n-layer (that plays the role of nucleation layer) substrate than in the case of CVD ZnO covered with a poorly microcrystalline n-layer.

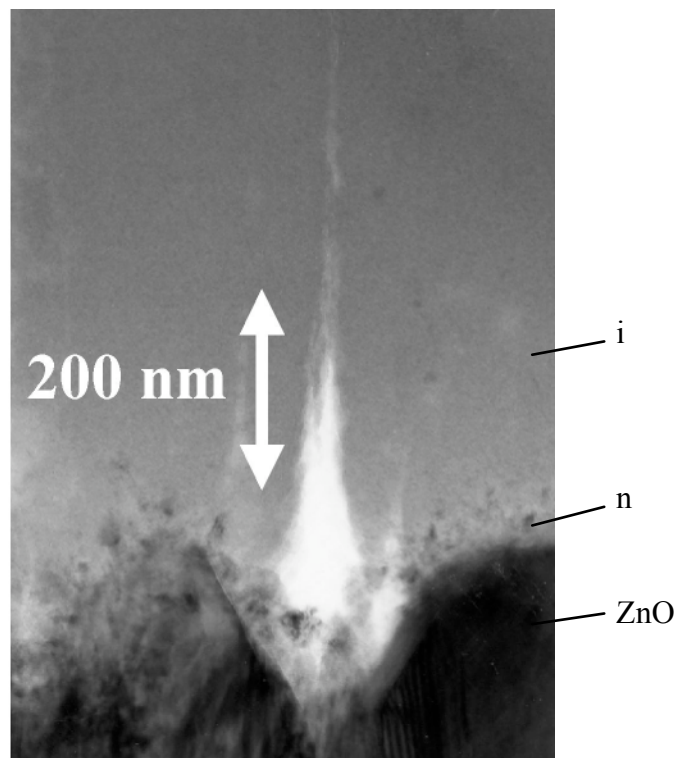


Fig. 4.20: TEM bright field micrograph of the ZnO-n-i interface of a solar cell deposited on LP-CVD ZnO, taken from [Bailat 2002]. ZnO pyramids are at the bottom of the picture. Note the disordered grainy contrast of the n-layer. Crack/void at the bottom of ZnO valley appears bright.

Bailat et al. [Bailat 2002] have shown that, for a given SC, the linear nuclei density n_d (defined as the average number of nuclei per micrometer) is slightly higher for the cells deposited on sputtered ZnO than for those on CVD ZnO. Fig. 4.21 shows that the Raman crystallinity of the beginning of growth of the solar cells (i.e. the bottom $n-i$ interface region crystallinity probed with 514 nm excitation light) increases linearly as the nuclei density increases. This dependence is observed for both SC series. However, for a given n_d , the crystallinity of the cells deposited on sputtered ZnO is slightly higher than that of cells deposited on CVD ZnO. This difference can be explained as well by the lower crystallinity of the n -layer deposited on CVD ZnO.

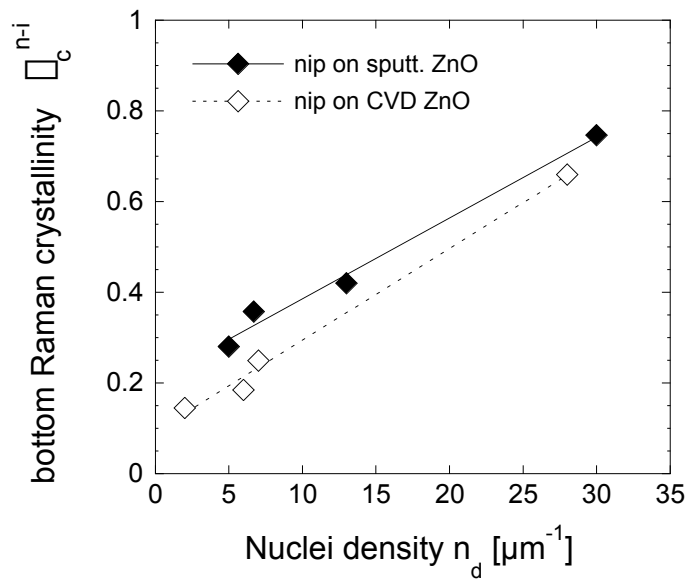


Fig. 4.21: Linear relation between the bottom Raman crystallinity χ_c^{n-i} measured at 514 nm and the nuclei density n_d (from [Bailat 2003]) measured on the two SC series of $n-i-p$ solar cells.

Actually, the whole microstructure of the solar cells deposited on sputtered ZnO differs quite a lot from that of the cells deposited on CVD ZnO, as illustrated in Fig. 4.14 and Fig. 4.18, respectively, and detailed in [Bailat 2003]. Due to the growth of the silicon crystallites in the direction perpendicular to the local surface of the substrate [Dubail 2000, Nasuno 2001a], the cells deposited on rough CVD ZnO present a fan-like growth of the conglomerates, resulting in cauliflower-like grains emerging at the surface. Their diameter is approximately twice that of the conglomerates emerging at the surface after pencil-like growth on sputtered ZnO substrate ($\sim 1 \mu m$ compared to $\sim 600 nm$ [Bailat 2003]).

For these two series of $n-i-p$ solar cells analysed here, the deposition conditions of the i -layer have been kept constant during the whole i -layer growth. In such cases, the bottom χ_c^{n-i} value at 514 nm induces the three other χ_c -values, the evolution of the latter depending on the value of SC. As first example, one can compare the χ_c -values got for the cell deposited at

SC = 7% on sputtered ZnO (see Fig. 4.15) with those got for the cell deposited at SC = 5.5% on CVD ZnO (Fig. 4.17), both having a thickness of about 2 μ m. In both cases, \square_c^{n-i} at 514 nm is about 25%. However, in the case of SC = 7%, the highest top crystallinity (i.e. the \square_c^{p-i} -value at 514 nm) equals about 50%, whereas in the case of SC = 5.5, \square_c^{p-i} at 514 nm equals nearly 80%. Indeed the growth of the i-layer deposited at SC = 7% (i.e. conditions near the \square c-Si:H/a-Si:H transition) evolve slowly towards highly microcrystalline material. On the other hand, the growth of the i-layer deposited at SC = 5.5% (i.e. conditions more favourable to microcrystalline growth) evolve rapidly towards highly microcrystalline material. As second example, one can compare two cells with their i-layer deposited with the same value of SC, but the bottom crystallinity of which being different (due to different substrates). This case corresponds to the cells deposited at SC = 6.5, where \square_c^{n-i} at 514 nm equals 18% for the sputtered ZnO substrate and 36% for the CVD ZnO substrate. After the 2 μ m of growth, the value of the top \square_c^{p-i} at 514 nm equals 51% in the first case and 65% in the second case (see Fig. 4.19, left). Here, similar deposition conditions for the i-layer lead to keep the initial difference in crystallinity while growth proceeds (at least as long as the top crystallinity does not saturate).

4.4.2.4. Average Raman crystallinity

From the Raman crystallinity factors measured on the top-side and on the bottom-side of a sample, one can define the **algebraic average \square_c^A of the Raman crystallinity factors**, calculated as follows for each wavelength:

$$\square_c^A = (\square_c^{top} + \square_c^{bottom}) / 2, \quad (\text{equ. 4.3})$$

with $\square_c^{top} = \square_c^{p-i}$ and $\square_c^{bottom} = \square_c^{n-i}$ for the n-i-p cells, and $\square_c^{top} = \square_c^{n-i}$ and $\square_c^{bottom} = \square_c^{p-i}$ for the p-i-n cells. \square_c^A calculated for both wavelengths is represented in Fig. 4.22 for each SC series.

In Fig. 4.22 is also represented the Raman crystallinity factor \square_c^{TEM} evaluated from spectra measured on cross-section samples of some solar cells of these SC series (these cross-section samples are those used for TEM observation). A microscope objective of 50 \times has been used for these measurements, in order to get a focused spot of about 2 μ m (see Chapter 2). Thus, if the spot is centred on the TEM sample, about the whole thickness of the sample is probed. \square_c^{TEM} evaluated in such conditions corresponds to the average crystallinity over the whole thickness of the sample. However, the lateral resolution of the measurement set-up is of the order of the micron and is adjusted manually. Therefore it is quite difficult to be sure to centre the spot in the middle of the sample. From Fig. 4.22, one sees that, in most cases, the value of \square_c^{TEM} corresponds to that of \square_c^{top} rather than to that of \square_c^A . The discrepancy between \square_c^{TEM} and the others \square_c -values at SC = 7% can be attributed to the lateral

inhomogeneities observed for these samples. Indeed, the Raman measurements presented in Fig. 4.22 have been performed on "real" solar cells, whereas TEM samples have been fabricated with another non-structured part of the total deposited area.

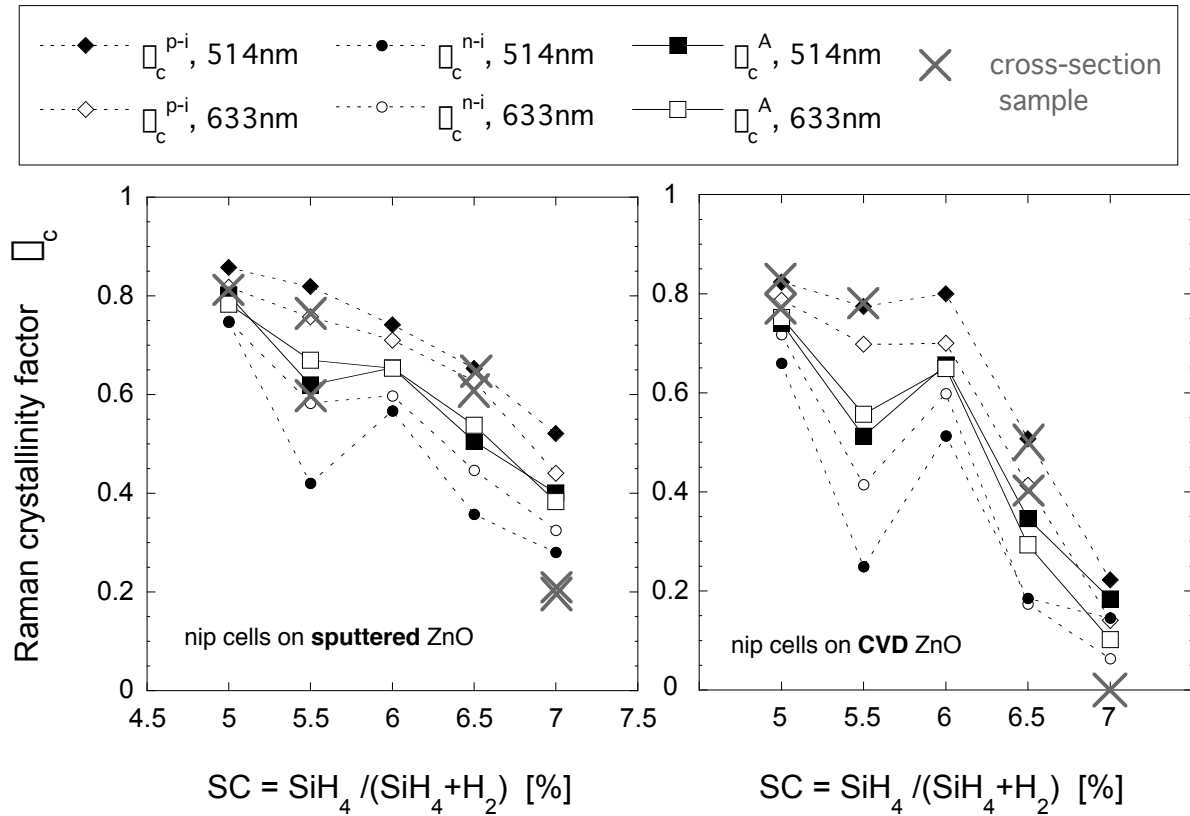


Fig. 4.22: Raman crystallinity factors ($\bar{\rho}_c$) for the SC series of $n-i-p$ solar cells deposited on sputtered ZnO (left) and on CVD ZnO (right). Same data as is Fig. 4.15 and Fig. 4.17, plus average values of the top and bottom crystallinities (equ. 4.3) for both 514 nm and 633 nm wavelength and $\bar{\rho}_c$ evaluated from Raman spectra measured on the cross-section TEM samples.

Surprisingly, for each series of cells, $\bar{\rho}_c^A$ vs. SC is similar for both wavelengths (see Fig. 4.22). This fact is partially explained by the presence of the highly microcrystalline n -doped layer that increases the measured Raman crystallinity factor at 514 nm evaluated within RCD of the bottom of the solar cell. Indeed, $\bar{\rho}_c^A$ evaluated in a similar way for the SC series of single i -layers (analysed in § 3.4) does not lead to similar $\bar{\rho}_c^A$ values for both wavelengths (see Fig. 4.23). In that case, for each value of SC, $\bar{\rho}_c^A$ at 514 nm is lower than $\bar{\rho}_c^A$ at 633 nm and $\bar{\rho}_c^A$ at 514 nm is actually similar to $\bar{\rho}_c^{bottom}$ at 633 nm.

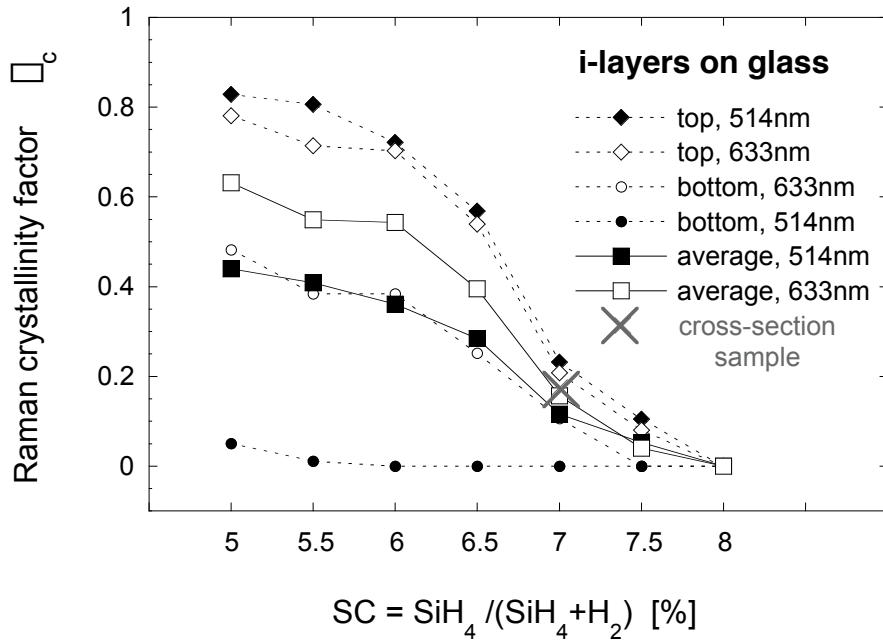


Fig. 4.23: Raman crystallinity factors (\bar{c}) for the SC series of *i*-layers deposited on glass. Same data as is Fig. 3.15, plus average values of the top and bottom crystallinities \bar{c}^A (equ. 4.3) for both 514 nm (filled squares) and 633 nm (open squares) wavelengths, and \bar{c} evaluated from Raman spectra measured on cross-section TEM samples.

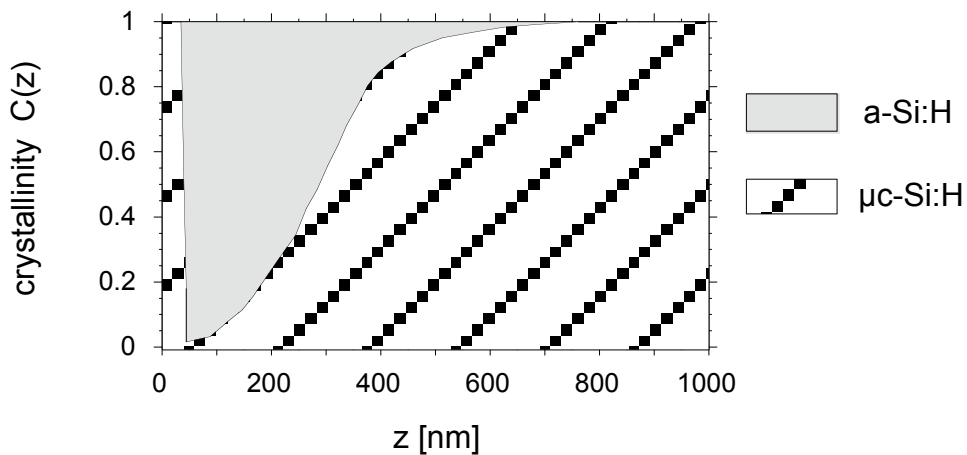


Fig. 4.24: Schematic crystallinity profile of the first micron of the growth of a *n-i-p* or *p-i-n* solar cell. The growth axis is given by the parameter z ; $z = 0$ corresponds to the TCO/doped-layer interface. In the first tens of nanometres, the material consist of $\mu\text{c-Si:H}$ phase (doped layer). Then, the material consist of *a-Si:H* and $\mu\text{c-Si:H}$ phases until the microcrystalline cones have coalesced.

This different behaviour regarding \bar{c}^A between entire cells and single *i*-layers is due to the presence of the first-deposited $\mu\text{c-Si:H}$ doped layer in the case of cells. Its influence on Raman spectra has already been discussed in § 4.4.1.2. Fig. 4.24 shows a schematic crystallinity profile of the beginning of growth (bottom-side) of a solar cell as a function of

the thickness of the silicon layers ($z = 0$ corresponding to the top surface of the substrate on which the silicon layers will be grown). This profile is similar to that obtained for single i-layers (see Fig. 2.17), except that in the case of solar cells, the first tens of nanometres are \square c-Si:H, due to the doped layer. One can thus clearly understand how this layer influences the \square -values measured on the bottom-side of solar cells. The difference in the value of \square that should be obtained by changing the probing depth (i.e. the wavelength) if only the i-layer would be probed is consequently weakened.

4.4.3. Discussion

We have seen that the "four bifacial depth-dependent \square representation" of a sample (single-layer or entire solar cell), as given in Fig. 3.15, Fig. 4.15 and Fig. 4.17 for SC series, gives a good information about the sample microstructure (provided the total thickness is also known). It is especially useful for the comparison of various samples. One has to keep in mind that in such Raman measurements, we always probe contributions that add up from the silicon layer surface until the Raman collection depth (see Chapter 2). The probing beam is perpendicular to the substrate (i.e. parallel to the growth axis) and obviously encounters first the doped layer and then the i-layer. In such configuration, it is, thus, impossible for the probing beam to go through the doped layer without it influencing the resulting spectrum and \square -value. As previously discussed, in the case of bottom-side measurements, the presence of the doped-layer makes the measurement of the thickness non-uniformity (as observed on TEM micrographs) less apparent. Thus, the microstructure of the i-layer itself is not precisely characterised. On the other hand, such measurements taking into account the complete doped layer / i-layer interface region should correlate with the electrical performances of solar cells. Indeed, with the motivation to find a link between electrical and microstructural properties of solar cells, it is certainly best if the doped-layer quality is also incorporated into the parameter evaluating the microstructure.

4.5. Raman crystallinity versus electrical performances

The main interest of characterising the microstructure of \square c-Si:H solar cells with the help of Raman measurements is to enable a direct comparison with the electrical properties of the solar cells. Indeed, Raman spectra were measured on the very same cell where electrical measurements were also performed. Actually, for each cell plate, a precise test cell was first chosen on the basis of its electrical performances (as a representative amongst the whole plate), and then bifacial depth-dependent Raman measurements were performed on this selected test cell. This systematic way to characterise the electrical and microstructural properties of a solar cell at the very same position enables to get rid of any discrepancy due to lateral inhomogeneity that may have occurred during deposition of the silicon layers.

In order to establish a relationship between the Raman crystallinity and the electrical performances of the solar cells, the results of the measurements on both n-i-p and p-i-n type solar cells devices will be discussed below. For this purpose, some other n-i-p type solar cells as well as several p-i-n type solar cells were electrically characterised and were also evaluated with the same specific technique of Raman spectroscopy (as described above for the two SC series of n-i-p cells).

4.5.1. Dependence of the open-circuit voltage on the microstructure

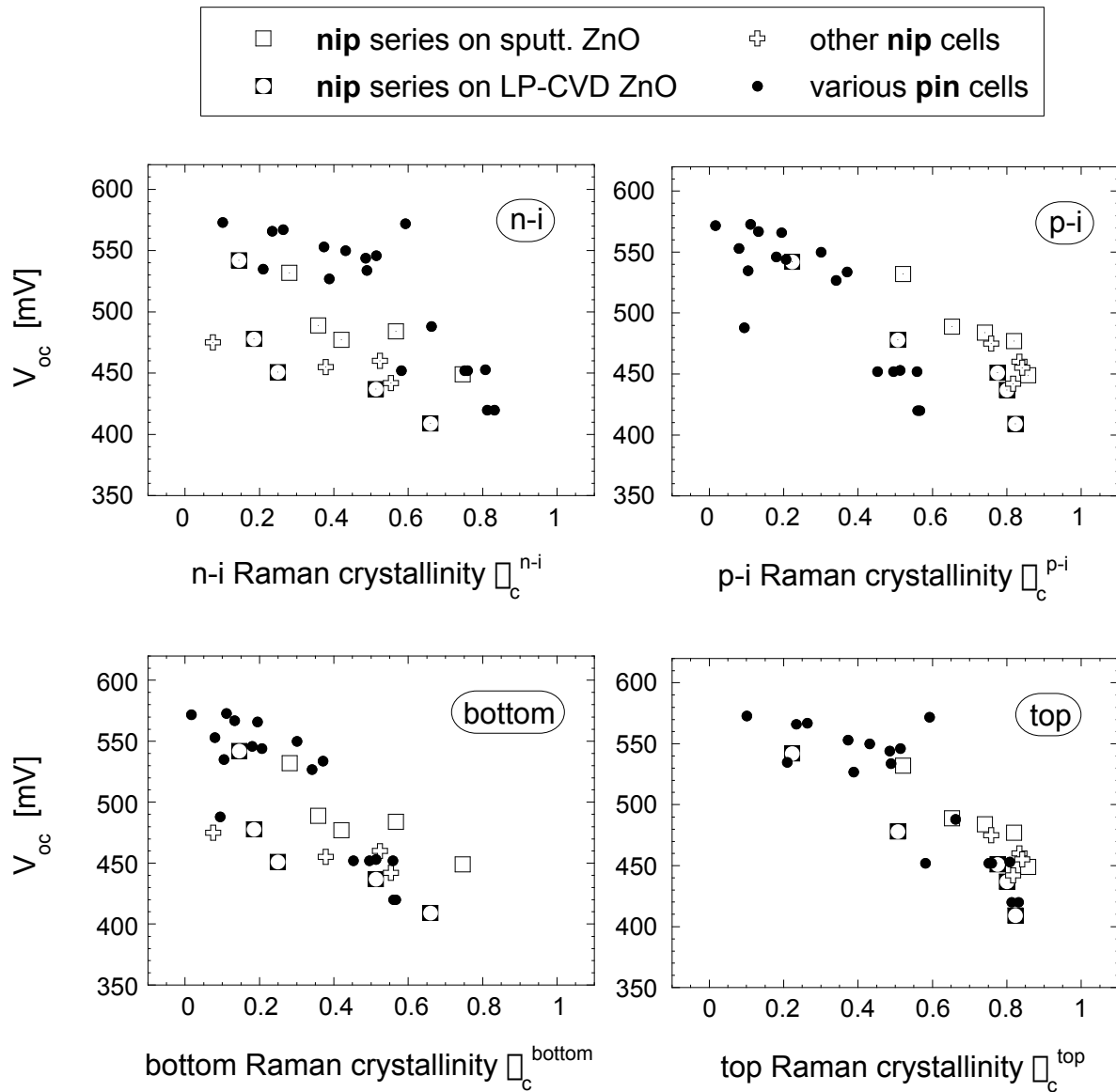


Fig. 4.25: Dependence of V_{oc} on the n-i, p-i, bottom and top Raman crystallinity factors (\square) measured at 514 nm for the two SC series of n-i-p solar cells, as well as for various other n-i-p and p-i-n solar cells. Note that \square_c^{bottom} probes the beginning of growth and \square_c^{top} probes the end of growth of the sample. For the n-i-p cells $\square_c^{n-i} = \square_c^{bottom}$ and $\square_c^{p-i} = \square_c^{top}$, whereas for the p-i-n cells $\square_c^{n-i} = \square_c^{top}$ and $\square_c^{p-i} = \square_c^{bottom}$.

An effect that is generally observed [Klein 2002, Meier 2001] when one increases the silane concentration (SC) used for the deposition of the i-layer is a steady increase in the open-circuit voltage (V_{oc}), followed by an abrupt change close to the \square c-Si:H/a-Si:H transition [Roschek 2002]. The evolution of V_{oc} with SC for the two n-i-p series deposited on sputtered ZnO and on CVD ZnO has been given in § 4.3.1.2.

In order to establish the relationship between the Raman crystallinity factors \square_c and the V_{oc} of solar cells, the results of the measurements on both n-i-p and p-i-n type solar cells have been taken into account. Note that for p-i-n solar cells, contrary to n-i-p cells, the top-side Raman measurements probe the n-i interface region (i.e. end of growth) whereas the bottom or glass-side Raman measurements probe the p-i interface region (i.e. beginning of growth). Fig. 4.25 shows the dependence of V_{oc} on the n-i and p-i \square_c -values measured at 514 nm for the two SC series of n-i-p solar cells, as well as for various other n-i-p and p-i-n \square c-Si:H solar cells. Fig. 4.25 also shows, for the same data, the representation of V_{oc} as a function of the bottom and top \square_c -values at 514 nm.

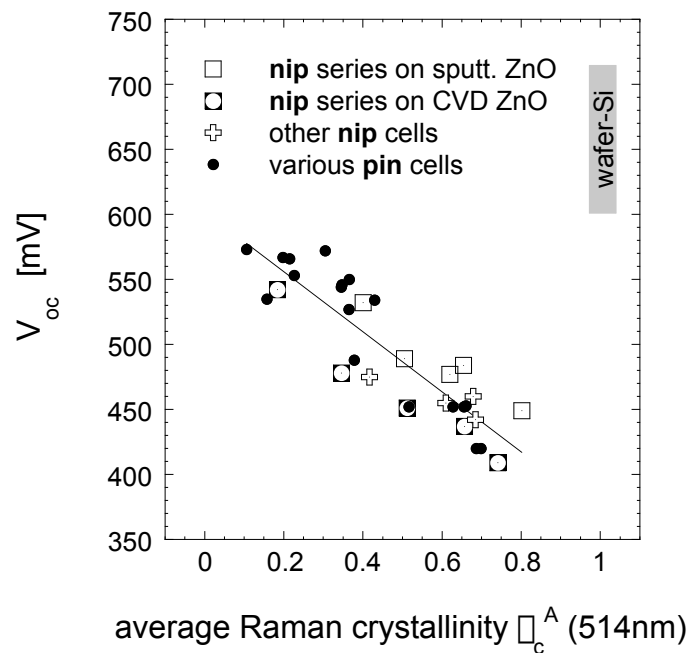


Fig. 4.26: Dependence of the open-circuit voltage (V_{oc}) of the two SC series of n-i-p solar cells, as well as of various other n-i-p and p-i-n solar cells on the average Raman crystallinity factor (\square_c^A) (equ. 4.3) measured at 514 nm. The full line is a linear fit to all data using the Least Squared Error method where the Linear Correlation Coefficient is $R = 0.89$. The range for V_{oc} -values obtained for wafer-based crystalline silicon solar cells is indicated; note that for amorphous silicon cells, V_{oc} -values reach a maximum of about 900-950 mV, for current, state-of-the-art solar cell technology.

When only one of the Raman crystallinity factors measured either on one side or on the other is used as monitor of the device material, a decrease in V_{oc} is observed with an increase

in \square (Fig. 4.25). However, the scattering of the data set is quite pronounced, especially for the V_{oc} vs. \square^{n-i} case.

On the other hand, when the average Raman crystallinity \square^A (equ. 4.3) at 514 nm is used as monitor of the device material, a linear dependence of V_{oc} with \square^A is observed (Fig. 4.26). This **linear increase observed for V_{oc} as \square^A decreases** is indeed seen for both individual n-i-p series (Fig. 4.26 open squares and open circles/squares), as well as for the complete set of solar cells studied here, including a large variety of solar cells deposited in the n-i-p and p-i-n configurations in our laboratory, as also shown in Fig. 4.26 (all symbols).

In its definition and in the way \square^A is measured, this quantity includes the contributions of both doped and undoped layer crystallinities. Highly crystalline p-doped layers have been shown to be beneficial for the electrical performance (FF and V_{oc}) of p-i-n type solar cells [Vallat-Sauvain 2001]. Indeed, such highly microcrystalline layers act as seeding layers for the microcrystalline growth of the i-layer; in fact these layers can also, in general, be very effectively doped, and their Fermi level pushed down to near the valence band edge, this being a necessary condition for obtaining high values of the built-in voltage and, thus, also a pre-condition for obtaining a high value of V_{oc} . In our case, the Raman probe beam always enters first the doped microcrystalline p- or n-layer. Then, it probes the initial region of the i-layer, starting with the interface region and then penetrating more or less deeply into the bulk of the i-layer (see Fig. 4.8), depending upon whether we use the 633 nm probe beam or the 514 nm probe beam. As both n-i and p-i junctions contribute to the building of the internal field in open-circuit conditions, \square^A takes indeed into account both contributions by averaging the crystallinity of the top and bottom parts of the cell.

From our measurements (see Fig. 4.25 and Fig. 4.26) it becomes clear that **the interface regions have a major influence on the value of V_{oc} and that it is the average crystallinity (factor) of the two interface regions that counts**. Fig. 4.26 has shown that the more amorphous-like these two interface regions are, on an average, the higher V_{oc} becomes. However, this statement must be moderated. Indeed, one knows that highly microcrystalline doped layers are beneficial for the electrical performances of solar cells. Therefore, the dependency of Fig. 4.26 should be better interpreted as: an increase of amorphous material incorporated in the interface regions of the i-layer tends to increase the V_{oc} . The two SC series enable to compare the effect of the quality of the first deposited doped layer. Fig. 4.27 shows V_{oc} as a function of \square^A at 514 nm for the two SC series of n-i-p solar cells.

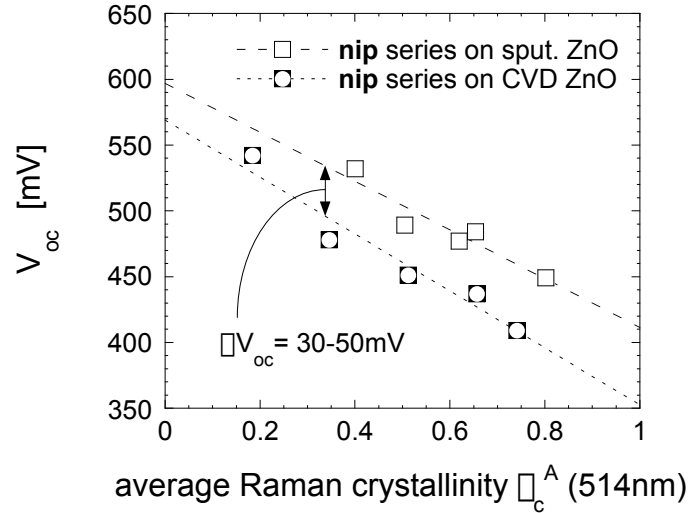


Fig. 4.27: Linear dependence of the V_{oc} on χ_c^A (equ. 4.3) measured at 514 nm for the two SC series of n-i-p solar cells. The full lines are linear fits to each series. The only difference between the two series is the TCO substrate that is, in one case (square), flat sputtered ZnO (on which a highly microcrystalline n-layer is obtained) and, in the other case (circles/squares), rough CVD ZnO (on which a n-layer of poor crystalline quality is obtained, see Fig. 4.20).

One can notice that, for equal values of χ_c^A , the cells deposited on sputtered ZnO have a V_{oc} -value about 30 to 50 mV higher than the V_{oc} of the cells deposited on CVD ZnO. We have seen in § 4.4.2 that, for similar deposition conditions, the growth of the n-layer is highly microcrystalline on sputtered ZnO, whereas it is of poor quality on CVD ZnO. Thus, except the geometrical aspect (sputtered ZnO is flat whereas CVD ZnO is rough), the only difference between these two series of n-i-p cells is the n-layer quality (or crystallinity) and its influence on the i-layer growth (i.e. for a given SC-value, the cells deposited on CVD ZnO are less crystalline). For both series, V_{oc} as a function of the crystallinity (Fig. 4.27) results in a linear dependence with about the same slope. However, the curve for the series on sputtered ZnO is shifted to higher V_{oc} -values as compared to the curve for the series on CVD ZnO. In other words, one can say that, for a given χ_c^A -value, the V_{oc} will be higher if the n-layer has a good crystallinity (and, consequently, the i-layer has a lower crystallinity than the cell on CVD ZnO that has the same χ_c^A -value). On the other hand, for a given (or wanted) V_{oc} -value, the cells on CVD ZnO "require" lower χ_c^A -values. However, these cells have lower FF -values as compared to those deposited on sputtered ZnO (see Fig. 4.5). This is in accordance with [Vallat-Sauvain 2001] where, in the case of p-i-n cells, highly microcrystalline p-doped layer has been shown to lead to higher values of FF and V_{oc} than partially microcrystalline p-doped layer. One can, thus, think that the scattering of ± 30 -40 mV around the linear fit of Fig. 4.26 (especially observed for the various p-i-n cells) could be due to the difference in the crystallinity of the first deposited doped layer. On the other hand, the slopes of the linear fits to all data (Fig. 4.26) and to the specific n-i-p series (Fig. 4.27) correspond about to an

increase in the V_{oc} of 20 mV for a decrease of the average crystallinity of both interfaces of $\square_c^A = 0.1$. It is interesting to notice that, if one considers a difference in crystallinity of one ($\square_c^A = 1$), the difference in V_{oc} calculated with the relation above results in $\square V_{oc} \approx 200$ mV, what is about the difference of V_{oc} between state-of-the-art a-Si:H and c-Si solar cells.

In the case of the two SC series of n-i-p solar cells, the i-layer has been grown with constant deposition parameters. For such cells, \square_c^{top} , although probing the top interface region, actually comprises information of the bulk \square c-Si:H material, as the top crystallinity corresponds to the "result" of the evolution of growth of the i-layer plus the p-layer. On the other hand, \square_c^{bottom} does not contain any indirect information, as it probes the bottom interface region that is the beginning of growth of the silicon-based layers.

We have to note that, even if the V_{oc} is plotted as a function of \square_c^A at 633 nm (instead of 514 nm), the trend observed in Fig. 4.26 is practically conserved. Indeed, as the bulk of the i-layer also changes in crystallinity if SC is changed, we are, however, not yet able to say whether it is solely the interface region, as other experiments have suggested [Meier 1998a], or also the bulk material, as proposed in [Vetterl 2001b], that determine V_{oc} . To be able to discriminate here between these two hypotheses, further experiments would be necessary.

4.5.2. Dependence of the short-circuit current on the microstructure

Similarly to what has been presented in the preceding section for the open-circuit voltage, one can try to relate the short-circuit current I_{sc} with the crystallinity. Fig. 4.28 shows I_{sc} as a function of the average Raman crystallinity \square_c^A measured at 514 nm (Fig. 4.28, left) and as a function of the top Raman crystallinity \square_c^{top} measured at 633 nm (Fig. 4.28, right), for the same samples as those used in the preceding analysis about the V_{oc} . In both representations, one sees a **general tendency for I_{sc} to increase as the crystallinity increases**. \square_c^A at 514 nm (as used in the left representation of Fig. 4.28) is the algebraic average Raman crystallinity factor as a function of which the V_{oc} was best related (see 4.5.1), whereas \square_c^{top} at 633 nm (as used in the right representation of Fig. 4.28) should best represent the "bulk" crystallinity of the device. One could expect that I_{sc} relates rather to the latter (\square_c^{top} at 633 nm). However, the data are quite scattered in both representations. Each kind of solar cell (both n-i-p series and the p-i-n cells) seems to follow its own trend (as highlighted by the different linear fits). The slope of the dependency of I_{sc} with \square_c is larger for the p-i-n cells than for both series of n-i-p cells. This should, however, not be directly dependent on the solar cell configuration (i.e. n-i-p or p-i-n type). Indeed, none of the n-i-p solar cells studied here have any back reflector, whereas most of the p-i-n cells have a reflector. This explains at least partly the higher current exhibited by the p-i-n cells.

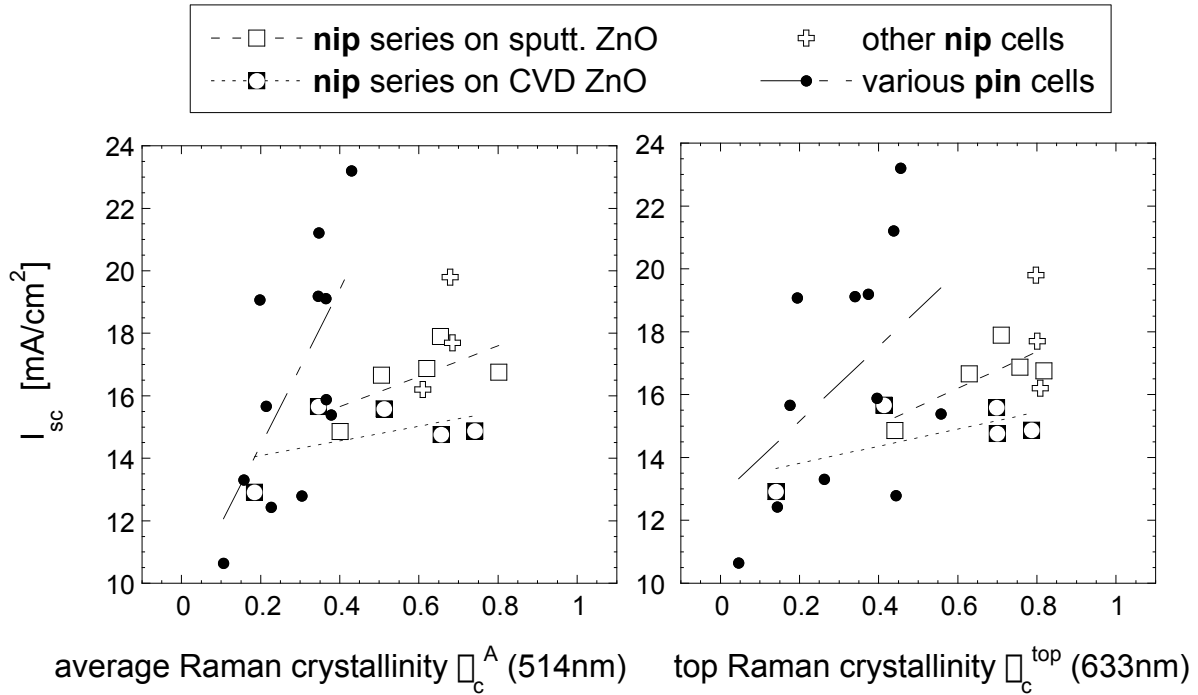


Fig. 4.28: Dependence of the short-circuit current (I_{sc}) of the two SC series of $n-i-p$ solar cells as well as of various other $n-i-p$ and $p-i-n$ \square c-Si:H solar cells on the average Raman crystallinity factor (equ. 4.3) measured at 514 nm (left) and on the top Raman crystallinity measured at 633 nm (right). The lines are individual linear fit to each SC series of $n-i-p$ cells and to all the $p-i-n$ solar cells.

One has to keep in mind that the current furnished by a solar cell depends upon various factors. Besides the nature itself (i.e. mainly the absorption) of the i -layer, the current of a solar cell depends on the thickness of the i -layer and on the efficiency of the light trapping that increases the light path inside the device and, thus, increases the probability for the photons to be absorbed. The collection efficiency over the i -layer (related to the i -layer quality and to the field created by the doped layers) also affects I_{sc} . The light trapping is enhanced by rough TCO layers, by the introduction of a back reflector, and, to a lesser extent, by the roughness of the i -layer itself. If one would like to find a more precise relation between the I_{sc} and the crystallinity than that observed in Fig. 4.28, one should, thus, analyse solar cells having the same i -layer thickness, the same (ideally flat) TCO layers, and no reflector.

4.5.3. Discussion

4.5.3.1. Dependence of the open-circuit voltage

One can calculate the theoretical upper limit for V_{oc} as a function of the material bandgap E_g in the case of an ideal $p-n$ junction [Shah 1995b]. Such limits calculated from Kiess theory [Kiess 1995] and from Green semi-empirical values [Green 1998] are given in Fig. 4.29. For

both cases, V_{oc} linearly increases as E_g increases, with a similar slope.

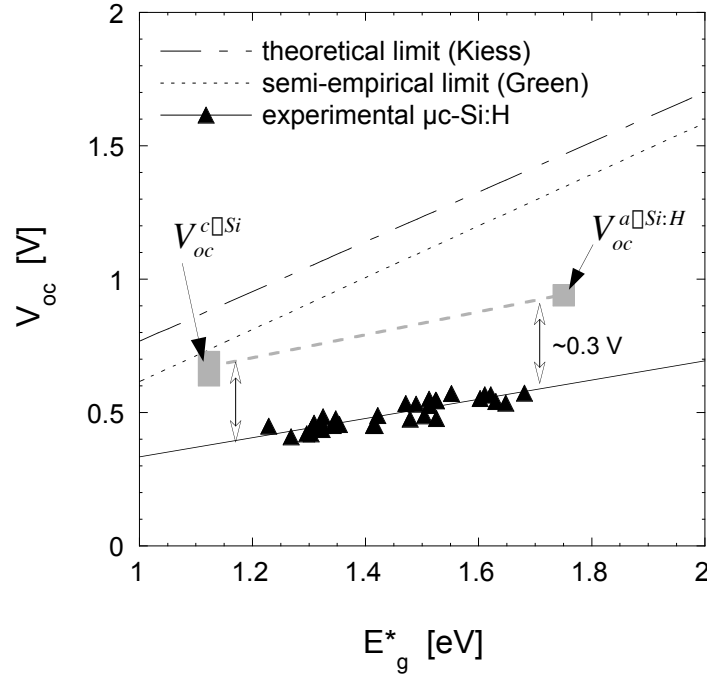


Fig. 4.29: Upper limits (black dotted lines) calculated from Kies theory [Kies 1995] and from Green semi-empirical values [Green 1998] for the open-circuit voltage (V_{oc}) as a function of the material bandgap E_g ; V_{oc} -values measured on various p-i-n and n-i-p solar cells (triangles), as well as a linear fit, as a function of the weighted bandgap E_g^* as defined in (equ. 4.4) (the data are those of Fig. 4.26). Typical V_{oc} -values obtained for state-of-the-art c-Si and a-Si:H solar cells are also given (grey rectangles). Note that the linear fit to the experimental data obtained on \square c-Si:H solar cells (full black line) has roughly the same slope as the line linking the typical V_{oc} -values for c-Si and a-Si:H solar cells (grey dotted line).

In Fig. 4.26, we demonstrated an experimental linear relation between the V_{oc} -values and the crystallinity of various \square c-Si:H solar cells. In order to compare our experimental results with such theoretical limits, we have calculated an "equivalent average bandgap" value E_g^* , by somewhat arbitrarily weighting the bandgap of a-Si:H ($E_g^{a-Si:H} = 1.75$ eV) and c-Si ($E_g^{c-Si} = 1.1$ eV) materials with the Raman crystallinity measured on the samples:

$$E_g^* = \square_c^A \cdot 1.1 + (1 - \square_c^A) \cdot 1.75 . \quad (\text{equ. 4.4})$$

In Fig. 4.29 is also represented the evolution of the V_{oc} -values measured on the solar cells as a function of E_g^* calculated from (equ. 4.4), for all the p-i-n and n-i-p solar cells analysed in this work (see data of Fig. 4.26). Since V_{oc} vs. \square_c^A gave rise to a linear relation (Fig. 4.26), it is not astonishing that V_{oc} vs. $E_g^*(\square_c^A)$ also results in a linear dependency.

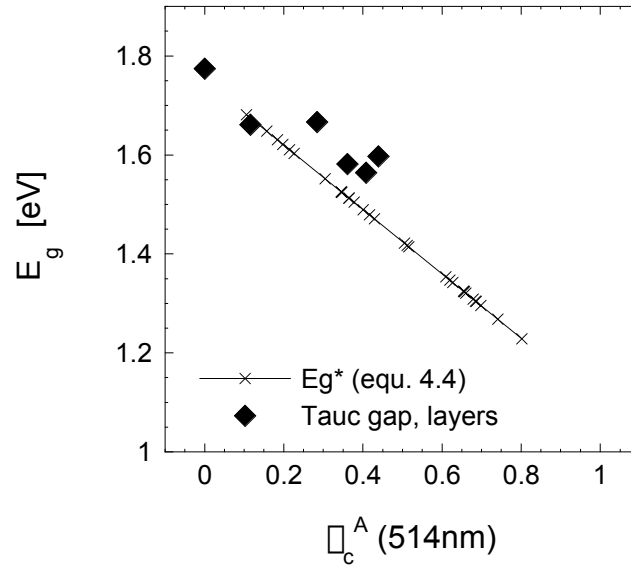


Fig. 4.30: Weighted bandgap value E_g^* calculated by weighting the respective gaps of a-Si:H and c-Si with the fraction of each phase present in the solar cells (equ. 4.4) (crosses and full line), as well as experimental optical bandgap evaluated by the Tauc method from CPM data measured on the SC series of single layers (see § 4.4.3.5) (diamond) as a function of \square_c^A measured on these layers.

Before discussing the results of Fig. 4.29, one can wonder if the weighted gap defined by (equ. 4.4) has an actual meaning. The best way for that would be to evaluate the optical gap of the solar cells studied here, and to compare it with the data obtained from (equ. 4.4). Such evaluation would be possible from CPM (constant photocurrent method) measurements performed directly on the solar cells [Poruba 1997]. However, we do not have such measurements for our solar cells. On the other hand, we have evaluated in Chapter 3 the optical gap E_g by the Tauc method from CPM measurements performed on the SC series of single i-layers (see § 3.4.3.5). From Fig. 4.30, one sees that these values of E_g , when represented as a function of \square_c^A at 514 nm evaluated on the same layers, are well in accordance with the relation between \square_c^A and E_g^* given by (equ. 4.4) and used in Fig. 4.29. Such a linear relation between the crystallinity and optical properties could seem surprising. Indeed, we do observe that the optical properties suddenly change as the silane concentration (SC) used for the deposition increases. However, the crystallinity also decreases abruptly with increasing SC [Houben 1998, Lambertz 2003]. Such a sharp decrease has indeed been observed for the SC series of layers in Fig. 3.15. Therefore a linear relation between optical properties and \square_c should not be a priori excluded. It turns out that best \square c-Si:H solar cells are those with the i-layer deposited near the transition to amorphous material. However, such \square c-Si:H material has not been extensively studied as yet and the values for optical parameters as are generally attributed to \square c-Si:H material are mostly those of "highly microcrystalline" material (as deposited for low values of SC).

In Fig. 4.29 are also given the range for experimental V_{oc} -values obtained for state-of-the-art crystalline silicon (V_{oc}^{c-Si}) and amorphous silicon ($V_{oc}^{a-Si:H}$) solar cell technology. Whereas V_{oc}^{c-Si} is nearly attaining the semi-empirical limit given by Green, $V_{oc}^{a-Si:H}$, although higher than V_{oc}^{c-Si} , is still quite lower than the theoretical or semi-empirical limit. The limits of Fig. 4.29 consider a p-n junction formed with a crystalline material having a given bandgap value (x-axis value), which corresponds to c-Si solar cell technology. On the other hand, the technology of a-Si:H solar cells consists in p-i-n (or n-i-p) structure and amorphous material. These both aspects are explanations for lower V_{oc} -values as compared to the theoretical limits. a-Si:H material contains an important quantity of localised states in the bandtails. Therefore, compared to a crystalline material with a bandgap value equal to that of a-Si:H ($E_g \approx 1.75$ eV), one can expect lower V_{oc} -values due to the localisation of carriers that do no longer contribute to the built-in field, i.e. to the V_{oc} .

From Fig. 4.29, one can observe that the slope of V_{oc} vs. E_g from theoretical values is about 2.5 times higher than that of the linear fit to our experimental data. (Note that this difference holds if \square_c^{p-i} or \square_c^{n-i} is used in (equ. 4.4) instead of \square_c^A). The variation of the gap in our samples as evaluated by (equ. 4.4) is due to the incorporation of a certain quantity of amorphous phase. Fig. 4.29 shows that this incorporation of a-Si:H material in \square c-Si:H does not enable to increase the V_{oc} in a similar way as for crystalline material (as observed in the theoretical limit evolution with E_g).

One observes from Fig. 4.29 that, surprisingly, the slope of the fit to our experimental data measured on various \square c-Si:H solar cells is roughly the same as the slope between V_{oc}^{c-Si} and $V_{oc}^{a-Si:H}$. Indeed, one can note on Fig. 4.29 that for both extreme cases (i.e. E_g^* approaching E_g^{c-Si} and E_g^* approaching $E_g^{a-Si:H}$), our experimental V_{oc} -values are about 0.3 V lower than V_{oc}^{c-Si} and $V_{oc}^{a-Si:H}$, respectively. Note that such comparison between V_{oc} obtained for our \square c-Si:H solar cells and for state-of-the-art c-Si and a-Si:H cells can also be done on the basis of Fig. 4.26 (that uses \square_c^A as x-axis). This comparison and the following discussion are therefore independent of the weighted gap E_g^* introduced with (equ. 4.4). Although a difference of 0.3 mV is indeed observed for both extreme values of the crystallinity ($\square_c^A \approx 1$ and $\square_c^A \approx 0$, respectively, see Fig. 4.26), it is probably not due to the same reasons in both cases. We will try to give below some possible explanations for each case:

- **Comparison with c-Si cells (Fig. 4.26: $\square_c^A \approx 1$; Fig. 4.29: $E_g^* \approx 1.1$ eV):** in this case, the lower V_{oc} obtained for our \square c-Si:H solar cells can be due to two factors. First, our \square c-Si:H samples have a p-i-n (or n-i-p) structure, whereas c-Si cells have a p-n structure. Second, \square c-Si:H material compared to c-Si material contains a lot of disordered material at the grain boundaries. Indeed, already for the case of poly-Si solar cells (which have a p-n structure), the presence of the grain boundaries (and,

thus of localised states) reduces the value of V_{oc} as compared to c-Si cells [Ghosh 1980].

- **Comparison with a-Si:H cells (Fig. 4.26: $\mu_c^A \approx 0$; Fig. 4.29: $E_g^* \approx 1.75$ eV):** one of the main difference, in this case is the thickness between state-of-the-art a-Si:H solar cells (i-layer: 0.2 - 0.3 μm) and cells grown with $\mu\text{c-Si:H}$ characteristics (i-layer: 1 - 3 μm). On the other hand, for a series of a-Si:H solar cells fabricated by reducing the SC for the i-layer deposition (thickness ≈ 0.25 μm), it has been observed that the V_{oc} -value is kept about constant around 890 - 900 mV for SC = 100% down to 20%, whereas it suddenly falls to 700 mV for SC = 10% [Niquille 2003]. The interface between the doped layers and the i-layer is also crucial for high V_{oc} -values. Here, we are comparing state-of-the-art a-Si:H solar cells (with optimized interfaces), and a kind of "hybrid" solar cells (non-optimized) that have some characteristics of $\mu\text{c-Si:H}$ cells (doped layers, thickness of the i-layer), but an intrinsic layer material close to that of an a-Si:H cell.

4.5.3.2. Dependence of the short-circuit current

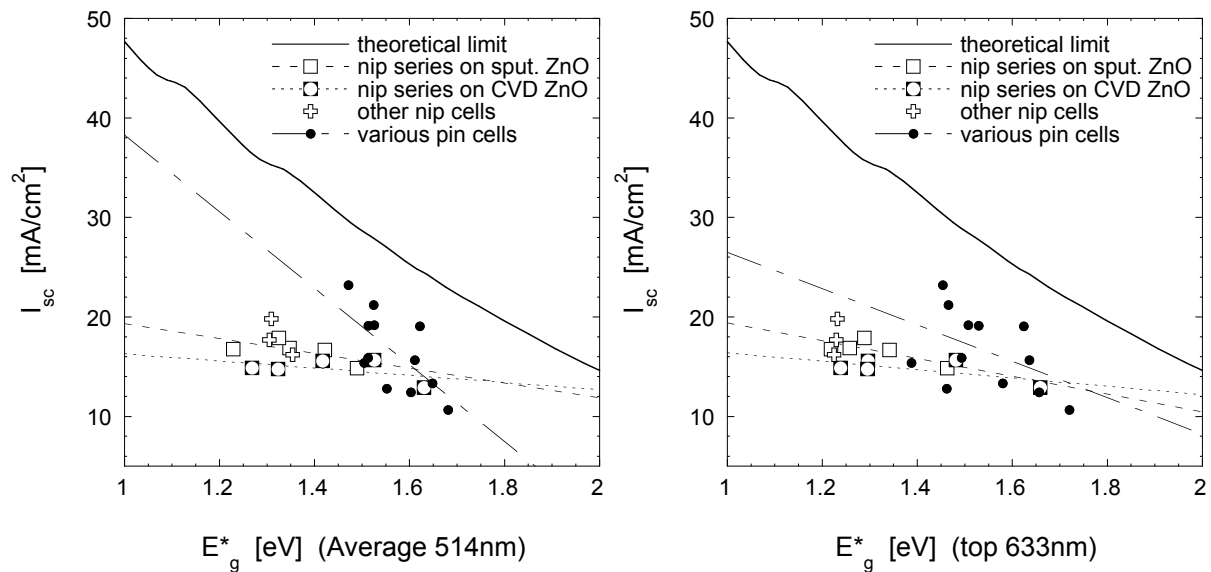


Fig. 4.31: Upper limit (full line) of the short-circuit current (I_{sc}) as a function of the material bandgap E_g and I_{sc} -values measured on the two SC series of n-i-p solar cells as well as on various other n-i-p and p-i-n $\mu\text{c-Si:H}$ solar cells, as a function of the weighted bandgap E_g^* as defined in (equ. 4.4) (the data are those of Fig. 4.28). The dotted lines are individual linear fit to each SC series of n-i-p cells and to all the p-i-n solar cells. E_g^* is calculated with μ_c^A at 514 nm in left-hand representation and with μ_c^{top} at 633 nm in the right-hand representation.

A representation similar to that of Fig. 4.29 for V_{oc} can be done for comparing our experimental I_{sc} -values with the theoretical upper limit for the current. In Fig. 4.31, the upper limit for I_{sc} has been calculated on the basis of the AM1.5 spectrum and assuming that each

photon of energy higher than that of the bandgap E_g is transformed into electrical current. In Fig. 4.31 are also represented the I_{SC} -values measured on the SC series of n-i-p cells as well as on the other n-i-p and various p-i-n cells (same data as in Fig. 4.28) as a function of the weighted bandgap E_g^* (equ. 4.4) calculated with \square_c^A measured at 514 nm (Fig. 4.29, left) and with \square_c^{top} measured at 633 nm (Fig. 4.29, right). One sees that, on the whole, the trend observed for our experimental data corresponds to that of the theoretical limit. However, the experimental data are quite scattered, and the values are much lower than the theoretical limits. As already discussed in 4.5.2, it is difficult to compare these data regarding I_{sc} , as some of the devices have reflectors, some are deposited on flat substrates and others on rough substrates, and the thickness of the i-layer is different.

4.6. Conclusions

In this chapter, we have first analysed the microstructure of \square c-Si:H single-junction solar cells with the bifacial depth-dependent Raman spectroscopy technique introduced in Chapter 2. Then, we have studied the link between the microstructure and the electrical performances of n-i-p and p-i-n solar cells.

The evaluation of the crystallinity of solar cells with the Raman spectroscopy, as performed in this work, has many advantages. It is a fast technique that does not need any sample preparation and is consequently non-destructive. Moreover, it can be applied for monitoring the crystallinity at various depths in actual, complete (functioning) solar cells on which electrical performances can also be measured.

The application of bifacial depth-dependent micro-Raman measurement to entire solar cells is quite easy and is not different from its application to single i-layers (as studied in Chapters 2 and 3). The presence of TCO layers (either in top-side or in bottom-side measurement configuration) on the light path does not hinder the measurement itself and does not distort the deconvolution and interpretation of the spectra. In bottom-side configuration, the presence of the doped layer (especially if it is highly microcrystalline) tends to weaken the measured crystallinity as compared to the real the crystallinity inhomogeneity in thickness of the i-layer observed in TEM micrograph. Indeed, as Raman measurements always probe the doped layer plus a more or less important part of the i-layer, the deduced crystallinity is an average of these two parts. Such measurement, thus, cannot distinguish a highly microcrystalline doped layer followed by an amorphous layer from a doped layer with a moderate crystallinity followed by an i-layer with similar crystallinity.

The Raman crystallinity of two series of n-i-p solar cells deposited simultaneously on flat sputtered ZnO and on rough CVD ZnO has been extensively studied. The cells of these series have been deposited with the same deposition parameters, except the silane concentration of

the i-layer that has been varied from 5% to 7%. The evaluation of the Raman crystallinity \square from deconvoluted Raman spectra revealed the advantage of such quantitative representation as compared to the qualitative information of "raw" Raman spectra. Indeed, the representation of a solar cell by its four \square_c -values deduced from the bifacial depth-dependant Raman measurements is quite effective to analyse a series of solar cells or to compare individual samples. For the SC series of cells, the four \square -values representation as a function of SC are analysed and compared to TEM micrographs of some devices. For each SC, the four \square -values are always ordered similarly, corresponding to an increase of the crystallinity as growth proceeds, in accordance with TEM observations. On the other hand, each \square decreases as SC increases. The top-side \square -value reveals that the upper (top) microcrystalline "bulk" part of devices deposited at different SC values contains a more or less significant amorphous part, even if they appear quite similar on (low-resolution) TEM micrographs. In such case, the quantitative information brought by Raman measurements is therefore more significant than the qualitative information supplied by TEM micrographs.

We have identified the two Raman crystallinity factors which probe the regions close to the n-i and p-i interfaces, as constituting fundamental microstructural parameters for solar cell device characterisation, because they are directly related to the value of V_{oc} . Indeed, V_{oc} linearly decreases when the algebraic average of the top crystallinity and bottom crystallinity factors increases. This has been observed for a large set of solar cells in both n-i-p and p-i-n configurations. Nevertheless, as the first deposited interface region influence the growth of the bulk material, and as the crystallinity of last deposited interface region depends on that of the bulk, further investigations would be necessary in order to identify more accurately the precise thickness of the solar cell region that is important for forming V_{oc} .

The difference in V_{oc} between highly \square c-Si:H solar cells and c-Si cells is observed to be the same as the difference in V_{oc} between \square c-Si:H solar having a very low crystallinity compared to state-of-the-art a-Si:H cells. However, this similitude cannot be fully explained.

For the various solar cells analysed in this work, one observed a general tendency for I_{sc} to increase as the crystallinity increases. However, our data are quite scattered. In order to get a more precise relation between I_{sc} and the crystallinity, one should as next step analyse solar cells having the same i-layer thickness, the same (ideally flat) TCO layers, and no reflector.

Chapter 5: Final conclusions

In this thesis, we have studied hydrogenated microcrystalline silicon ($\mu\text{c-Si:H}$). Since several years now, this material has been used as active layer for photovoltaic conversion. It is successfully introduced into complete $\mu\text{c-Si:H}$ solar cells in both p-i-n and n-i-p configurations, as well as coupled with hydrogenated amorphous silicon (a-Si:H) to form "micromorph" tandem solar cells. Although conversion efficiencies over 9% are now obtained for single-junction solar cells, the link between the complex microstructure of $\mu\text{c-Si:H}$ and the electrical performances is still not clear. One agrees only that the best conversion efficiencies are obtained for $\mu\text{c-Si:H}$ material deposited near the transition to amorphous material. **This thesis attempts to identify which microstructural features govern electrical transport properties in intrinsic $\mu\text{c-Si:H}$ layers, on one hand, and electrical performances of entire solar cells, on the other hand.**

The $\mu\text{c-Si:H}$ material studied in this work has been exclusively deposited by the Very High Frequency Plasma Enhanced Chemical Vapour Deposition (VHF PE-CVD) technique. With this technique, it is quite easy to pass from amorphous silicon (a-Si:H) material to $\mu\text{c-Si:H}$ material by adjusting the deposition parameters. Amongst them, the Silane Concentration in the plasma gas phase, $SC = \text{SiH}_4/(\text{SiH}_4+\text{H}_2)$, is the one that is most effective in varying the microstructure of the silicon thin films across the transition. Therefore, we have principally studied series of intrinsic layers and complete solar cells where the SC used for the deposition of the i-layer has been varied.

The microstructure of $\mu\text{c-Si:H}$ is very complex, especially for material deposited near the $\mu\text{c-Si:H}$ / a-Si:H transition. For such conditions, an amorphous incubation layer is frequently observed at the bottom of the layer. As growth proceeds, the nucleation of the microcrystalline phase occurs. This phase consists of pencil-like conglomerates (of about half a micron diameter) made of nanocrystals of few tens of nanometres. Between nanocrystals, as well as between conglomerates, a certain form of amorphous material constitutes the boundaries of nanocrystals and conglomerates.

The most illustrative way to present such complex microstructure is probably to make

Transmission Electron Microscopy (TEM) micrographs of cross-section samples. However, this technique requires a time-consuming and destructive preparation of the samples. Moreover, TEM imaging has a limited resolution for distinguishing amorphous material within the microcrystalline phase. Therefore, we have sought for a characterisation technique that enables a depth-dependent monitoring of the crystallinity. From this point of view, Raman spectroscopy is an interesting method. A Raman spectrum consists of peaks whose position is characteristic of the vibrational energies within a material. Thus, the respective amorphous and crystalline phases present in a \square c-Si:H sample can be evaluated with this technique.

In this work, we have essentially investigated Raman spectroscopy as a probing tool for monitoring of the crystallinity within \square c-Si:H samples. Provided that some care is taken regarding experimental conditions (in order to avoid material recrystallisation), Raman spectroscopy is a very convenient and fast technique. In particular, we have introduced the concept of "**bifacial depth-dependent**" **micro-Raman technique**. For that, we use two excitation wavelengths ($\lambda = 514$ nm and 633 nm) that are focused either on the top, i.e. the last deposited part of the sample, or on the bottom (glass-side), i.e. the first deposited part of the sample. In the latter case, a microscope objective with a long working distance microscope objective must be used, in order to focus light at the interface between glass and silicon layer. Thus, for each sample, one obtains four Raman spectra characteristic of the evolution of the microstructure along the growth axis. The depth from which the collected Raman signal arises (Raman collection depth, RCD) depends on the absorption coefficient α of the material under test at the given excitation wavelength ($RCD = 1/[2\alpha]$). As the 514 nm laser light is strongly absorbed within silicon-based material, the collected Raman spectra is indicative of a short volume of about $RCD \approx 50$ nm (in a-Si:H material) to 120 - 170 nm (in \square c-Si:H material) below the sample surface. On the other hand, at $\lambda = 633$ nm, $RCD \approx 500$ nm for both a-Si:H and \square c-Si:H materials.

Bifacial depth-dependent micro-Raman spectroscopy is easily carried out in actual, complete \square c-Si:H solar cells. Indeed, the presence of a TCO (transparent conductive oxide) layer within a device does not hinder the Raman measurement and its interpretation. **Therefore, this non-destructive technique enables monitoring of the crystallinity in solar cells on which electrical performances can also be measured.** At $\lambda = 514$ nm, the probed volume contains the doped layer (~ 20 -40 nm) plus a small part of the i-layer. At $\lambda = 633$ nm, the probed volume still contains the doped layer, plus a substantial part of the i-layer.

From a Raman spectrum, one can determine quantitative information on layer crystallinity. For that, one has to evaluate the scattered intensities arising from the amorphous and crystalline phases, respectively. In the case of our samples, we fitted the Raman spectra within a range of 360 to 580 cm^{-1} with a quadratic baseline and three Gaussian contributions:

the peak at 520 cm^{-1} corresponds to the **crystalline phase**, the peak around 510 cm^{-1} is attributed to the **defective crystalline part** (and is therefore included into the crystalline phase) and the broad peak at 480 cm^{-1} corresponds to the **amorphous phase**. The "Raman crystallinity factor" \square_c is then defined as the ratio of the area of the peaks related to the crystalline phase (i.e. 520 cm^{-1} and 510 cm^{-1} peaks) over the total area.

For intrinsic $\square\text{c-Si:H}$ layers, the four bifacial depth-dependent \square_c -values are representative of the **increase in crystallinity within the layers as growth proceeds**. Results thus obtained are in good agreement with TEM micrographs. In a SC-series of layers deposited around the transition, the bottom \square_c -value at 514 nm is equal to zero for each value of SC, indicating the presence of an amorphous incubation layer. On the other hand, the top \square_c -values decrease from about 0.8 to practically zero as SC increases, with a marked decrease at the onset of the $\square\text{c-Si:H/a-Si:H}$ phase transition ($\square_c \approx 0.5$) for intermediate SC-values. As the top \square_c -values obtained with 514 and 633 nm excitation light are nearly the same for each value of SC, one can say that the **crystallinity saturates with the sample thickness** (at least within the last 500 nm, i.e. the value of RCD at 633 nm), and that **the saturated value depends on the deposition conditions** (i.e. SC here).

In series of solar cells in which the i-layer has been deposited at varying SC, no amorphous incubation layer is observed, and the four \square_c -values are closer to each other. This is due to the highly microcrystalline doped layer that, in addition to contributing to the Raman signal, favours the crystallinity of the subsequent i-layer. Indeed, if the microcrystalline quality of the doped layer is low, the \square_c -values measured on the whole cells are consequently lowered.

The Raman crystallinity factor \square_c does not reflect the actual crystalline volume fraction, as its evaluation does not include the **ratio (y) of the Raman cross-section for $\mu\text{c-Si}$ over that for a-Si:H** . In order to evaluate y , we have compared the bifacial depth-dependent \square_c -values obtained on one $\square\text{c-Si:H}$ layer with TEM micrographs of the same sample. Assuming that the crystallinity within the $\square\text{c-Si:H}$ phase itself is constant and does not vary with the thickness, we have obtained $y \approx 1.7$ at 633 nm and $y \approx 1.8$ at 514 nm. Such y -values that are clearly higher than unity mean that our \square_c -value overestimates slightly (up to 30%) the actual crystalline volume fraction. However, these values are quite sensitive to the parameters we used for their evaluation. In order to confirm these values for y , similar comparison between \square_c -values and TEM micrographs for a larger set of thin ($\sim 0.5 - 1 \mu\text{m}$) $\square\text{c-Si:H}$ layers should be made.

Coplanar electrical transport under illumination as measured in $\square\text{c-Si:H}$ layers has been compared to that measured in a-Si:H layers. It turns out that **transport properties in $\square\text{c-Si:H}$ behaves similarly to a-Si:H** . Moreover, **the mobility \square lifetime ($\square\tau$) products measured in**

□c-Si:H samples are similar to those measured in annealed a-Si:H and slightly higher than for degraded a-Si:H. For a SC series of layers, coplanar transport properties have been studied in relation with selected microstructural parameters. One observes that the normalized mobility μ lifetime product $\mu\tau$ relates to the size of nanocrystal conglomerates (as observed by TEM and AFM) rather than to the average size of the individual nanocrystals (as evaluated from XRD). Moreover, the ambipolar diffusion length measured in these samples equals, in average, half of the diameter of the conglomerates. **These experimental observations indicate that coplanar transport in □c-Si:H is limited by the defective material present at the conglomerate boundaries.**

It is well known from technological work that the □c-Si:H solar cells with best efficiencies are obtained when the intrinsic material is deposited near the a-Si:H / □c-Si:H transition. In order to clarify the relationship between solar cell performances and their crystallinity, bifacial Raman measurements have been performed on the very same cells where electrical performances were also measured.

We have identified the two Raman crystallinity factors which probe the regions close to the n-i and p-i interfaces, as constituting the fundamental microstructural parameters for solar cell device characterisation, because they are directly related to the value of V_{oc} . Indeed, **V_{oc} linearly decreases when the algebraic average of the top crystallinity and bottom crystallinity factors increases.** This has been observed for a large set of solar cells representative of our in-house solar cell technology based on VHF-PECVD, for both n-i-p and p-i-n type solar cells. Nevertheless, further investigations are needed in order to identify more accurately the precise thickness of the solar cell region that is decisive in forming V_{oc} .

We have not been able to establish a "strong link" between I_{sc} and the crystallinity. Indeed, our samples were too different regarding thickness and presence (or not) of reflector layers (that are added in the device in order to increase I_{sc} by reflecting the non-absorbed light back into the device). Therefore, comparisons similar to those made in this work between Raman crystallinity and electrical parameters should be done on others better-defined sets of solar cells. Also, systematic analysis regarding light-induced degradation in □c-Si:H solar cells deposited near the transition should be carried out.

Thus, this work has allowed to clarify the role of the microstructure on coplanar electronic transport in □c-Si:H layers, indicating that the conglomerates boundaries rather than the nanocrystal boundaries do limit transport in □c-Si:H material. Furthermore, our bifacial depth-dependent Raman measurements have, for the first time, revealed a clear relationship between material crystallinity at the p-i and n-i junctions and the open-circuit voltage. Nevertheless, a phenomenological model for this observation is still lacking, and will have to be developed.

Appendix: Comparison of the $\mu\tau$ products for a-Si:H and μ c-Si:H evaluated in intrinsic layers and in solar cells

Fig. A.1 shows the normalised "mobility \times lifetime" product $\mu\tau$ evaluated from photoconductivity and SSPG measurements (see Chapter 3 and [Beck 1996b]) in various μ c-Si:H and a-Si:H intrinsic layers, as a function of the thickness of the layers. In Fig. A.1, one observes that $\mu\tau$ does increase as the thickness increases. Such changes of the transport properties with the thickness have previously also been reported, for example, in [Kocka 2003]. On the other hand, the vertical scattering of the data within one category of samples (μ c-Si:H, annealed or degraded a-Si:H) more or less overlaps with the different values observed for the three categories.

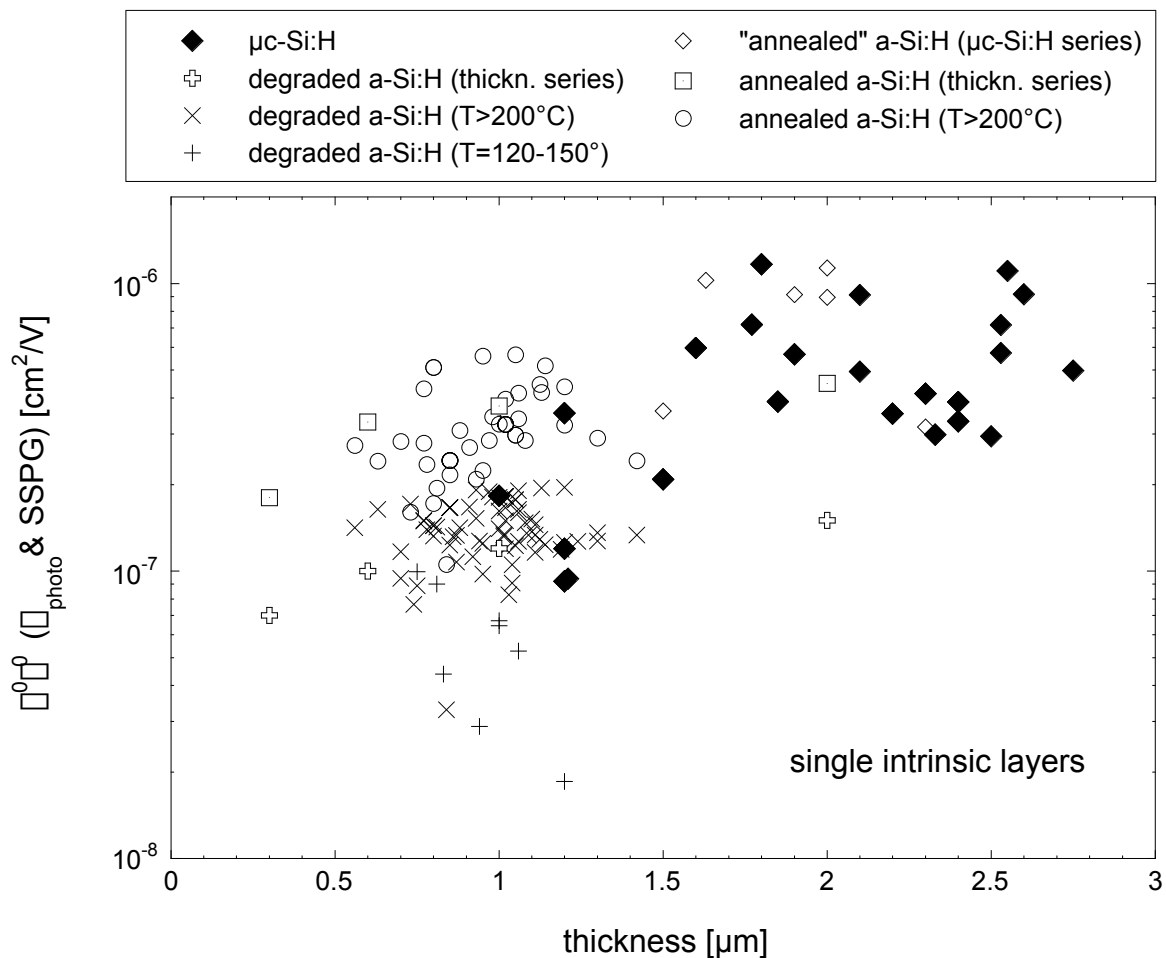
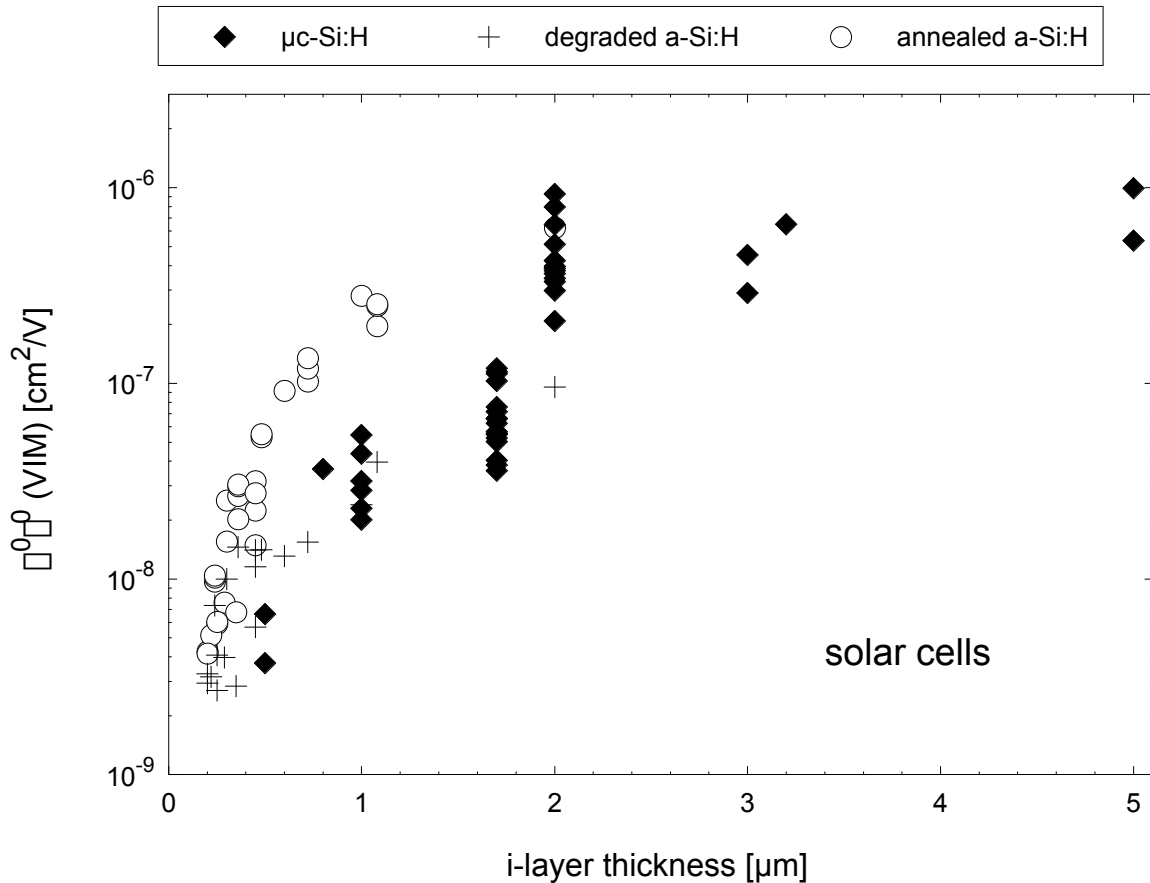


Fig. A.1: $\mu\tau$ product of various μ c-Si:H (filled symbols), annealed a-Si:H (open symbols) and degraded a-Si:H (crosses) intrinsic layers, as a function of the layer thickness. Within the a-Si:H data, we have distinguished between a-Si:H samples being part of μ c-Si:H series crossing the transition, a thickness series taken from [Hof 1999], and a-Si:H layers deposited either at a temperature (T) lower than 200°C ($T = 120-150^\circ\text{C}$) or at moderately high temperature ($T > 200^\circ\text{C}$), see [Ziegler 2001]. The degraded state of the a-Si:H samples was obtained after applying the fast degradation technique using pulsed laser light [Hof 1998].

A $\int^0 \int^0$ -product characteristic of the i-layer within entire solar cells can be determined by carrying out Variable Illumination Measurements (VIM). The VIM technique is described in [Hof 1999] and leads to the evaluation of a collection voltage $V_{collection}$. The $\int^0 \int^0$ -product is then calculated with the following expression:

$$\int^0 \int^0 (VIM) = \frac{\int \cdot L^2}{V_{bi}} \frac{\int V_{Collection}}{V_{bi}} \int 1 \int, \quad (\text{equ. A.1})$$

where \int is a "form factor" due to the deformation of the electric field, L is the i-layer thickness and V_{bi} is the built-in voltage. In [Fig. A.2](#) we have represented the $\int^0 \int^0$ -product evaluated on various \int c-Si:H, annealed and degraded a-Si:H solar cells with (equ. A.1), with $V_{bi} = 1.1$ V and $\int = 1$ (i.e. one assumes a constant electric field within the i-layer) in each case. Similarly to what was observed in [Fig. A.1](#), [Fig. A.2](#) shows that $\int^0 \int^0$ does, indeed, also increase with increasing thickness of the i-layer when evaluated within entire solar cells, according to the approximation procedure defined by (equ. A.1).



[Fig. A.2](#): $\int^0 \int^0$ products evaluated from VIM measurements carried out on various \int c-Si:H and a-Si:H solar cells as a function of the thickness of the i-layer.

Fig. A.3 compares, on a log-log representation, the $\sigma^0 \tau^0$ -products obtained on various μ c-Si:H, annealed and degraded a-Si:H layers (same data as in Fig. A.1) with the $\sigma^0 \tau^0$ -products evaluated from VIM measurements on various μ c-Si:H, annealed and degraded a-Si:H solar cells (same data as in Fig. A.2), as a function of the i-layer thickness.

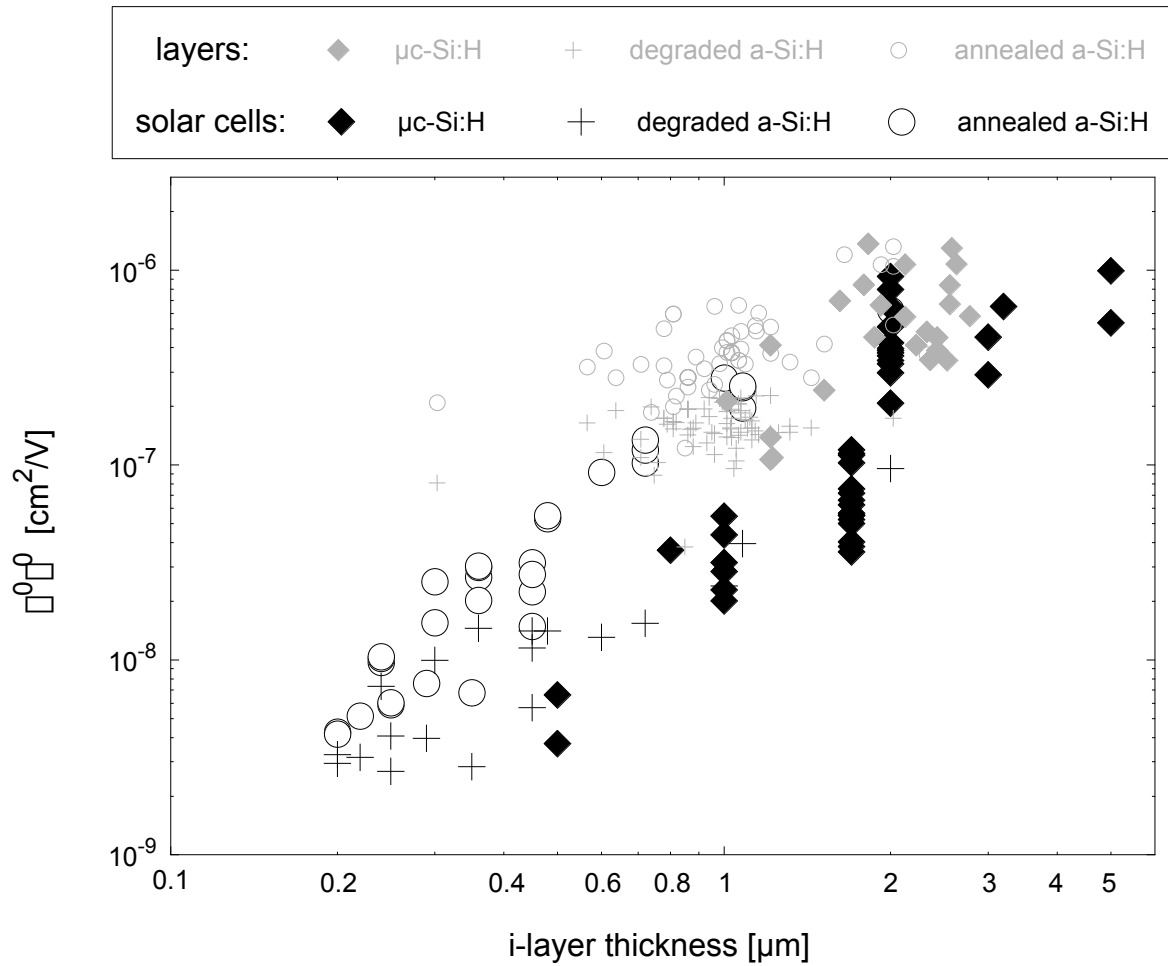


Fig. A.3: $\sigma^0 \tau^0$ as a function of the i-layer thickness for various a-Si:H and μ c-Si:H layers and solar cells. The data are the same as those of Fig. A.1 (layers) and Fig. A.2 (solar cells), except that the a-Si:H layers deposited at $T = 120-150^\circ\text{C}$ are not represented, and no distinction is made here between the various a-Si:H layers.

References

- [ADER 1997] ADER, *L'énergie au futur* (Editions d'en bas, Lausanne, 1997). ISBN 2-8290-0224-5.
- [Anastassakis 1999] E. Anastassakis, *J. Appl. Phys.* 86/1 (1999) 249.
- [Bailat 2002] J. Bailat, E. Vallat-Sauvain, L. Feitknecht, C. Droz, and A. Shah, *J. Non-Cryst. Solids* 299-302 (2002) 1219.
- [Bailat 2003] J. Bailat, E. Vallat-Sauvain, L. Feitknecht, C. Droz, and A. Shah, *J. Appl. Phys.* 93/9 (2003) 5727.
- [Balberg 1992] I. Balberg, *Mat. Res. Soc. Symp. Proc.* 258 (1992) 693.
- [Beck 1994] N. Beck, A. Shah, and N. Wyrsh, *Proceedings of the 1st World Conference on Photovoltaic Energy Conversion (WCPEC1)*, Hawaii (1994) 476.
- [Beck 1996a] N. Beck, J. Meier, J. Fric, Z. Remes, A. Poruba, R. Flückiger, J. Pohl, A. Shah, and M. Vanecek, *J. Non-Cryst. Solids* 198-200 (1996) 903.
- [Beck 1996b] N. Beck, N. Wyrsh, C. Hof, and A. Shah, *J. Appl. Phys.* 79/12 (1996) 9361.
- [Benedict 1992] J. Benedict, R. Andersen, and S. J. Klepeis, *Mat. Res. Soc. Symp. Proc.* 254 (1992) 121.
- [Brodsky 1977] M. H. Brodsky, M. Cardona, and J. J. Coumo, *Phys. Rev. B* 16 (1977) 3556.
- [Bustarret 1988] E. Bustarret, M. A. Hachicha, and M. Brunel, *Appl. Phys. Lett.* 52/20 (1988) 1675.
- [Cerqueira 1999] M. F. Cerqueira and J.A. Ferreira, *J Mater Proces Tech* 93 (1999) 235.
- [Chapin 1954] D. M. Chapin, C. S. Fuller, and G. L. Pearson, *J. Appl. Phys.* 25 (1954) 676.
- [Cullity 1978] B. D. Cullity, in *Elements of X-ray diffraction*, 2nd ed., edited by Addison-Wesley (1978), p. 102.
- [Curtins 1987] H. Curtins, N. Wyrsh, M. Favre, and A. V. Shah, *Plasma Chem. Plasma Proc.* 7/3 (1987) 267.
- [Curtins 1987] H. Curtins, N. Wyrsh, M. Favre, and A. V. Shah, *Plasma Chem. Plasma Proc.* 7/3 (1987) 267.
- [Droz 2000] C. Droz, M. Goerlitzer, N. Wyrsh, and A. Shah, *J. Non-Cryst. Solids* 266-269 (2000) 319.
- [Droz 2001] C. Droz, E. Vallat-Sauvain, J. Bailat, L. Feitknecht, and A. Shah, *Proceedings of the 17th European Photovoltaic Solar Energy Conference, Munich, Germany* (2001) 2917.
- [Droz 2003] C. Droz, E. Vallat-Sauvain, J. Bailat, L. Feitknecht, J. Meier, X. Niquille, and A. Shah, *Proceedings of the 3rd World Conference on Photovoltaic Energy Conversion (WCPEC3)*, Osaka (2003) 5O.A3.01.
- [Droz 2004] C. Droz, E. Vallat-Sauvain, J. Bailat, L. Feitknecht, J. Meier, and A. Shah, *Sol. En. Mat. and Sol. Cells*, 81/1 (2004) 61.
- [Dubail 2000] J. Dubail, E. Vallat-Sauvain, J. Meier, S. Dubail, and A. Shah, *Mat.*

- Res. Soc. Symp. Proc. 609 (2000) A13.6.1.
- [Faÿ 2003] S. Faÿ, Ph. D. Thesis, EPFL Lausanne, 2003.
- [Flückiger 1995] R. Flückiger, Ph. D. Thesis, University of Neuchâtel, 1995, ISBN 3-89191-965-4.
- [Feitknecht 2001] L. Feitknecht, O. Kluth, Y. Ziegler, X. Niquille, P. Torres, J. Meier, N. Wyrsh, and A. Shah, *Sol. En. Mat. and Sol. Cells* 66 (2001) 397.
- [Feitknecht 2003] L. Feitknecht, Ph. D. Thesis, University of Neuchâtel, 2003.
- [Flückiger 1995] R. Flückiger, Ph. D. Thesis, University of Neuchâtel, 1995, ISBN 3-89191-965-4.
- [Fonrodona 2003] M. Fonrodona, D. Soler, J. M. Asensi, J. Bertomeu, and J. Andreu, *Proceedings of the 3rd World Conference on Photovoltaic Energy Conversion (WCPEC3)*, Osaka (2003).
- [Ghosh 1980] A. K. Ghosh, C. Fishman, and T. Feng, *J. Appl. Phys.* 51/1 (1980) 446.
- [Goerlitzer 1996] M. Goerlitzer, N. Beck, P. Torres, J. Meier, N. Wyrsh, and A. Shah, *J. Appl. Phys.* 80/9 (1996) 5111.
- [Goerlitzer 1997] M. Goerlitzer, N. Beck, P. Torres, U. Kroll, H. Keppner, J. Meier, J. Koehler, N. Wyrsh, and A. Shah, *Mat. Res. Soc. Symp. Proc.* 467 (1997) 301.
- [Goerlitzer 1998a] M. Goerlitzer, Ph. D. Thesis, University of Neuchâtel, 1998, ISBN 2-9700197-0-1.
- [Goerlitzer 1998b] M. Goerlitzer, P. Torres, N. Beck, N. Wyrsh, H. Keppner, J. Pohl, and A. Shah, *J. Non-Cryst. Solids* 230 (1998) 996.
- [Green 1998] M. A. Green, *Solar cells: operating principles, technology and system applications* (University of New South Wales, 1998). ISBN 0 85823 580 3.
- [Hang 1988] Z. Hang, H. Shen, and F. H. Pollak, *J. Appl. Phys.* 64/6 (1988) 3233.
- [Hof 1995] C. Hof, N. Beck, N. Wyrsh, D. Fischer, and A. Shah, *Proceedings of the 13th European Photovoltaic Solar Energy Conference*, Nice, France (1995) 1634.
- [Hof 1998] C. Hof, Y. Ziegler, R. Platz, N. Wyrsh, and A. Shah, *J. Non-Cryst. Solids* 230 (1998) 287.
- [Hof 1999] C. Hof, Ph. D. Thesis, University of Neuchâtel, 1999, ISBN 3-930803-78-X.
- [Howling 1992] A. A. Howling, J.-L. Dorier, C. Hollenstein, U. Kroll, and F. Finger, *J. Vac. Sci. Technol. A* 10 (1992) 1080.
- [Houben 1998] L. Houben, M. Luysberg, P. Hapke, R. Carius, F. Finger, and H. Wagner, *Phil. Mag. A* 77/6 (1998) 1447.
- [Houben 2002] L. Houben, C. Scholten, M. Luysberg, O. Vetterl, F. Finger, and R. Carius, *J. Non-Cryst. Solids* 299-302 (2002) 1189.
- [Hubin 1992] J. Hubin, A. V. Shah, and E. Sauvain, *Phil Mag Lett* 66/3 (1992) 115.
- [Hubin 1995] J. Hubin, A. V. Shah, E. Sauvain, and P. Pipoz, *J. Appl. Phys.* 78/10

- (1995) 6050.
- [Islam 2001] M. N. Islam and S. Kumar, Appl. Phys. Lett. 78/6 (2001) 715.
- [Kiess 1995] H. Kiess and W. Rehwald, Sol. En. Mat. and Sol. Cells 38 (1995) 44.
- [Klein 2002] S. Klein, F. Finger, R. Carius, B. Rech, L. Houben, M. Luysberg, and M. Stutzmann, Mat. Res. Soc. Symp. Proc. 715 (2002) A26.2.1.
- [Klein 2003] S. Klein, F. Finger, R. Carius, T. Dylla, B. Rech, M. Grimm, L. Houben, and M. Stutzmann, Thin Solid Films 430/1-2 (2003) 202.
- [Kobliska 1973] R. J. Kobliska and S. A. Solin, Phys. Rev. B 8 (1973) 3799.
- [Kocka 2002] J. Kocka, H. Stuchlikova, J. Stuchlik, B. Rezek, T. Mates, V. Svrcek, P. Fojtik, I. Pelant, and A. Fejfar, J. Non-Cryst. Solids 299-302 (2002) 355.
- [Kocka 2003] J. Kocka, A. Fejfar, H. Stuchlikova, J. Stuchlik, P. Fojtik, T. Mates, B. Rezek, K. Luterova, V. Svrcek, and I. Pelant, Sol. En. Mat. and Sol. Cells 78/1-4 (2003) 493.
- [Kroll 1996] U. Kroll, J. Meier, A. Shah, S. Mikhailov, and J. Weber, J. Appl. Phys. 80/9 (1996) 4971.
- [Kuendig 2002] J. Kuendig and A. Shah, Proceedings of the 29th IEEE Photovoltaic Specialist Conference, New Orleans (2002) 974.
- [Kuendig 2003] J. Kuendig, Ph. D. Thesis, EPFL Lausanne, 2003.
- [Lambertz 2003] A. Lambertz, F. Finger, and R. Carius, Proceedings of the 3rd World Conference on Photovoltaic Energy Conversion (WCPEC3), Osaka (2003) 5P.D4.22.
- [Liu 1986] H. N. Liu and M. D. Xu, Sol. State Comm. 58/9 (1986) 601.
- [Luysberg 1997] M. Luysberg, P. Hapke, R. Carius, and F. Finger, Phil. Mag. A 75 (1997) 31.
- [Markvart 2000] T. Markvart, *Solar electricity*, 2nd ed. (John Wiley & Sons, 2000). ISBN 0-471-98853-7.
- [Marquardt 1963] D. W. Marquardt, J. Soc. Ind. Appl. Math. 11/2 (1963) 431.
- [Mates 2003] T. Mates, A. Fejfar, M. Ledinsky, K. Luterova, P. Fojtik, H. Stuchlikova, I. Pelant, J. Kocka, A. Mackova, M. Ito, K. Ro, and H. Uyama, Proceedings of the 3rd World Conference on Photovoltaic Energy Conversion (WCPEC3), Osaka (2003) 5P.A9.10.
- [Meier 1994a] J. Meier, S. Dubail, R. Fluckiger, D. Fischer, H. Keppner, and A. Shah, Proceedings of the 1st World Conference on Photovoltaic Energy Conversion (WCPEC1), Hawaii (1994) 409.
- [Meier 1994b] J. Meier, R. Flückiger, H. Keppner, and A. Shah, Appl. Phys. Lett. 65 (1994) 860.
- [Meier 1998a] J. Meier, S. Dubail, J. Cuperus, U. Kroll, R. Platz, P. Torres, J. A. A. Selvan, P. Pernet, N. Beck, N. P. Vaucher, C. Hof, D. Fischer, H. Keppner, and A. Shah, J. Non-Cryst. Solids 227-230 (1998) 1250.
- [Meier 1998b] J. Meier, H. Keppner, S. Dubail, Y. Ziegler, L. Feitknecht, P. Torres, C. Hof, U. Kroll, D. Fischer, J. Cuperus, J. A. A. Selvan, and A. Shah, Proceedings of the 2nd World Conference on Photovoltaic Energy

- Conversion (WCPEC2), Vienna (1998) 375.
- [Meier 2001] J. Meier, E. Vallat-Sauvain, S. Dubail, U. Kroll, J. Dubail, S. Golay, L. Feitknecht, P. Torres, S. Faÿ, D. Fischer, and A. Shah, *Sol. En. Mat. and Sol. Cells* 66 (2001) 73.
- [Meier 2002] J. Meier, J. Spitznagel, S. Faÿ, C. Bucher, U. Graf, U. Kroll, S. Dubail, and A. Shah, *Proceedings of the 29th IEEE Photovoltaic Specialist Conference, New Orleans (2002)* 1118.
- [Meier 2003] J. Meier, J. Spitznagel, U. Kroll, C. Bucher, S. Faÿ, T. Moriarty, and A. Shah, *Proceedings of the 3rd World Conference on Photovoltaic Energy Conversion (WCPEC3), Osaka (2003)* S20.B9.06.
- [Nasuno 2001a] Y. Nasuno, M. Kondo, and A. Matsuda, *Mat. Res. Soc. Symp. Proc.* 664 (2001) A15.5.1.
- [Nasuno 2001b] Y. Nasuno, M. Kondo, and A. Matsuda, *Appl. Phys. Lett.* 78/16 (2001) 2330.
- [Niquille 2003] X. Niquille, Private communications, (2003).
- [Noda 2003] M. Noda, T. Nishimiya, K. Yamaguchi, K. Kawamura, H. Sonobe, M. Kuroda, A. Yamada, H. Takatsuka, Y. Yamauchi, and Y. Takeuchi, *Proceedings of the 3rd World Conference on Photovoltaic Energy Conversion (WCPEC3), Osaka (2003)* 5P.D4.34.
- [Overhof 1989] H. Overhof and P. Thomas, in *Springer tracts in modern physics: Electronic transport in hydrogenated amorphous silicon, Vol. 114*, edited by Springer-Verlag (1989), p. 26.
- [Paillard 2002] V. Paillard, P. Puech, and P. R. I. Cabarrocas, *J. Non-Cryst. Solids* 299-302 (2002) 280.
- [Poruba 1997] A. Poruba, Z. Remes, J. Fric, M. Vanecek, J. Meier, P. Torres, N. Beck, N. Wyrsh, and A. Shah, *Proceedings of the 14th EC Photovoltaic Solar Energy Conference, Barcelona (1997)* 260.
- [Poruba 2000a] A. Poruba, A. Fejfar, Z. Remes, J. Springer, M. Vanecek, J. Kocka, J. Meier, P. Torres, and A. Shah, *J. Appl. Phys.* 88/1 (2000a) 148.
- [Poruba 2000b] A. Poruba, A. Fejfar, O. Salyk, M. Vanecek, and J. Kocka, *J. Non-Cryst. Solids* 271/1-2 (2000b) 152.
- [Raman 1928] C. V. Raman and K. S. Krishnan, *Nature* 121/3048 (1928) 501.
- [Renishaw] Renishaw Raman Imaging Microscope, WIRE™ (Windows-based Raman Environment) User Guide, M/8012/1798/02.
- [Repmann 2001] T. Repmann, W. Appenzeller, T. Roschek, B. Rech, O. Kluth, and J. Müller, *Proceedings of the, Munich (2001)* 2836.
- [Repmann 2003] T. Repmann, B. Sehrbrock, C. Zahren, H. Siekmann, J. Müller, B. Rech, W. Psyk, R. Geyer, and P. Lechner, *Proceedings of the 3rd World Conference on Photovoltaic Energy Conversion (WCPEC3), Osaka (2003)* 50.A6.03.
- [Ritter 1986] D. Ritter, E. Zeldov, and K. Weiser, *Appl. Phys. Lett.* 49/13 (1986) 791.
- [Ritter 1987] D. Ritter, K. Weiser, and E. Zeldov, *J. Appl. Phys.* 62/11 (1987) 4563.

- [Roschek 2002] T. Roschek, T. Repmann, J. Muller, B. Rech, and H. Wagner, *J. Vac. Sci. Technol. A* 20/2 (2002) 492.
- [Rose 1963] A. Rose, *Concepts in photoconductivity and allied problems* (Interscience Publishers, John Wiley & Sons, 1963).
- [Saito 2003] K. Saito, M. Sano, H. Otsoshi, A. Sakai, S. Okabe, and K. Ogawa, *Proceedings of the 3rd World Conference on Photovoltaic Energy Conversion (WCPEC3)*, Osaka (2003) S20.
- [Sauvain 1992] E. Sauvain, Ph. D. Thesis, University of Neuchâtel, 1992.
- [Schropp 2003] R. E. I. Schropp, J. Adams, A. Bink, P. C. P. Bronsveld, J. Francke, R. H. J. Franken, H. D. Goldbach, A. Gordjin, R. J. Jimenez Zambaro, H. Li, R. W. Lof, J. Löffler, G. van der Mark, J. K. Rath, M. Rusche, R. L. Stolk, M. K. van Veen, and C. H. M. van der Werf, *Proceedings of the 3rd World Conference on Photovoltaic Energy Conversion (WCPEC3)*, Osaka (2003) 5P.D4.33.
- [Shah 1995a] A. Shah, in *Matériaux électroniques amorphes, Vol. 1*, 3ème ed. (EPFL - Université de Neuchâtel, 1995), p. 65.
- [Shah 1995b] A. Shah, in *Matériaux électroniques amorphes, Vol. 2*, 3ème ed. (EPFL - Université de Neuchâtel, 1995), p. 44.
- [Shah 1997] A. Shah, E. Sauvain, J. Hubin, P. Pipoz, and C. Hof, *Philos Mag B* 75/6 (1997) 925.
- [Shah 2002] A. Shah, J. Meier, E. Vallat-Sauvain, C. Droz, U. Kroll, N. Wyrsh, J. Guillet, and U. Graf, *Thin Solid Films* 403 (2002) 179.
- [Shah 2003] A. Shah, J. Meier, E. Vallat-Sauvain, N. Wyrsh, U. Kroll, C. Droz, and U. Graf, *Sol. En. Mat. and Sol. Cells* 78/1-4 (2003) 469.
- [Smith 1978] R. A. Smith, *Semiconductors* (Cambridge University Press, 1978). ISBN 0-521-21824-1.
- [Staebler 1977] D. L. Staebler and C. R. Wronski, *Appl. Phys. Lett.* 31/4 (1977) 292.
- [Stiebig 2000] H. Stiebig, T. Brammer, J. Zimmer, O. Vetterl, and H. Wagner, *J. Non-Cryst. Solids* 266 (2000) 1104.
- [Sze 1981] S. M. Sze, *Physics of semiconductors*, 2nd ed. (John Wiley & Sons, 1981). ISBN 0-85226-846-7.
- [Takenaka 2003] A. Takenaka, T. Hatsukaiwa, and T. Nomura, *Proceedings of the 3rd World Conference on Photovoltaic Energy Conversion (WCPEC3)*, Osaka (2003) 6CN.C.02.
- [Tauc 1966] J. Tauc, R. Grigorovici, and A. Vancu, *Physica Status Solidi* 15 (1966) 627.
- [Terrazzoni-Daudrix 2003] V. Terrazzoni-Daudrix, J. Guillet, X. Niquille, L. Feitknecht, F. Freitas, P. Winkler, A. Shah, R. Morf, O. Parriaux, and D. Fischer, *Proceedings of the 3rd World Conference on Photovoltaic Energy Conversion (WCPEC3)*, Osaka (2003) 5O.D14.03.
- [Torres 1996] P. Torres, J. Meier, R. Fluckiger, U. Kroll, J. A. A. Selvan, H. Keppner, A. Shah, S. D. Littelwood, I. E. Kelly, and P. Giannoules, *Appl. Phys. Lett.* 69/10 (1996) 1373.
- [Torres 1997] P. Torres, J. Meier, U. Kroll, N. Beck, H. Keppner, and A. Shah,

- Proceedings of the 26th IEEE Photovoltaic Specialists Conference, Anaheim, CA (1997) 711.
- [Torres 1998] P. Torres, PH. D. Thesis, University of Neuchâtel, 1998.
- [Tsu 1982] R. Tsu, J. Gonzalez-Hernandez, S. S. Chao, S. C. Lee, and K. Tanaka, *Appl. Phys. Lett.* 40/6 (1982) 534.
- [Turrell 1996] G. Turrell and J. Corset, *Raman microscopy, developments and applications* (Academic Press, 1996). ISBN 0-12-189690-0.
- [Underwood 1970] U. Underwood, in *Quantitative Stereology*, edited by Addison-Wesley (Reading, Massachusetts, 1970), p. 175.
- [Vallat-Sauvain 2000] E. Vallat-Sauvain, U. Kroll, J. Meier, A. Shah, and J. Pohl, *J. Appl. Phys.* 87/6 (2000) 3137.
- [Vallat-Sauvain 2001] E. Vallat-Sauvain, S. Faÿ, S. Dubail, J. Meier, J. Bailat, U. Kroll, and A. Shah, *Mat. Res. Soc. Symp. Proc.* 664 (2001) A15.3.1.
- [Vanecek 1981] M. Vanecek, J. Kocka, J. Stuchlik, and A. Triska, *Sol. State Comm.* 39 (1981) 1199.
- [Vanecek 1995] M. Vanecek, J. Kocka, A. Poruba, and A. Fejfar, *J. Appl. Phys.* 78/10 (1995) 6203.
- [Veprek 1968] S. Veprek and V. Marecek, *Sol. State Comm.* 11 (1968) 683.
- [Vetterl 2001a] O. Vetterl, Ph. D. Thesis, Forschungszentrum Jülich, 2001, ISSN 0944-2952
- [Vetterl 2001b] O. Vetterl, A. Lambertz, A. Dasgupta, F. Finger, B. Rech, O. Kluth, and H. Wagner, *Sol. En. Mat. and Sol. Cells* 66/1-4 (2001) 345.
- [Viera 2001] G. Viera, S. Huet, and L. Boufendi, *J. Appl. Phys.* 90/8 (2001) 4175.
- [Weber 2000] W. H. Weber and R. Merlin, *Raman scattering in materials science* (Springer, 2000). ISSN 0933-033X, ISBN 3-540-67223-0.
- [Wyrsh 1998] N. Wyrsh, P. Torres, J. Meier, and A. Shah, *J. Non-Cryst. Solids* 230 (1998) 1272.
- [Wyrsh 2000] N. Wyrsh, L. Feitknecht, C. Droz, P. Torres, A. Shah, A. Poruba, and M. Vanecek, *J. Non-Cryst. Solids* 266 (2000) 1099.
- [Yamamoto 2002] K. Yamamoto, M. Yoshimi, Y. Tawada, S. Fukuda, T. Sawada, T. Meguro, H. Takata, T. Suezaki, Y. Koi, K. Hayashi, T. Suzuki, M. Ichikawa, and A. Nakajima, *Sol. En. Mat. and Sol. Cells* 74 (2002) 449.
- [Xia 1995] H. Xia, Y. L. He, L. C. Wang, W. Zhang, X. N. Liu, X. K. Zhang, D. Feng, and H. E. Jackson, *J. Appl. Phys.* 78/11 (1995) 6705.
- [Zi 1996] J. Zi, H. Buscher, C. Falter, W. Ludwig, K. M. Zhang, and X. D. Xie, *Appl. Phys. Lett.* 69/2 (1996) 200.
- [Ziegler 2001] Y. Ziegler, V. Daudrix, C. Droz, R. Platz, N. Wyrsh, and A. Shah, *Sol. En. Mat. and Sol. Cells* 66/1-4 (2001) 413.

Acknowledgements

I would like to thank:

Professor Arvind Shah, who accepted me in his research group and gave me the opportunity to effectuate my thesis in the motivating field of photovoltaics. His humanity as well as the pleasant atmosphere that always prevailed in the Thin-Film Silicon and Photovoltaics Laboratory definitively very positively contributed to the achievement of my work.

Prof. J. Faist, Dr. A. Perret, Dr. B. Rech, Dr. H. Schade and Dr. M. Vaněček, who have spontaneously accepted to join the examination board and who have devoted their time to the reading of this thesis.

The Swiss National Science Foundation (Fonds National Suisse de la recherche scientifique, FNS) and the Swiss Federal Office of Energy (Office Fédéral de l'Energie, OFEN), for their financial support.

Evelyne Vallat-Sauvain, who significantly contributed to the accomplishment of this thesis by letting me benefit from her impressive scientific competence and her enthusiasm for scientific research. Her guidance and ability to focus on essential points have been extremely valuable for the achievement of this work. I am also indebted to her for all the time she kindly spent on reviewing this manuscript.

Julien Bailat, for sharing his knowledge and results (especially the TEM micrographs) about microcrystalline silicon. I really appreciated the numerous discussions we had together, either about the growth of \square c-Si:H or about anything around a glass of beer.

Luc Feitknecht as well as Johannes Meier, the microcrystalline "technologists", for the samples they provided to me. It was also very fruitful to compare my ideas with the experience and point of view of "cell-makers".

Magali Goerlitzer and Nicolas Wyrsh who introduced me to the "magic" world of the microcrystalline silicon.

Mireille Leboeuf and Massoud Dadras for their help with the preparation and observation of TEM samples.

The administrative team of the IMT: Sylvie Baillod, Joëlle Banjac, Brigitte Khan, Sandrine Piffaretti and Martial Racine, as well as Hassan Laaroussi for his precious help with computer-related problems, and Reto Tschärner for his contribution to solve various administrative and technical problems.

Vanessa Terrazzoni-Daudrix and Sylvie Faÿ, with whom I had the pleasure to share my office during these last years. Their friendship and the various discussions we had together contributed also to a great extent to my motivation to reach this goal.

Cédric Bucher, Xavier Niquille, Sébastien Dubail, Joëlle Vuille, Fanny Meillaud, Mirko Nagel, for the good time we had together and for their good sense of humour.

Anybody I did not mention but who contributed in one way or another to the accomplishment of this work.

My parents as well as Anne Sophie and Laurent for their continuous encouragement to lead this work to a good end.

Finally, a special thank to Marc, for his endless and very precious moral and logistical support during the last couple of years.

Curriculum vitae

Corinne DROZ

Born on 18th of June 1974 in Neuchâtel

Swiss Nationality, single



Professional experience

- 1998-2003 **Institute of Microtechnology, University of Neuchâtel, Thin-Film Silicon and Photovoltaics Laboratory**
Research assistant:
- Electrical and microstructural characterisation of thin film amorphous and microcrystalline silicon layers and solar cells
- Students supervision (projects follow up, exercises, teaching)
- 1997-1998 **NEC Corporation (research and development centre), Tokyo, Japan**
Industrial training (study of crystals with non-linear optical properties)

Education

- 1998-2003 **Ph.D candidate**, University of Neuchâtel, Institute of Microtechnology
- 1992-1997 **M.Sc. degree in Microtechnical Engineering**, Swiss Federal Institute of Technology, Lausanne (EPFL)
- 1989-1992 **Swiss Federal Maturity, scientific orientation (type C)**, Gymnase Cantonal, Neuchâtel

Continuing education

- 2001-2002 **Introduction to management practice and company management**, Haute Ecole de Gestion (HEG), Neuchâtel
- November 2001 **Sustainable development: from international concept to local implementation – references, tools, methodology, practice**, University of Fribourg
- Sept-Oct. 2000 **The way to renewable energies and to energy efficiency**, University of Lausanne (UNIL), Association for the Development of Renewable Energies (ADER), Solar Energy and Building Physics Laboratory of EPFL (LESO)

Languages

- French native language
- English Good level ("Cambridge First Certificate in English" obtained in 2001; scientific articles writing, oral presentations at conferences)

German	Average level
Italian	Basic to average level (course taken since April 1999)
Japanese	Basic level (intensive course of 3 months in 1997)

Interests

Music (choir, piano, oboe), classical ballet, walking, cycling, swimming

Member of the committee of the SSES (Swiss Society of Solar Energy), section of Neuchâtel

Publications

- C. Droz, E. Vallat-Sauvain, J. Bailat, L. Feitknecht, J. Meier, and A. Shah, *Relationship between Raman crystallinity and open-circuit voltage in microcrystalline silicon solar cells*, Solar Energy Materials & Solar Cells, 81/1 (2004) 61.
- C. Droz, E. Vallat-Sauvain, J. Bailat, L. Feitknecht, J. Meier, X. Niquille, and A. Shah, *Electrical and microstructural characterisation of microcrystalline silicon layers and solar cells*, Proceedings of the 3rd World Conference on Photovoltaic Energy Conversion (WCPEC3), Osaka (2003) 5O.A3.01.
- C. Droz, E. Vallat-Sauvain, J. Bailat, L. Feitknecht, and A. Shah, *Application of Raman spectroscopy for the microstructure characterisation in microcrystalline silicon solar cells*, Proceedings of the 17th European Photovoltaic Solar Energy Conference, München, Germany (2001) 2917.
- C. Droz, M. Goerlitzer, N. Wyrsh, and A. Shah, *Electronic transport in hydrogenated microcrystalline silicon: similarities with amorphous silicon*, Journal of Non-Crystalline Solids 266 (2000) 319.
- C. Droz, H. Kouta, and Y. Kuwano, *Walk-off compensated 266-nm generation with two beta-BaB₂O₄ crystals*, Optical Review 6/2 (1999) 97.
- J. Bailat, E. Vallat-Sauvain, L. Feitknecht, C. Droz, and A. Shah, *Microstructure and open-circuit voltage of n-i-p microcrystalline silicon solar cells*, Journal of Applied Physics 93/9 (2003) 5727.
- L. Feitknecht, C. Droz, J. Bailat, X. Niquille, J. Guillet, and A. Shah, *Towards microcrystalline silicon n-i-p solar cells with 10% conversion efficiency*, Materials Research Society Symposium Proceedings Vol. 762 (2003) A13.5.
- U. Graf, J. Meier, U. Kroll, J. Bailat, C. Droz, E. Vallat-Sauvain, and A. Shah, *High rate growth of microcrystalline silicon by VHF-GD at high pressure*, Thin Solid Films 427/1-2 (2003) 37.
- A. Shah, J. Meier, E. Vallat-Sauvain, N. Wyrsh, U. Kroll, C. Droz, and U. Graf, *Material and solar cell research in microcrystalline silicon*, Solar Energy Materials & Solar Cells 78/1-4 (2003) 469.
- J. Bailat, E. Vallat-Sauvain, L. Feitknecht, C. Droz, and A. Shah, *Influence of substrate on the microstructure of microcrystalline silicon layers and cells*, Journal of Non-Crystalline Solids 299 (2002) 1219.

- A. Shah, J. Meier, E. Vallat-Sauvain, C. Droz, U. Kroll, N. Wyrsh, J. Guillet, and U. Graf, *Microcrystalline silicon and 'micromorph' tandem solar cells*, Thin Solid Films 403 (2002) 179.
- W. Soppe, J. Bailat, C. Droz, U. Graf, U. Kroll, J. Meier, and A. Shah, *Microwave plasma assisted VHF-PECVD of micro-crystalline silicon*, Materials Research Society Symposium Proceedings Vol. 715 (2002) A19.7.1.
- N. Wyrsh, C. Droz, L. Feitknecht, and J. Spitznagel, *Transport path in microcrystalline silicon*, Materials Research Society Symposium Proceedings Vol. 715 (2002) A25.3.1.
- N. Wyrsh, C. Droz, L. Feitknecht, P. Torres, E. Vallat-Sauvain, J. Bailat, and A. Shah, *Effect of the microstructure on the electronic transport in hydrogenated microcrystalline silicon*, Journal of Non-Crystalline Solids 299 (2002) 390.
- V. Daudrix, J. Guillet, C. Droz, L. Feitknecht, N. Wyrsh, X. Niquille, P. Winkler, and A. Shah, *Towards higher efficiency micromorph solar cells: the "inverted" (substrate n-i-p) configuration*, Proceedings of the 17th European Photovoltaic Solar Energy Conference, Munich, Germany (2001) 2846.
- J. F. Randall, C. Droz, M. Goetz, A. Shah, and J. Jacot, *Comparison of 6 photovoltaic materials across 4 orders of magnitude of intensity*, Proceedings of the 17th European Photovoltaic Solar Energy Conference, Munich, Germany (2001) 603.
- A. Shah, J. Meier, L. Feitknecht, E. Vallat-Sauvain, J. Bailat, U. Graf, S. Dubail, and C. Droz, *Micromorph tandem solar cells in the superstrate configuration (glas pin): status report and future perspective*, Proceedings of the 17th European Photovoltaic Solar Energy Conference, Munich, Germany (2001) 2823.
- Y. Ziegler, V. Daudrix, C. Droz, R. Platz, N. Wyrsh, and A. Shah, *More stable low gap a-Si:H layers deposited by PE-CVD at moderately high temperature with hydrogen dilution*, Solar Energy Materials & Solar Cells 66/1-4 (2001) 413.
- V. Daudrix, C. Droz, N. Wyrsh, Y. Ziegler, X. Niquille, and A. Shah, *Development of more stable amorphous silicon thin film solar cells deposited at "moderately high" temperature*, Proceedings of the 16th European Photovoltaic Solar Energy Conference, Glasgow, UK (2000) 385.
- M. Goerlitzer, P. Torres, C. Droz, and A. Shah, *Extension of the a-Si:H electronic transport model to $\mu\text{-Si:H}$: use of the $\mu^0\tau$ product to correlate electronic transport properties and solar cell performances*, Solar Energy Materials & Solar Cells 60/2 (2000) 195.
- A. Shah, E. Vallat-Sauvain, P. Torres, J. Meier, U. Kroll, C. Hof, C. Droz, M. Goerlitzer, N. Wyrsh, and M. Vanecek, *Intrinsic microcrystalline silicon ($\mu\text{-Si:H}$) deposited by VHF-GD (very high frequency-glow discharge): a new material for photovoltaics and optoelectronics*, Materials Science and Engineering B-Solid State Materials for Advanced Technology 69 (2000) 219.
- N. Wyrsh, C. Droz, L. Feitknecht, M. Goerlitzer, U. Kroll, J. Meier, P. Torres, E. Vallat-Sauvain, A. Shah, and M. Vanecek, *Hydrogenated microcrystalline silicon: from material to solar cells*, Materials Research Society Symposium Proceedings Vol. 609 (2000) A15.1.1.
- N. Wyrsh, L. Feitknecht, C. Droz, P. Torres, A. Shah, A. Poruba, and M. Vanecek, *Hydrogenated microcrystalline silicon: how to correlate layer properties and solar cell performance*, Journal of Non-Crystalline Solids 266 (2000) 1099.